ENVIRONMENT SENSITIVE FRACTURE OF Al-Zn-Mg WELDS

UNDER CYCLIC LOADING CONDITIONS

by

George Kotsikos BSc

(Sponsoring establishment
Dundee Institute of Technology
in collaboration with
Alcan International Ltd)

Thesis submitted to the CNAA in
partial fulfilment of the requirements
of the degree of Doctor of Philosophy

March 1992

DECLARATION

I hereby declare that the following work has been composed by myself and that this thesis has not been presented for any previous award of the C.N.A.A. or any other university.

George Kotsikos

ACKNOWLEDGMENTS

The author would like to thank Dr J.M. Sutcliffe, of the Department of Mechanical Engineering at Dundee Institute of Technology and Dr N.J.H. Holroyd of Alcan International Ltd for their supervision of the work and also to Dr Holroyd for his provision of valuable information and comment during the course of the project.

He is indebted also to the technical staff at Dundee Institute of Technology, in particular Mr I. Mc Nabb of the Mechanics of Materials Laboratory and Mr G. Baxter and Mr A. Stewart of the department's workshop.

Special thanks also to the staff at Alcan International Ltd, especially Dr W. Hepples and Mr D. Boomer, for their invaluable help and advice at various stages of the work and Mr C. Wiseman, for securing supplies of welded material.

Financial assistance by the Scottish Office Education Department and Alcan International Ltd is gratefully acknowledged.

ENVIRONMENT SENSITIVE FRACTURE OF Al-Zn-Mg WELDS UNDER CYCLIC LOADING CONDITIONS

George Kotsikos

A B S T R A C T

The environment sensitive fracture under cyclic loading of the white-zone of commercial 7017-T651 alloy weldments has been investigated. The K1c value for the white-zone was determined by using small cylindrical circumferentially grooved specimens as proposed by Stark & Ibrahim and a value of $22MNm^{3/2}$ was established Fatigue crack growth rates for the white-zone were obtained by utilising small arc-type specimens, similar to the one described in ASTM E399, over a wide range of frequencies from 0.01Hz to 10Hz. The enhanced growth rates in acidified (pH3) salt-chromate environment compared with dry air are not compatible with a simple superposition model as applied to 7079-T651 alloy. An enhancement of crack growth rates observed near the 1Hz load cycling frequency has been attributed to crack tip solution modification owing to the motion of electrolyte in and out of the crack enclave during fatigue. Fracture mode changes have been observed to take place at certain crack velocities and their dependence upon the square root of the reciprocal of the loading frequency are shown to be consistent with an environment enhanced crack growth rate involving diffusion of hydrogen ahead of the crack tip during each cycle. Striations observed on the fatigue fracture surface indicate a discontinuous crack propagation mechanism with the ACPD technique providing evidence of cracking initiating ahead of the crack tip, remote from the environment , with subsequent growth there and link up with the original crack. Such a model is consistent with indirect evidence that hydrogen accumulates at the region of maximum stress ahead of the crack tip facilitating cracking to initiate there. Acoustic emission results also point to such a mechanism. Crack closure effects have also been demonstrated to take place at the high frequency and low stress intensity ranges.

An interesting further observation was that for test frequencies above 10Hz fatigue cracks grew in a direction almost parallel to the loading axis invariably into the heat affected zone as soon as the environment was introduced, with the presence also of severe crack branching effects.

CONTENTS

INTRODUCTION

Aluminium alloys, originally developed for use by the aerospace industry, are now finding increasing use in other areas of engineering.

When London Underground completes its refurbishment of the Central Line, aluminium alloys will almost certainly be the main materials from which its new trains will be built. The basic train body design involves aluminium alloy profiles which run the full length of each carriage and are welded together at the ends. Germany's experimental high-speed trains, designed in Denmark, and the latest Paris Metro trains are also based on this design principle. In the automotive industry, the largest potential user of aluminium alloys in mechanical engineering applications, aluminium alloys have long been used for the cylinder head, cylinder block and pistons with many automotive component manufacturers working on further applications. Already a major Japanese automotive manufacturer has unveiled the first all aluminium vehicle and other major European manufacturers their experimental prototypes.

Aluminium alloys are also making their mark in the marine and offshore-oil industries, where the low density and relatively good corrosion resistance, compared with structural steels, are valuable assets. A recent Department of Energy report suggests that by turning to aluminium alloys, oil rig constructors could save between 40 and 70 per cent on the cost of offshore structures (1).

Engineering construction has been dominated by welding as its main joining process, making weldable aluminium alloys very promising in such engineering applications. Their increase in strength and ductility with falling temperature makes them particularly suitable for welded cryogenic assemblies. The extent of susceptibility of aluminium alloy welds to the various forms of cracking associated with welds and environment sensitive fracture is very important for their success as alternatives to steel. Alloys such as Al-Mg and Al-Mg-Si have been used successfully, with instances of service failure of weldments being rare and restricted to Al-Mg alloy welds.

The greatest potential for commercial exploitation is offered by the medium strength Al-Zn-Mg alloys (7xxx series) which are stronger than other weldable alloys, (Yield stress: 300-450 MPa) and in addition they offer a unique advantage when welded, in that heat affected zones, rather than having as-annealed properties, recover up to 80% of the parent material strength by precipitation hardening at room temperature. Commercial exploitation of these alloys in structural and transportation applications nevertheless remains limited owing to fears of weldments suffering environment sensitive fracture in service, usually taking place at the interface between the weld bead and the heat affected zone, termed "white-zone".

Tanks of the second and third stages of the European Ariane rocket, as well as the water torus on the second stage, are fabricated from aluminium 7020 alloy, artificially aged after welding. During tests on the L33-R2 prototype tank a crack about

100mm long appeared at a weld line. A similar crack appeared in the PT2 water tank after 17 days under pressure tests as low as 4 bar. In both cases the cracks were intergranular and the cause was found to be stress corrosion (2).

This is just one of many examples(3,4,5) of failure of Al-Zn-Mg alloy weldments by environment sensitive cracking in service, and there are numerous examples of similar failure occurring under laboratory conditions.

Environment sensitive cracking can be enhanced by the application of cyclic loading but, although a substantial amount of research has been carried out on the corrosion fatigue behaviour of aluminium alloys, relatively little attention has been paid to the interfacial region between stress corrosion cracking and corrosion fatigue, where intergranular environment induced fracture processes are accelerated by cyclic loading. Work published in this area on aluminium alloys is restricted to 7xxx series alloys in saline environments. The mechanisms whereby cyclic loading enhances crack growth rates in certain environments have been suggested to be similar to those proposed for stress corrosion cracking itself.

A complete mechanistic interpretation of stress corrosion cracking is still elusive, with authors divided between two basic mechanisms for stress corrosion crack propagation in 7xxx series alloys. One envisages cracking as highly localised anodic dissolution of grain boundary regions under the combined influence of stress and the environment and the other suggests embrittlement and loss of ductility promoted after the ingress of an aggressive

species (usually atomic hydrogen) onto or into the alloy.

In view of this, theories proposed thus far to account for crack growth rates observed in corrosion fatigue are open to debate. Attempts by various authors to establish mathematical models to predict corrosion fatigue crack growth rates (da/dN)cf, by using simple summation of components for crack growth rates applicable to fatigue in an inert environment, (da/dN)f, and crack growth rates appertaining to stress corrosion cracking, (da/dN)scc, have had limited success. The influence of frequency, particularly below 5Hz, has not been investigated in detail, leaving the theories proposed to date inadequate.

Furthermore, only a limited amount of work has been carried out on the intergranular crack growth enhancement by cyclic loading of Al-Zn-Mg weldments. In fact, to the author's knowledge, there have been no quantitative studies made for the "white-zone" of Al-Zn-Mg alloys, owing mainly to the small size of the area in question. The data existing so far on the white-zone are for tests performed under static or dynamic loading conditions interpreted in terms of time to failure or loss of ductility.

This work is an attempt to provide quantitative data for white-zone cracking under cyclic loading conditions. The work has been divided in two parts. Firstly in view of the limited amount of material available in typical weldments, a technique using subsize specimens had to be developed for the determination of the loading/ frequency domain within which Al-Zn-Mg weldments can

suffer environment sensitive fracture over a wide range of frequencies. The second part was an in depth investigation into the micromechanisms operative in the crack process zone.

CHAPTER 1

1. ALUMINIUM ALLOYS

1.1 General

Aluminium is the third most abundant element in the earth's crust. Since its first extraction in 1855 by H. Sainte-Claire Deville it remained an interesting curiosity until independent discoveries by Heroult in France and Hall in America in 1886 led to an economically viable method of extraction of aluminium from bauxite ore.

Aluminium is hardly used in a pure unalloyed form because of its poor mechanical properties. Although most metals will alloy with aluminium very few have sufficient solid solubilities to act as major alloying elements. These include zinc, magnesium, copper and silicon. Careful alloying has led to some very strong materials with good anti-corrosion properties, making aluminium alloys attractive alternatives to steel in engineering applications.

1.2 Age or Precipitation Hardening

The most important feature of aluminium alloys is their high strength-to-weight ratios achieved through their marked response to age or precipitation hardening. The term is applied both to the strengthening phenomenon and the process to achieve it.

The age hardening potential of aluminium alloys was first discovered accidentaly by Wilm in 1906, working on a 4%Cu, 0.5%Mg

alloy, later known as Duralumin. The fundamental reasons for the age hardening of the alloy remained unknown to Wilm until work by Mercia et al in 1919 demonstrated the decreasing solid solubility of copper in aluminium with decreasing temperature. By the late 1950's two concepts were postulated for the hardening mechanisms of aluminium alloys. One was that hardening was the result of interference to slip by particles precipitating on crystallographic planes. The other was that maximum hardening was associated with a critical particle size. Modern concepts of precipitation hardening take account these two ideas together with dislocation theory, since the strength of an age hardened alloy is controlled by the interaction of moving dislocations with precipitates. The size and shape of the precipitate particles, their nature, and the nature of the interface between a precipitate and its matrix, all have a great influence on the mechanical properties of the aged alloy, as these factors often determine whether or not glide dislocations moving in the matrix can pass through the precipitate.

The principles can be explained by referring to a specific Al-4%Cu alloy, fig(1.2.i). At approximately 550°C (eutectic temp.) the solubility of Cu in Al is about 5wt%, whereas at room temperature it is extremely low - ie the solubility of Cu in Al diminishes markedly as the temperature falls. At 550°C, the 4%Cu alloy, if in equilibrium, will consist entirely of the solid solution phase α. Slow cooling to room temperature will produce a two-phase condition - Θ (intermetalic compound, $CuAl_2$) precipitated in a matrix. The Θ will be precipitated on a coarse scale, and the alloy will not be in the strongest condition available.

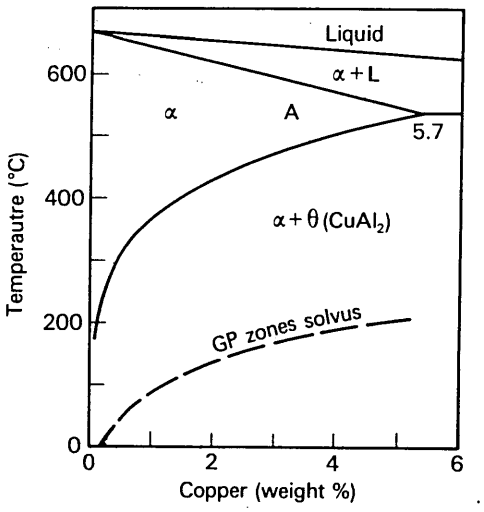

Fig 1.2.i. Equilibrium diagram of an Al-4%Cu alloy

A much stronger condition can be obtained through:

a) **solution treatment** :reheating the alloy to approximately 550°C and keeping in that temperature until all θ has redissolved and the α has obtained uniform composition, and then quenching into cold water. this simply retains the single phase α condition (supersaturated solid solution) at room temperature. The alloy would be soft and ductile.

b) **ageing** : heating the alloy to say 130°C and holding there; this resulting in an increase of hardness with time, eventually reaching a maximum. The alloy can then be used after returning to room temperature.

1.2.1 Hardening processes

X-ray diffraction and electron microscopy studies have indicated that the following sequence of changes occur within the alloy when it is held at the precipitation hardening temperature.

1. Clustering of Cu atoms into sheets occurs along specific planes in the Al matrix. The clusters, called 'Guinier-Preston' zones (G.P. zones) are in the form of circular discs about 30 atoms in diameter and 2 atoms thick, and are coherent with the matrix. Abundance of G.P. zones is approximately 10^{17}-10^{18} per cm^3.

2. The G.P. zones transform in situ by growth of some at the expense of others, to precipitates of Θ", which are some 1000Å in diameter and 100Å thick. This Θ" phase contains both Cu and Al atoms and has the composition of approximately $CuAl_2$. Θ" is also coherent with the matrix. These particles give the alloy its maximum hardness, but are too small to be seen under the optical microscope.

3. On further holding the Θ" particles dissolve in the matrix and are replaced by coarser particles of a phase called Θ'. These are only semi-coherent with the matrix and their formation is accompanied by reduction in hardness.

4. The final stage in the precipitation sequence is the formation of the equilibrium phase Θ, $CuAl_2$.

If Θ' and Θ are produced, the alloy is said to be overaged, these precipitates having a lower hardening effect than Θ" .
Several alloys such as Al-Zn-Mg age harden at room temperature over a period of time.

1.3 Aluminium-Zinc-Magnesium alloys (7xxx series)

Aluminium zinc magnesium alloys are medium to high strength alloys and can be used for both castings and wrought products. Poor castability due to a strong tendency toward shrinkage porosity, which lowers the mechanical properties of complex castings , has resulted in the bulk being used as wrought products. These alloys have been used in both road and rail transport applications, for lightweight military bridges and for armour plate. They are also especially suitable for cryogenic assemblies.

The importance of the Al-Zn-Mg system relies in its great potential for age hardening as compared with all other aluminium alloys. The medium strength alloys which contain very little or no copper have also the advantage of being readily weldable. These alloys differ from other weldable aluminium alloys in that they age harden significantly at room temperature. Moreover, the resulting strengthening effect is relatively insensitive to the cooling rate from high temperatures and they posses a very wide solution treatment temperature range, ie 350°C and above. For this reason there is a considerable recovery of strength after welding without any further heat treatment. The yield strengths of welded components can be as much as double those of common weldable alloys such as Al-Mg and Al-Mg-Si alloys.

Generally the content in both major and minor alloying elements governs the properties of the alloys. All the alloys in

this group contain more zinc than magnesium. The Zn:Mg ratio is critical with high ratios resulting in best strength and heat treatment response, together with the highest stress corrosion susceptibility, as shown by Gruhl (fig 1.4.i) ; low ratios producing the best weldability and lowest quench sensitivity.

Magnesium affects the energy expended during hot working and manufacturers produce low magnesium content alloys that can be extruded at low pressures and higher speeds. Low magnesium content though makes the alloys less quench sensitive resulting in a higher tendency to hot cracking. This is usually overcome by using filler wires with higher magnesium content than the parent plate when welding.

Copper favourably influences strength and stress corrosion susceptibility. The total amount of zinc plus magnesium plus copper is the controlling factor of the alloy properties and a short description is given in table 1.

Manganese, chromium and zirconium improve stress corrosion resistance and achieve better mechanical properties by inhibiting recrystallisation in wrought products. Zirconium also refines the size of the weld pool thus reducing tendency to hot cracking.

Boron and titanium additions are used to refine cast grain size, but titanium is said to reduce the general corrosion resistance in the heat affected zone of welds.

Alloy	Property	Annealed or as cast	Naturally aged	Artificially aged	Remarks
Wrought	Hv	500-600	1200-1300	1500-1700	high strength, low
High strength	UTS	250-350	450-350	550-650	corrosion resistance,
Zn+Mg+Cu >10%	YS	100-200	300-400	500-550	formability and weldability
	%el	10-20	10-15	5-10	
Wrought	Hv	400-500	900-1100	1200-1400	good weldability
Medium strength	UTS	200-300	400-500	450-550	and formability
Zn+Mg+Cu: 7-9%	YS	80-150	250-350	300-400	
	%el	12-25	15-20	8-15	
Wrought	Hv	300-400	700-900	900-1200	Highest stress corrosion
Low strength	UTS	150-250	300-400	400-500	resistance, best fabricability
Zn+Mg+Cu <6%	YS	60-120	200-300	300-400	
	%el	20-30	20-25	10-20	

UTS and YS values in MN/m^2
Cu does not exceed 2wt% in all cases

Table 1. Influence on properties of Al-Zn-Mg alloys (7xxx series) of total Zn+Mg+Cu content.

1.4 Age Hardening of Al-Zn-Mg alloys

The ageing of a supersaturated solid solution of Al-Zn-Mg, involves the following stages:

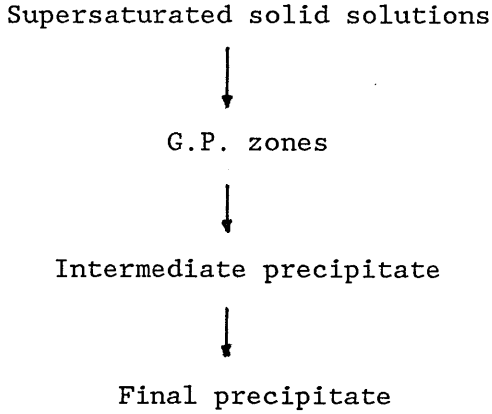

Above a critical temperature, the G.P. zones disappear and only coarse particles form from the beginning. The movement of excess vacancies enhances the formation of G.P. zones. At lower temperatures there is no nucleation barrier for the formation of zones but above the critical temperature nucleation is mainly on lattice defects, among which are prominent the dislocation groups that result from condensation and collapse of vacancies. There are indications that the zones start mainly as zinc clusters and the magnesium difuses into them at a slower rate. During ageing the diameters of the zones increase reaching a maximum of 100Å after prolonged ageing. The solute concentration in the zones exceeds 50% at this stage and keeps increasing with time even though only a small fraction of the total solute is present in the zones and most of it is still in the matrix.

Precipitate free zones form around the grain boundaries and sub-boundaries and around undissolved particles and precipitated

particles of Mn-Cr-Fe compounds.

Some coarse precipitates may form at the grain boundaries and two types are known to form in the Al-Zn-Mg system: hexagonal η ($MgZn_2$) and cubic T ($[AlZn]_{49}\,Mg_{32}$). Both types may form in air cooled specimens but only η has been observed to form in quenched specimens. The controlling parameter for the amount of hardening and time required for precipitation is the Zn:Mg ratio. (6)

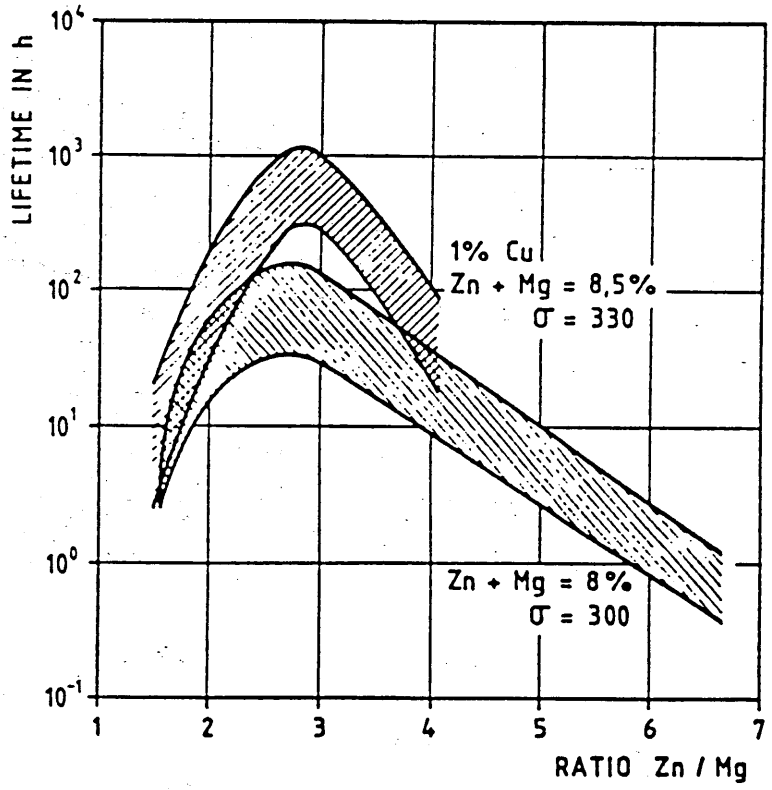

Fig 1.4.i Effect of Zn:Mg ratio on the susceptibility of Al-Zn-Mg alloys to stress corrosion cracking (6).

Maximum strength is achieved when the Zn:Mg ratio is between 2:1 and 4:1 and the higher the Zn+Mg content the greater the strength but at the expense of stress corrosion resistance, fig 1.4.i.

1.5 Welding of Al-Zn-Mg alloys.

In most structural applications Al-Zn-Mg alloys are joined by one of the inert-gas shielded processes. The metal inert gas (MIG) process is used for section thicknesses above 6mm while either the tungsten inert gas (TIG) or pulsed metal inert gas (PIG) processes for thicknesses below 6mm.

If an alloy is said to posses good weldability then the welds produced should be free of defects, such as hot cracks, and any reduction in strength, ductility, corrosion resistance and stress corrosion resistance of the weld or the heat affected zone, should not be to an unacceptable level.

1.5.1 Factors affecting hot cracking strength and ductility.

The magnesium content is found to affect the hot cracking tendency of welds, which increases with decreasing magnesium content. Hot cracking tendency can also be reduced by the introduction of zirconium into the weld pool.

The choice of filler wire composition affects the mechanical properties of welds and the most commonly used is an Al-5%Mg alloy wire which gives adequate strength in most applications and is readily available.

One of the most important factors for the strength of welds is the natural ageing time (7). Strength and ductility of Al-Zn-Mg welds increase with time for periods greater than a year (fig 1.5.1.i)

Time after welding	0·2% PS tonf/in²	(MN/m²)	UTS tonf/in²	(MN/m²)	El., %	Position of failure
Immediately after welding	7·4	(114)	14·8	(228)	19	HAZ, 1 in (25 mm) from weld centreline
Naturally aged for 1 week	11·0	(170)	20·0	(309)	12	"
Naturally aged for 1 month	12·7	(196)	21·2	(327)	14	"
Naturally aged for 3 months	13·2	(204)	20·9	(322)	11	Edge of weld

Parent metal: ¼ in (6 mm) extrusion Al : 4·6% Zn : 1·2% Mg
Weld filler: Al : 5% Mg
*Military Engineering Experimental Establishment unpublished results

Fig 1.5.1.i Effect of natural ageing time on the strength of Al-Zn-Mg alloy welds.

1.5.2 Mechanical aspects of cracking of welds.

Al-Zn-Mg welds exhibit stress corrosion susceptibility which is a phenomenon requiring the conjoint action of a tensile stress component and an aggressive environment. In welded fabrications apart from residual stresses introduced during misfits in assembly, applied constant stresses from clamps etc., residual stresses arise as a result of shrinkage or distortion due to the welding process and for most reported failures on Al-Zn-Mg welds, these stresses were responsible. The level of these stresses increases with the thickness of the sections being welded and the total amount of welding carried out. Various methods have been adopted over the years to reduce the effects of residual stresses for various types of welds but an analysis of these is beyond the scope of this work.

1.5.3 Metallurgical aspects of cracking of welds.

As with Al-Zn-Mg parent plate, the stress corrosion susceptibility of the weld depends on precipitation hardening. Precipitation in the weld and the heat affected zone continues for many years at ambient temperature and that may be responsible for welds developing cracks after many years in service, since it is known that stress corrosion susceptibility decreases at first and then increases with prolonged ageing times. Another factor that has been found to affect cracking susceptibility and mechanical properties of welds is microsegregation that occurs during weld solidification. The mechanisms and the degree of segregation taking place during solidification are still not well understood and a lot of work is being carried out worldwide in this area (7).

CHAPTER 2

2. STRESS CORROSION CRACKING

2.1 General

Stress corrosion cracking is defined as the premature failure of metallic alloys in the presence of a tensile stress and an often mildly corrosive environment. There are several characteristics of this phenomenon that are intriguing:

a) It is often that alloys which are most resistant to general uniform corrosion that are most susceptible to stress corrosion cracking. For example some aluminium and titanium alloys, Fe-Cr-Ni (austenitic) stainless steels etc. which resist corrosion because of the presence of passive films.

b) Some alloy environment couples are particularly susceptible to stress corrosion cracking. For example aluminium alloys are most susceptible in seawater (Cl and other halides)

c) Pure unalloyed metals are generally resistant to stress corrosion cracking.

d) Normally ductile materials fail in what appears to be a brittle manner in the presence of certain environments.

2.2 Mechanisms of stress corrosion carcking.

The various models of stress corrosion cracking can be divided into two basic classes: those which consider that crack propagation proceeds by anodic dissolution (dissolution models) and those which consider that cracking is essentially mechanical.

a) Crack propagation by the dissolution of film-free metal due to an increase in the number of active sites provided by plastic deformation at the crack-tip.

b) Crack propagation by the dissolution of metal at the crack-tip as a consequence of the rupture of otherwise protective surface films by emergent dislocation (film rupture or slip step dissolution model).

c) Propagation of cracks by the repeated formation and rupture of a brittle film growing into the metal at the crack tip.

d) Adsorption (stress sorption) of surface active species, the consequence of which is a reduction in the surface energy required to form a crack and, therefore, reduced fracture stress (embrittlement mechanism).

Fig 2.2.i. shows diagramatically all the important processes that affect stress corrosion cracking (8)

An evaluation of the mechanisms of stress corrosion cracking in general is beyond the scope of this work, therefore attention will concentrate in the knowledge so far of the stress corrosion behaviour of Al-Zn-Mg alloys.

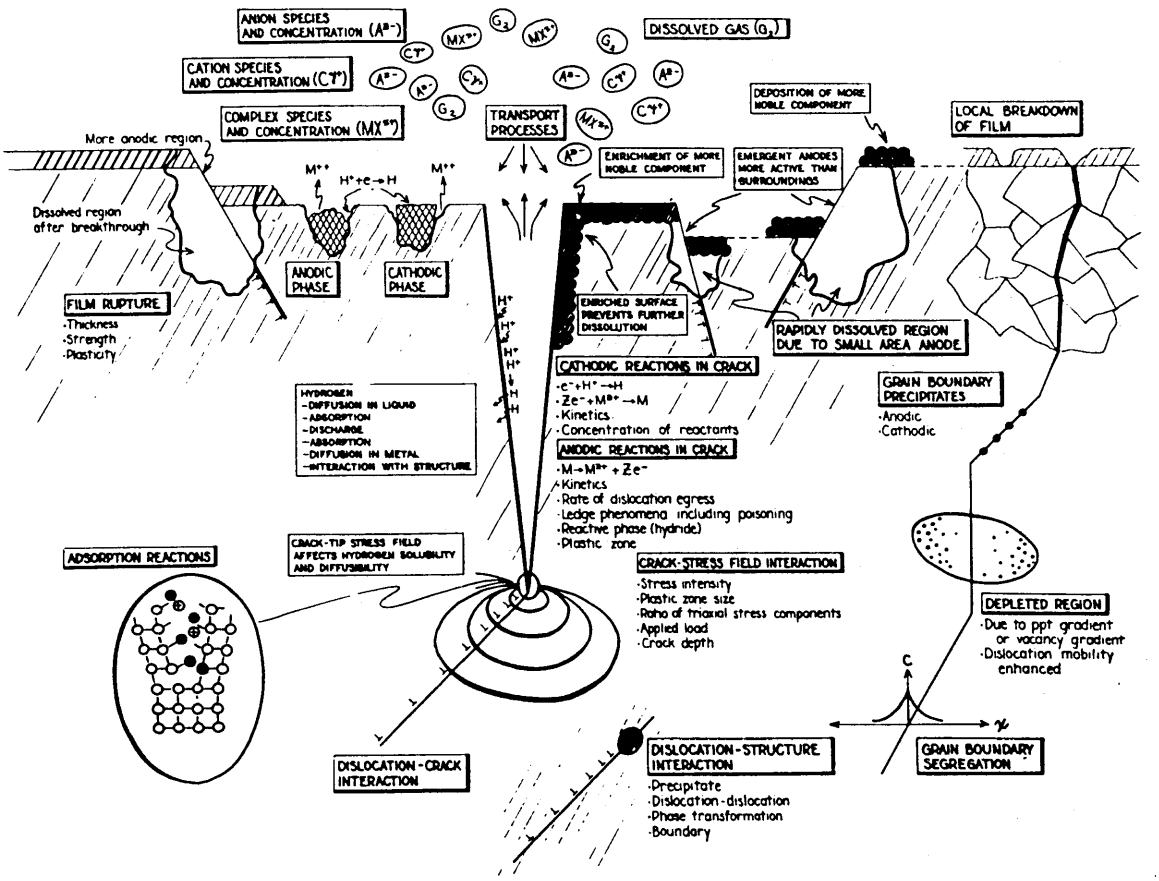

Fig 2.2.1 Montage showing important processes which affect stress corrosion cracking (8)

2.3 Stress Corrosion Cracking of Al-Zn-Mg alloys

Generally the corrosion resistance of Al-Zn-Mg alloys is good, especially for alloys with lower copper and zinc contents. Unfortunately all the alloys of this group are at least to some extent, susceptible to stress corrosion cracking or exfoliation, and there are numerous reported cases of service failures. Corrosion cracking susceptibility can be improved by careful alloying, eg. with additions of copper or silver, but that may be at the expense of other properties or production costs. More commonly improvements in the corrosion cracking susceptibility of Al-Zn-Mg alloys is achieved by various thermal treatments.

2.3.1 Effect of thermal treatments

The effect of thermal treatments relies on the changes that take place in the alloy's microstructure and several attempts have been made to correlate stress corrosion cracking susceptibility with the various associated microstructural changes. As yet, no single microstructural parameter has been found that controls the stress corrosion cracking of 7xxx series alloys. The reasons for that are firstly the virtual impossibility of varying only one parameter during heat treatments, when it is known that most parameters could change during ageing of a solution heat treated and quenched alloy, and secondly the dependence of stress corrosion cracking susceptibility with one parameter does not dismiss the possible dependence on other parameters. In addition, most of the work has been carried out on laboratory cast and processed alloys

subjected to laboratory heat treatments which differ from commercial thermal mechanical practices and wrought products of commercial alloys.

For the case of solution treated alloys Pickens & Langan (9) for a laboratory cast Al-7Zn-3Mg alloy and Taylor & Edgar for 7004 alloy (10) have shown that stress corrosion cracking susceptibility increases as the solution temperature decreases, while Shastry et al for 7075 alloy (11) have found the opposite. This difference is attributed to recrystallisation and grain growth which agrees with Taylor and Edgar's result for their high solution temperature test at 575°C where significant grain growth takes place (fig 2.3.1.i, ii)

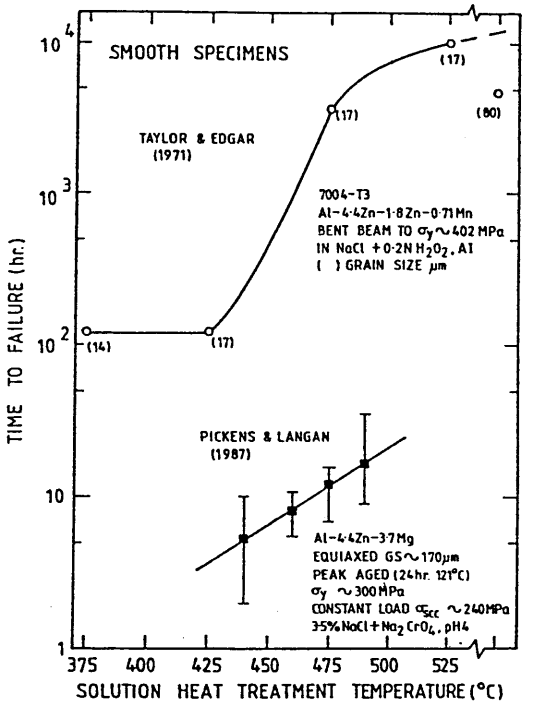

Fig 2.3.1.i Effect of solution heat treatment upon SCC behaviour of Al-Zn-Mg smooth specimens in saline environments (9,10)

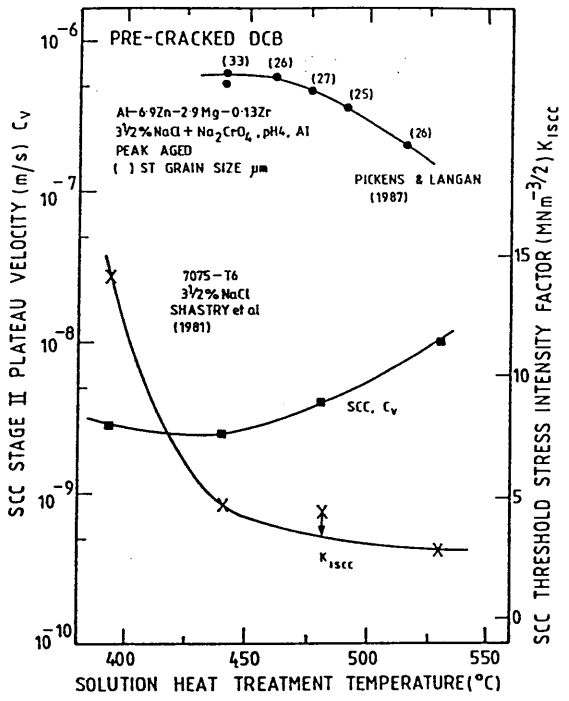

Fig 2.3.1.ii Effect of solution heat treatment upon SCC behaviour of Al-Zn-Mg pre-cracked specimens in saline environments (9,11).

The effect of quench rate has not been established for 7xxx series alloys. The generally accepted view relates quench rate with copper content. For low copper content alloys stress corrosion cracking susceptibility is reduced by slower quench rates (12, 13) where the reverse is true for alloys containing more than 1% copper.(13)

2.3.2 Effect of thermal ageing

The response to age hardening of 7xxx series alloys is well established with Speidel demonstrating the effect of isothermal ageing upon stress corrosion susceptibility (fig 2.3.2.i). As can

be seen from fig 2.3.2.i the max strengths resulting from peak ageing cannot be fully exploited because of stress corrosion susceptibility peaking prior to maximum strengths. Ageing, as discu. ed earlier (section 1.2), depends on the dislocation/ precipitate interactions, it is reasonable therefore to argue that

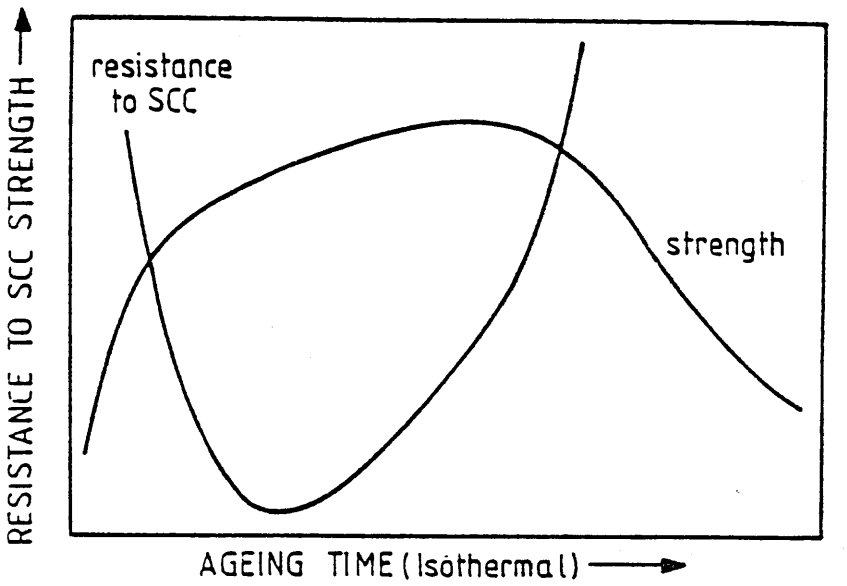

Fig 2.3.2.i Dependence of SCC resistance with thermal ageing for precipitate hardening aluminium alloys (14).

stress corrosion cracking susceptibility must involve to some extent the nature, volume fraction and coherency of the precipitate. The precipitate- free zone width is unlikely to be a critical parameter as most investigations have shown little or no effect upon stress corrosion cracking. The only involvement of the precipitate free zone comes from Lynch's investigation (15), where he has reported that at some instances cracking involves microvoid coalescence and propagates within the precipitate-free zone.

Middleton & Parkins (16) suggest a grain boundary propagation mechanism, where propagation takes place via $MgZn_2$ grain boundary

precipitates acting as an active path for corrosion, with creep not allowing passivation of the crack tip thus allowing dissolution to take place at grain boundaries. Poulose et al (17) modified these ideas and claim that grain boundary precipitates act as sacrificial anodes retarding stress corrosion cracking. They also found that

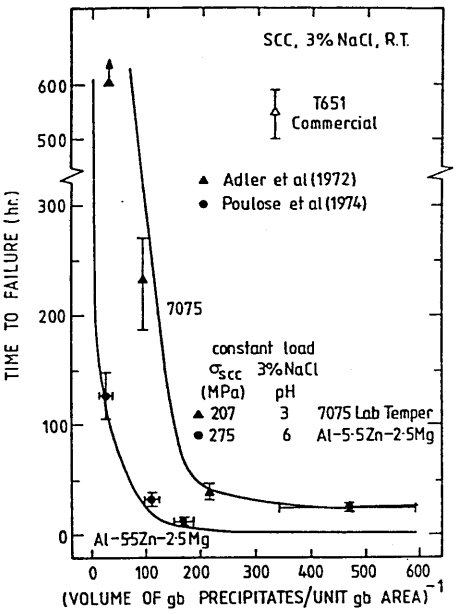

Fig 2.3.2.ii. Relationship between SCC behaviour and the volume fraction of grain boundary precipitates for 7xxx series alloy smooth specimens in 3 to 3.5% NaCl

crack growth rates in the K independent domain are inversely proportional to the volume fraction of $MgZn_2$ precipitate (fig 2.3.2.ii) maintaining that the volume fraction of precipitate is critical rather than the number or size of the grain boundary precipitate. Park (18) has recently shown though for alloy 7075 in 3.5% saline environment that a logarithmic relationship exists between K independent region crack velocities and the volume of grain boundary precipitates / unit grain boundary area (fig 2.3.2.iii).

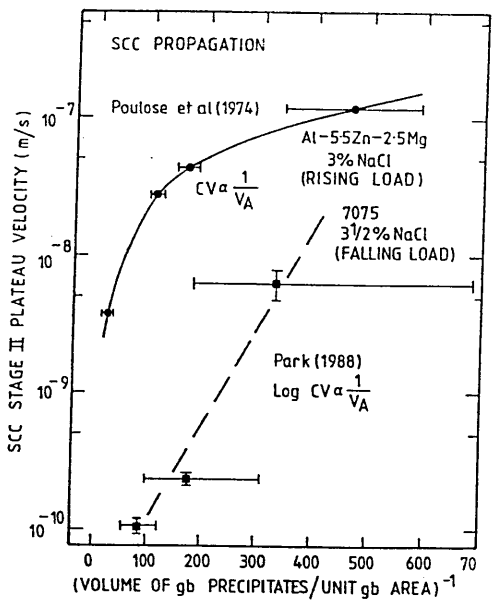

Fig 2.3.2.iii Relationship between the SCC stage II velocity and the volume fraction of grain boundary precipitates for 7xxx series alloys (17,18).

For 7xxx series alloys the beneficial effects that can result from overageing depend largely on the copper content (19). Alloys with copper contents below around 1% require gross overageing before high resistances are achieved while alloys with higher copper contents need only sacrifice 10 to 15% of the maximum strength (20) as is exploited in the commercial T73 duplex ageing practices developed in the 60's (21).

Sarkar et al (22) investigated the effect of ageing upon stress corrosion cracking of commercially cast and fabricated Al-6Zn-2Mg-xCu alloys containing various copper levels and suggested the following for alloys in the T651 temper:

a) In region 1 copper levels up to 1wt% had little influence upon either stress corrosion crack growth rates or deformation mode, whereas for higher copper levels, slip homogeneity increased and crack velocities decreased.

b) In region 2 the stress corrosion crack growth rates progressively decreased with increasing copper level because copper entered hardening precipitates, making them more electrochemically noble and reducing electrochemical differences in the crack tip region.

For overaged copper free alloys the transition of the deformation mode from predominantly inhomogeneous to a homogeneous one promoting reduced stress concentration at grain boundaries was thought to be responsible for the reduced crack growth rates.

For copper containing alloys, both copper enrichment of precipitates and homogenisation of deformation were thought to be important, fig 2.3.2.iv, v.

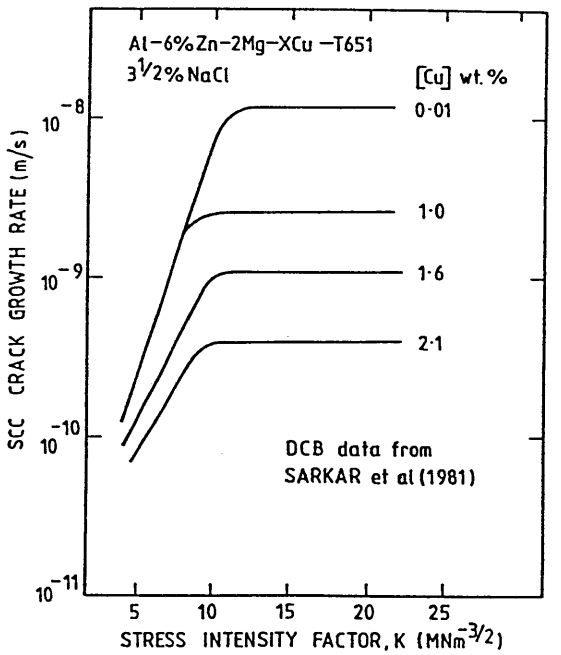

Fig 2.3.2.iv Effect of copper content on the sc crack growth rate of Al-6Zn-2Mg-xCu alloys in 3% NaCl (22).

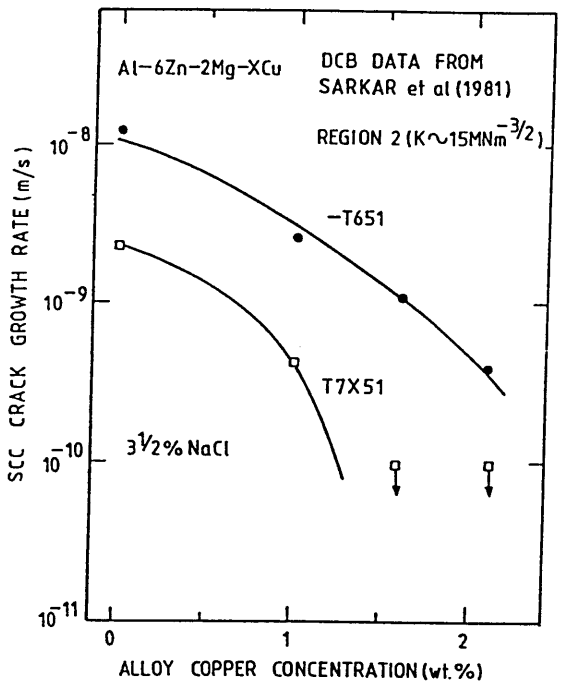

Fig 2.3.2.v Effect of various copper concentrations on the stage II plateau velocity of Al-6Zn-2Mg-xCu alloys in 3% NaCl (22)

2.3.3 Effect of gaseous environments

Since early times it has clearly been demonstrated that air does promote stress corrosion susceptibility relative to tests performed in vacuum. At first oxygen was considered the responsible agent for this, since the presence of oxygen in aqueous solutions had been demonstrated as necessary to induce cracking for certain systems. However oxygen is not an absolute requirement for the inducement of corrosion cracking and the role of hydrogen has been reported.

Although most of the data available on the SCC of aluminium alloys are for aqueous environments some data exist on the 7xxx series alloys in gaseous environments and Speidel (23) has

summarised the influence of gaseous environments upon the scc of 7xxx series alloys as follows:

1) scc initiation or propagation does not take place in dry gases
2) scc initiates almost immediately in wet gases when precracked specimens are loaded to levels near K_{1c}
3) stress corrosion cracks are predominantly intergranular and the humidity level rather than gas composition controls the crack growth rate
4) since scc is observed at low humidity levels where condensation at the crack tip does not occur, the cracking cannot be attributed to anodic dissolution and the most probable controlling mechanism must be hydrogen embrittlement.

2.3.4 Effect of aqueous environments

Most of the information on the influence of solution composition, pH, viscosity etc is restricted on 7xxx series alloys with the majority of data being contributed by Speidel (21) and Speidel and Hyatt's work (24) on a 7079 T651 alloy. Even though these results are debatable, since the 7079 alloy is not representative of the 7xxx series alloys as it exhibits stress corrosion crack growth rates significantly higher than other 7xxx series alloys, many points of their work are still accepted in the absence of a quantitative study of the scc of 7xxx series alloys in aqueous environments.

Speidel has proposed that the stress corrosion crack growth in 7xxx series alloys is not specificaly affected by the presence of Na^+, K^+, Li^+, Al^{3+}, NH_4^+, cations in neutral chloride environments, except perhaps influencing the solubility products and limiting the local concentration of specific ions. Existing data on testing smooth specimens of a 7075 T651 alloy suggest that crack initiation is not affected by chloride ion concentrations above 0.5M. A different picture emerges for crack propagation where there is a minimal effect for concentrations up to 0.1M but an increase for levels above 0.1M with crack growth rates peaking at 1M concentration. That was associated with dissolved oxygen levels which peak at similar chloride concentrations.

2.3.5 Effect of solution pH

It is well established in the literature that bulk solution pH does have an effect on the stress corrosion behaviour of aluminium alloys and for saline environments stress corrosion susceptibility is reduced as the solution becomes more alkaline. Constant load tests carried out by McHarty and Hollingworth (26) on a 7075 T651 alloy in NaCl solutions have shown that stress corrosion susceptibility decreases with increasing pH exhibiting a sharp improvement for pH values above 10, fig 2.3.5.i. Later constant strain rate tests on the same material and evironment carried out by de Jong (27) revealed a different picture where no appreciable change occurs for pH values between 4 and 12 but a sharp drop in stress corrosion cracking resistance is exhibited for pH values below 4, fig 2.3.5.ii. The results have also been

reproduced by Holroyd & Scamans (28). De Jong's data though if plotted as crack growth rates vs pH show a logarithmic increase of crack growth rates either side of pH 7 with a discontinuity at around pH 10, fig 2.3.5.iii.

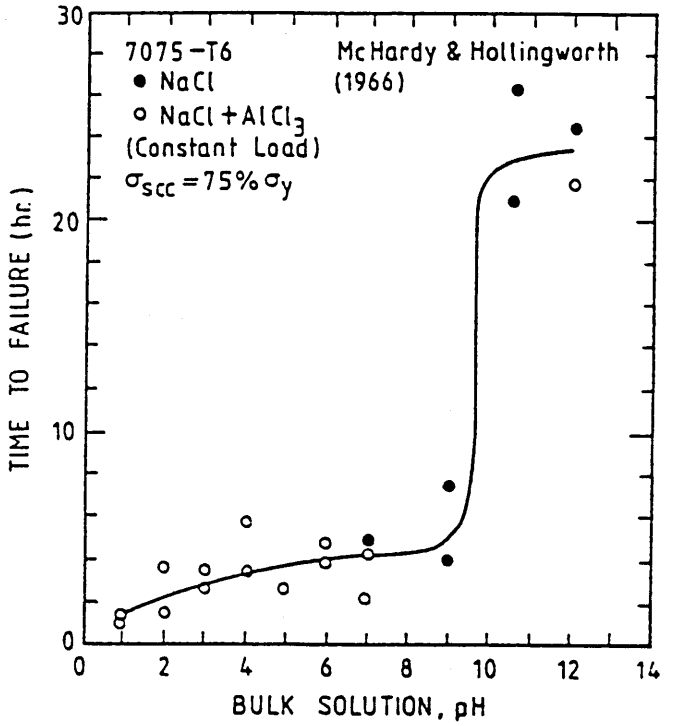

Fig 2.3.5.i. Effect of bulk solution pH on the SCC behaviour of a 7075-T6 alloy under constant loading conditions. (26)

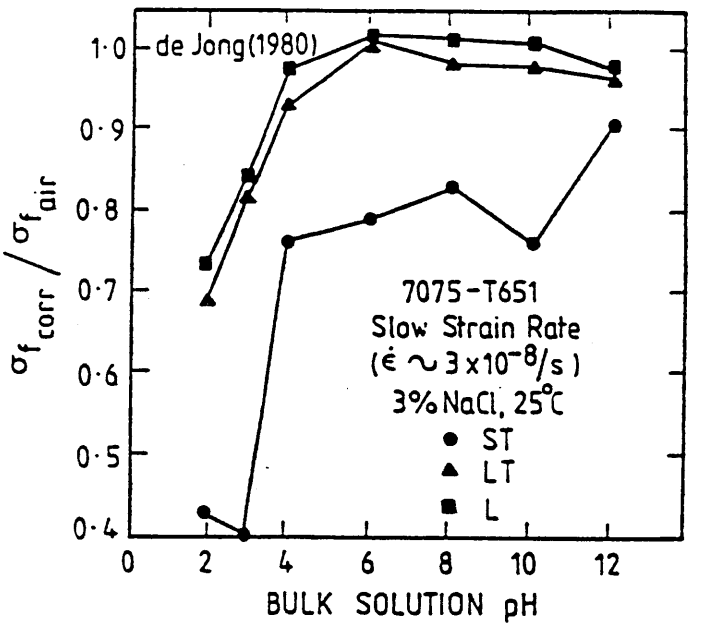

Fig 2.3.5.ii Effect of bulk solution pH on the SCC behaviour of a 7075-T651 alloy under slow constant strain rate testing (27).

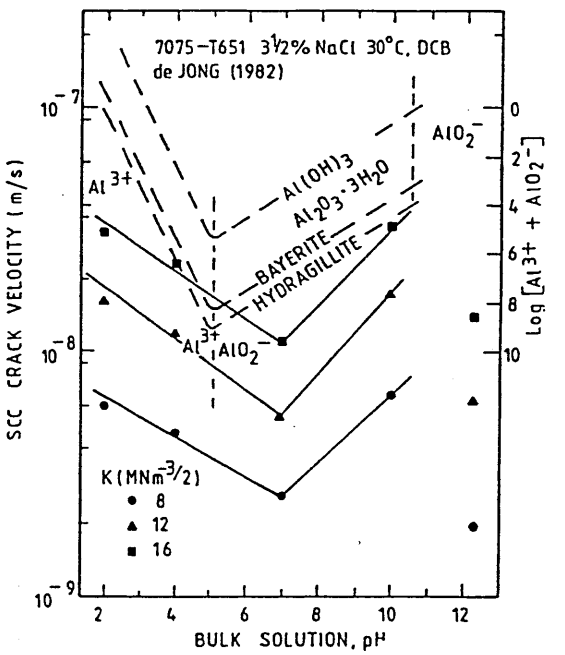

Fig 2.3.5.iii. Crack growth rates as a function of bulk solution pH for 7075-T651 suffering SCC in 3.5% NaCl at various stress intensity factors (119)

2.3.6 Environmental conditions within cracks

It is well known that most phenomena of localised corrosion in the presence of aqueous solutions take place under conditions where the access of the electrolyte is restricted, due to a particular geometry of the corroding material, like riveted plates, threaded joints, or narrowness of intergranular or transgranular cracks. In fact for many metals and alloys susceptible to stress corrosion cracking immunity or general corrosion is exhibited (without the development of cracks) in the abs ence of restricted geometries.

The fact that the environmental conditions within the crack enclave differ significantly from bulk solution conditions has been known for over 20 years and a lot of work has concentrated in trying to analyse these solution conditions in the effort to understand the stress corrosion cracking process operative in aluminium alloys. The difficulty with such analysis is the limited volume of solution and its inaccessibility and several attempts have been made to overcome these difficulties by:

1) simulation of local environment conditions by minimizing solution volume to surface area ratio, done by immersing alloy shavings into restricted amounts of solution

2) monitoring local solution pH and electrochemical potential within real and artificial cracks using in-situ microelectrodes

3) ex-situ methods by extracting frozen solution from cracks or using a room temperature freezing technique by using specific solution gelling agents and

4) post fracture analysis of fracture surfaces using high resolution electron microscopy and surface spectroscopy techniques.

The shavings approach was adopted by Sedricks et al (28) as far back as 1970 on a 7475 T651 alloy with encouraging results. Later Holroyd et al (29) working on the same alloy observed that if the initial solution pH was below 3.5 then their results were identical to the ones quoted by Sedricks but if the solution pH was above 3.5 the solution pH in the shavings became alkaline within a few minutes. In addition if experiments were extended to longer times (ie. > 2hrs) all solution pHs eventually became alkaline unless the initial pH was below 2, fig 2.3.6.i. If the shavings prior to testing were given a short wash in NaOH to replace the "as machined" oxide layer with one formed in an aqueous environment, solution pHs went acidic and approached values quoted for stress corrosion cracks (fig 2.3.6.ii). From this observation it was suggested that the shavings approach is a reasonable simulation of a crack enclave region for 7xxx series alloys when the surface condition of the shavings is similar to the oxide composition of crack walls close to crack tips. The shavings approach gives reproducible results if the V/A (volume solution/metal area exposed) ratios are below 0.08cm (29). It is not clear as yet whether the V/A ratio alone is sufficient to describe the geometry required for crack-tip solution to develop.

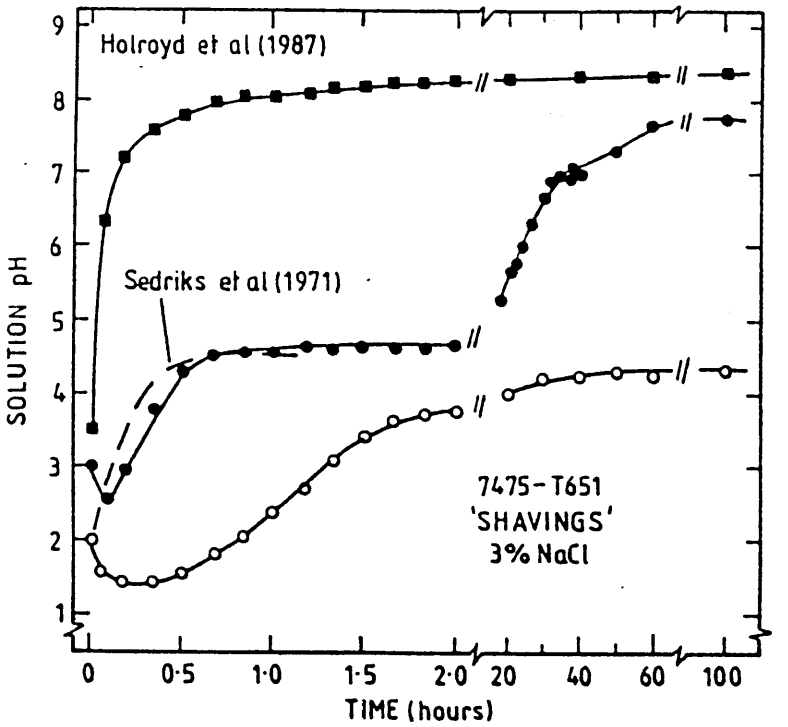

Fig 2.3.6.i. Solution pH as a function of time for 7475 shavings exposed to 3% NaCl solutions with various critical pH values (28,29).

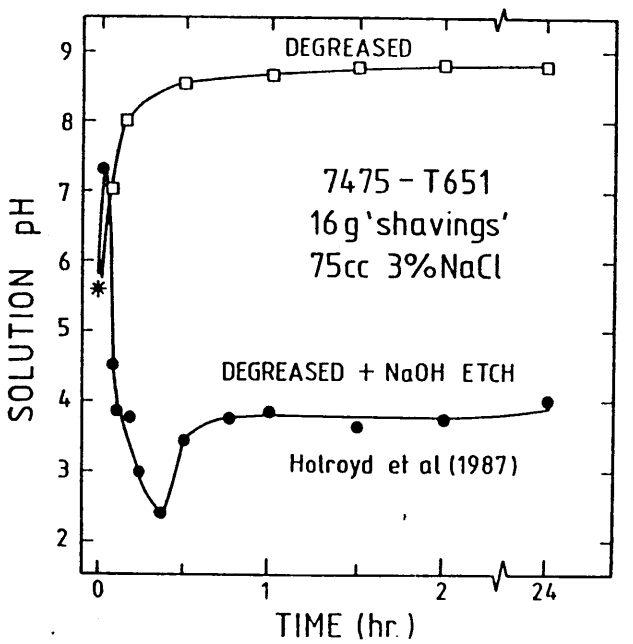

Fig 2.3.6.ii. Influence of solution pretreatment upon pH-time behaviour given by 7475 shavings exposed to 3% NaCl solution (29).

Direct in situ measurements had first been carried out by Davis in 1970 who used specially developed microelectrodes to measure solution pH and electrochemical potentials within stress corrosion cracks for 7075 T651 exposed to 4.5% potassium chloride solution (30) . The results confirmed the significant difference between solution pH within the crack enclave and bulk solution pH and showed that solution pH's within cracks move to values around 3.5 to 4 independent of the bulk solution pH in the range between 2 to 10. Davis's results have been reproduced by other workers, like Foley et al (31) for a 7075 alloy in chloride solution where pH 3 was measured within cracks, but it cannot be confidently claimed that these are conditions at the crack tips but rather near the crack tip region due to the large size of the electrodes as compared with the crack tip geometries.

The freezing thawing technique developed by Brown (32) and the extraction method of Holroyd et al (29,33) have produced a more quantitative characterization of solution chemistries within stress corrosion crack enclaves for 7075 type alloys. Solution pH's at the crack tip are consistent with the equilibrium process:

$$Al^{3+} + H_2O \rightleftharpoons Al(OH)^{2+} + H^+ \qquad (1)$$

controlling local pH, if solution pHs are below about 4.
Nguyen and Foley (31) have suggested the possibility of other processes

$$Al(OH)^{2+} + Cl^- \rightleftharpoons Al(OH)Cl^+$$

$$Al^{3+} + Cl^{-} \rightleftharpoons AlCl^{2+}$$

Such processes not only tie up chloride ions but may also react further to form $Al(OH)_2Cl$ or $Al(OH)Cl^{+}$ as reported by Turner and Ross (34) as the initial solid phases formed during the hydrolysis of aluminium chloride.

It has been suggested that crack tip solution chemistries alone are not sufficient to trigger stress corrosion cracking. This reasoning has been supported by the work of Nguyen et al[31] who showed identical local chemistry in both susceptible and immune to stress corrosion cracking alloys, and crack initiation in chloride environments when crack tip solution has not been acidified. This implies that a further critical process seems to be necessary to initiate cracking in aluminium alloys (31).

2.3.7 Effect of electrochemical potential

It is known that the electrochemical potential influences stress corrosion cracking susceptibility in aluminium alloys and it has been shown that all medium and high strength alloys can suffer stress corrosion cracking under appropriate anodic polarization. (35,36). The relationship between external potential and crack tip potential is important. Davies (37) and later Edwards (38) have shown that the effect of external anodic or cathodic polarization becomes less influential upon crack tip potentials as external potentials move away from the free corrosion potential, fig 2.3.7.ia,b. The influence of crack tip potential upon stress corrosion cracking is currently under debate, especially its effect

on hydrogen embrittlement, with some researchers using the result that mild cathodic polarization retards stress corrosion cracking while anodic polarization accelerates it, thus excluding any hydrogen embrittlement effects (39), while others have shown that anodic polarization enhances hydrogen entry (40).

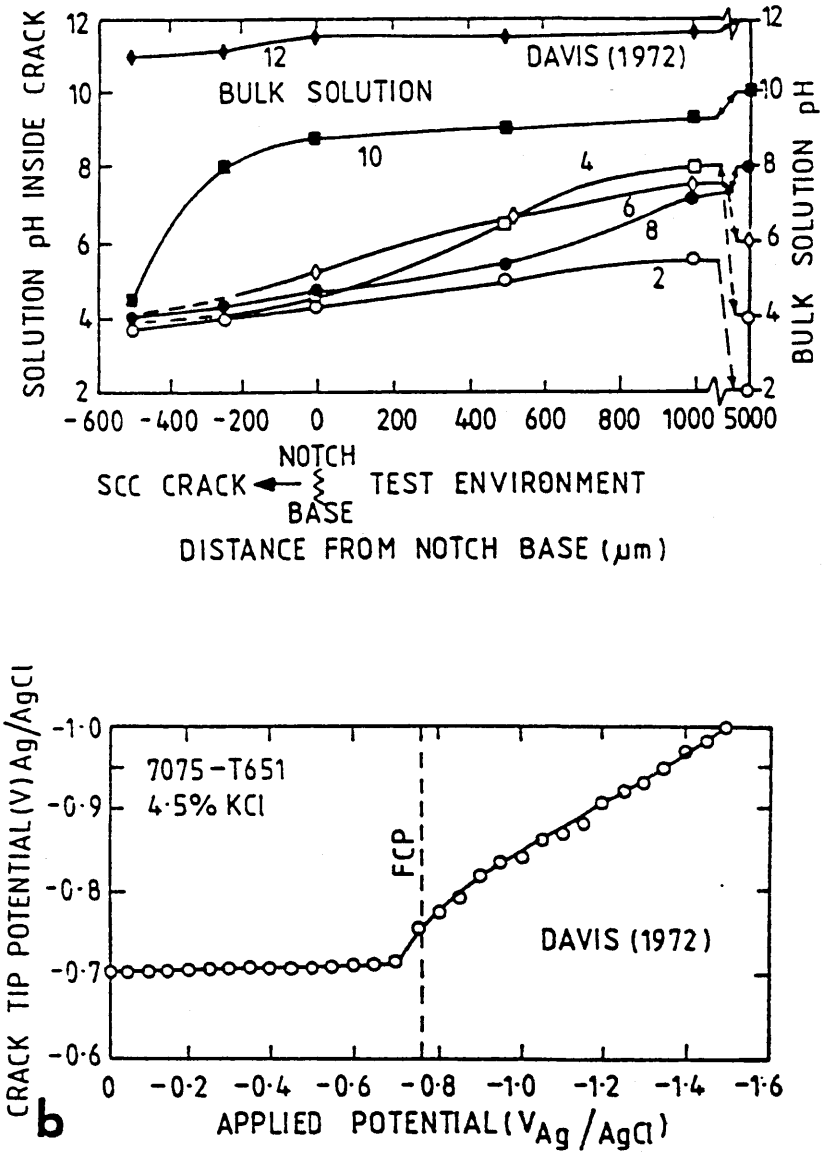

Fig 2.3.7.i Environmental conditions within propagating SCC cracks for 7075-T651 immersed in 4% KCl bulk solution; a) solution pH in crack as a function of distance from the starter notch for a range of bulk solution pHs and b) crack-tip electrode potential as a function of externally applied potential in a neutral pH 4.5% KCl solution (37).

2.4 Hydrogen embrittlement

Hydrogen embrittlement was first identified as a problem as far back as 1874 by Reynolds and 1880 Hughes who were the first to observe the detrimental effects of hydrogen on the ductility of iron. It is now well established in the literature that hydrogen present either as an external gas environment or dissolved cations can cause internal cracking or reduce dramatically the toughness of various metals and alloys. Hydrogen entry may be described by the equation:

$$H^{+} + e^{-} \longrightarrow H_{ads} \longrightarrow H_{abs}$$

The effects of hydrogen can depend either on mechanical variables such as strain rate, loading mode, temperature or metallurgical variables such as composition, microstructure and thermal treatment

The sources of hydrogen are numerous and once hydrogen enters the material its transport and subsequent locations are critical. Fig (2.4.i) describes briefly the sources, transport, microstructural locations and fracture modes in hydrogen processes and an explanation is given below.

a) Hydrogen can be present in three forms in a metal:

i) as a dissolved atomic species in equilibrium with a general or local potential

ii) adsorbed in heterogeneities of varying strengths

iii) recombined in molecular form.

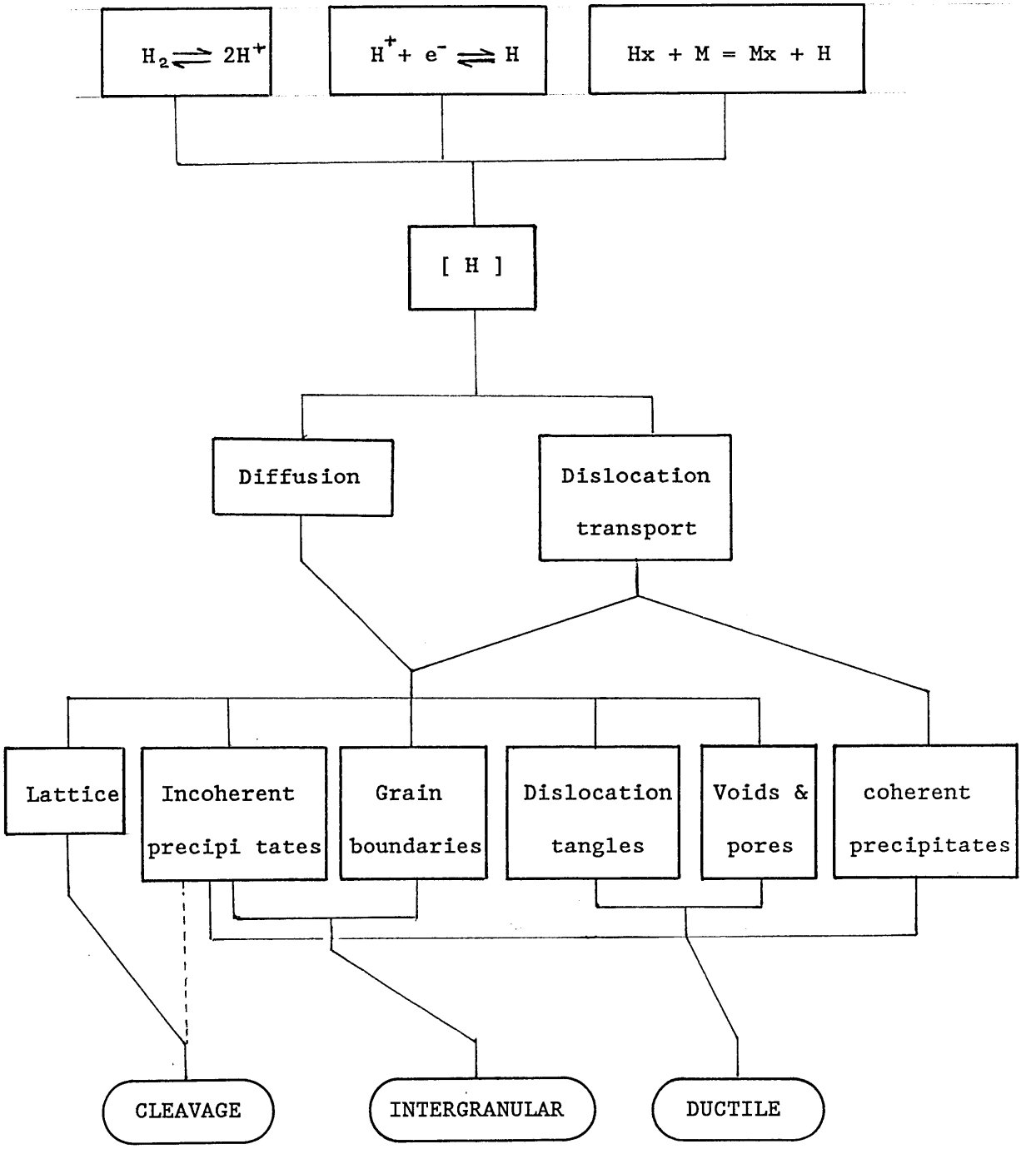

Fig 2.4.i Schematic representation of Hydrogen processes. Sources, transport, microstructural locations and fracture modes.

b) Hydrogen is seen to move by lattice diffusion and as Cotrell atmospheres on mobile dislocations (41) with the former applicable to high diffusivity metals and the latter to low diffusivity ones.

c) Dislocation transport is accelerated in materials exhibiting planar slip. The slip planarity can be either intrinsic or a result of hydrogen modifying the stacking fault energy (41).

d) Hydrogen is attracted to perhaps all heterogeneities in the lattice; dislocations, grain boundaries, particles, voids, local stress fields, all positively interact with hydrogen. Concentration around heterogeneities will depend upon the local chemical potential or the binding energy. A special case of this is found in alloys capable of forming hydrides.

2.4.1 Mechanisms of hydrogen embrittlement

The sources of hydrogen as stated above are important in determining the mechanism of hydrogen embrittlement and depending on which one dominates, different mechanisms for embrittlement may operate. The possible mechanisms operative are:

1. Hydrogen can affect interatomic forces between bonds and in particular reduce the cohesive force at or near the crack tip (42). This theory is supported by the observation of excess hydrogen accumulation at regions of high triaxial stress. If the above mechanism is operative the following observations have to be satisfied.

a) Cracking should be discontinuous in nature, since a running crack would leave the hydrogen excess concentration behind, so reaccumulation should be necessary.

b) In the case of excessive crack tip blunting, linking of separated, widely spaced microcracks would be necessary for sustained cracking. The degree of difficulty of link up would therefore be the rate controlling step and not any direct hydrogen effect.

c) If absorption of hydrogen is not rate controlling, materials should behave the same under internal and external hydrogen environments.

2. Adsorbed hydrogen lowers the surface energy of the material, γ, (42) therfore lowering the fracture stress of the material σ according to:

$$\sigma = (E\gamma/b)^{1/2}$$

b=interatomic spacing

E=Young's modulus

thus facilitating crack propagation. This can be viewed as a special case of the cohesive force concept when the crack extension is reversible. The possibilities of such a mechanism taking place are:

i) preferential hydrogen adsorption on an interface or grain boundary in sufficient amounts to facilitate interfacial separation,

ii) localized gas recombination generating high local stresses,

iii) formation of local brittle regions due to hydrogen interaction

or reaction with other adsorbed species.

The above arguments could be tested as follows:

a) crack susceptibility would be dependent on the nature of the particle or interface,

b) presence of a near continuous path capable of being sensitized by adsorbed hydrogen,

c) reduction of the stress for crack nucleation,

d) stronger adsorbates should screen the effect of hydrogen.

3. Localized generation of internal stresses due to the pressure developed when hydrogen recombination takes place at heterogeneities. This simply lowers the critical stress for crack propagation, implying that hydrogen is not unique because of its high transport rate in the lattice.

The generality of this theory has been questioned in recent years and is considered applicable in cases where dislocation movement can transport hydrogen in areas of high triaxiality. The pressure model can be tested in the following ways:

a) For similar transport conditions, materials exhibiting high planar slip should be more susceptible. The effect will be enhanced if hydrogen induces planarity

b) Fracture processes dominated by void growth rather than nucleation should be more susceptible.

c) If localized pressure can induce sharp cracks in ductile materials the local stress field must be shielded to suppress plastic relaxation.

2.4.2 Hydrogen embrittlement in 7xxx series alloys.

For high strength aluminium alloys it has not as yet been unequivocaly established whether stress corrosion cracking in aqueous environments is controlled by hydrogen embrittlement. The earliest suggestions that hydrogen embrittlement may be responsible for the stress corrosion cracking of 7xxx series aluminium alloys in aqueous environments came from Gruhl and coworkers in Germany (43) with their work on pre-exposure embrittlement and Haynie et al in the United States (44) who showed that stress increases the solubility of hydrogen at grain boundaries. Most of the work on hydrogen embrittlement was triggered after the work of Gest and Troiano in 1974 (45) who proposed that a high strength 7075-T651 alloy was susceptible to a strain ageing type of reversible hydrogen embrittlement and that this played a major role during stress corrosion cracking in aqueous environments. They provided hydrogen permeation data ($D_o \approx 2 \times 10^{-13}$ m^2/s) and related their internal friction and lattice parameter measurements directly to hydrogen uptake from the environment.

Scamans & Tuck (46) detected hydrogen diffusion through a thin sheet of an Al-Zn-Mg alloy and found that it depended on the ageing treatment, ie corrosion susceptibility (fig 2.4.2.i). Similar experiments with Al-Mg-Si alloy showed no hydrogen diffusion. Measurements of the hydrogen generated on the surface of the specimens showed that the amount generated decreased with increasing susceptibility, showing that, for susceptible alloys, hydrogen penetrates into the lattice and that takes place at grain

boundaries, as proved by transmission microscopy studies. Later work by Scamans et al (47) who precharged high purity Al-Zn-Mg alloys and then tensile tested to failure in a vacuum chamber with a mass spectrometer attached, showed almost complete irreversibility and hydrogen outgasing.

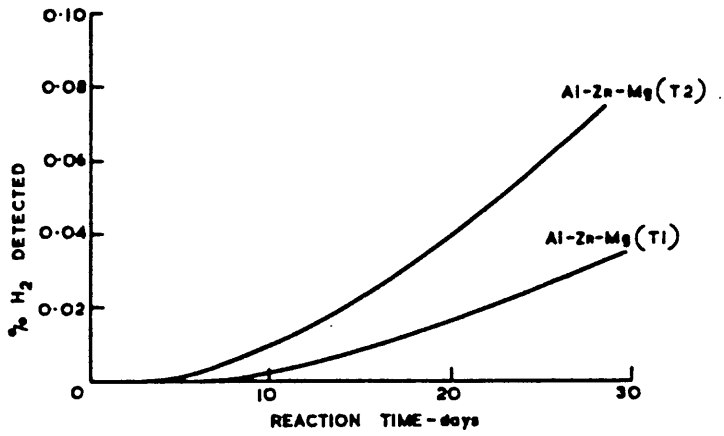

Fig 2.4.2.1 Hydrogen diffusion through thin sheets of Al-Zn-Mg alloy with different ageing treatments (46).

The best evidence of hydrogen embrittlement controlling the stress corrosion cracking in 7xxx series alloys in saline environments was provided by the work of Gruhl and Ratke (49). Their experiments involved loading in tension externally notched hollow tubes, with the inside of the tube filled with a saline environment while the outside surface was carefully protected to prevent the access of moisture (fig 2.4.2.ii). Fractographic studies showed that stress corrosion crack growth initiation was internal and took place at a region ahead of the notch. They explained these observations by suggesting that during the stress corrosion cracking test hydrogen was generated via a cathodic electrochemical process in the aqueous electrolyte with some

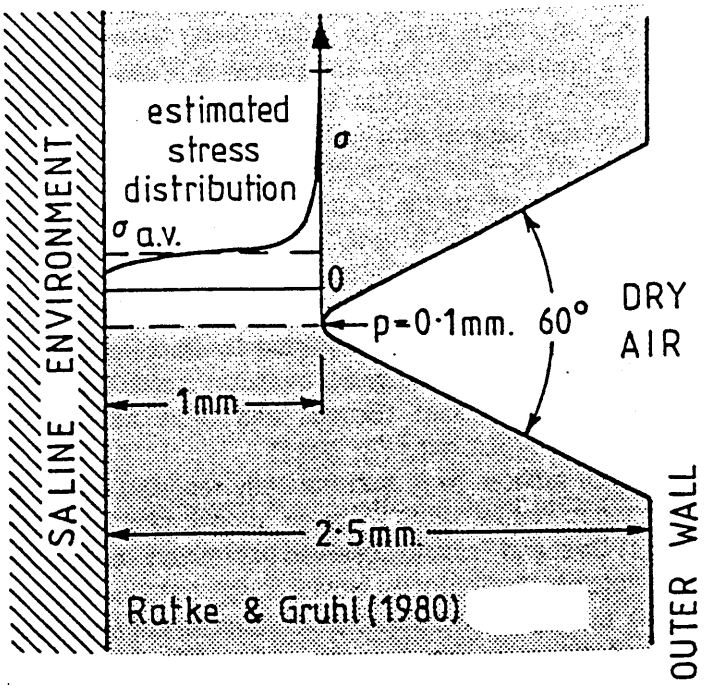

Fig 2.4.2.ii Notched hollow tube design used by Ratke & Gruhl to show SCC initiation from a notch can occur internally (49).

diffusing into the alloy via grain boundary diffusion to accumulate at high stress regions ahead of the notch and lead to internal cracking.

Such a mechanism is supported by Hashimoto & Latanison (134) who suggest that crack propagation due to hydrogen embrittlement in aluminium alloys is a repetition of the following steps until fracture:

i) localisation or accumulation of hydrogen at critical locations

ii) microcrack formation, the nature of which depends on the local hydrogen concentration and stress state and

iii) hydrogen redistribution after microcrack formation

The mechanism explains the discontinuous nature of crack propagation and strong strain rate dependence of hydrogen embrittlement.

More recent indirect evidence that hydrogen embrittlement controls the stress corrosion cracking of 7xxx series alloys in aqueous environments came from the work of Martin et al (50) who used the acoustic emission technique during stress corrosion tests of 7075-T651 alloy in 3.5%NaCl solution and humid air. They detected identical acoustic emission signal count rates per unit crack advance in both environments and concluded that the same stress corrosion cracking mechanism must be operative. Having excluded the possibility of a dissolution mechanism in humid air they suggested that hydrogen embrittlement must be responsible during the stress corrosion cracking in aqueous environments.

2.4.3 Role of dislocations in hydrogen embrittlement.

The correlation between deformation mode and hydrogen embrittlement susceptibility suggests that hydrogen is transported by mobile dislocations in aluminium alloys.

Hydrogen transport by mobile dislocations was first suggested by Bastien & Azou (83) with the first experimental evidence reported by Frank (84) who observed enhanced hydrogen outgasing in mild steels due to plastic deformation. Since then hydrogen transport by mobile dislocations has been reported for a number of materials.

It has been shown (82) that the presence of dislocations enhances the solubility of hydrogen in metals and hydrogen atoms are trapped around dislocations forming a highly concentrated atmosphere. Since diffusing hydrogen should fill these dislocations while diffusing through lattice sites, hydrogen-dislocation interactions hinder the lattice diffusion of hydrogen.

Further evidence for mobile dislocation involvment in hydrogen embrittlement comes from the strong dependence of hydrogen embrittlement and strain rate. At high strain rates no hydrogen effects are observed. The commonly accepted argument for this is that at high strain rates, the transport of hydrogen to critical locations is not sufficient and ductile failure occurs.

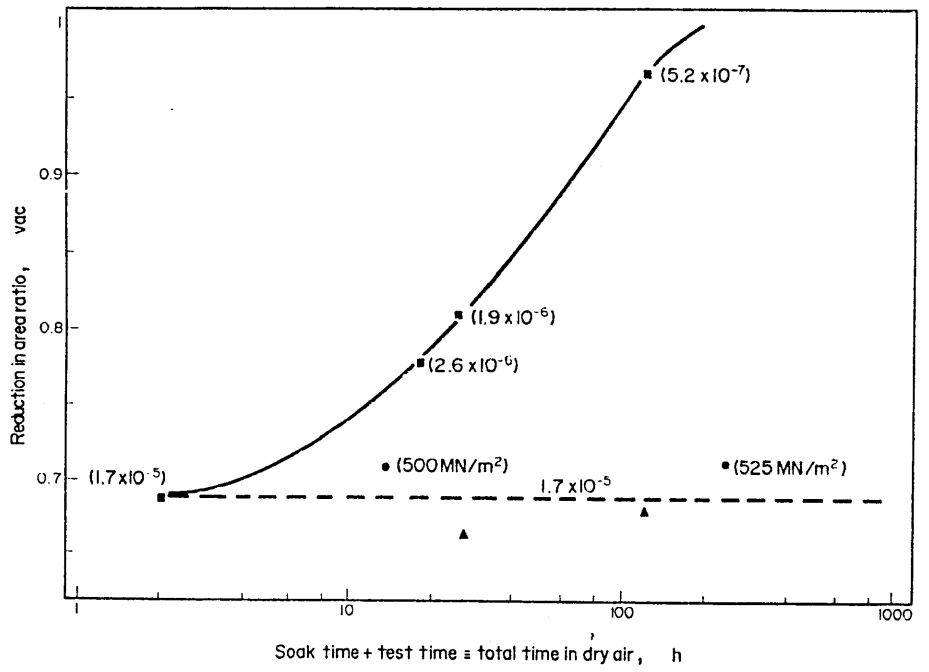

Fig 2.4.3.i Reduction in area ratio for 7049-T651W tested in dry air i) at various strain rates (■), and ii) at a strain rate of 10^{-5} s^{-1} after holding at various times in dry air either without stress (▲) or with an applied stress (●).

Holroyd and Hardie working on 7049-T651 alloy observed complete recovery of pre-exposure embrittlement when tensile specimens were pre-exposed to aqueous environments were strained to failure at appropriate strain rates in dry air. An important observation was that pre-exposure embrittlement was not operative for strain rates above about 10^{-3}/s and was complete for strain rates below about $5x10^{-7}$/s (fig 2.4.3.i). This demonstrates that hydrogen embrittlement of 7xxx series alloys is a time - strain dependent phenomenon (59).

CHAPTER 3

3. THE WHITE-ZONE AND ITS CORROSION CRACKING SUSCEPTIBILITY.

3.1 General

The process of fusion welding introduces high temperatures and rapid thermal cycling which may have marked effects on the heat affected zones of the metal or alloy being welded. These changes may, in turn, modify the properties of the welded region in a manner that is detrimental to its perfomance in service.

The weldable Al-Zn-Mg alloys posses the advantage that, during welding the heat affected zone (HAZ) close to the weld undergoes solution treatment in the usual way, but reversion occurs in the remainder of the HAZ acompanied only by insignificant overaging, unless welding conditions are such that the HAZ remains at 200-250°C for periods greater than 1 min. Either Al-Mg or Al-Zn-Mg alloys are chosen as weld fillers, so that after dilution with parent metal the weld pool contains both zinc and magnesium. Subsequently both the HAZ and the weld will age-harden at room temperature, while if higher strengths are required the welded fabrications can be aged at elevated temperatures in the range 120-180°C. The advantages of the Al-Zn-Mg alloys are clearly seen in the hardness surveys shown in fig(3.1.i) for an Al-Zn-Mg alloy (51) and an Al-Mg-Si alloy (12) commonly used for structural applications.

Despite these advantages the use of the weldable Al-Zn-Mg alloys, 7000 series, has been limited due to their susceptibility to

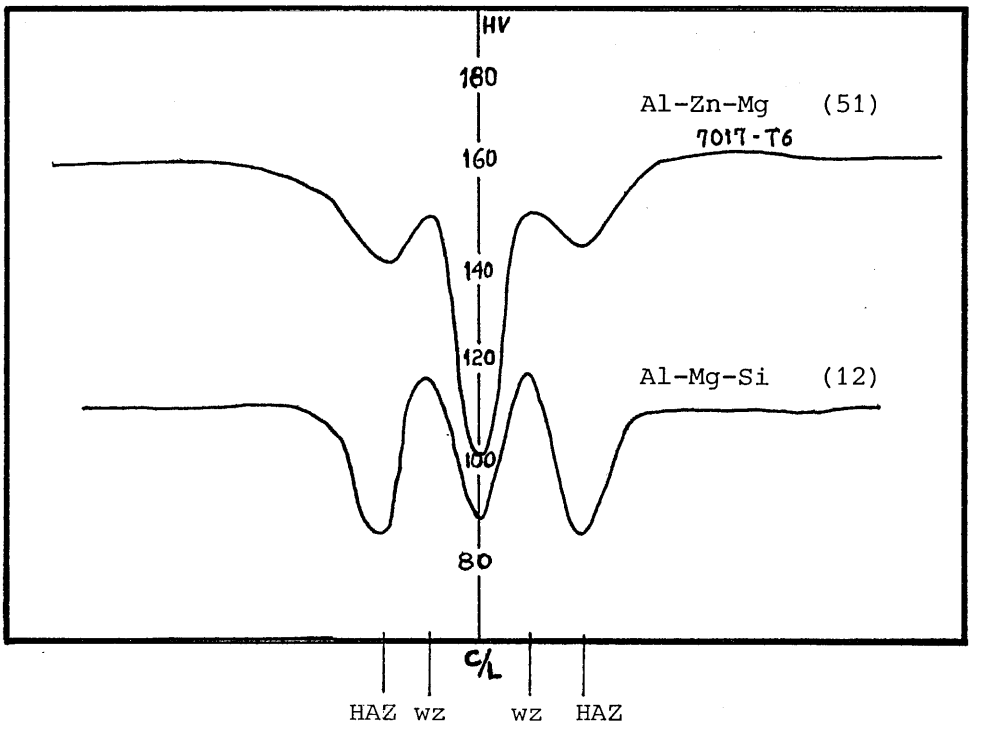

Fig 3.1.i Typical hardness surveys of Al-Zn-Mg and Al-Mg-Si welds.

intergranular stress-corrosion cracking in a non-etching band, of approximately 0.6mm thickness, called "white-zone", in the heat affected zones of the parent alloy adjacent to the weld bead.

The significance of weld-toe cracks depends on their location in the structure in relation to the stress field or load path and on the application of the component. For example, subcritical cracks might grow in fatigue and result in rapid failure, but others might not extend substantially during service. Fig(3.1.ii) shows three examples of potentially undesirable effects of weld-toe cracking.

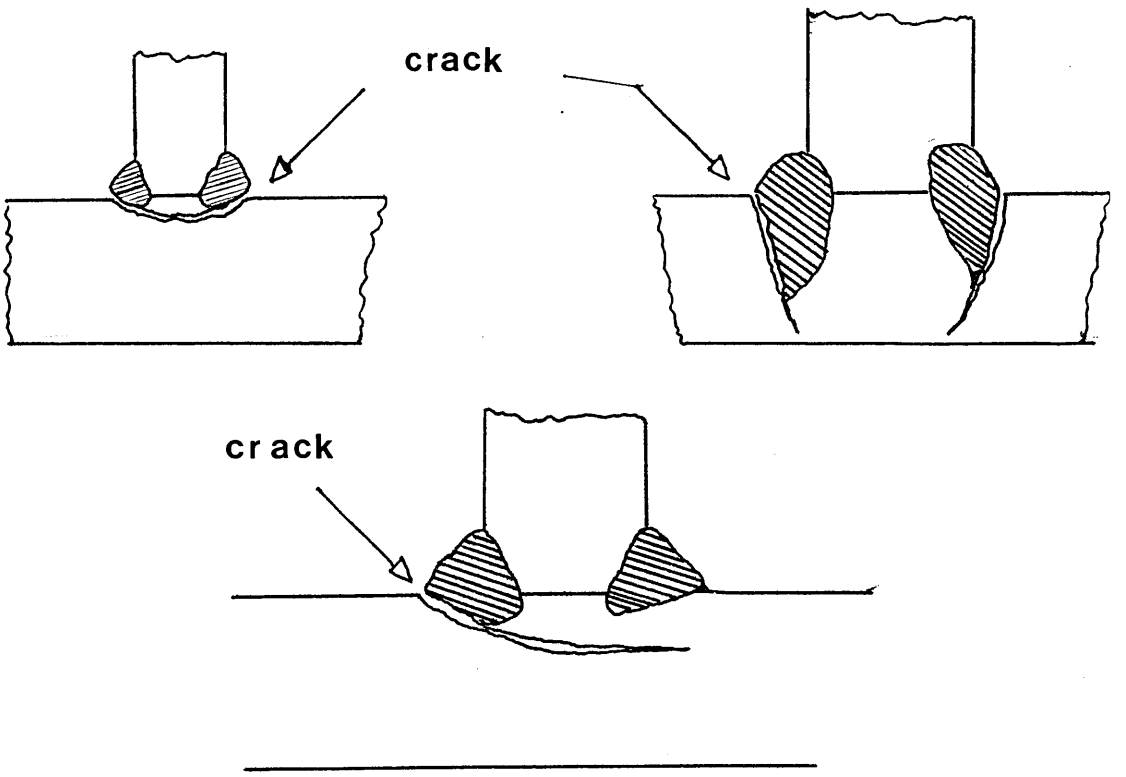

Fig 3.1.ii Examples of common types of weld cracks

3.2 Mechanisms of white-zone/weld-toe cracking.

Weld-toe cracking, as indeed most scc systems, requires the conjoint action of a susceptible metallurgical structure, a tensile stress and a corrossive environment. Welding is an essential contributor to the modification of the parent plate microstructure, introduction of residual stresses, the development of stress concentration effects and the introduction of localised regions which differ markedly in electrochemical characteristics.

The mechanism of white-zone/weld-toe cracking is a complex phenomenon involving at least a two-stage process. In the first

stage the presence of an aggressive environment gives rise to localised corrosion processes at the weld toe (usually as exfoliation corrosion) providing both a path to the white-zone and an acidified electrolyte (pH values of 3 have been measured in 'activated' weld-toe regions (52)). Alternatively since the weld-toe/plate interface is relatively weak, weld-toe lifting can be mechanically driven. In the second stage the exposed white-zone provides a highly scc susceptible path for crack growth. However cracking does not initiate immediately, but a second initiation process is involved probably requiring the establishment of local environmental conditions for white zone cracking, for example development of pits or crevices. This second initiation stage was established by the observation that cracking in dressed welds (the weld bead mechanically removed) are resistant to crack initiation even though the white zone is exposed (53,54).

3.3 Microstructure of the white zone.

Comparison of the microstructure of the white zone with that of the parent alloy unaffected by welding reveals the following differences:

i) The grains within the white zone tend to be equiaxed whereas they are elongated elsewhere in the parent alloy due to the rolling process.

ii) Deep etching in Nitric acid leads to general attack in the grains of the parent alloy whereas little attack is apparent in the white zone grains.

iii) Examination of unetched specimens indicates that intermetallic compounds are present in some grain boundaries of the white zone whereas they are generally absent in these boundaries elsewhere in the parent alloy.

v) There is a tendency for dislocations to line up in bands in the equiaxed grains.

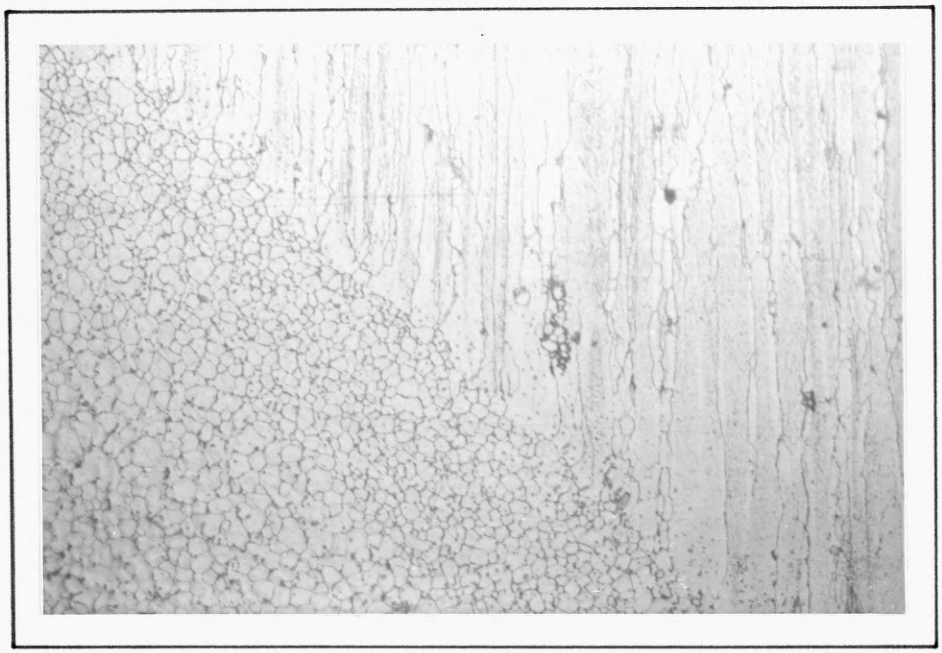

Fig 3.3.i Typical microstructure of the white-zone of 7017-T651 alloy

The change in grain shape suggests significant grain boundary movement has occured. This is true because in the white zone region the parent plate has been heated to temperatures approaching the solidus and then rapidly quenched. The solidus may even be locally exceeded at grain boundaries and partial liquation may occur together with extensive grain boundary movement. Cordier et al (55) have attributed the resistance to etching of the white

zone to the removal of submicron intermetallic compounds, such as $ZrAl_3$, from the grains of the white zone and presence in the grain boundaries. The fact that intermetallic compounds are present in the grain boundaries of the white zone whereas most appear to have been removed from within the grains suggests that these compounds have been removed by migrating boundaries. The most probable way for the movement of the particles seems to be liquation of the grain boundary regions and since some of these intermetallic compounds are large in size suggests that coalescence has taken place which is also indicative of localised melting (56).

Transmission electron microscopy studies carried out in the grain boundary regions of the white zone has shown a great number of precipitates present which suggests that migrating boundaries in the region also sweep up solute atoms and that this solute has subsequently precipitated there. X-ray microanalysis has shown broad Zn and Mg peaks (fig 3.3.ii). It has been suggested that a high temperature non-equilibrium segregation process of Zn and Mg is operative. Schmeidel & Gruhl (57) suggest that the presence of zinc in grain boundaries controls the cracking susceptibility of Al-Zn-Mg welds. A role for Zn at grain boundaries has been reported by Scamans & Tuck (46) who suggest that Zn could promote hydrogen chemisorption because it has more electron orbitals available for surface chemisorption bonds than either aluminium or magnesium. On the other hand for 7xxx series alloys it has been reported that Mg segregation in white zone boundaries makes them highly reactive. It has also been reported that magnesium segregation is responsible for hydrogen entry and its grain boundary permeation, but it is only

when a certain level of grain boundary precipitation has occured that cracks due to hydrogen embrittlement can be nucleated and the microstructure becomes stress corrosion susceptible (58).

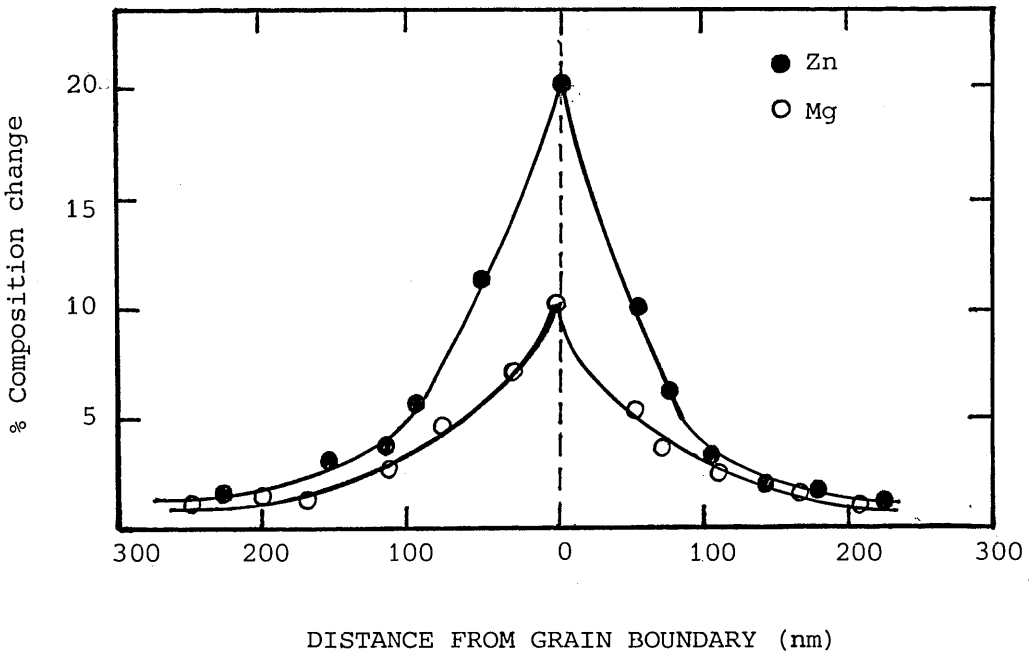

Fig 3.3.ii Contents of zinc and magnesium in a grain boundary of the white zone as compared with the concentration of these elements in the grain centres.

Furthermore, slow crack growth studies both on parent plate and white-zones point to a hydrogen embrittlement mechanism being operative. Support for this proposition is given by the observation that reversible embrittlement is produced by slow straining in a dry environment after pre-exposure to aqueous environments (59). Also fractures produced in relatively mild environments, e.g. laboratory air, show little evidence of anodic dissolution. To date though, no detailed hydrogen effect studies have been made in segregated white-zone grain boundaries.

3.4 Electrochemical effects in the white-zone region.

Localised corrosion of welded Al-Zn-Mg joints has been observed to occur generally as exfoliation corrosion within a heat affected zone region, a few millimeters from the weld bead or as a type of stress corrosion cracking, weld toe cracking, which initiates at weld toes and propagates through the white zone. It is a complex phenomenon which involves at least two processes; the first being separation of the mechanically weak/chemically reactive weld overlap region from the plate (weld toe region) and the second, crack initiation and propagation in the white zone driven by hydrogen embritlement.

Weldable aluminium alloys, such as Al-Mg or Al-Mg-Si have "white-zones" with microstructures and grain boundary concentrations of magnesium similar to those of Al-Zn-Mg alloys. These regions have recrystalised grain structure, high concentrations of chemically reactive species on the grain boundaries but are immune to stress corrosion cracking susceptibility in contrast to Al-Zn-Mg weldments which are highly susceptible.

An explanation for the difference in stress corrosion susceptibility of Al-Zn-Mg alloys and the rest of the weldable alloys, can be derived by analysis of work by Schumaker et al (60), describing electrochemical potential profiles across weldment cross-sections during exposure to aqueous saline solutions of Al-Zn-Mg, Al-Cu, Al-Mg and Al-Mg-Si alloys. It was observed that

weld beads are electronegative with respect to the heat affected zone and the parent plate for all the alloys, except Al-Zn-Mg (7000 series) fig 3.4.i. The potential data quoted by Schumaker et al are for a 7039 T651 alloy weldment which is representative of the 7000 series alloys in general and correspond closely to data reported by Tuck (61) for a 7017 T651 alloy, the one used in this study.

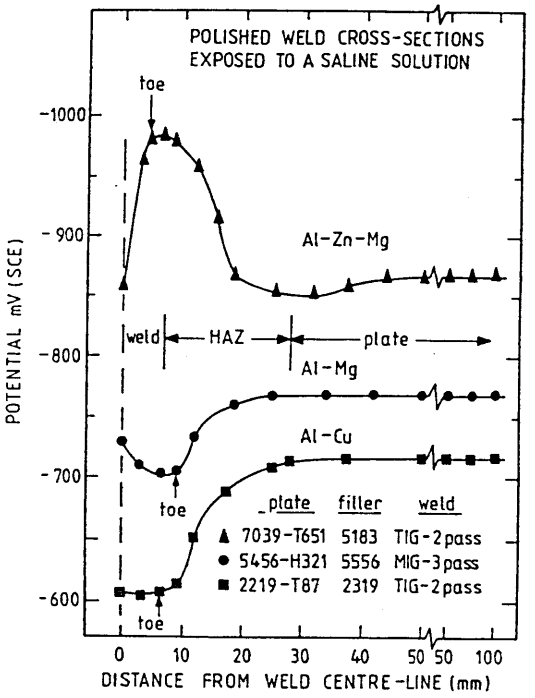

Fig 3.4.i Electrochemical potential profiles across medium strength weldable alloy weldments (60).

In view of the above results it can be argued that white-zone regions are sacrificially protected by the weld beads for weldable alloys with the exception of Al-Zn-Mg alloys for which this electrochemical condition is not established.

CHAPTER 4

4. CORROSION FATIGUE

4.1 General

Corrosion fatigue is a term used to describe the phenomenon of cracking (including both initiation and growth) in materials under the combined actions of a fluctuating (or cyclic) stress and a corrosive environment. The term corrosion fatigue can conjure up the notion of severe disintegration of the material through chemical attack, accompanied by fatigue cracking. However relatively innocuous environments (such as atmospheric moisture) can greatly enhance fatigue cracking without producing any visible corrosion in the commonly accepted sense. To avoid this misconception, the term environmentally assisted fatigue cracking is now preferred and the term corrosion fatigue is to be understood within this context.

Since 90% of engineering components failures are fatigue failures the importance of corrosion fatigue was recognised at an early stage. Corrosion fatigue had been investigated since the 30's and with the development of the aerospace industry, extensive research was carried out in this field, particularly for aluminium alloys.

A review by Gilbert[131] in which he summarised all the pre-1956 knowledge made the following points which are still valid today:

1. Corrosion fatigue cracks are usually transcrystalline, although in a minority of cases they may be intercrystalline.
2. Corrosion fatigue often produces branched cracks rather than the single fronted cracks characteristic of air fatigue.
3. Corrosion fatigue crack growth rates are independent of metallurgical conditions and microstructure and show little correlation with strength in contrast to the generaly good correlation between the tensile strength and air fatigue strength of many alloys. However it has been reported by Pelloux (62) that ageing treatment can affect crack propagation rates in Al-Zn-Mg alloys.
4. Corrosion fatigue in immersed conditions is an electrochemical phenomenon because sometimes it can be prevented by cathodic protection or by adding inhibitors to the corroding solution.

4.2 Effect of gaseous environments on corrosion fatigue

As with stress corrosion cracking fatigue strength has been found to reduce in air, relative to tests in vacuum. Particular attention has been paid to the roles of oxygen or hydrogen since it has been shown that inert atmospheres have the same effect on corrosion fatigue as vacuum.

The influence of gas pressure on the environment assisted fatigue crack growth in high strength aluminium alloys has been investigated for many years and there is a relationship between gas pressure and cyclic frequency. Wei et al (63) have shown that the rate of fatigue crack growth for 7075-T651 alloy exposed to water

vapour (in the abs ence of capillary condensation at the crack tip) was significantly affected by pressure and frequency. At a 5Hz fequency they found that a threshold pressure exists below which crack growth rates are essentially unaffected by water vapour fig 4.2.i. The threshold pressure effect has been observed in many systems and for example Snowden (66) produced typical S-shaped curves (fig 4.2.ii) for lead in air and in various levels of vacuum showing that there is a critical partial pressure of oxygen where fatigue resistance is unaffected by the environment, and an upper partial pressure above which increasing partial pressures of the gaseous species does not increase fatigue resistance any further.

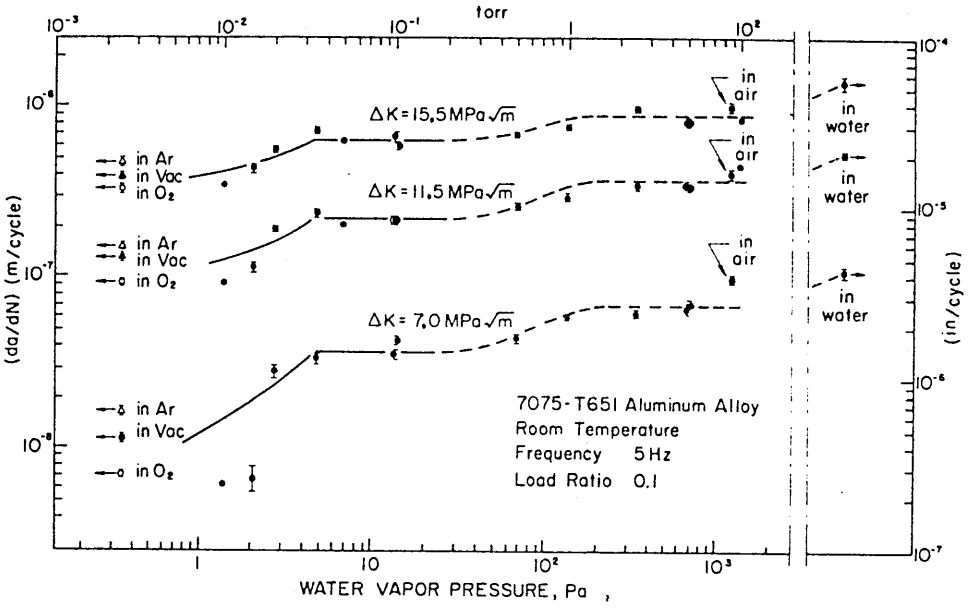

Fig 4.2.i Influence of water vapour pressure on fatigue crack growth rates for a 7075-T651 aluminium alloy at room temperature (63).

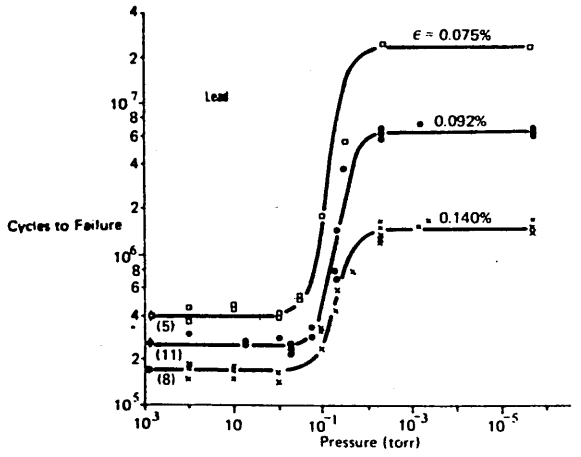

Fig 4.2.ii Effect of oxygen partial pressure on the fatigue life of lead in air (66).

This behaviour can be explained by a consideration of the rate of surface coverage of a growing crack as compared to the generation of new surface at the crack tip. A mathematical model was developed by Hordon (65) which is based on the kinetic gas theory where the critical pressure is expressed as:

$$Pc=2x10^{2}(da/dN)f \quad (torr) \qquad f=\text{frequency of applied stress}$$

an equation which agrees well with published data for the critical pressure Pc.

Bradshaw and Wheeler (108) for an aluminium alloy showed that the fatigue crack growth rate at a given K level appeared to be dependent on the product of water vapour pressure and cyclic load period (1/freq) and suggested that the observed frequency effect resulted from the time available for the reaction of water vapour with the newly created crack surfaces.

4.2.1 Effect of temperature

The effect of temperature of various gaseous environments has been investigated by Miller & Smith (67) for 7075-T 6 aluminium alloy and the results are presented in fig (4.2.1.i). It can easily be seen that a decrease in temperature decreases the crack growth rates. It is important to note that dry air at -55°C decreases crack growth rate further than dry Nitrogen at room temperature and it has been reported, for aluminium alloys, that nitrogen has the same effect as vacuum. Furthermore Vogelsang & Schijve (68) have reported that temperature has no effect on crack growth rates in vacuum.

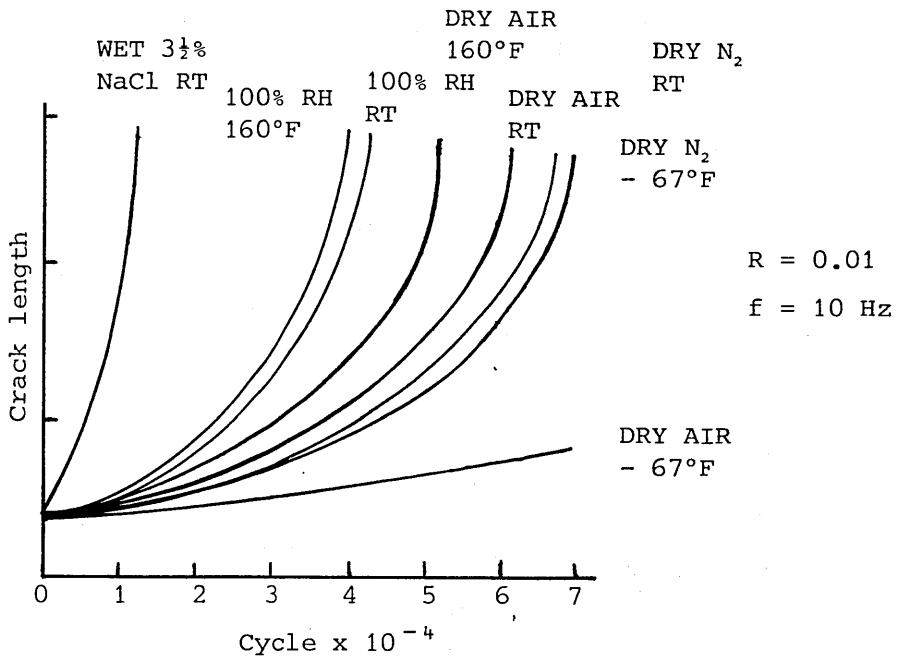

Fig 4.2.1.i Effect of temperature of various environments on the fatigue crack growth rate of 7075-T6 alloy (67).

4.3 Mechanisms of crack propagation in gaseous environments.

The specific mechanisms proposed for how the gaseous environments act to reduce fatigue resistance are generally divided into four categories:

1) Interference with otherwise reversible slip.
2) Prevention of slip band rewelding.
3) Surface energy reduction at the crack tip due to gas phase adsorption
4) Bulk oxide interference with slip processes

However experiments conducted on aluminium noted that the atmospheric effect decreases with increasing crack length suggesting that a rewelding mechanism could not explain delayed cracking in vacuum, particularly when high local stresses and increased cold work should intensify rewelding effects. Furthermore as mentioned earlier, the observation that nitrogen had the same effect as vacuum on the fatigue crack growth rate for an aluminium alloy, implies that neither interference with a rewelding process, nor gas phase adsorption could be an acceptable proposition (69).

On the bulk oxide interference with slip processes Peloux (70) has reported that aluminium alloys tested in vacuum do not show the striations associated with stage II crack growth normally observed when specimens are cyclically sressed in air and proposed that completely reversible slip must occur in vacuum (fig 4.3.i).

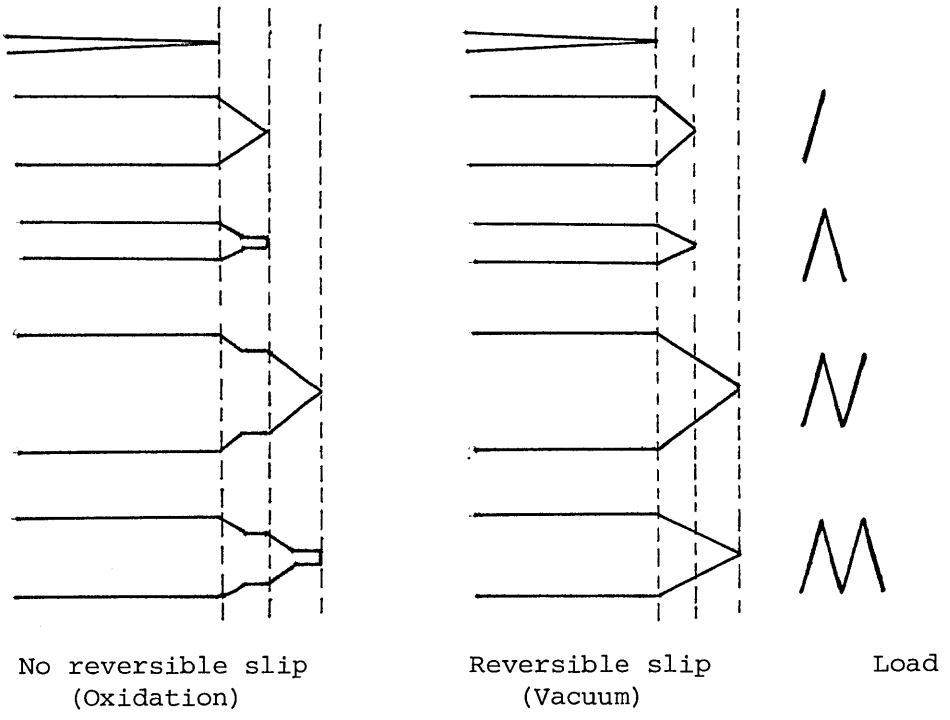

Fig 4.3.i Comparison of crack tip extension after two load cycles, in air and in vacuum.

In air on the other hand the fracture surface oxidises, striations are formed due to irreversible slip and crack growth is accelerated. Shen et al (71) based on previous work which showed that the mechanical properties of the oxide film are markedly improved in vacuum, postulated a mechanism to explain accelerated crack initiation and growth in a 1100 aluminium alloy, in which it is suggested that surface regions are strengthened by oxide films preventing dislocation escape through the alloy free surface, leading to large accumulations of dislocation debris in near surface regions. The formation of cavities and voids is enhanced and crack propagation rates increase. At low pressures oxidation of newly created surfaces is slower, dislocation escape from the surface is more common and cavity formation and void linkage delayed (fig 4.3.ii)

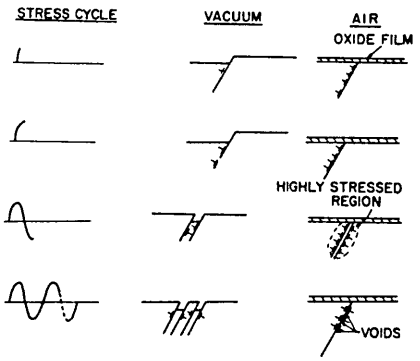

Fig 4.3.ii Model of void nucleation under oxide films to accelerate crack initiation in gaseous environments.

4.4 Mechanisms of corrosion fatigue in aqueous environments

It is well known that the initiation of fatigue cracks in a corrosive environment is controlled by a different process to fatigue crack growth. Initiation can be induced by localised plastic deformation unaided by any stress concentrators whereas for fatigue crack propagation, fracture toughness parameters become dominant in determining the rate of crack extension and the crack tip stress intensity factor becomes the controlling parameter. Thus initiation and propagation mechanisms will be reviewed separately in this section.

4.4.1 Corrosion fatigue initiation.

Aqueous fatigue theories have generally relied on one or more of the following mechanisms:

i) Stress concentration at the base of hemispherical pits created by the corrosive medium.

ii) Electrochemical attack at plastically deformed areas of metal with non-deformed metal acting as cathode.

iii) Electrochemical attack at ruptures in an otherwise protective surface film.

iv) Lowering of surface energy of the metal due to environmental adsorption.

Early investigators favoured the mechanism of pits acting as stress concentrators for the initiation of corrosion fatigue cracking. However it was shown by Simnad & Evans (72) and Duquette & Uhlig (73) that corrosion pits are not essential for easier crack nucleation and they obtained corrosion fatigue of steel in acid solutions in the abs ence of pitting corrosion conditions. This does not dismiss the corrosion pit model which can be applicable in some cases, but suggests that several mechanisms of initiation are possible and the one with the fastest kinetics will dominate. For example in the air fatigue of polycrystaline aluminium fatigue crack initiation occurs at persistent slip bands at low stress, but by grain boundary initiation at high stresses. If the tests are carried out in 3.5% NaCl solution at pH 7, crack initiation occurs at persistent slip bands rather than grain boundaries over a wide range of stresses. The reason for this is that the chloride

environment produces pitting at the persistent slip bands and so encourages these as sites for crack nucleation rather than the

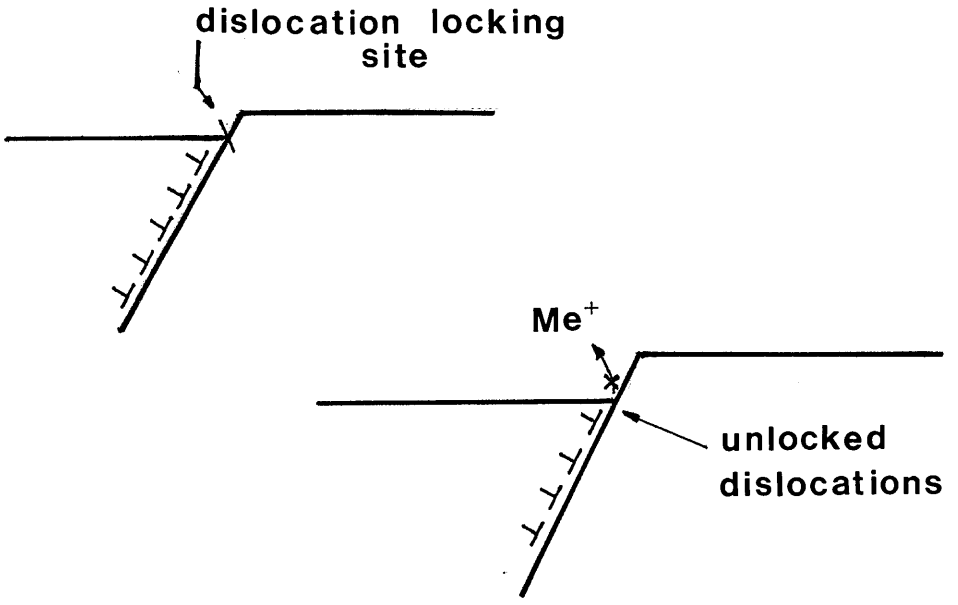

Fig 4.4.1.i Schematic diagram of model to explain increased deformation and early crack nucleation in corrosion fatigue.

grain boundaries. It has also been suggested that metal atoms associated with mobile dislocations in persistent slip bands are more active than surrounding metal atoms, leading to strain relief in the surface and significant increases in surface deformation. As a result of corrosion at these numerous persistent slip bands numerous crack initiation sites are produced. This is shown schematically in fig (4.4.1.i).

4.4.2 Effect of solution pH

For aluminium in NaCl solutions pH has a significant effect on the initiation of corrosion fatigue with high pH (say pH 10) retarding crack initiation. The reason for the effect of pH is its influence on the solubility of Al_2O_3; at pH 7 it is relatively insoluble, giving rise to localized attack at disruptions in the surface oxide coupled with favourable conditions for passivation of the crack sides, thus forming sharp cracks. The increased solubility at pH 10 removes the passive condition and lateral dissolution occurs at persistent slip bands. Indeed, the general corrosion observed at pH 10 retards initiation relative to air tests. General corrosion also affects the geometry of pits, which become blunt, delaying initiation or even enhancing fatigue life. There is evidence that for aluminium in 3.5% NaCl solutions corrosion fatigue crack initiation depends upon the details of pit formation.

Another mechanism suggested for the initiation of fatigue cracks is the adsorption of damaging ionic species. Experiments on a 7075-T6 commercial aluminium alloy indicate that a mechanism of localised hydrogen embrittlement may be responsible for the poor corrosion fatigue resistance of the alloy.

Whatever the mechanisms of initiation of corrosion fatigue there is still plenty of work required before satisfactory conclusions are drawn. The difficulties in research to fatigue crack initiation have two main causes:

i) The arbitrary nature of defining initiation, ie. when can an intrusion or deep pit be described as a crack ?

ii) Corrosion fatigue is often characterised by the development of many cracks rather than a single crack, so that obtaining quantitative data on crack initiation a tedious task.

4.5 Corrosion fatigue crack propagation.

Once a crack has initiated on the surface of a component the process of crack growth is governed by fracture mechanics parameters and crack tip stress intensity factor controls the process. The relevant parameters to corrosion fatigue crack propagation are briefly reviewed below.

The tensile stress ahead of a sharp crack is given by the Westergaard equation:

$$\sigma = K / \sqrt{(2\pi r)}$$

where σ is the stress normal to the plane of the crack and

r the distance measured from the crack tip.

The stress field just ahead of a sharp crack can be characterised by K (the stress intensity) and appropriate corrections can be made to allow for finite-sized specimens and various crack geometries.

Fatigue data are collected using the fracture mechanics approach because different geometry specimens of the same material should produce the same crack growth versus K data. The important parameters for corrosion fatigue data collection are:

the mean stress ratio R ($R=\sigma_{min}/\sigma_{max}$)

the Kmax and Kmin values and

the stress intensity range $\Delta K=Kmax-Kmin$

R, ΔK and Kmax are not independent test variables and care should be necessary when interpreting data where all these parameters are varied.

It is very difficult to give a general explanation of the mechanisms possible during corrosion fatigue crack growth because particular mechanisms may be relevant to particular systems. The overall crack growth rate will be determined by the relative kinetics of the alternative processes. Most of the research done in trying to explain the mechanisms of corrosion fatigue crack growth has concentrated on the crack tip, with attention to crack opening displacement, δ, and strain rate, $\dot{\epsilon}$. The following relationships have been developed :

$$\delta = \frac{\alpha K^2}{\sigma_y E}$$

$$\dot{\epsilon} = \frac{d \ln \frac{\delta_t}{\delta_o}}{dt} = \frac{1}{K^2} \frac{dK^2}{dt}$$

where α = const , E = Young's modulus

The effects of loading waveform and loading frequency at the crack tip have also been examined. The load waveform can affect the corrosion fatigue crack growth rate, with sinusoidal, triangular and positive saw tooth giving the maximum effect. This is because the crack growth enhancement has been shown to take place in the loading half cycle (74). Square and negative sawtooth waveforms do not allow sufficient time for any crack growth enhancing mechanisms such as, anodic dissolution, or passivating reactions or absorption of reaction products, due to very short rise times. Hold times as in square or trapezoidal waveforms have not been reported to influence crack growth significantly. Contrary to the observations of several workers that crack growth rates depend on the load waveform Hudak and Wei (76) have presented data for a 7075-T651 alloy showing that the load waveform does not influence crack growth rates significantly.

The effect of the loading frequency is more easily understood. In any crack growth situation the crack growth rate is likely to be controlled by the most dominant cracking mechanism. Thus, at high frequencies the rate of fatigue crack growth is independent of the environment, since there is not enough time available for any corrosion effects to influence it. At low frquencies there is enough time for environmental reactions to take place at the crack tip and the influence of stress corrosion cracking has received some attention. For many air fatigue systems there is a threshold stress intensity factor amplitude, ΔK_{th}, below which no fatigue growth occurs. The crack growth per cycle, (da/dN), then increases rapidly with increasing ΔK above ΔK_{th}, then

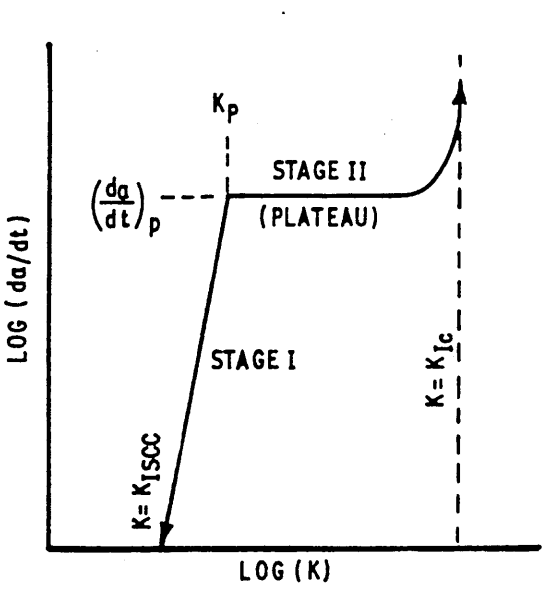

Stress corrosion crack growth

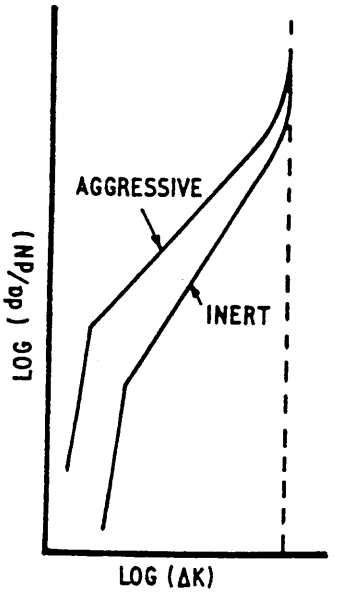

(a) True corrosion fatigue (TCF)

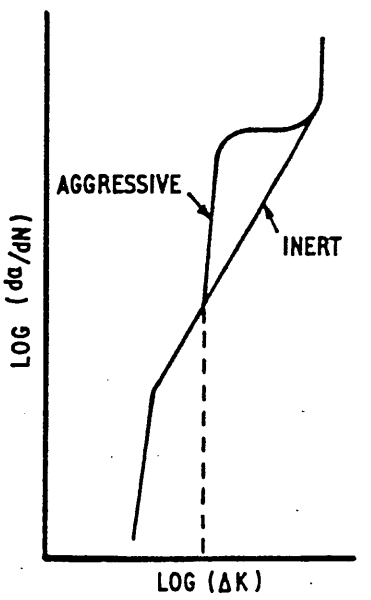

(b) Stress corrosion fatigue (SCF)

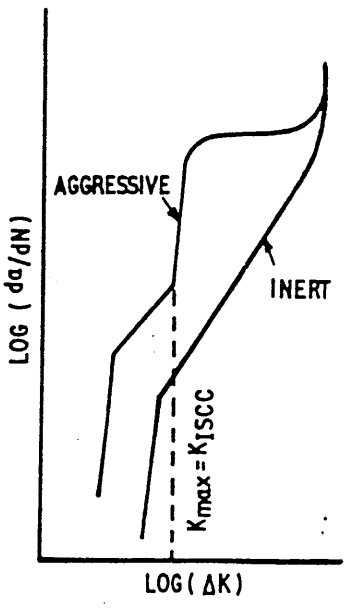

(c) SCF on TCF

Fig 4.5.i Schematic representation of basic types of corrosion fatigue behaviour.
SCC : stress corrosion cracking
TCF : true corrosion fatigue
SCF : stress corrosion fatigue

becomes linearly dependent to ΔK and finally increases rapidly again as ΔK approaches Kc or K_{Ic}. In contrast for stress corrosion cracking systems there is a definable K value below which stress corrosion cracking will not occur, termed K_{Iscc}, then the crack growth rate increases rapidly with increasing K reaching a plateau where crack growth is independant of K, usually called stage II crack growth, and then increases rapidly again on approach to Kc or K_{Ic} (fig 4.5.i(a) & (b)). For corrosion fatigue there are two forms of log da/dN versus log ΔK curves depending on whether there is a synergistic effect or not of the corrosive environment and cyclic stress and the relation of K_{Iscc} to ΔK_{th} fatigue. These cases are shown schematically in fig 4.5.i(b),(c)

In 1963 Paris & Erdogan (77) suggested that stage II of the fatigue crack growth conformed to a relationship:

$$\frac{da}{dN} = C\Delta K^{n}$$

The exponent, n, varies considerably and there is a systematic variation of C with n. As can be seen from fig 4.5.i (a) above, the corrosion fatigue curve shows different values of C and n from those relevant to an inert environment. Fig 4.5.i (c) shows the typical behaviour of systems exhibiting stress corrosion cracking under static loads when the stress intensity is greater than K_{Iscc}. Fig 4.5.i(b) Shows systems that exhibit increase in fatigue growth rates when ΔK is such that the maximum stress intensity during the fatigue cycle is greater than K_{Iscc}. Wei and Landes (78) and later other workers have presented an explanation to case (b) by adopting a simple summation model of fatigue crack growth as follows:

$$\left[\frac{da}{dN}\right]_{cf} = \left[\frac{da}{dN}\right]_{scc} + \left[\frac{da}{dN}\right]_{f}$$

This hypothesis does not apply to all systems exhibiting stress corrosion cracking and also does not give a reasonable explanation to fatigue crack growth rate enhancement in a corrosive environment for systems not exhibiting stress corrosion cracking susceptibility (ie (da/dN)scc =0).

Variation of stress rates and frequency has been shown to transform the behaviour of certain systems from the one shown in fig 4.5.i(c) to the one in fig 4.5.i(e) and vice versa. A better explanation of the corrosion fatigue process is the development of a process competition model which assumes that stress corrosion cracking and fatigue are mutually competitive. On this basis the crack will propagate by the fastest available mechanism which relates to the applied stress intensity (79).

There are many views on the manner in which the localized corrosion reactions at the crack tip and cyclic loading interact to produce corrosion fatigue, which depends on various factors, such as pH of the environment (especially near the crack tip), cyclic frequency and mean stress. The greatest interest on the electrochemical reactions that influence corrosion fatigue enhancement has concentrated, as with stress corrosion cracking, to (i) metal dissolution and (ii) hydrogen embrittlement.

4.6 Corrosion fatigue of Al-Zn-Mg alloys.

Developments of aluminium alloys have been concentrated in producing alloys that provide good strength, fracture toughness, stress corrosion resistance and fatigue resistance. Improvements have been achieved in all but fatigue and corrosion fatigue resistance which still remain a problem, inhibiting the use of several aluminium alloys in structural design, in particular Al-Zn-Mg alloys.

4.6.1 Fatigue in air

Examination of published data on the corrosion fatigue crack propagation rates of Al-Zn-Mg alloys has revealed two important features.

a) At low and intermediate stress intensity ranges the fatigue crack growth rates are similar for all aluminium alloys, indicating that neither composition nor microstructure influence crack growth. The controlling parameter is the stress intensity range ΔK (fig 4.6.1.i). Speidel has suggested that fatigue crack growth rates depend on the material's modulus of elasticity (80).

b) Crack growth rates increase substantially as ΔK approaches the fracture toughness Kc (fig 4.6.1.i). The above observation shows that at relatively higher ΔK values the material fracture toughness is the controlling parameter. This has been observed and expressed mathematically by Forman(133)

Forman's law : $\frac{da}{dN} = \frac{C(\Delta K)}{(1-R)K - \Delta K}$

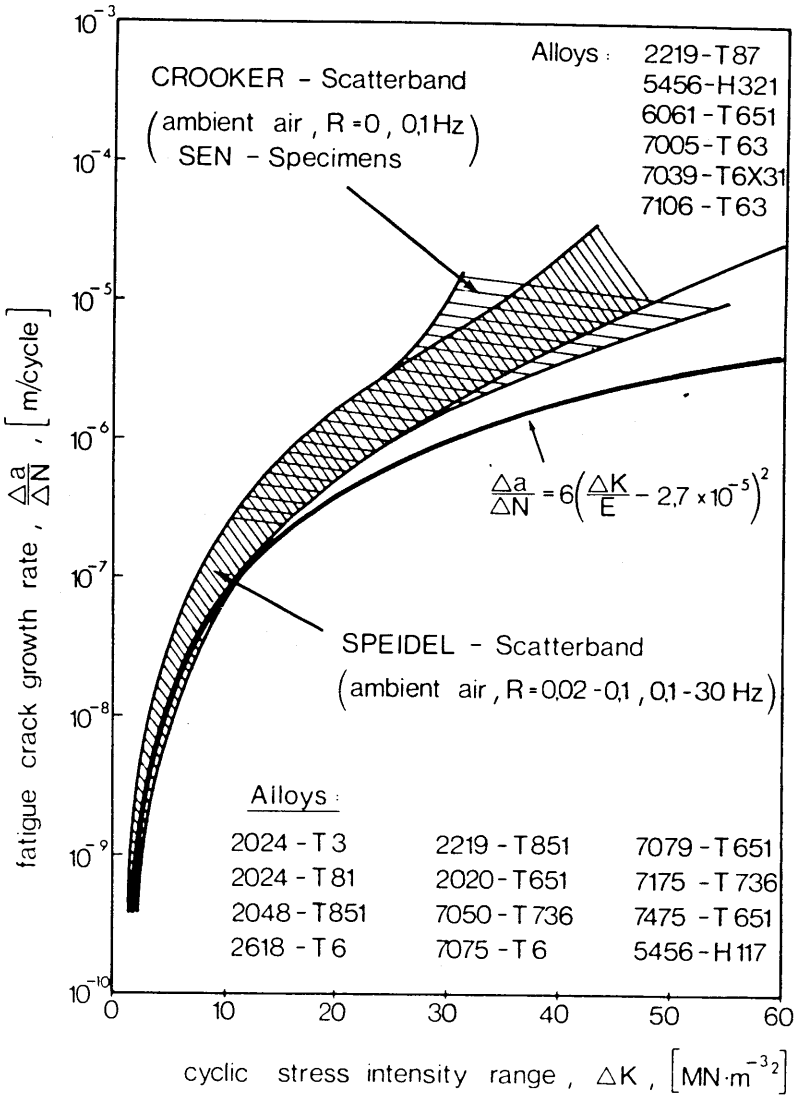

Fig 4.6.1.i Fatigue crack growth rates for various alloys in air presented as scatterbands (80)

4.6.2 Fatigue in an aggressive environment

Certain applications of thick aluminium alloy products (forgings, plates) anticipate cyclic design loads in either longitudinal or short transverse directions. The fatigue crack growth rates in an aggressive environment depend on the direction of the applied cyclic load relative to the alloy's grain orientation.

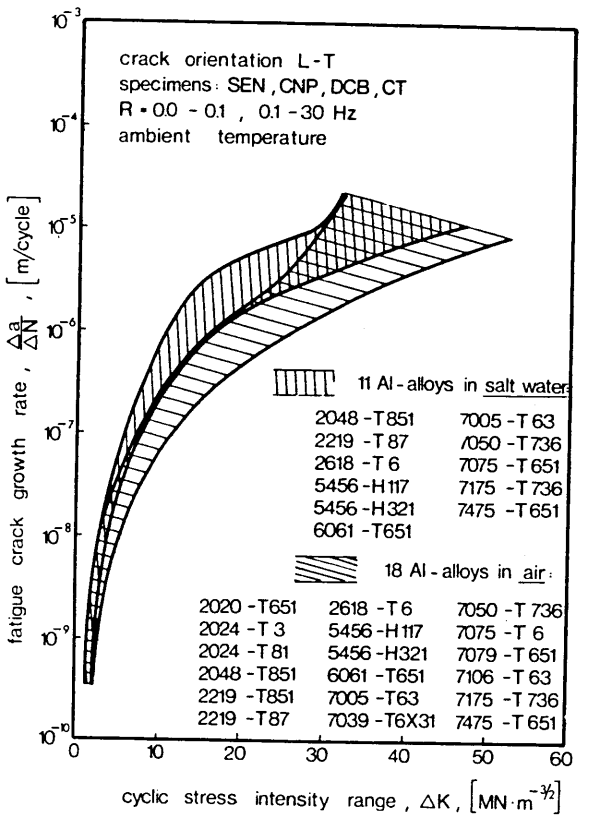

Fig 4.6.2.i Comparison of fatigue crack growth rates in air and salt water (80).

Fig 4.6.2.i represents published results by several workers for various alloys exposed in 3.5% NaCl solution loaded in the longitudinal direction with crack orientations in the long transverse direction. Results in air are also represented for comparison.

It can be seen that in an aggressive environment, at intermediate stress intensity ranges, there is an increase of the crack growth rates by a factor of 3 or 4. The overlap region represents alloys that show identical behaviour in both air and 3.5% NaCl solution like 2219-T87 alloy reported by Crooker (81).

At very low ΔK values the effect of the environment vanishes. This led to Speidel suggesting that the environment does not affect the threshold stress intensity for fatigue crack growth ,ΔKo, in aluminium alloys (82), although no extensive research has been carried out to establish this.

At high stress intensity ranges there is also no appreciable effect on the crack growth rates by the environment. This can be readily explained by the observation that at high ΔK levels a major part of the crack growth per load cycle is due to void nucleation, void growth and void coalescence, this happening inside the material ahead of the crack tip where the environment cannot reach.

When the applied cyclic load acts in the short transverse direction, the corrosion fatigue behaviour is different in certain aluminium alloys. This difference arises from the fact that short

transverse is the preferred direction for growth of stress corrosion cracks.

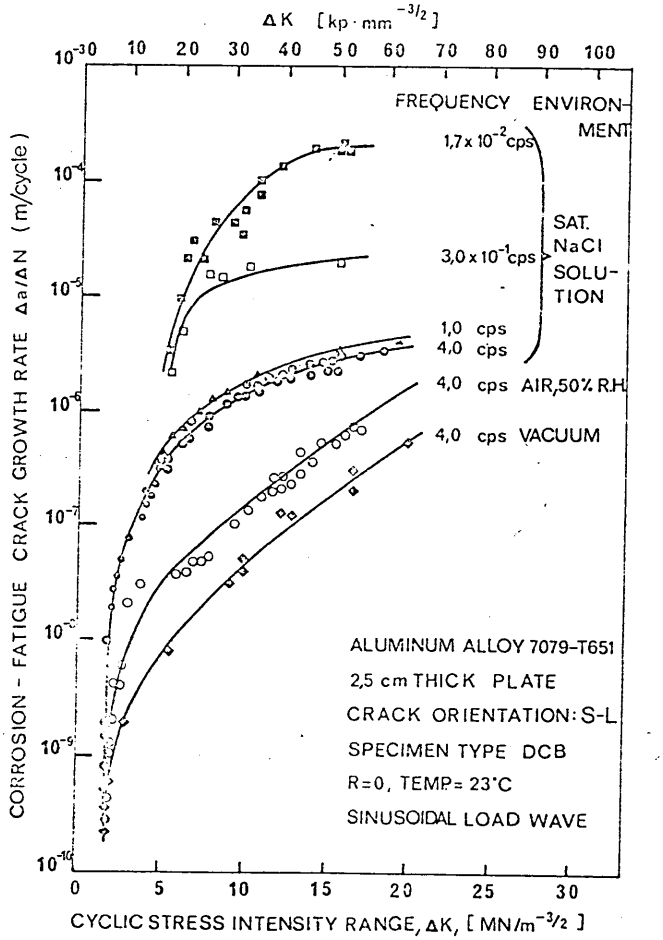

Fig 4.6.2.ii. Corrosion fatigue behaviour of a SC susceptible alloy tested in vacuum, air and salt water(80)

For alloys that exhibit stress corrosion cracking susceptibility the corrosion fatigue behaviour is shown in fig 4.6.2.ii. It can easily be seen that the fatigue crack growth rate increases dramatically in the presence of salt water. This crack growth rate is frequency dependent, furthermore, at very low frequencies (10^{-2} and below) the corrosion fatigue crack growth rate

The most relevant to this work results on 7xxx series alloys come from the work of Holroyd and Hardie (85), on 7017-T651 alloy tested in the short transverse direction for a range of frequencies from 0.1 to 70Hz. Their results, given in fig 4.6.2.v, show the effect of loading frequency and environment on crack growth rates and are in agreement with the general observations reported above.

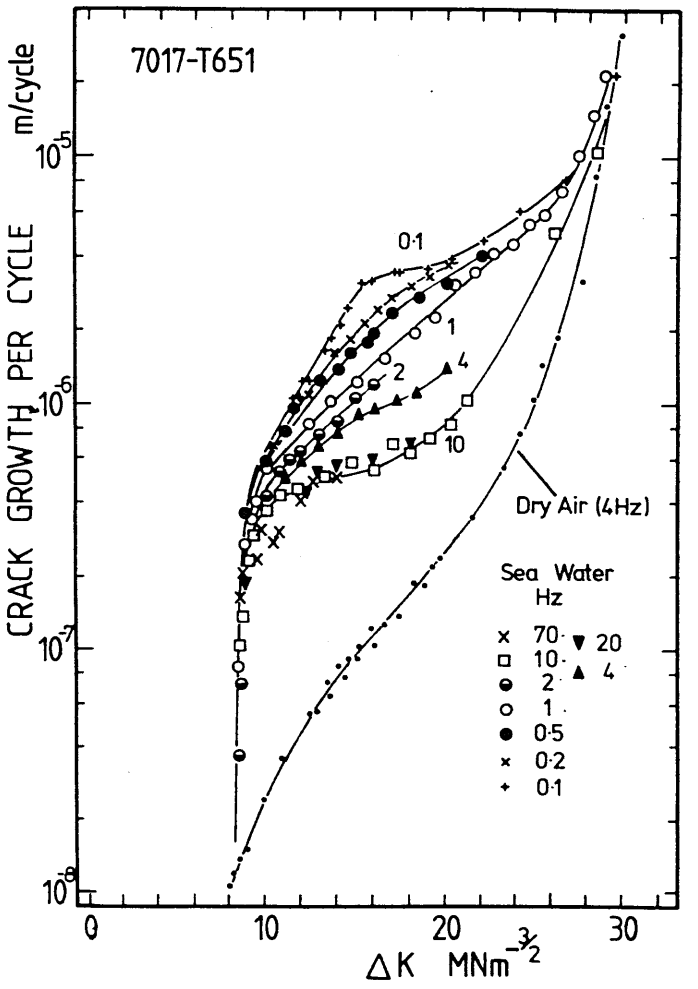

Fig 4.6.2.v. Fatigue crack growth rates of 7017-T651 in dry air at 4Hz and in seawater at frequencies from 0.1 to 70Hz (85).

alloys there is an increase of fatigue crack growth rates in salt water by a factor of 3 or 4 without any significant further increase at very low frequencies. This is similar to the behaviour of alloys with other crack path orientations as described earlier.

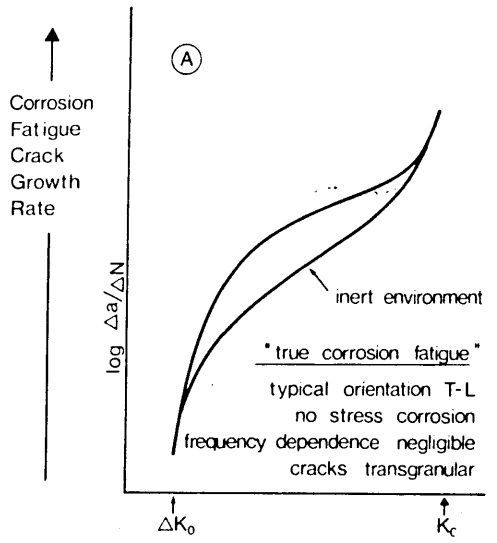

Fig 4.6.2.iv Typical fatigue crack growth behaviour in aggressive environments for systems not exhibiting SCC

Fractographic examination of corrosion fatigued specimens of alloys susceptible to stress corrosion cracking has shown an almost exclusively intergranular fracture path. On the other hand non stress corrosion susceptible alloys show a predominant transgranular fracture path. A distinction between the two types of corrosion fatigue cracking behaviour of aluminium alloys as described above has been suggested and the term "true corrosion fatigue" is used for the corrosion fatigue behaviour of alloys not exhibiting stress corrosion cracking suceptibility and "stress corrosion cracking under cyclic loading" the behaviour of the stress corrosion susceptible ones.

is linearly dependent on the loading frequency (fig 4.6.2.iii). This indicates that crack growth at very low frequencies is time dependent rather than cycle dependent. Another important observation is that the effect of the environment on the fatigue crack growth almost vanishes at low stress intensity ranges close to ΔKo. This is important for design engineers because it shows that corrosion fatigue is independent of crack path orientation at ΔK values near or below ΔKo.

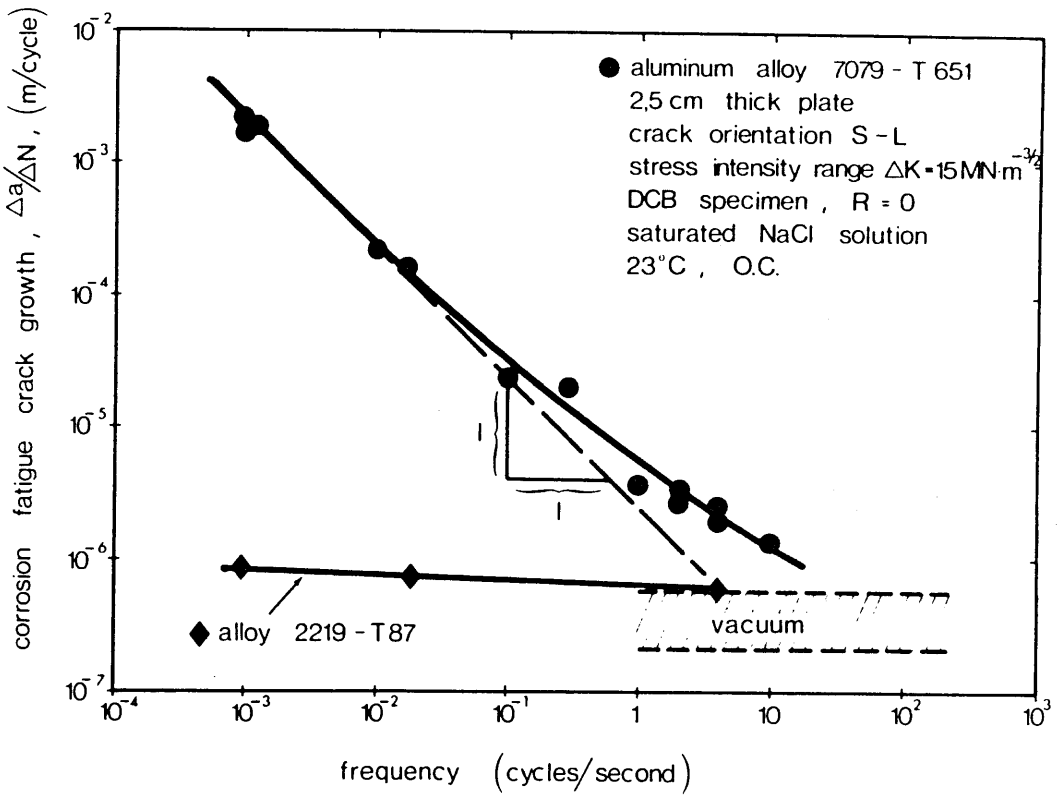

Fig 4.6.2.iii. Effect of frequency on the corrosion fatigue crack growth rate of 7079-T651 alloy (80).

For alloys not exhibiting stress corrosion cracking susceptibility the behaviour is shown in fig 4.6.2.iv. For such

4.7 Corrosion fatigue of Al-Zn-Mg welds.

To the authors knowledge there are no detailed quantitative results so far in the literature on corrosion fatigue cracking of Al-Zn-Mg welds. A recent publication deals with the fatigue strength of Al-Mg welds tested in air (86), the results being presented in the form of S-N curves. The corrosion fatigue behaviour of the white-zone, the area where Al-Zn-Mg welds are known to be stress corrosion susceptible, has not been investigated in detail. Even studies of the stress corrosion behaviour of the white-zone have provided data either in the form of loss of ductility or time to failure. The following work is an attempt to provide detailed crack propagation studies of the white-zone and explain the micro-mechanisms involved.

CHAPTER 5

5. SPECIMEN DESIGN

Although the stress corrosion cracking and corrosion fatigue behaviour of Al-Zn-Mg wrought products has been studied in detail, the sensitivity of the "white-zone" to environmental fracture can scarcely be experimentally established, since it is very difficult to test this narrow region alone and the heat treatment to which it is subjected can be varied and checked only to a very limited degree. The small amount of material available in a typical weld makes the use of conventional fracture mechanics specimens very difficult. One way of overcoming this would be the production of simulated welds along the lines of the work by Schmeidel & Gruhl (82) so that large specimens could be produced to enable a detailed study of the "white-zone". The problem with this approach is that although it is a good approximation of the welding process it is still not an actual weld and the results cannot confidently describe the "white-zone" behaviour.

A major part of this work concentrated on the employment of appropriate specimen designs that could be succesfully used for determination of the fracture toughness of the white-zone and corrosion fatigue testing. The small size of the weld meant that it would have to be a subsize specimen and comply with the fracture mechanics test requirements.

Two types of welds were investigated.

i) fillet welds, used for the determination of the fracture toughness of the white-zone;

ii) bead-on-plate welds, which were considered to be more appropriate for environment sensitive fracture studies of the white-zone because of the greater dilution (50% as opposed to 30% for fillet welds) which produces the most stress corrosion susceptible condition the weld can be in.

5.1 Specimen design for fracture toughness studies.

Standard fracture mechanics specimens require large amounts of material and are difficult and expensive to manufacture. The small size of the weld makes obvious the need of a sub-size specimen for the determination of the fracture toughness of the white-zone. Such a specimen should also comply with the International standards of materials testing. A survey of the literature showed that a method has been developed by Stark & Ibrahim (88) for determining K_{1c} values using small cylindrical circumferentially notched specimens.

The specimen design is shown below:

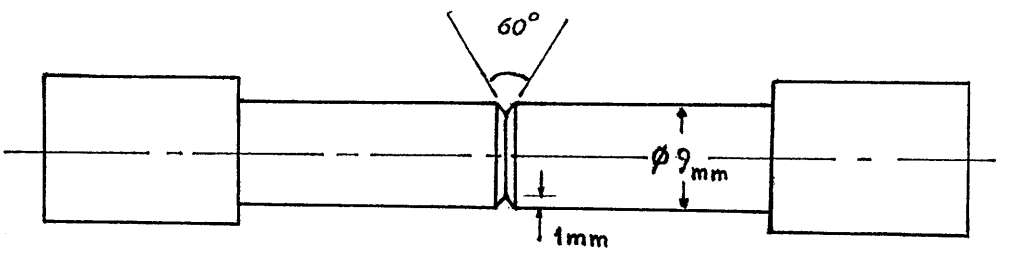

Fig 5.1.i Specimen for fracture toughness determination as proposed by Stark & Ibrahim

The Stark & Ibrahim type specimens were machined out of the fillet welds in such a way so that the notch plane would lie exactly on the white-zone as shown in fig 5.1.ii

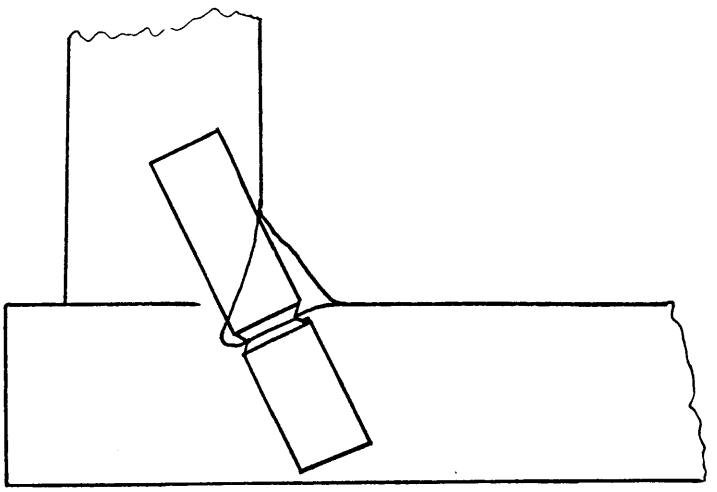

Fig 5.1.ii. Specimens as obtained from fillet welds.

Recently Kocak et al (89,90) have been studying the fracture toughness of the fusion line in structural steel welded joints and have been able to use standard specimens by producing bead on plate welds which have one side of the fusion line normal to the plate surface. They achieved that by tilting the welding gun at a certain angle. The same approach was also adopted in this work, prior to the publication of above mentioned work, but it was not possible to produce the required white-zone orientation despite efforts by the staff at Alcan International.

5.2 Specimen design for fatigue testing of the white-zone

5.2.1 Specimen type I

Initially specimens similar to the ones previously used for stress corrosion testing of welds by other workers (87) were machined and tested in tension-tension fatigue. Some specimens were produced that would include the weld toe and some with the weld toe machined off, (dressed welds) with or without a sharp notch introduced at the white-zone (fig 5.2.1.i). The sides of the specimens were masked off with "Turco" laquer (tests at Alcan laboratories have shown that it has good adhesive properties and does not crack or harden in the presence of aggressive environments) thus ensuring that any environmental effects would be confined at the weld toe or the notch root.

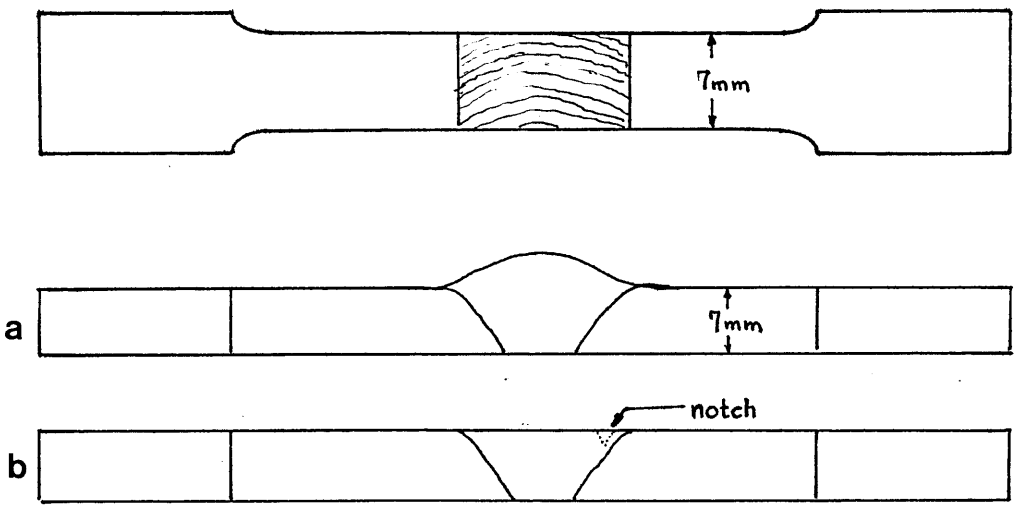

Fig 5.2.1.i Design of specimen type I.

As the white-zone path was not at right angles to the line of action of the load The K values values were expected to be obtained as described in the Compendium of Stress Intensity Factors (91).

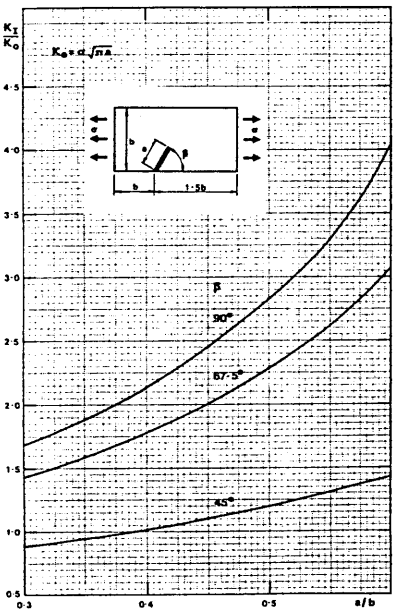

Fig 5.2.1.ii K for a slant edge crack in a rectangular sheet.

a) Specimens including weld toe.

Tests initially carried out at low frequencies (0.01, 0.02 Hz), where the environmental effects were expected to predominate, were unsuccesful, with specimens being cyclically loaded in the environment for up to 40 days without any signs of cracking at the white zone region or even the expected exfoliation corrosion at the overlap between weld toe and parent plate. Tests carried out with a maximum load of 70% of the yield strength of the material were also unsuccessful . (These tests were carried out establish whether the level of stress was important for crack initiation.)

b) Dressed welds.

The same procedure as described above was followed with dressed welds but no cracking was evident.

c) Notched specimens.

Although the notch was a sufficient stress raiser to initiate a crack, the latter never followed the white-zone path but always propagated through the heat affected zone to result in failure at right angles to the loading line. The results were similar to both low and higher frequencies.

5.2.2 Specimen type II.

The second type of specimen, designed for 3-point bending, had a rectangular cross-section and again either included the weld toe or had a notch introduced near the "white-zone" after the weld was dressed. The sides of the specimens were masked off with Turco lacquer. The stress intensity, K, values were expected to be given by the equation:

$$K = [6PW/BW^2]\sqrt{\pi a}F$$

where $F=\{1.19/[1-(a/w)^{1\cdot4}]^{1\cdot87}\} - 0.9\sin(3a/w)$ for $a/w < 0.7$

as quoted by Gray (93).

a) Specimens including weld toe.

Tests were carried out at frequencies of 0.05, 0.1 and 4 Hz but cracks never initiated in the 15 day period allowed for each test.

b) Notched specimens

These specimens had a notch machined such that the precracking would meet the white-zone . The environment was then introduced and the specimens were tested at various frequencies from 0.02 to 4 Hz. At very low frequencies (ie 0.02, 0.03, 0.05 Hz), cracks would propagate in the white-zone for approximately 1 to 1.5 mm and then continue to failure in the heat affected zone. At higher frequencies the cracks followed a straight path to failure. Results for the tests at 0.02, 0.03, 0.05 Hz are given in fig (7.3.v.). As there were some encouraging results from this type of specimen, in that corrosion fatigue does take place in the white-zone, the method was pursued further. The high frequency tests showed that the mechanical stress component predominates any environmental effects. The problem lies in the geometry of the white zone path in that it is not normal to the surface of the specimen. It was thought that shifting the specimen so that the middle loading point would lie not directly above the notch, as described in the standards, but at the point of emergence of the white-zone on the opposite face of the specimen would result in a more favourable stress field and cause the crack to propagate along the white-zone (fig 5.2.2.i).

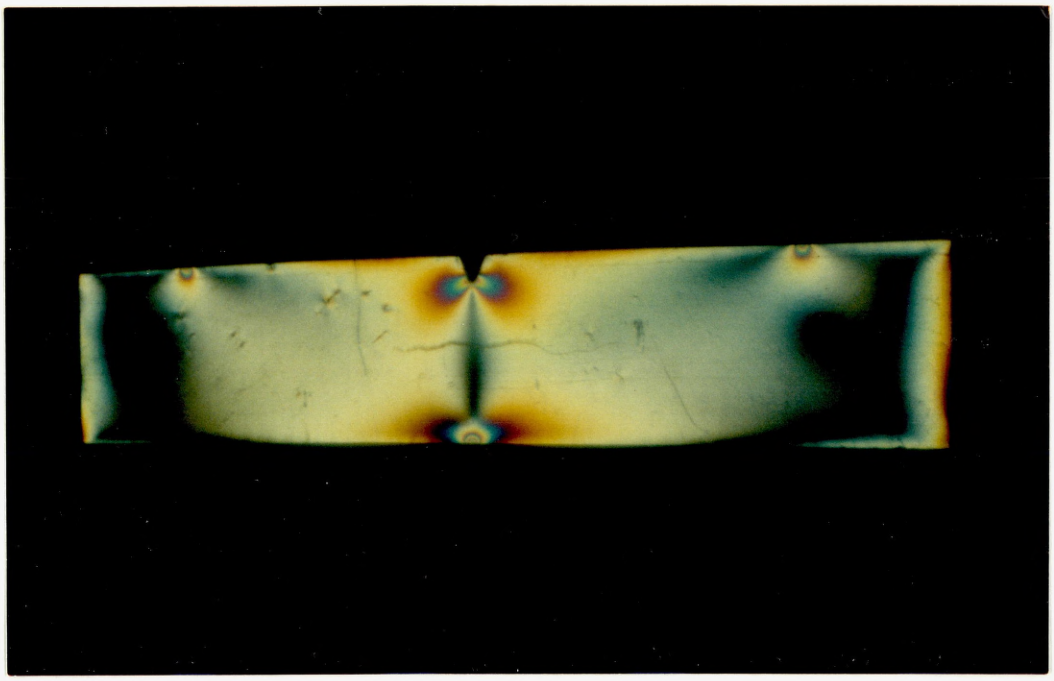

a

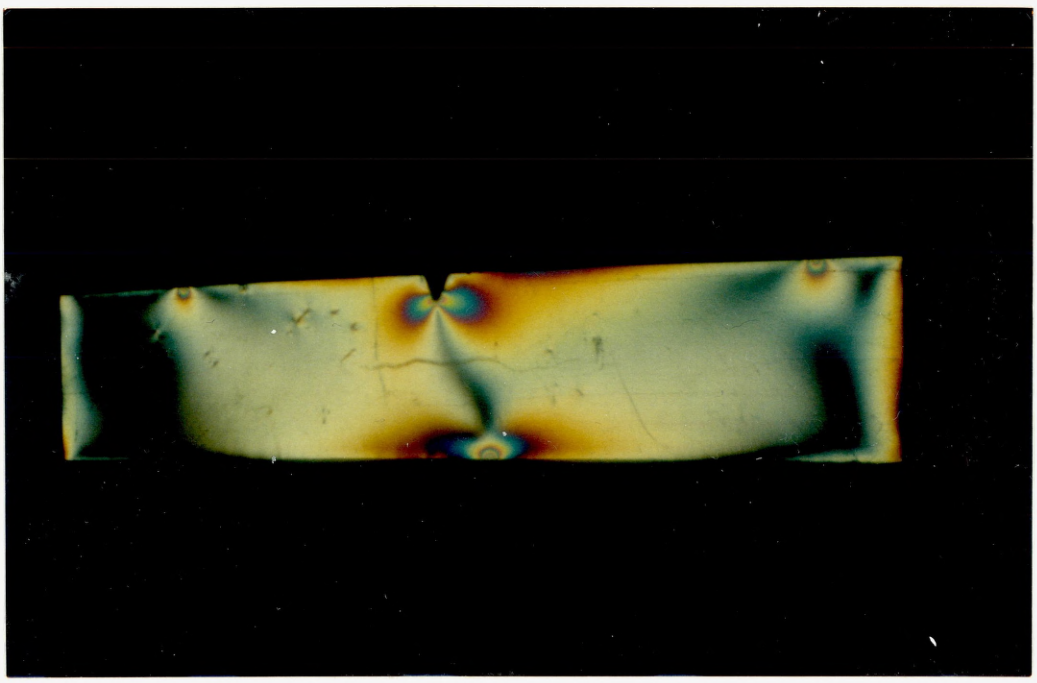

b

Fig 5.2.2.i Stress paterns for 3-point bend specimens as given by photoelastic models a) mid-point directly below the notch, b) mid point at an angle to the notch.

5.3 Analysis of the stress field in 3-point bend specimens for the white zone

Generally, the shape, dimensions and orientation of the weld bead allowed the production of specimen of 12x6 mm^2 cross-section with weld bead geometry as shown below:

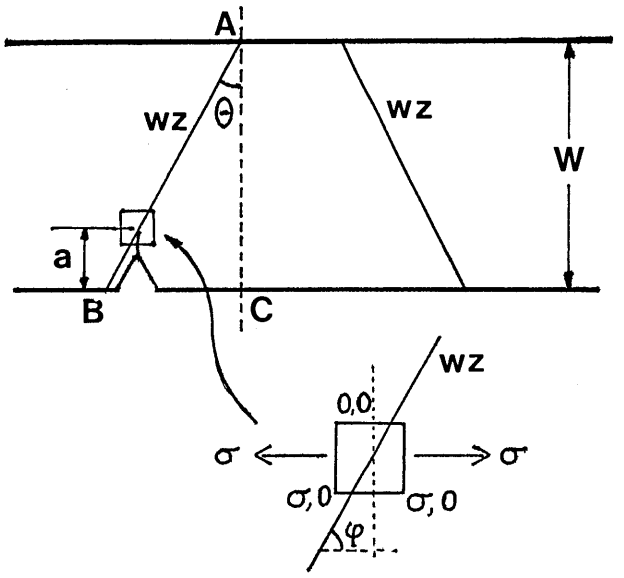

$\Theta \approx 19^0$

$\phi \approx 71^0$

$\sigma = M/S$

$s = I/c$

Using beam theory, the bending stress distributions along AB and AC were calculated and the results are shown in fig 5.3.i. The bending stress is approximately 17% lower at B than at C and this difference is reduced as point A is approached. Consider now the presence of a sharp crack at the white-zone.

In the case of a crack travelling along CA the bending stress σ will be vertical to the crack plane (case 1) and this is the crack opening force. In the case of the crack travelling along BA (the white-zone) the bending stress σ acts at an angle ϕ. Analysing the stresses in a small square element of material at the "white-zone" crack path gives:

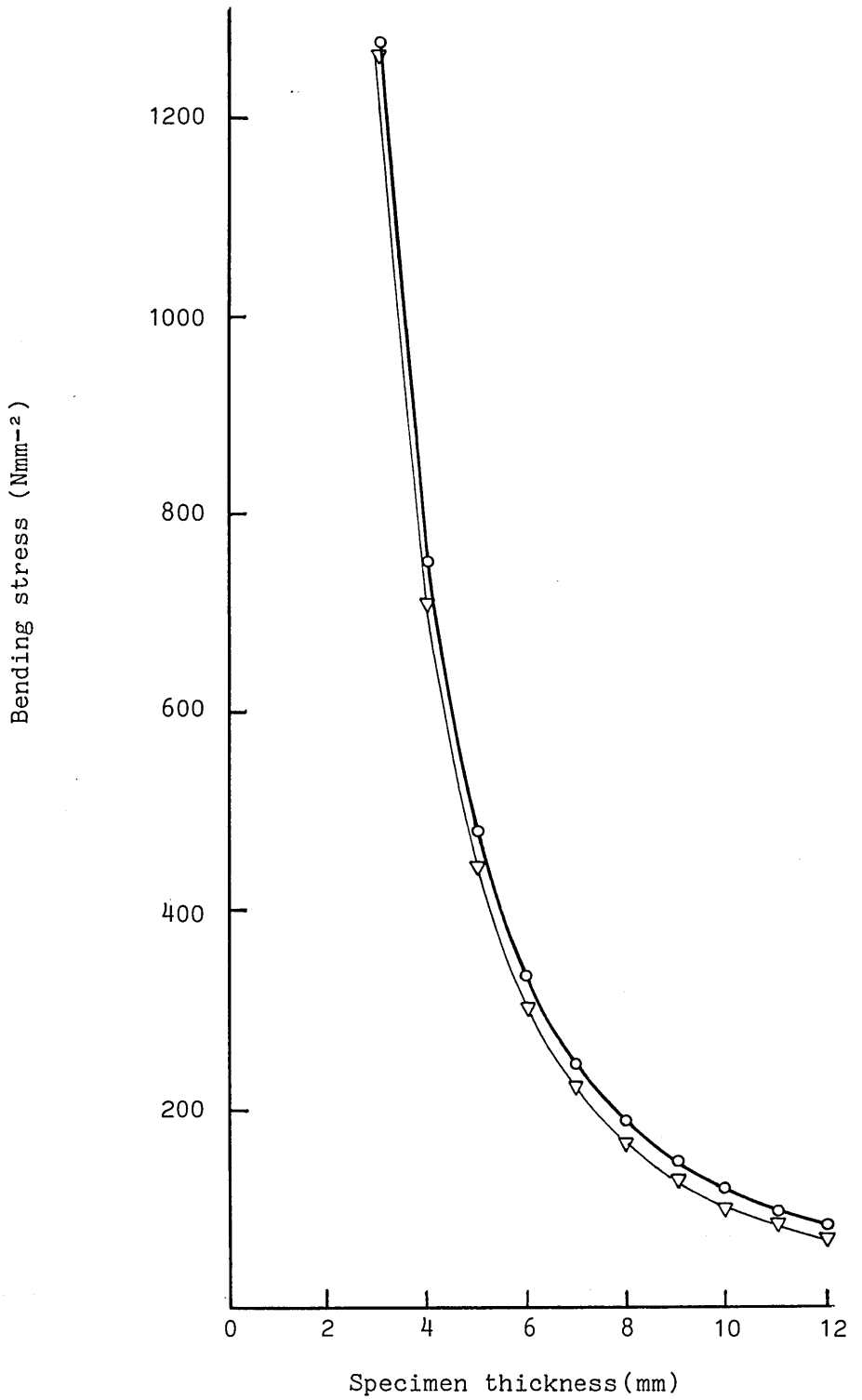

Fig 5.3.i Variation of bending stress along AB (○) and AC (▽)

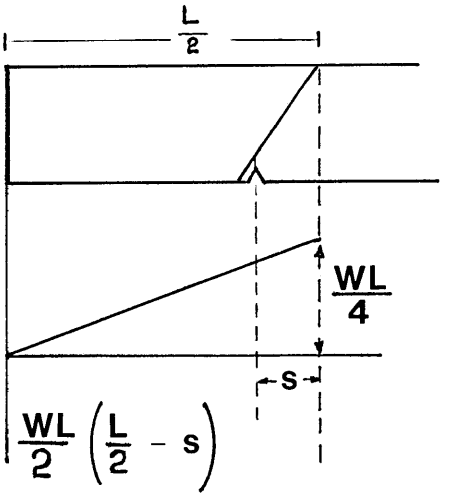

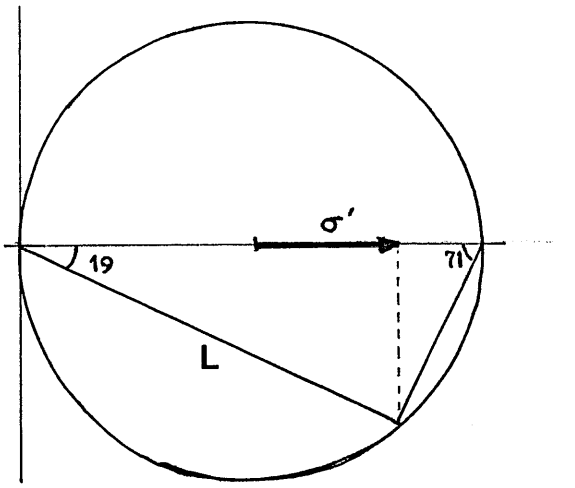

$L/\sin(71) = \sigma/1$ therefore $L = 0.945\ \sigma$

$\cos(19) = \sigma'/L$ therefore $\sigma' = 0.945\ L$

$\sigma' = 0.893\ \sigma$

Therefore, for a small element,

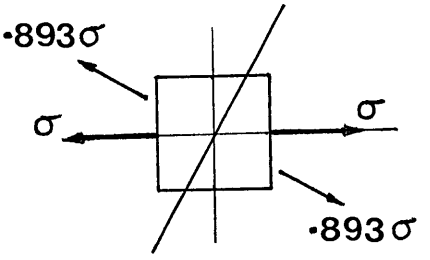

the stress will always be lower in the direction vertical to the "white-zone" plane.

As the crack propagates, at any instant

$Ieq = [B(w-a)^3]/12$

$Ymax = (w-a)/2$

$\sigma = (P/2)[(L/2)-S]\ \{12(w-a)/2B(w-a)^3\}$

$= \sigma - 3PS/B(w-a)^2$

Therefore $\sigma' = 0.893\ (\sigma - 3PS/B(w-a)^2)$

where B=specimen thickness
w=specimen depth
a=crack length
P=applied load
σ =bending stress for a vertical crack path

The analysis indicates that the crack would always propagate in a direction normal to the specimen surface unless the corrosion process provides a preferential crack path. Tests carried out with the notch displaced from the loading line, as catered for in the foregoing analysis, were not in fact successful, since cracking did not follow the desired white-zone path, and it was therefore necessary to seek a testing arrangement whereby the maximum stress component lay normal (as near as practicable) to the plane of the white-zone.

The most likely explanation of the failure of the above technique to produce white-zone cracking seemed to be

either:

a) corrosion fatigue propagation is not possible at white-zone regions or,

b) the specimen designs selected did not provide the appropriate loading conditions.

Since some results had been produced by the 3-point bend specimens and the stress corrosion cracking susceptibility of the white-zone is clearly established the former suggestion was rejected. If the suggestion that, hydrogen embrittlement is responsible for the environment sensitive fracture of 7xxx series alloys, and the argument by Ratke & Gruhl (49), that only when the correct state of stress triaxiality is established at the crack tip hydrogen embrittlement is operative, are accepted, then an alternative specimen design should have to be found for testing the white-zone. It was clear that the only way of producing any crack

growth by cyclic loading in the white zone, would be by having the applied load normal to the white-zone plane. Attempts to produce favourable white-zone orientations by producing bead on plate welds by either tilting the plate or the welding gun (as mentioned in section 5.1) were unsuccessful.

After attempts to obtain different weld bead - specimen configurations it was decided that the only way to achieve the required configuration was by employing an arc-shaped specimen. A survey of the lit erature showed that such a specimen existed (ASTM E399) and it is mainly employed for crack propagation studies of cylinder walls. The basic specimen design is given below, fig 5.3.ii). And this was the specimen employed throughout this work.

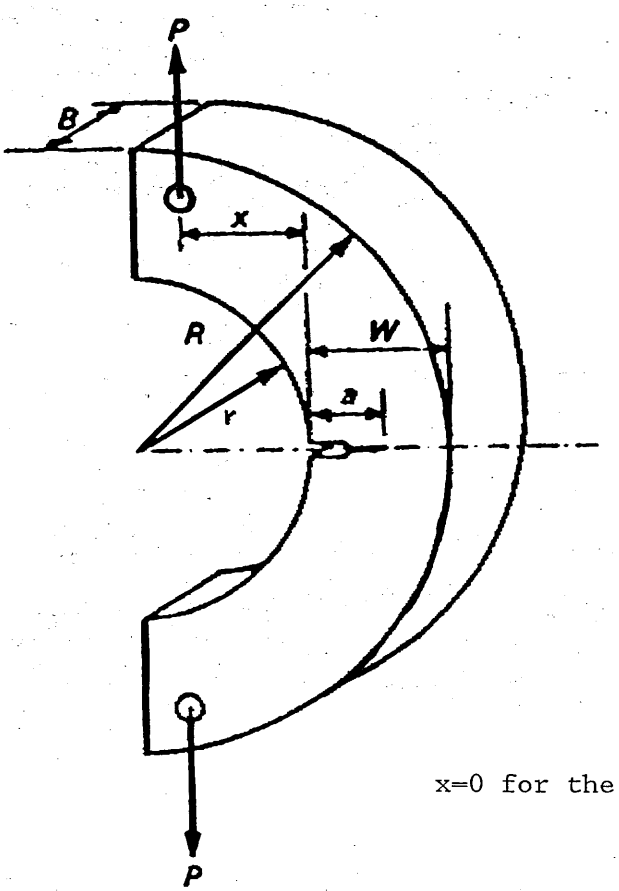

a=crack length

W=specimen width =R-r

B=specimen thickness =W/2

x=0 for the specimens used in this work

Fig 5.3.ii Arc shape specimen (ASTM E399)

The K factor is given by the equation:

$$K=[P/BW^{0.5}]\{1+0.5(a/W)\}\{1+0.221(1-(a/W)^{0.5})(1-r/R)\}\ f(a/W)$$

$$f(a/W)=18.23(a/W)^{0.5}-106.2(a/W)^{1.5}+389.7(a/W)^{2.5}-582(a/W)^{3.5}+$$
$$+369.1(a/W)^{4.5}$$

The specimen was machined out of the weld in the following way. First the welded plate was cut in slices of 10 or 12 mm thickness and the sides polished. Macroetching with Kellers reagent revealed the position of the white-zone. An arc was then drawn on the surface whose centre was on a line drawn on the white-zone. In this way the white-zone was in a radial direction and the points of the application of the load were normal to the white-zone plane.

CHAPTER 6

6. MATERIALS AND EXPERIMENTAL TECHNIQUES.

6.1 Material

The material used for this work was the medium strength Al-Zn-Mg alloy 7017 in the T651 condition, supplied as rolled plate of 25mm and 15mm thickness. Two types of weld were produced

a) fillet welds using the 15mm thick plate and

b) bead on plate welds using the 25mm thick plate.

No particular preparation of the plate was made for the fillet weld but for the bead on plate weld a notch of 14mm depth and 60^{o} included angle was machined on the plate in the transverse direction where the weld bead was laid. Both weld types were single pass MIG welds with the following welding parameters:

Current : 363 Amps

Voltage : 29.4 Volt

Filler wire : NG61

The composition (wt%) of the plate and filler wire were as follows:

	Zn	Mg	Cu	Fe	Si	Mn	Ti	Zr
7017-T651 (actual)	4.7	2.02	0.07	0.27	0.11	0.34	0.055	0.18
NG61 filler (typical)	0.2	5.2	0.1	0.18	0.09	-	-	-

6.2 Aqueous solution

All test solutions were made from Analar grade chemicals and water that had been passed through an "Elgastat" laboratory

deioniser. The solution was 2.5%NaCl + 0.5%Na_2CrO_4. The pH of the solution was adjusted to pH 3 with dilute HCl. The solution was acidified just prior to testing using a Jenway pH meter. The calibration of the pH meter was checked frequently with the aid of buffer solutions (pH 4,7 and 9) made with commercial tablets.

6.3 Test rig for fracture toughness experiments

The apparatus used for the determination of the fracture toughness of the white zone was an Avery cantilever beam rotating bending machine. The specimen was gripped from the shouldered end at the machine while on the other side a swivel roller bearing was fixed, from which the load was applied. The machine operated at a fixed speed of 3000 rpm, (ie 50Hz load cycling frequency).

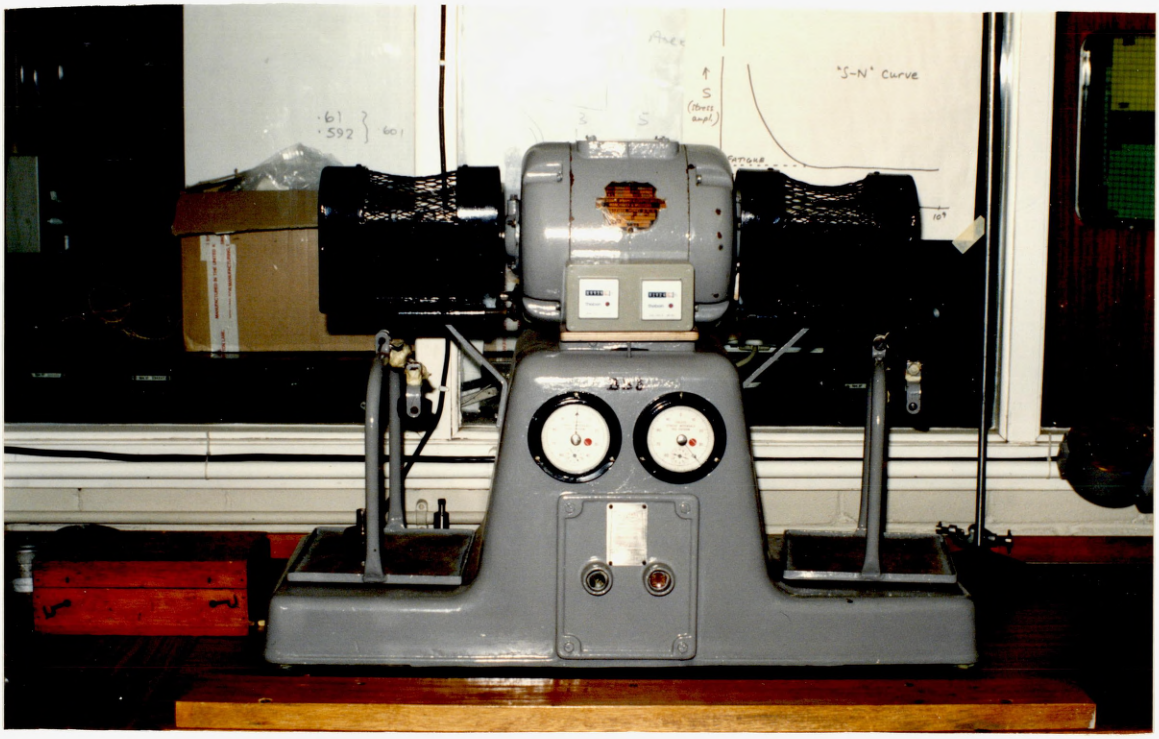

Fig 6.3.i Cantilever beam rotating bending machine.

6.4 Fatigue testing apparatus

The tests were set up on the small station, 60 kN capacity, of a Dartec universal testing machine. The Dartec has facilities for both constant-load and constant-deflection fatigue testing with an internal oscillator to provide sinusoidal waveform signals. An external signal input is also provided for connection with a function generator to provide other waveforms such as triangular, square or saw-tooth. The load cell was calibrated with the aid of a Solartron digital millivolt meter and the load cell resolution was found to be 6.7 N per millivolt.

Fig 6.4.i DARTEC fatigue testing machine.

Some tests were also carried out at the Alcan laboratories using a 100 kN capacity computer controlled hydraulic fatigue testing machine, Instron 8501, for high frequency work and a 100kN capacity, screw type computer controlled universal testing machine, Instron 8561, for low frequency and acoustic emission tests.

Fig 6.4.ii. Instron 8501 fatigue testing rig

6.4.1 Fatigue testing procedure

All tests were carried out in the constant load mode using a sinusoidal waveform with a load ratio (Min load/Max load), R=0.1. Constant load tests mean that fatigue crack propagation rates would be assessed with respect to increasing stress intensity factors. Specimens were precracked at 20Hz frequency and load ratio of 0.1

for approximately 0.5 to 0.7 mm. The fatigue machine was stopped and an optical measurement of the prec rack length was made and checked against the CGM5 reading for calibration purposes. The CGM5 reading was then zeroed, the environment was introduced and the required fatigue test frequency selected. Testing was then initiated but readings were not logged until the crack grew a certain distance through the plastic zone associated with precracking.

Some tests were also carried out using an external function generator (Feedback TWG 500) to provide triangular waveforms.

Fig 6.4.iii Instron 8569 fatigue testing rig.

6.5 Crack Growth Monitoring

Three methods of monitoring crack growth are currently employed:

(i) the crack opening displacement method (COD)

(ii) the potential drop technique

(iii) the shadow optical method of caustics.

The COD method , could not be used in this work, owing to size limitations of the specimens and the likelihood of the saline environment around the specimen causing significant galvanic cells to be set up between the COD gauge legs and the specimen.

The caustics method exploits the phenomenon whereby the stress intensification in the vicinity of the crack tip region of a loaded specimen results in a reduction of thickness in this region. This induces a "lens" effect which, on illumination from a point source, creates a shadow image on a plane a certain distance behind the specimen, fig 6.5.i. In this shadow the crack tip region appears surrounded by a dark spot encircled by a concentration of bright light. The relationship

$$K_{1c}=md^{5/2}$$

where d= caustic diameter

developed by Manogg (120) and Kalthoff et al (121) gives the stress intensity factor for crack advance. Although the method has been

successfully used by many workers it was felt that difficulties could arise in measuring the caustic diameter as: (i) the image would move in a fatigue test and (ii) a continuous measurement was not possible with the existing laboratory facilities and iii) surface filming effects which for long term tests would distort the caustic image.

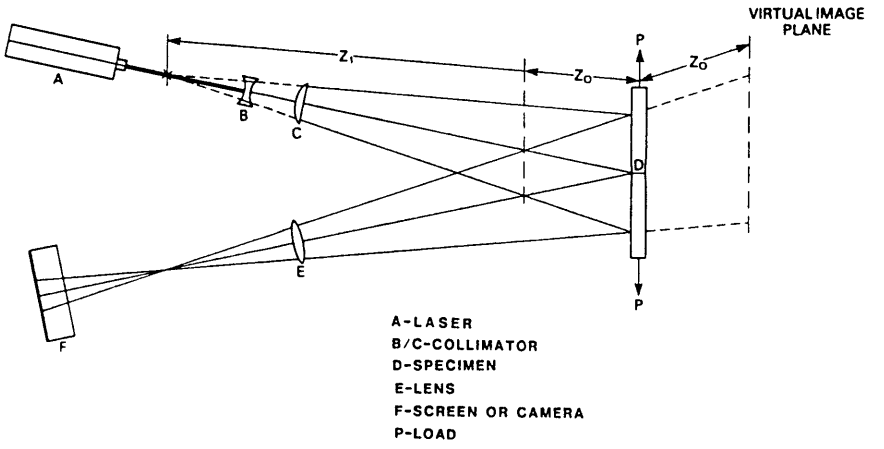

Fig 6.5.i Principle of the shadow optical method of caustics.

The potential drop technique essentially involves measurement of the potential drop across the mouth of a growing crack in a specimen through which an electric current, either AC or DC is flowing. The direct current version (DCPD) is well established and used in many laboratories. Recently a version that uses alternating currents has been developed (ACPD) and at least two models of ACPD crack growth monitor are now commercially available. Both DCPD and ACPD appear capable of high accuracy but the latter was chosen for this work since it uses small currents, 1-2 amps as opposed to 20-30 amps usually used with the DCPD, thus

avoiding the likelihood of heating the specimens significantly. There has been some scepticism over the use of alternating currents in corrosion tests for fears of interference with the electrochemical processes but research done by Kruger and Bird (94) has shown that, while current frequencies below 250 Hz can have some effect in the corrosion rate no effect was observed for higher frequencies. For crack growth measurements of aluminium and its alloys, the AC current frequency recommended is 1kHz and above, much higher than the frequency reported to affect corrosion reactions.

The highly compact MATELECT CGM5, incorporating power supply, potential meter, gain amplifier and AC current frequency selector for testing various metallic materials was selected, the basic operational circuitry being shown in fig 6.5.ii.

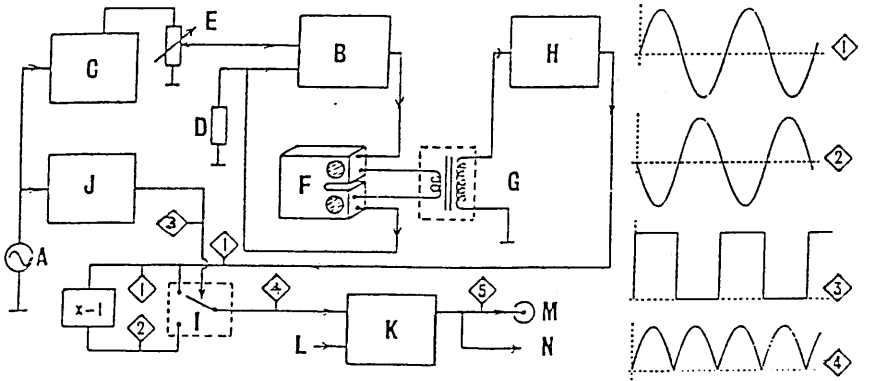

Fig 6.5.ii Operational circuitry of the CGM5 apparatus.

The resolution of the apparatus depends on:

a) the ambient temperature,

b) the lead configuration over the specimen, because of the interference between the electromagnetic field that is set round the ac current carrying specimen and the sensing leads,

c) the stress level applied to the specimen, because stress changes

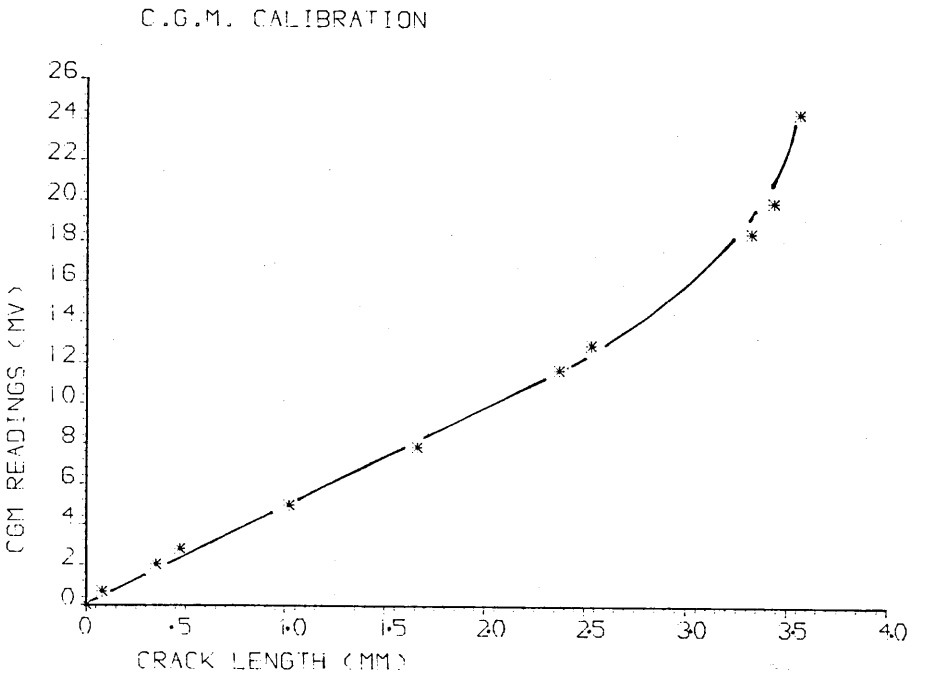

Fig 6.5.iii Calibration curve of the CGM5.

the electrical resistivity of metallic materials, thus affecting the electrical potential.

Cases a) and b) were solved by: monitoring the laboratory temperature and making corrections to the signal level for the first case, and performing calibration tests until the optimum lead configuration was achieved. The resolution of the crack advance

that was achieved was $2\mu m/10\ \mu V$. The relationship between crack length and potential output was linear for ratios up to 0.5 for crack length to specimen thickness.

6.6 Data acquisition

The potential drop was continuously recorded on a TEKMAN chart recorder via the analogue output of the CGM5, and data values were logged in an AMSTRAD 1640 personal computer via the RS232 communications port on the CGM5. (Communications software are given in appendix I.)

Crack propagation rates could thus be obtained in two ways:
a) "manually", by taking tangents at selected points on the chart recording and
b) "automatically", by handling data values through the PC to obtain crack propagation rates versus stress intensity factor range curves. (Data handling software are shown in appendix I.)

A difficulty was encountered with the handling of data for the calculation of crack propagation rates owing to signal variation with stress. The problem arose from the fact that there was no communication between the DARTEC fatigue testing machine and the PC, so that the software could trigger data to be stored each time the load reached a predetermined value during the load cycle. Data was stored through a time counter in the software that could be adjusted according to the test. (ie a reading stored every 10, 60, 100, 200 seconds etc.) As there was always a phase difference

between the timer and the fatigue frequency selector on the DARTEC data were recorded at various points on the loading cycle showing changes in the crack growth rates where there were not any.

As the sampling frequency of the CGM5 was 400ms this problem was more profound at the low fatigue frequencies. A schematic representation of the effect is shown on fig (6.6.i).

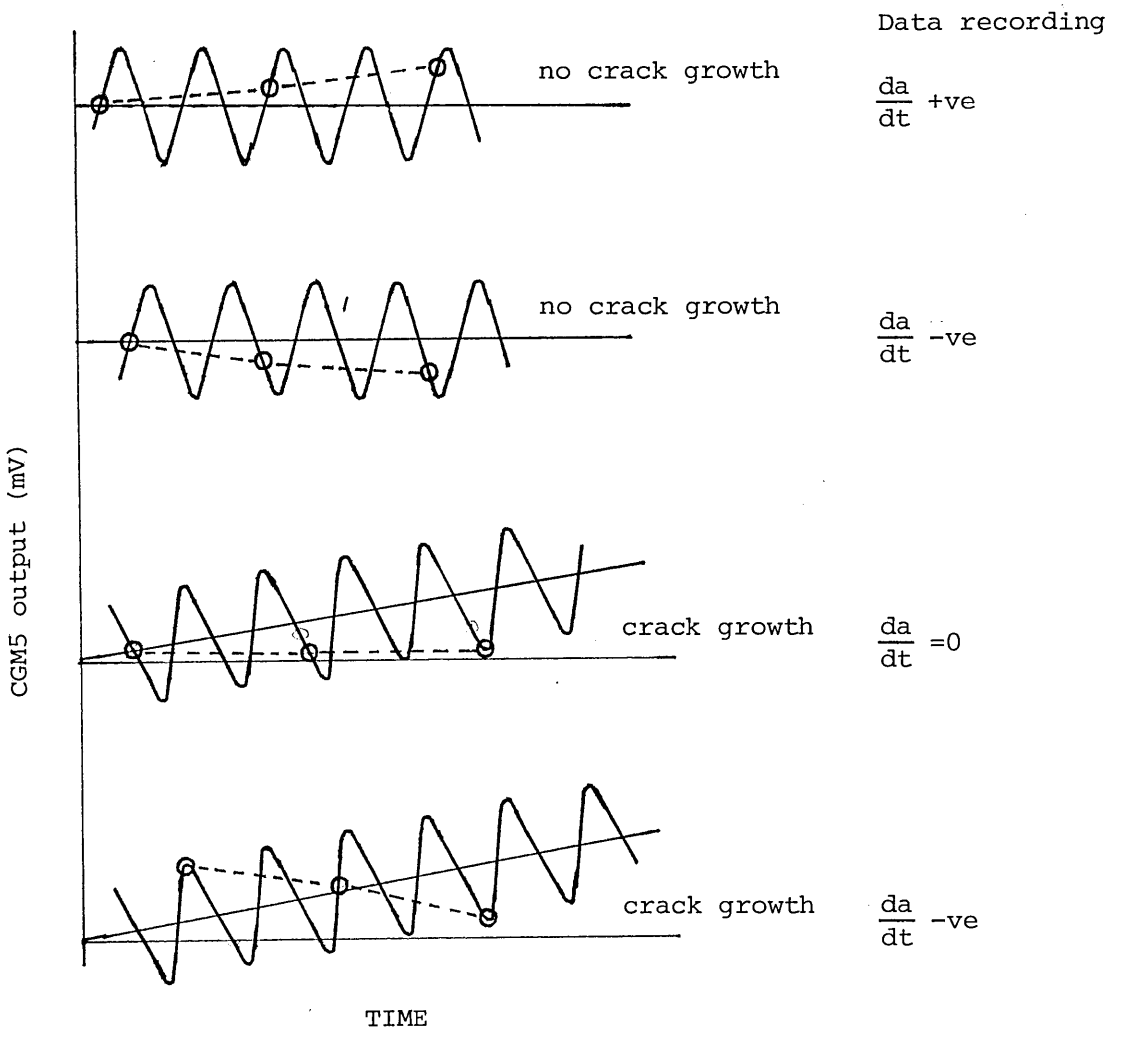

Fig 6.6.i Effect of phase difference between data logging timer and fatigue testing machine frequency selector on the recorded crack growth rates.

A series of modifications of the software both for data handling and logging were made in order to reduce this error. At first the time between successive data being logged was increased so that the slope between successive readings would be small, but it should not be so great as to allow any changes in the crack growth rates to be missed. After a series of calibration tests this was found to be not more than 5 minutes for fatigue frequencies 0.01 to 0.05Hz, 200 seconds for frequencies of 0.06 to 0.2Hz and 60 seconds or less for higher frequencies.

The data handling software was modified by making the following assumptions:

i) for any logged data value the next value to be logged will either be greater or equal to the previous one (smaller value means a reduced crack length, which is physically impossible);

ii) for two equal successive values the crack growth rate is zero.

Therefore if the data value to be logged was smaller or equal to the previously logged one, it was ignored and the next one was selected until a higher value was found, the number of cycles elapsed between these readings being counted. The crack growth rate was therefore the difference between the last value and the higher selected one divided by the total number of cycles elapsed.

The data was then smoothed out by applying the method of "moving averages", using the "MINITAB" statistical analysis package on the VAX mainframe computer at Dundee Institute of Technology.

The curves of crack propagation rate versus stress intensity range obtained with the method described above fitted extremely well with curves obtained "manually" by taking the tangents to the chart recording of crack length versus time.

6.6 Acoustic emission tests

It is common knowledge that fracture is accompanied by the generation of sound. What is not very widely known is that even extremely slow, ostensibly stable fracturing is not silent. These acoustic emission events are the transient elastic radiation produced by many microscopic deformation and fracture processes in materials. When this elastic radiation contacts a surface, it produces a displacement that can be detected and measured by a suitable sensor. The sensors are commonly made of piezoceramics, which convert displacement to voltage. After amplification, the voltage signal can be stored for later analysis. Typical acoustic emission signals appear as an oscillating voltage that quickly rises to peak value, then slowly decays to the background noise level.

Acoustic emission has been detected in many materials during elastic and plastic deformation and fracture. Possible sources of these elastic waves include the rapid collective motion of a large number of dislocations, inclusion and precipitate fracture or pull-out from the matrix, Luders band propagation in iron alloys, and rapid, brittle crack extension. (90). Because many of these processes occur during subcritical crack growth in materials, acoustic emission has the potential to be a monitor of crack initiation and propagation in engineering components. Acoustic emission has also the potential to provide information on the mechanism of crack extention (91, 92) in stress corrosion cracking.

Acoustic emission has been detected for environment induced subcritical crack growth in a number of materials. It is important to distinguish between anodic dissolution and hydrogen induced subcritical crack growth when evaluating the acoustic emission data because anodic dissolution induced subcritical crack growth may occur by atomistic dissolution or brittle crack jumps, while hydrogen induced subritical crack growth must occur by mechanical fracture. Distinguishing between these two processes can be difficult for some materials in aqueous solutions, since the mechanism of crack extention may be hydrogen related, while the source of hydrogen is the corrosion reaction. This complexity occurs for many materials including ferritic steels, aluminium alloys and titanium alloys.

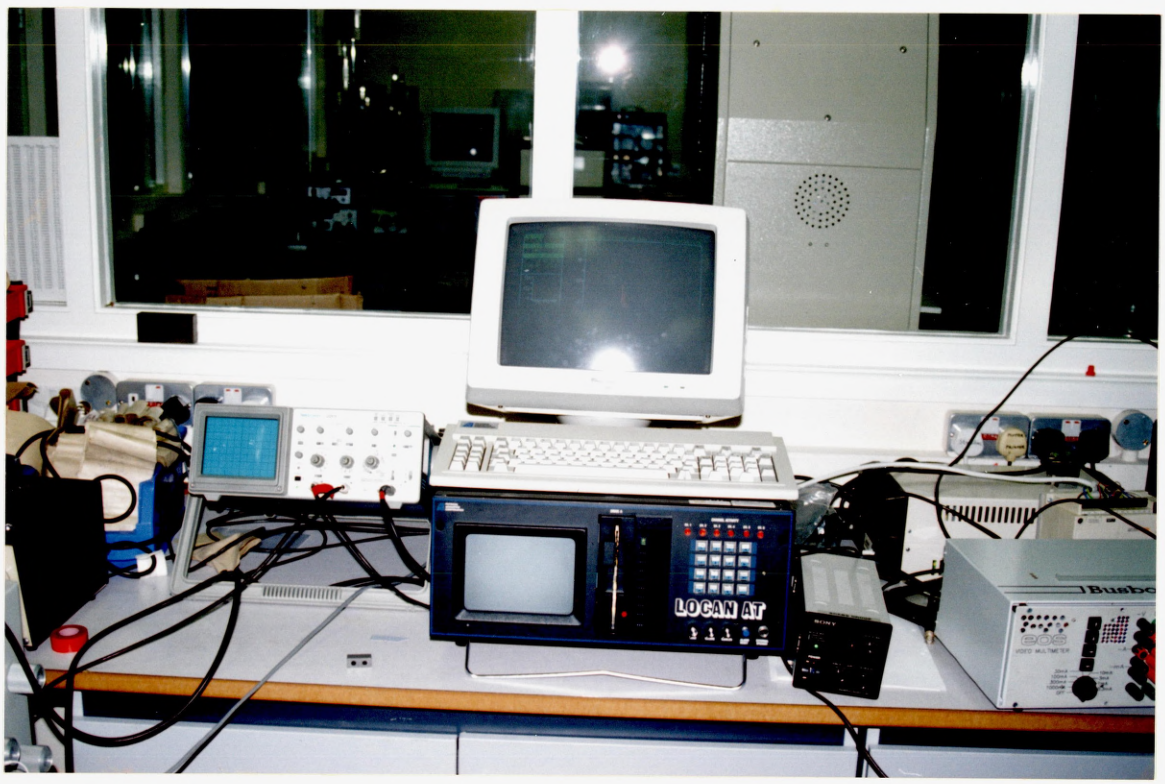

Fig 6.6.i LOCAN AT acoustic emission test apparatus.

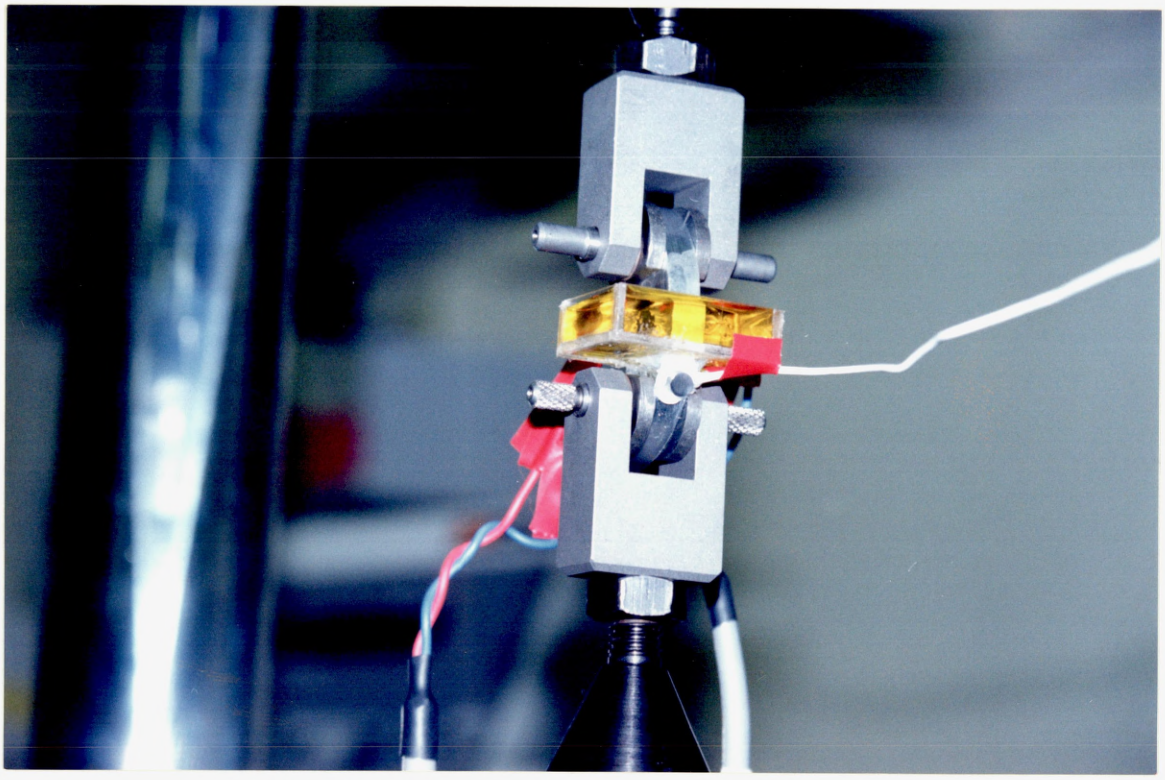

Fig 6.6.ii. Miniature piezoelectric transducer used for AE tests.

Acoustic emission tests were carried out using a LOCAN AT apparatus (fig 6.6.i) at the Alcan Laboratories for loading frequencies of 0.1 and 0.5Hz. The small size of the specimen required the use of a special miniature piezolelectric probe as shown in fig 6.6.ii. The probe was mounted using a small amount of mastic silicon.

6.7 Time-lapse video recording of crack growth in fatigue

Time lapse video recording was also made of the crack growth during corrosion fatigue, for test frequencies of 0.1 and 0.5 Hz, at Alcan Laboratories. The recording was done in an attempt to observe whether cracking was continuous or took place in distinct crack jumps.

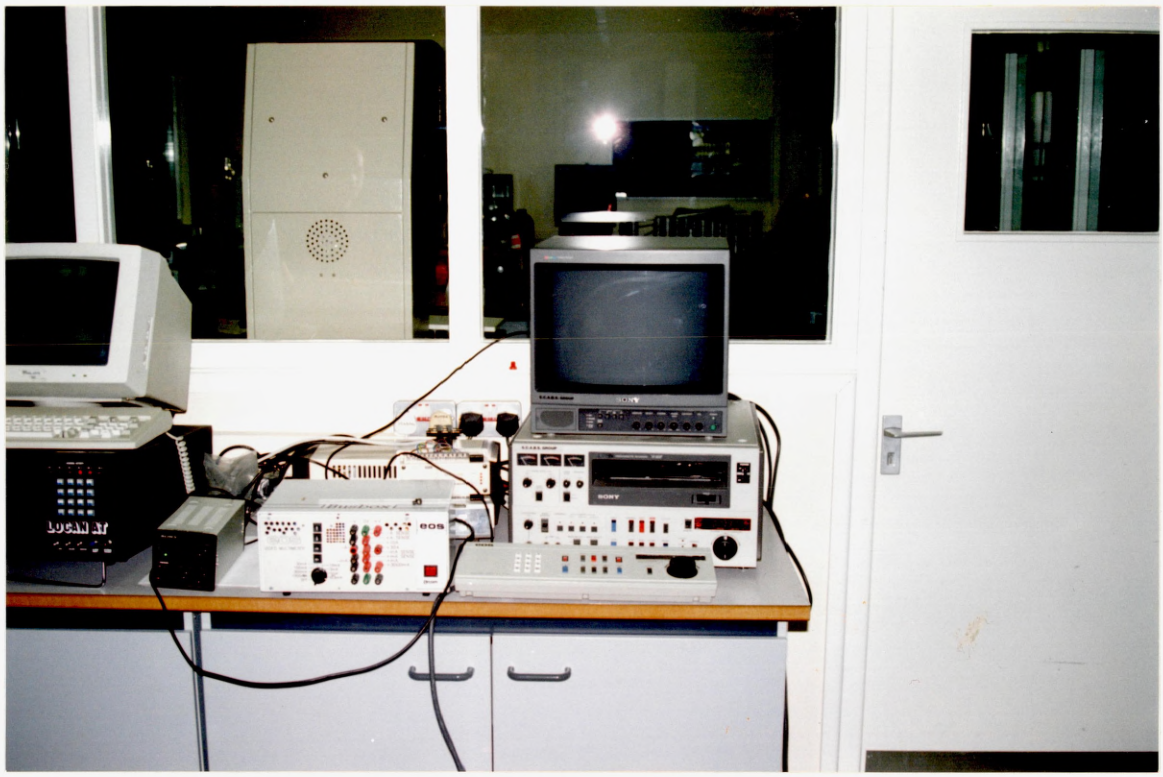

Fig 6.7.i Experimental set up for time-lapse video recording of crack growth.

CHAPTER 7

7. EXPERIMENTAL RESULTS.

7.1 Determination of Kıc value of the white-zone of 7017-T651 aluminium alloy weld.

Cylindrical specimens of 8.5 mm diameter and 60 mm length were machined out of fillet welds as described earlier (section 5.1). The specimens were fatigue precracked in air in an Avery cantilever-beam rotating bending fatigue machine. The presence of a crack was detected by a dial gauge placed over the load carrying bearing, with a 0.1 mm deflection indicating a crack of approximately 1mm depth. After precracking the specimens were tensile tested to failure in a 100 kN capacity Instron tensile testing machine, the load to failure being recorded. The average fatigue crack depth was then measured using a low power microscope by taking readings of crack depth, from the notch root, round the circumference at 30^0 intervals.

One of the major problems of using this method was the high proportion of specimens showing uneven crack growth leading to an eccentric ligament at fracture. As a result many of the specimens had to be discarded. More recently Stark & Ibrahim (98) carried out finite element analysis for a wide range of eccentricities and crack depths, giving the following functions for calculating Kıc.

$$K_{Ic} = (\sigma_t + \sigma_b)\sqrt{(\pi a F/10^3)}$$

where $\sigma_t = 4P/\pi D^2$

$\sigma_b = 16P\epsilon/\pi D^3$

$$F = Fo\ e^{\alpha(\epsilon/D)}$$

$$Fo = 1.25/[1-(2a/D)^{1.47}]^{2.4}$$

$$a = 22.188\ e^{4.889(2a/D)}$$

The eccentricity ϵ was calculated by determining the sum of the first moment of area of each 30^0 wedge about the x and y axes and dividing these moments by the ligament area.

The first estimate of Kic, that is K1, was calculated as above, then the Irwin correction, r_y, is calculated from:

$$r_y = (10^3/6\pi)[K1/\sigma y \cdot]^2$$

giving a corrected value of $\bar{a} = (a+r_y)$

Kic is then calculated using $\bar{a}$ instead of a.

In order to assess the validity of the method, specimens were machined out of the parent plate in the transverse direction and were tested as above. The results are shown in table 7.1.a.

Spec No	Load to failure	Kic	r	ϵ
	(N)	($MNm^{-3/2}$)	(mm)	(mm)
1	6300	32.7	0.24	0.73
2	7480	33.6	0.25	0.65
3	6370	32.8	0.23	0.55
4	7460	30.5	0.21	0.55

Table 7.1.a Kic values of 7017-T651 alloy rolled plate obtained using the Stark & Ibrahim approach.

The average value of Kıc from the above results is 32.4 ±1.6 $MNm^{-3/2}$ This value is very close to the published result for Kic of the alloy (33 $MNm^{-3/2}$) as obtained from standard fracture mechanics specimens and procedures.

Tests were then carried out on the welds and the results are given in table 7.1.b.

Spec No	Failure load (N)	Kıc ($MNm^{-3/2}$)	r_y (mm)	ϵ (mm)	a (mm)
1 *	6850	36.2	0.37	0.59	2.13
2	7100	20.7	0.16	0.27	1.70
3	5450	30.0	0.29	0.72	2.19
4	6540	24.0	0.21	0.42	1.89
5	7300	17.7	0.13	0.12	1.61
6	6100	23.6	0.20	0.34	2.03
7	4670	20.9	0.17	0.54	2.13
8	5750	19.5	0.15	0.11	2.08
9	6600	17.0	0.12	0.06	1.76
10	6720	22.9	0.19	0.16	2.00
11	7960	23.6	0.20	0.15	1.81
12	7360	21.3	0.17	0.12	1.82
13 *	4800	12.3	0.06	0.17	1.70

Table 7.1.b Kıc values of the white-zone of 7017-T651 alloy weld as obtained using the Stark & Ibrahim approach.

From the above results (1-12) the average value of Kıc is 22.3 ±6.5 $MNm^{-3/2}$. The asterisk denotes that the final fracture did not take

place at the white zone. It is also evident that for the white-zone tests there is much larger scatter than for the parent plate. This was expected for two reasons : a) the presence of residual stresses in the weld and b) the inhomogeneity of mechanical properties of microstructural regions near the white zone.

The determined value of 22.3 $MNm^{3/2}$ for the fracture toughness of the white-zone will probably be an underestimate for the following reasons:

i) Stark & Ibrahim recommend the use of a four-post die set during tensile testing to constrain the specimens in an axial direction without any rotation that might be generated by bending moments caused by any eccentricity of the ligament. Such a die was not used in the above tests; this would tend to cause the specimen to fail at a lower load, resulting in lower Kic values. Such errors, however, are small enough to be ignored since small changes of the load value in the equation for the calculation of Kic do not appreciably change the result which is always much smaller than the scatter of the results for the white-zone.

ii) Microscopic investigation of the failed surfaces showed in some cases that material has been drawn from the heat affected zone, as shown in fig 7.1.i, so that the specimen would fail at much lower load than expected.

iii) The material at the notch is not homogeneous and an assumed yield strength of 340 MN/m^2 was used in the above calculations. The value was chosen because it is widely known that 7xxx series alloy welds recover up to 80% of parent plate strength through room temperature precipitation hardening. This means that the strength

of the weld would vary depending on the time elapsed between the plate being welded and testing of the specimens. Also the weld showed signs of porosity which for some specimens would seriously reduce tensile strength.

In order to get a better approximation of the K_{Ic} values, Hounsfield specimens were machined out of the weld metal and tested to failure. The mean value of the yield strength was 220 MN/m^2. The calculations were then repeated and the results are shown in table 7.1.c.

Spec No	Failure load	K_{Ic}	r
	(N)	($MNm^{3/2}$)	(mm)
1	6850	invalid	-
2	7100	23.7	0.38
3	5450	41.5	0.66
4	6540	29.1	0.48
5	7300	invalid	-
6	6100	28.6	0.46
7	4670	24.4	0.38
8	5750	22.7	0.34
9	6600	18.9	0.27
10	6720	27.6	0.44
11	7960	invalid	-
12	7360	invalid	-
13	4800	13.0	0.15

Table 7.1.c. K_{Ic} values for the white-zone of 7017-T651 weld obtained by using weld metal yield strength.

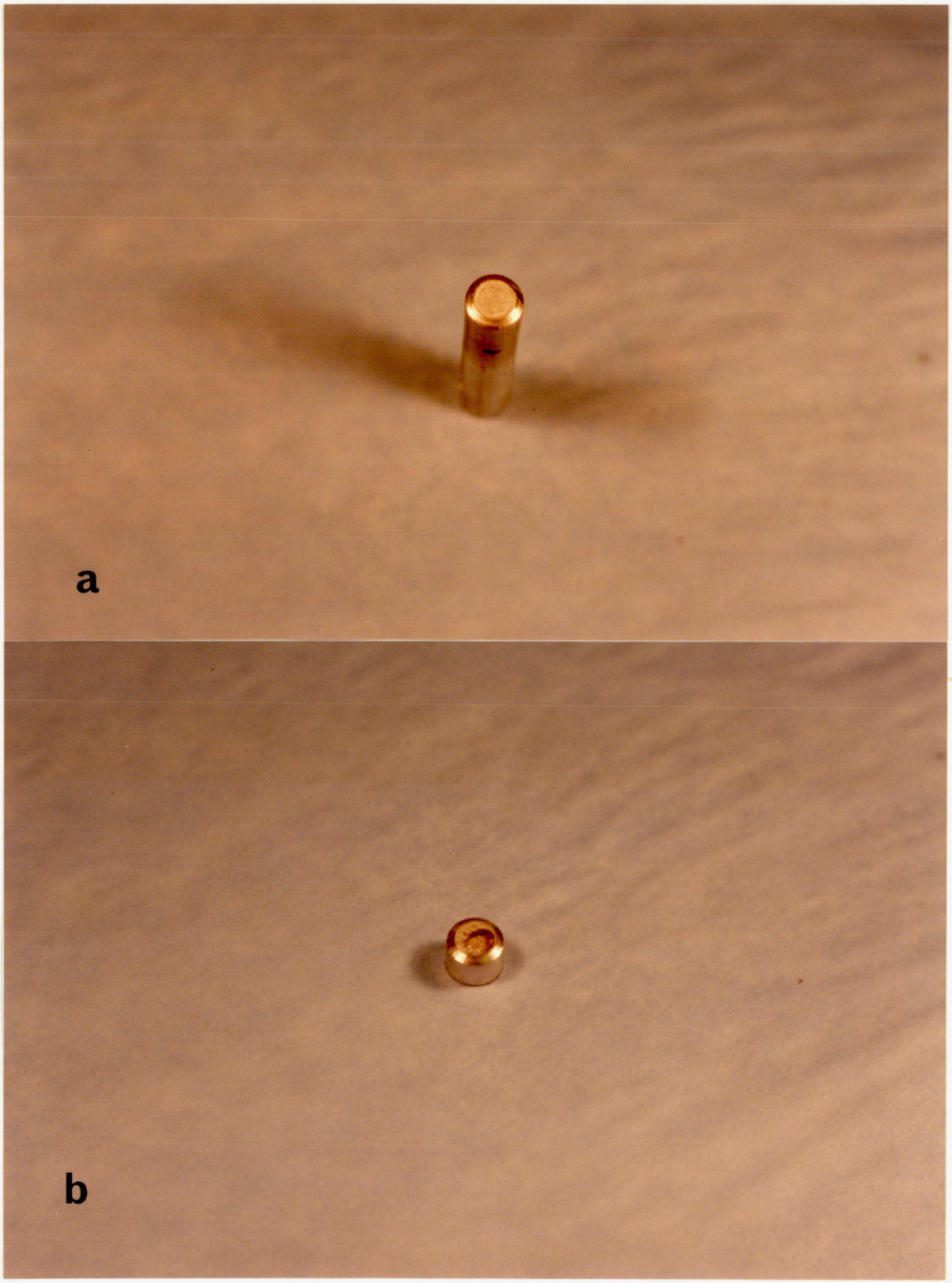

Fig 7.1.i Fracture surfaces of rotating bending specimens;
a) valid specimen, b)invalid specimen.

Some of the results were not valid since the deepest fatigue cracks were smaller than twice the plastic zone radius, r. The average value for Kıc was again 22.3 $MNm^{-3/2}$.

It can be seen from the mathematics that the Kıc values are inversely proportional to the tensile strength of the material. Since the Kıc value at the white-zone is to be determined then its yield strength has to be determined. This is very difficult since the width of the white-zone is only about 0.5 mm (99). An attempt was made to relate yield strength to the hardness of the material. Vickers hardness measurements were made across the weld and the results are represented in fig 3.1.i . The curves are typical of weldable aluminium alloys (13). The hardness of the weld metal is approximately 40% lower than that of the parent plate (160 HV). The tensile strength of the weld metal is about 45% lower than that of the parent metal. If linear relationship is assumed between hardness and tensile strength then it can be seen from fig 3.1.i that the area around the white-zone has almost the same hardness value as that of the parent metal. On this basis the Kıc value calculated using a yield strength 80% of the parent metal value would be a very good approximation.

Tests were carried out on another fifteen specimens machined out of fillet welds to better establish the Kıc value. The average value of Kıc was 22.5 $MNm^{3/2}$.

7.2 Corrosion fatigue testing of the white-zone.

7.2.1 Testing difficulties.

The results presented of the fatigue crack growth rates of the white-zone are averages from at least three tests, in order to reduce errors arising from experimental scatter. Repeat tests had also to be carried out for the following reasons.

Firstly, difficulties were encountered because the white-zone did not lie in a single plane, as shown in fig(7.2.1.i).

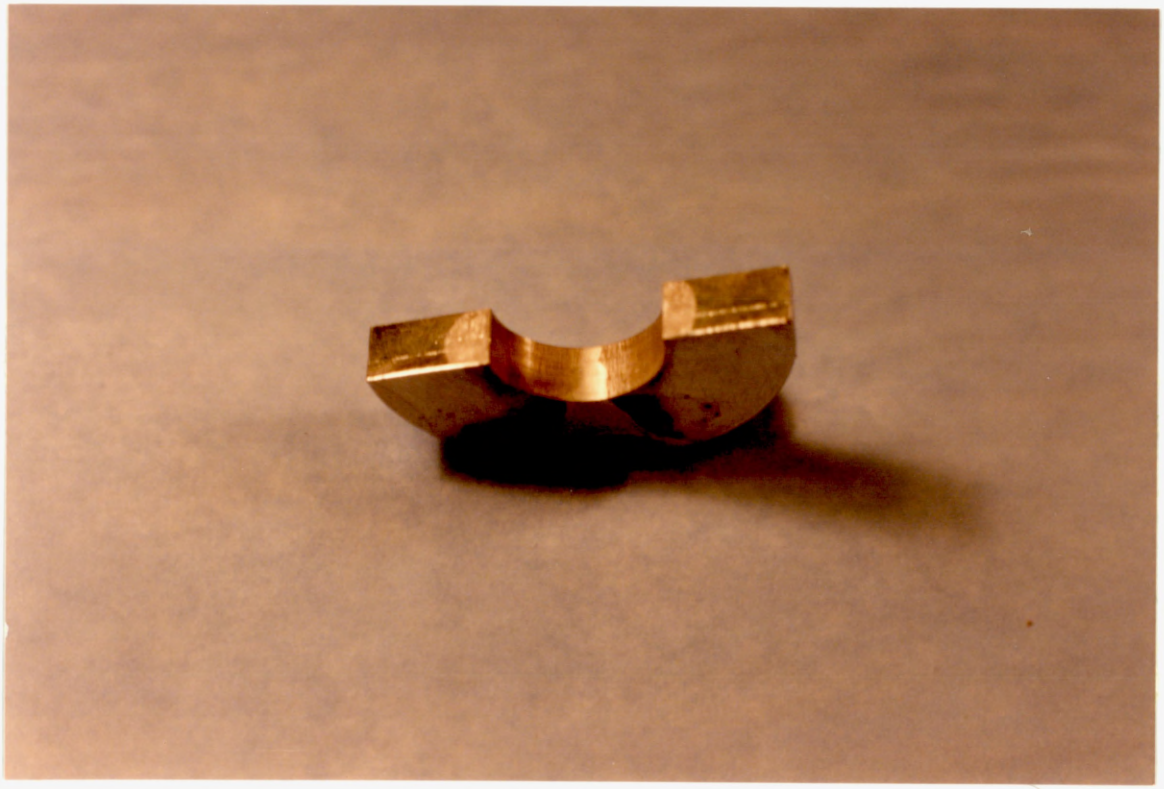

Fig 7.2.1.i. Photo showing the anomalous plane of the white zone.

This means that although the white-zone path at the sides of the specimen, after macro-etching, showed a straight line path,

this was not the case throughout the specimen cross-section. The propagating crack would thus meet either weld metal or parent plate grains and the result was usually i) either a reduction in crack growth rate or ii) a change in the crack path almost exclusively towards the parent plate, where the path was more favourable mechanically on account of the elongated grains.

The second problem arose from residual stresses, which were present even in the small specimens that were used in this study. The residual stress pattern in the specimen (or in any section of a bead on plate weld), shown in fig 7.2.1.ii below, leads to an irregular crack front during precracking, fig 7.2.1.iii. Results from such a specimen are invalid since fracture mechanics theory requires an even crack front (usually of a thumb-nail shape) for the stress intensity values to be correct. The effect of residual stresses is usually reduced by three methods.

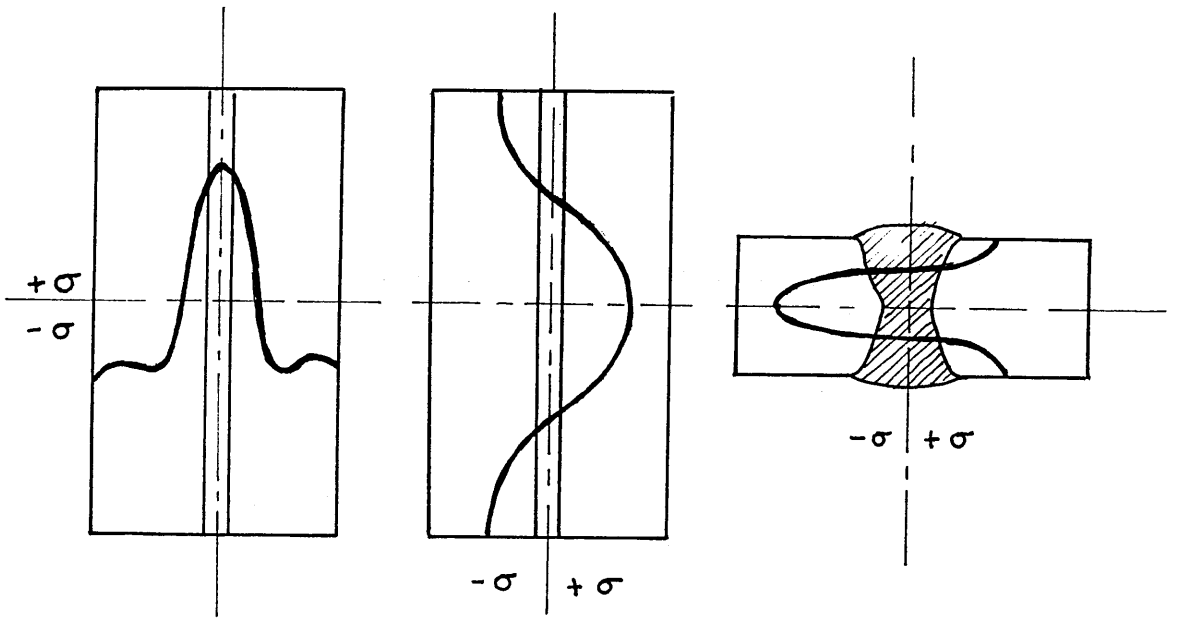

Fig 7.2.1.ii Residual stress pattern found in welded sections.

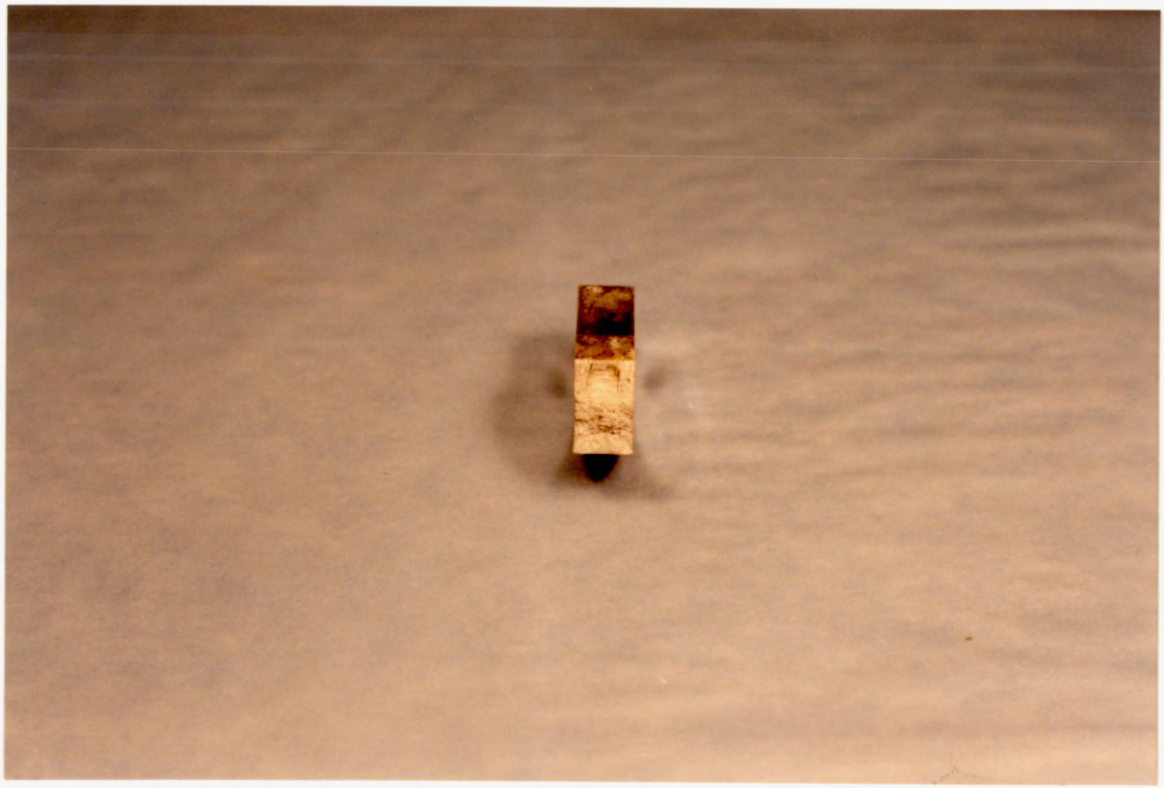

Fig 7.2.1.iii. Fatigue crack front shape owing to residual stresses.

a) Local compression. Relieving of residual stress is usually done by plastically compressing the ligament below the notch by nominally 1 per cent of the specimen thickness. Experience has indicated that local compression is needed for sections over 15mm thickness. The effect on the residual stresses is shown in fig 7.2.1.iv. Although the method is widely used it was thought that it would not be appropriate in this work because of the small size of the specimens (maximum thickness 7mm).

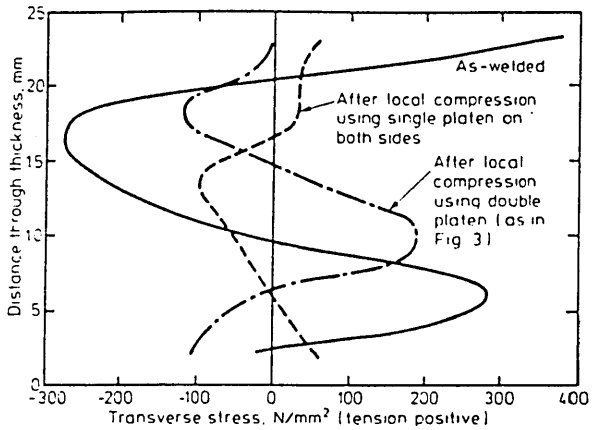

Fig 7.2.1.iv Effect of local compression on the residual stress pattern (100)

b) **Compressive loading.** This method involves prior loading of the notched specimen with the notch tip in compression. This introduces residual tensile stresses at the tip which counter balance the residual stresses from the welding process (100,101). In order for the method to be effective the compressive load should be at least three times higher than the highest load to be applied during fatigue testing. This is to ensure that sufficient stress redistribution (and probably relief) takes place. The method is similar in principle to local compression but the resulting stress distribution will almost certainly be different for the two techniques. The compressive loading technique is usually used for three-point bending specimens, where to carry out the operation the specimen is simply turned through 180^0. The method could not be applied in this work owing to the shape of the specimen used.

c) **High R-ratio.** High positive R-ratios have been found to improve the shape of fatigue cracks in the residual stress fields of multipass welds (102,103). The method has some drawbacks, such as an increase in number of cycles for crack growth above that required for low R ratios and, more importantly, an uncertainty as to the effect of high crack ratios on the fracture toughness values. Furthermore, even if the crack front is more straight, the residual stresses ahead of it still remain. A recent study has reported that pre-cracking first at an R ratio of 0.1 and then at R=0.7, keeping the same maximum load, produces results which do not affect the fracture toughness and do give an acceptable crack front (104). This was the method adopted in this work and proved successful.

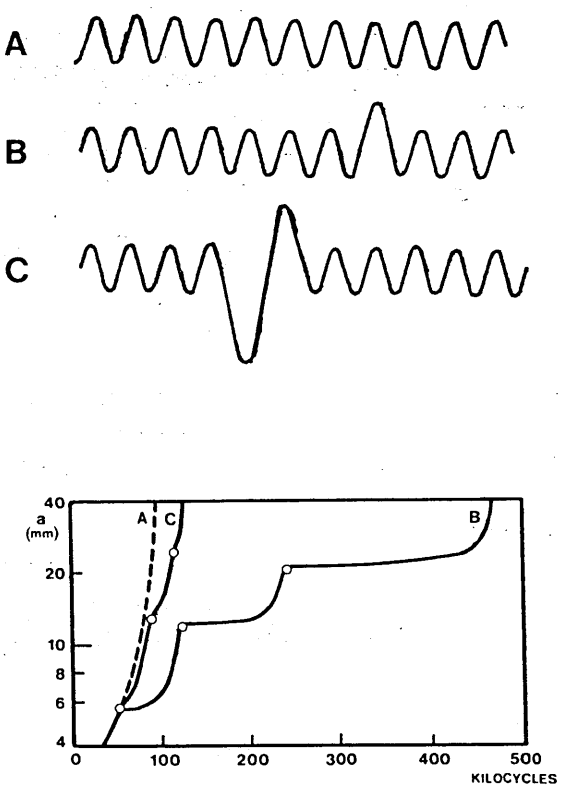

Fig 7.2.1.v Retardation due to overload.

The third problem encountered was a deceleration and sometimes arrest of propagation, during high frequency pre-cracking. This was eventually found to be due to overload. During pre-cracking at 20Hz in laboratory air, the cycling was interrupted for optical measurement of the crack length, usually as a check on the calibration of the crack growth monitor. Upon restarting the test, the fatigue testing machine would overshoot the maximum load for the first 3-4 cycles by up to 50 per cent. This introduced a larger plastic zone at the crack tip and a more extensive residual stress system than that existing before the overload. This acted against the applied stress and caused subsequent growth to be slower fig 7.2.1.v. The problem was easily overcome by reducing the amplitude setting prior to restarting the machine and then slowly bringing it back to the set value.

7.3 Tests results

Crack growth rates during fatigue of 7017-T651 white-zones at various frequencies in 2.5% NaCl + 0.5% Na CrO (pH 3) solution were assessed as a function of the stress intensity range, ΔK, fig 7.3.i From these results the following observations can be made:

i) the crack growth rates are enhanced in the presence of the environment at all frequencies tested.

ii) the crack growth rate enhancement is more marked at low frequencies

iii) the frequency effect on crack growth rates is more pronounced at intermediate ΔK values.

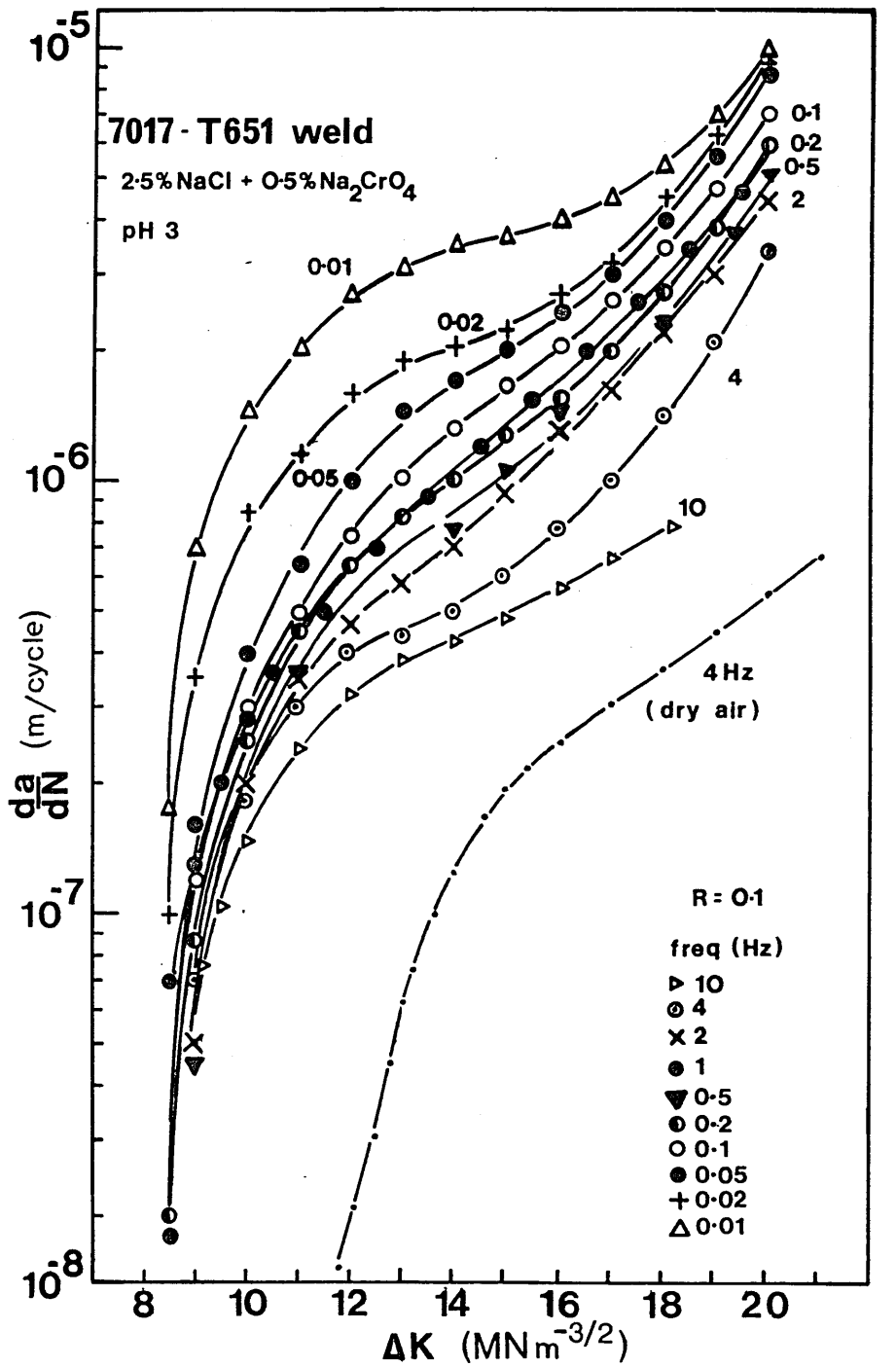

Fig 7.3.i Crack growth rates during fatigue of 7017-T651 white zone in 2.5%NaCl+0.5%Na_2CrO_4, pH3, at frequencies from 0.01Hz to 10Hz and in dry air at 4Hz, as a function of ΔK.

The dependence of crack growth rate upon frequency is not a straight forward one as a plot of crack velocity (m/s) against the stress intensity range, ΔK, shows (fig 7.3.ii).

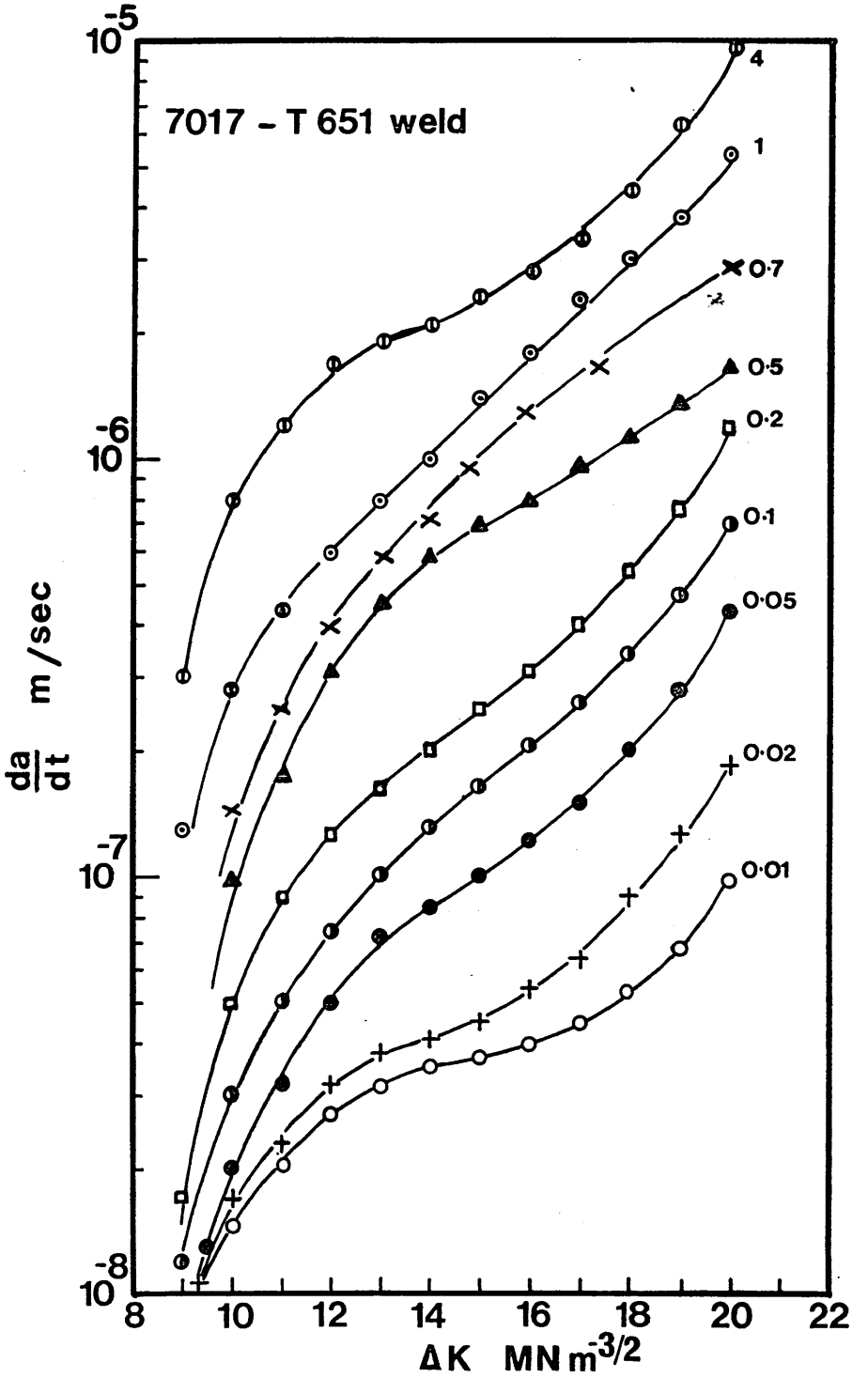

Fig 7.3.ii Crack velocities during fatigue of 7017-T651 white-zones in 2.5%NaCl+0.5%Na_2CrO_4 (pH3) at frequencies from 0.01 to 10Hz as a function of ΔK.

From this plot it can be seen that the crack velocity increases with frequency. The complex dependance of crack growth rate upon frequency can be better understood from a log plot of crack growth rate (m/cycle) against test frequency for specific values of ΔK (fig 7.3.iii).

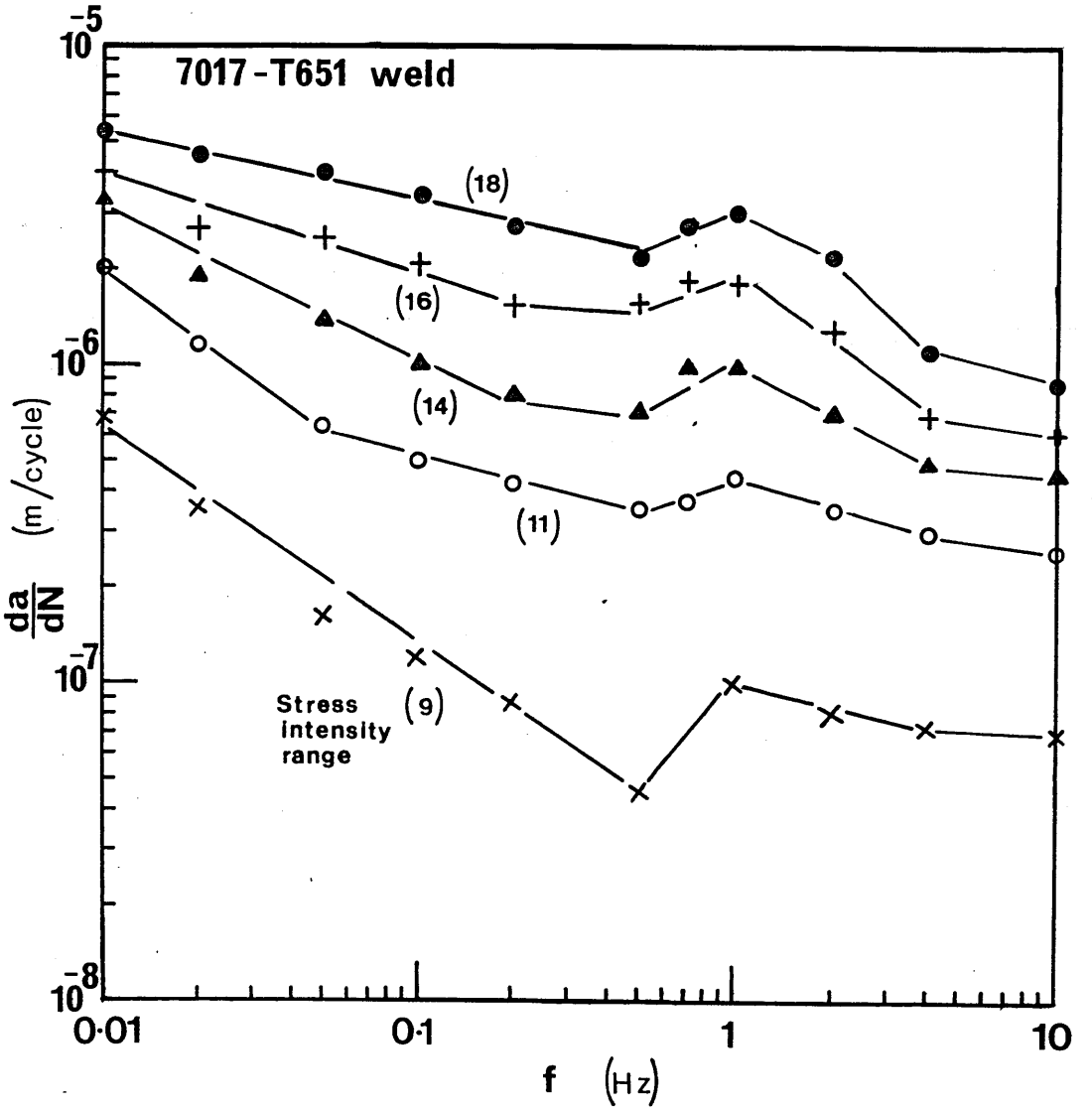

Fig 7.3.iii Variation of crack growth rate with frequency during fatigue of 7017-T651 white-zones in 2.5%NaCl+ 0.5%Na_2CrO_4, at pH3.

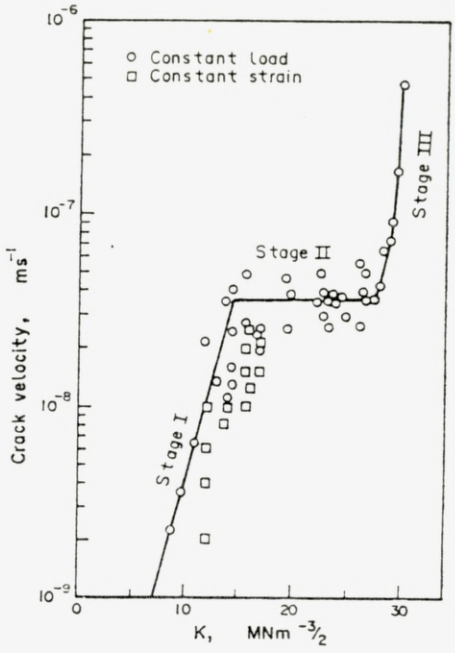

Fig 7.3.iv Relationship between crack velocity and stress intensity factor for stress corrosion of 7017-T651 in seawater at room temperature (85).

At the lower frequencies, that is below 0.1Hz, a plateau appears at the stage II crack growth in fatigue, approaching a value of 3.5×10^{-8} m/s (fig 7.3.ii). This is very close to the reported stage II crack velocity, of 3.4×10^{-8} m/s, during stress corrosion cracking under static loading of 7017-T651 plate tested in the short transverse direction fig (7.3.iv). This result implies that further reducing the cyclic loading frequency should have no significant effect on the crack velocity. Therefore at such low frequencies the cracking mechanism may be similar to stress corrosion cracking under static loading.

At the frequency of 1Hz there is an unexpected increase in the crack growth rates (fig 7.3.iii) for all stress intensity

values. Such a result has been observed by other workers (80, 79) which they have attributed to "true corrosion fatigue"

Results are also represented here of tests during corrosion fatigue of 7017-T651 welds using 3-point bend specimens in 2.5%NaCl + 0.5%Na_2CrO_4 acidified to pH3, fig 7.3.v.
These results are just an indication of the expected values since the 3-point bending method was not pursued further.

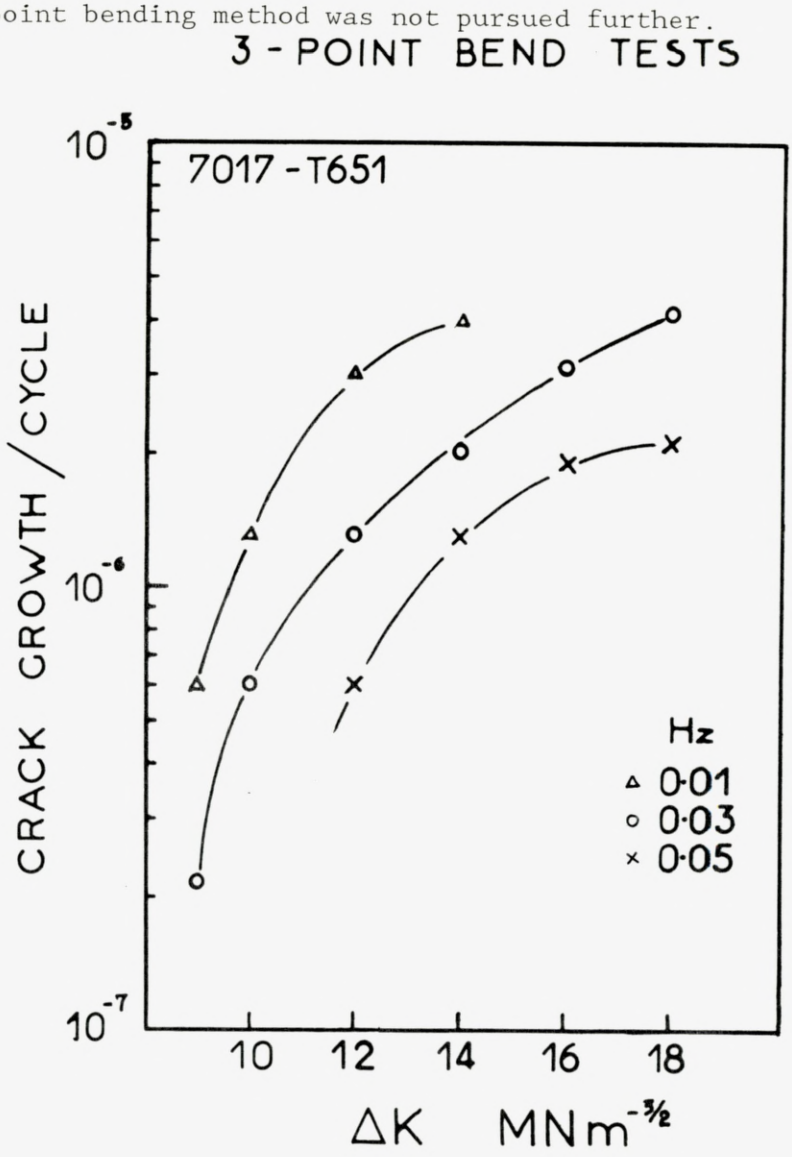

Fig 7.3.v. Crack growth rates during fatigue of 7017-T651 white zone in 2.5%NaCl+0.5%Na_2CrO_4 ,pH3, using 3-point bend specimens.

7.4 Fractography

Fractographic investigation of the failed specimens reveals at least three fracture morphologies:

a) intergranular fracture, which is virtually indistinguishable from stress corrosion intergranular fracture morphology

b) brittle transgranular and

c) ductile transgranular at failure. Fig(7.4.i)

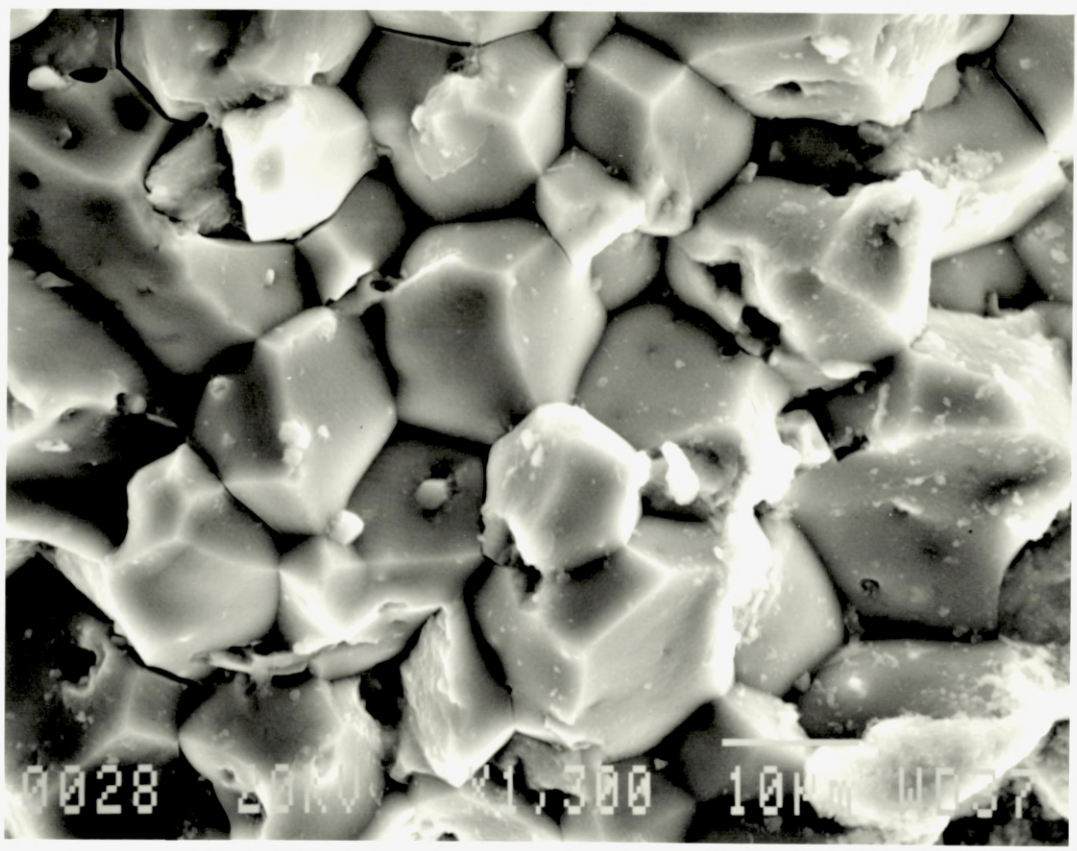

Fig 7.4.i.a Characteristic intergranular fracture mode observed after corrosion fatigue of 7017-T651 white-zone.

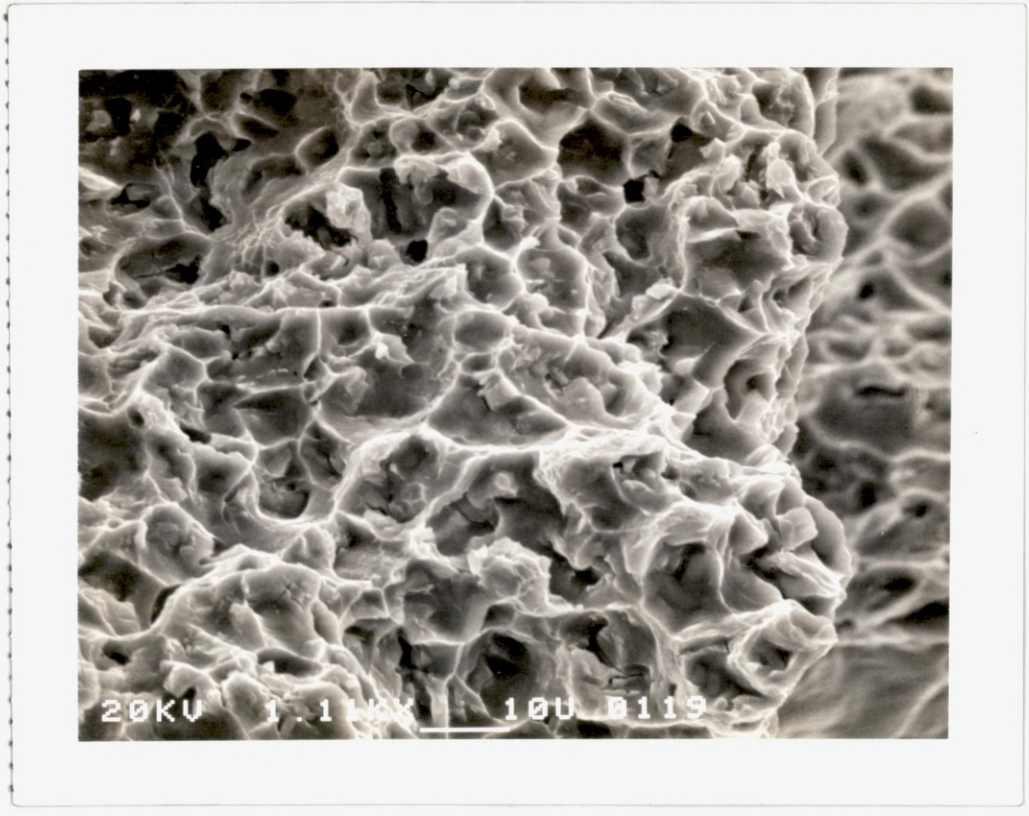

Fig 7.4.i Characteristic fracture modes observed during corrosion fatigue of 7017-T651 white zones b)brittle transgranular c) ductile transgranular.

At frequencies below 0.1Hz SEM work at low kV has revealed the presence of striations similar to those observed by Scamans (105) in a 7018 alloy during stress corrosion cracking under static loading (fig 7.4.ii). The striations are continuous from one grain to the next on the fracture surface and are strong evidence of a discontinuous mode of crack propagation. The presence of striations also suggests a hydrogen embrittlement mechanism of cracking under conditions of total immersion at the free corrosion potential.

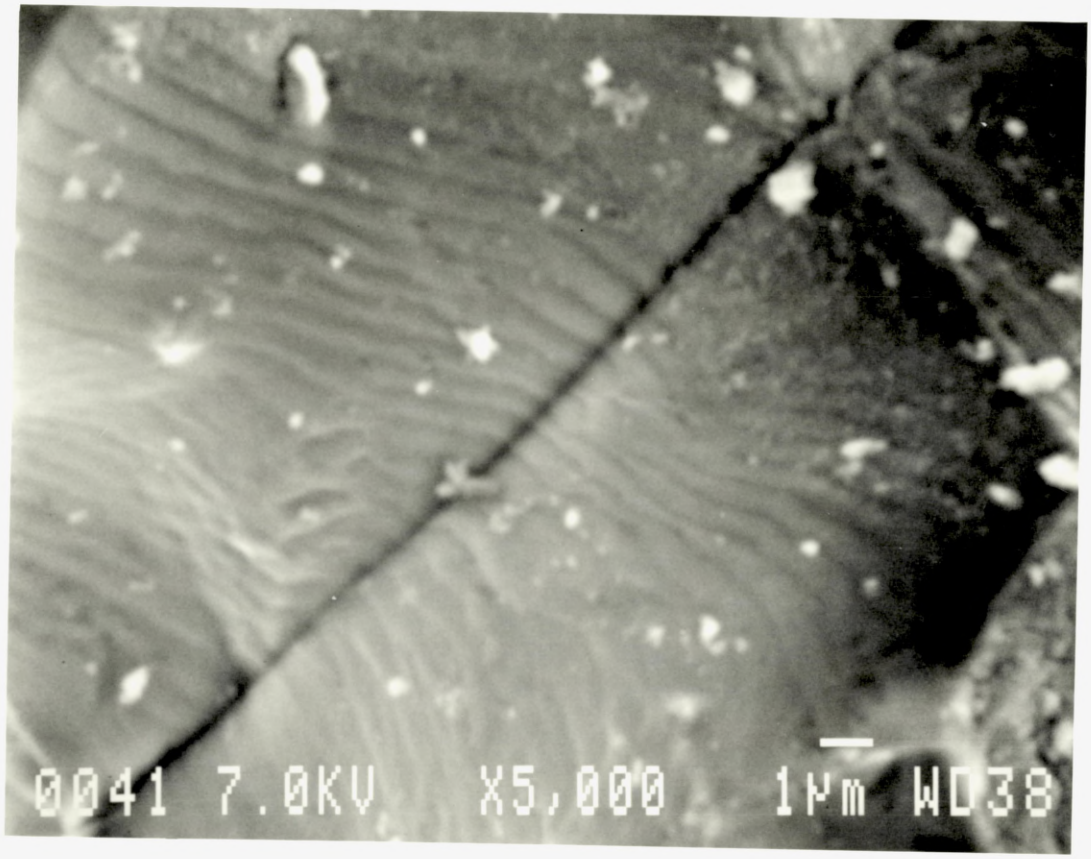

Fig 7.4.ii Striations observed on fatigue fracture surface of 7017-T651 white-zones at cyclic frequencies below 0.1Hz. (Photo is for 0.02Hz at ΔK=12)

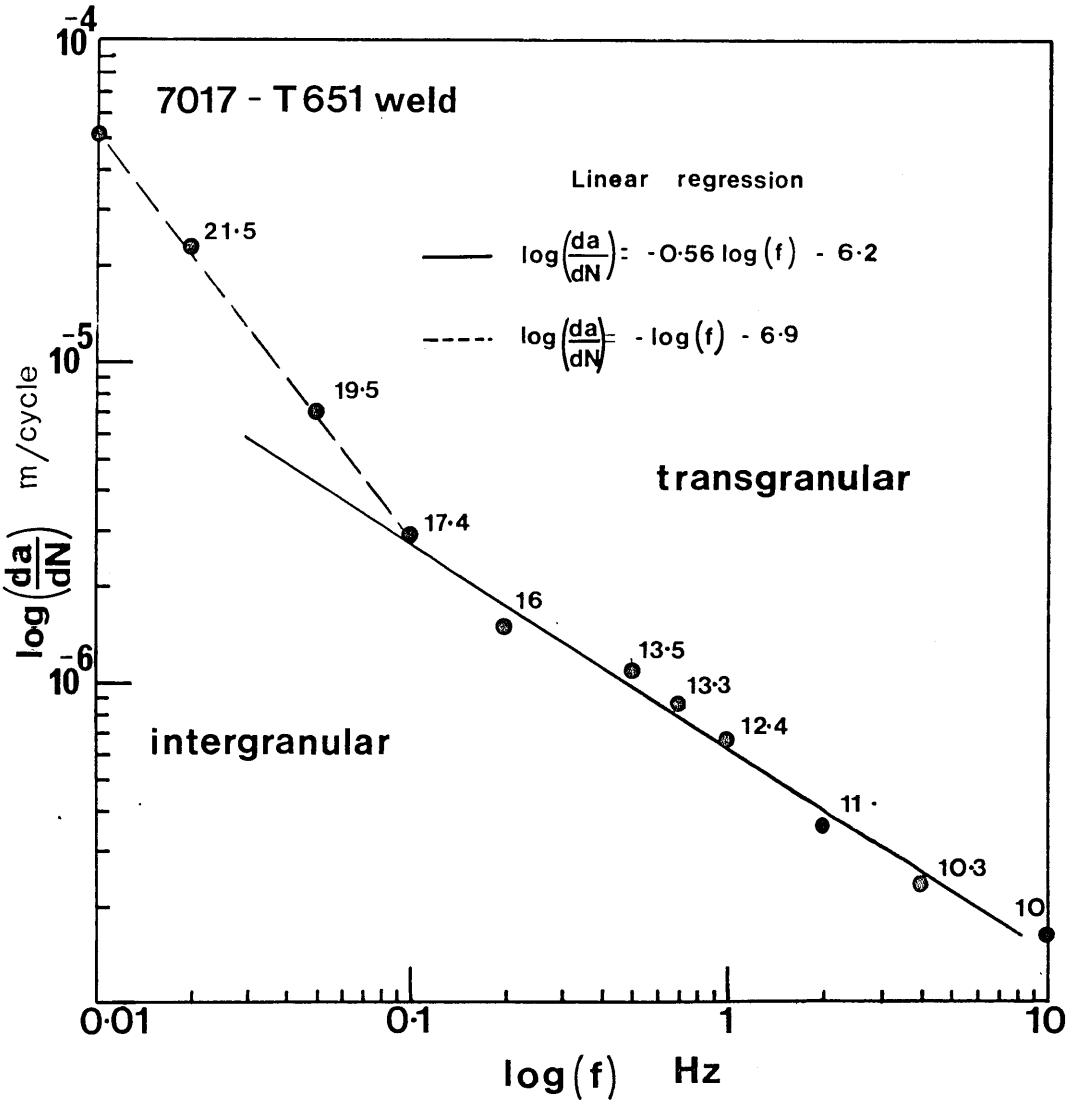

Fig 7.4.iii Dependence of the critical crack growth rate for fracture mode transition (IG/TG) upon loading frequency.

For frequencies between 0.1 to 10Hz, the crack growth rates at which transition from intergranular to transgranular cracking takes place depend upon the loading frequency and there is a linear dependence between log values of crack growth rate and frequency for the transition with a slope of approximately -0.5, fig(7.4.iii). This behaviour is indicative of environment enhanced

corrosion fatigue having a crack growth rate dependent upon the square root of the time available during each cycle, $(t)^{1/2}$, or upon $(1/f)^{1/2}$. This suggests that anodic dissolution is unlikely to be the dominant fracture mechanism as it has been reported that, for dissolution controlled fracture mechanisms, the transition from intergranular to transgranular fracture is associated with the attainment of a critical crack growth rate (107). For frequencies below 0.1Hz the slope is approximately -1. This implies that corrosion fatigue crack growth for those frequencies is a time dependent rather than a cycle dependent phenomenon, which means that crack growth at low frequencies is actually a kind of stress corrosion under cyclic loads. Fractographic investigation supports the above statement since fracture surfaces at very low frequencies are almost entirely intergranular.

7.5 Pre-exposure tests

As there is increasing evidence of hydrogen involvement in the environment sensitive cracking process of 7xxx series alloys, pre-exposure embrittlement tests were carried out to determine a diffusion coefficient for hydrogen. Specimens were fatigue precracked in air at 20Hz frequency and then immersed in 20ml of test solution. The sides of the specimens were masked off with Turco lacquer so that the environment would enter the crack through the notch. The crack plane was in a vertical direction to facilitate entrance of the solution. Specimens were then taken out of the solution after 5, 15 and 30 days and were tested in fatigue at 1Hz frequency, in immersed condition, with a

starting ΔK value of 12 $MNm^{3/2}$ (R=0.1) which is the value for the transition from intergranular to transgranular fracture mode for the particular frequency (fig 7.4.iii).

Fractographic examination revealed that the intergranular fracture mode extended for ΔK values higher than 12 and the results are given in table 7.5.a below. The diffusion coefficient D was determined from $x=4\sqrt{Dt}$ where t is the time in the environment and x is the distance hydrogen has diffused ahead of the crack tip.

Pre-exposure (days)	IG crack length (mm)	ΔK tranition ($MNm^{3/2}$)	D (m^2/s)
5	1.45	16.5	3.04×10^{-13}
15	2.5	21.4	3.03×10^{-13}
30	3.4	24	2.8×10^{-13}

Table 7.5.a. Transition from intergranular to transgranular fracture mode of the white-zone of a 7017-T651 aluminium alloy weld after various pre-exposure times in acidified 2.5%NaCl+0.5%Na_2CrO_4 solution.

The results give an average value for the diffusion coefficient D of 3×10^{-13} m^2/s which is in close ag reement with the reported value of 2×10^{-13} m^2/s from pre-exposure studies on 7075-T6 alloy (45) and 10^{-13} m^2/s for 7049-T651 (48). Also the result agrees well with Holroyd and Hardie's estimated value of 3.2×10^{-13} m^2/s for 7017-T651 plate (85).

7.6 Crack tip strain rate tests

The effect of crack tip strain rate has also been investigated since it has been suggested that crack tip strain rates could have an effect on the stageII crack propagation rate in fatigue which is envisaged to increase as the strain rate is increased whereas the intergranular to transgranular cracking transition would decrease (85). The effect of waveform on crack tip strain rate has been investigated by Scott and Truswell (106) (fig 7.6.i) and there is a significant difference between crack tip strain rates for sinusoidal and triangular waves. To investigate this fatigue tests were carried out at frequencies of 0.1, 0.5 and 1Hz using a triangular waveform. (All other testing in this work was done by using a sinusoidal waveform). The results are shown in figures 7.6.ii,a,b,c). For all frequencies tested there is an increase in stage II crack growth rates for the triangular waveform although the increase is not substantial and one could suggest that it falls within the experimental scatter. The fact though that the result is consistent for all frequencies tested suggests that this is a real effect.

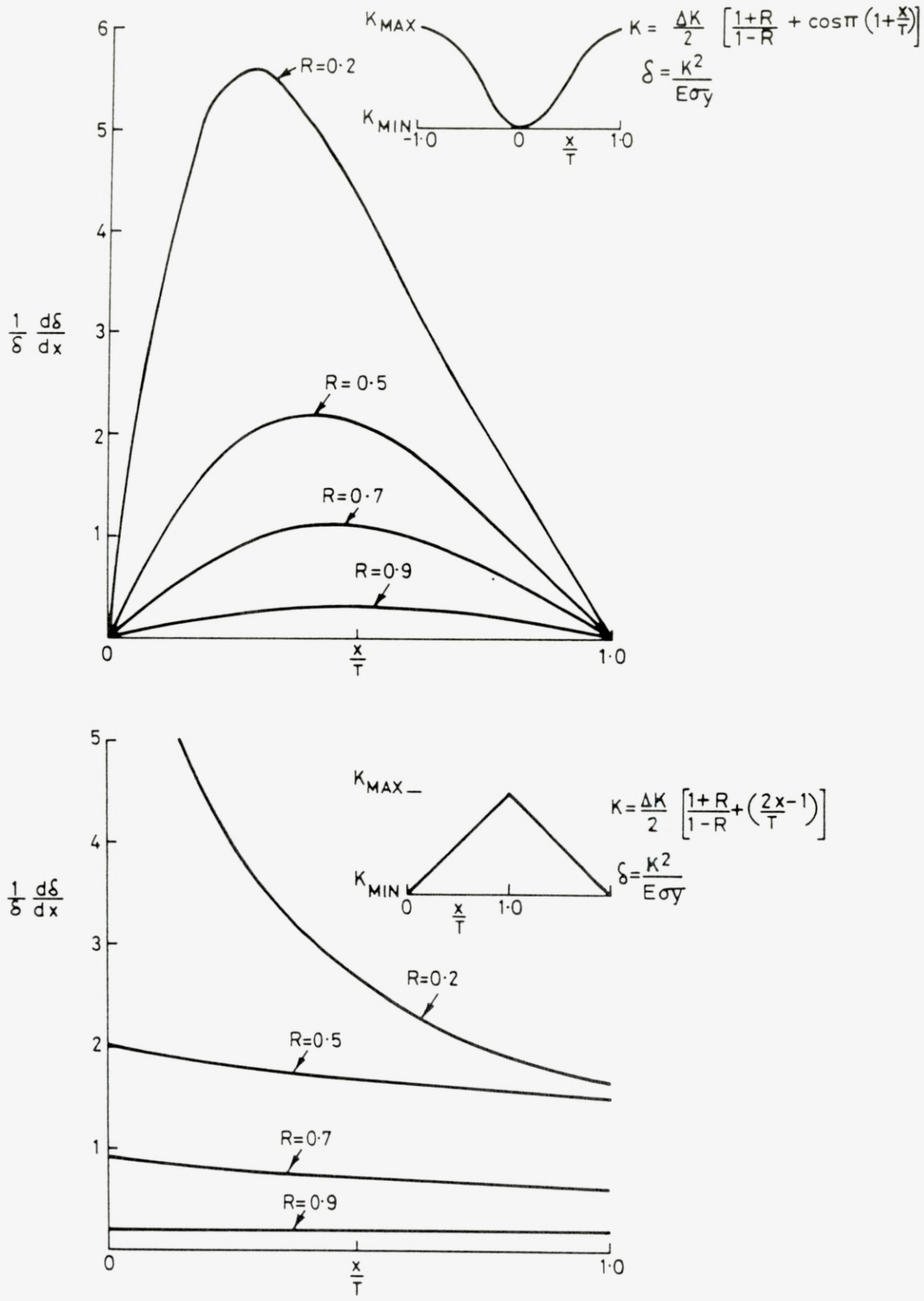

Fig 7.6.i Crack tip strain rates during sine and triangle fatigue cycles as given by Scott and Truswell (106).

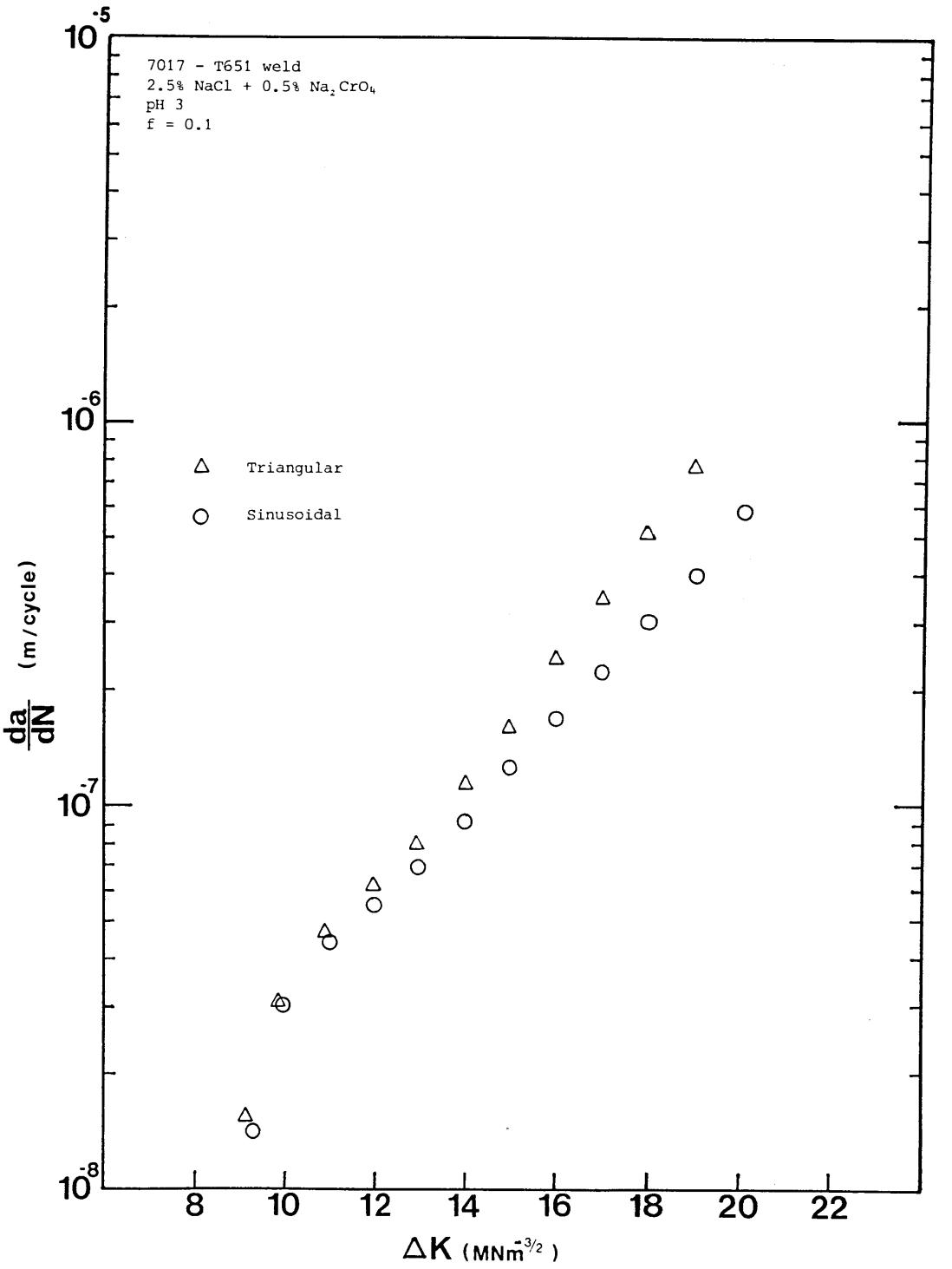

Fig 7.6.ii,a Comparison between fatigue crack growth rates obtained using triangular and sinusoidal waveforms at 0.1Hz frequency.

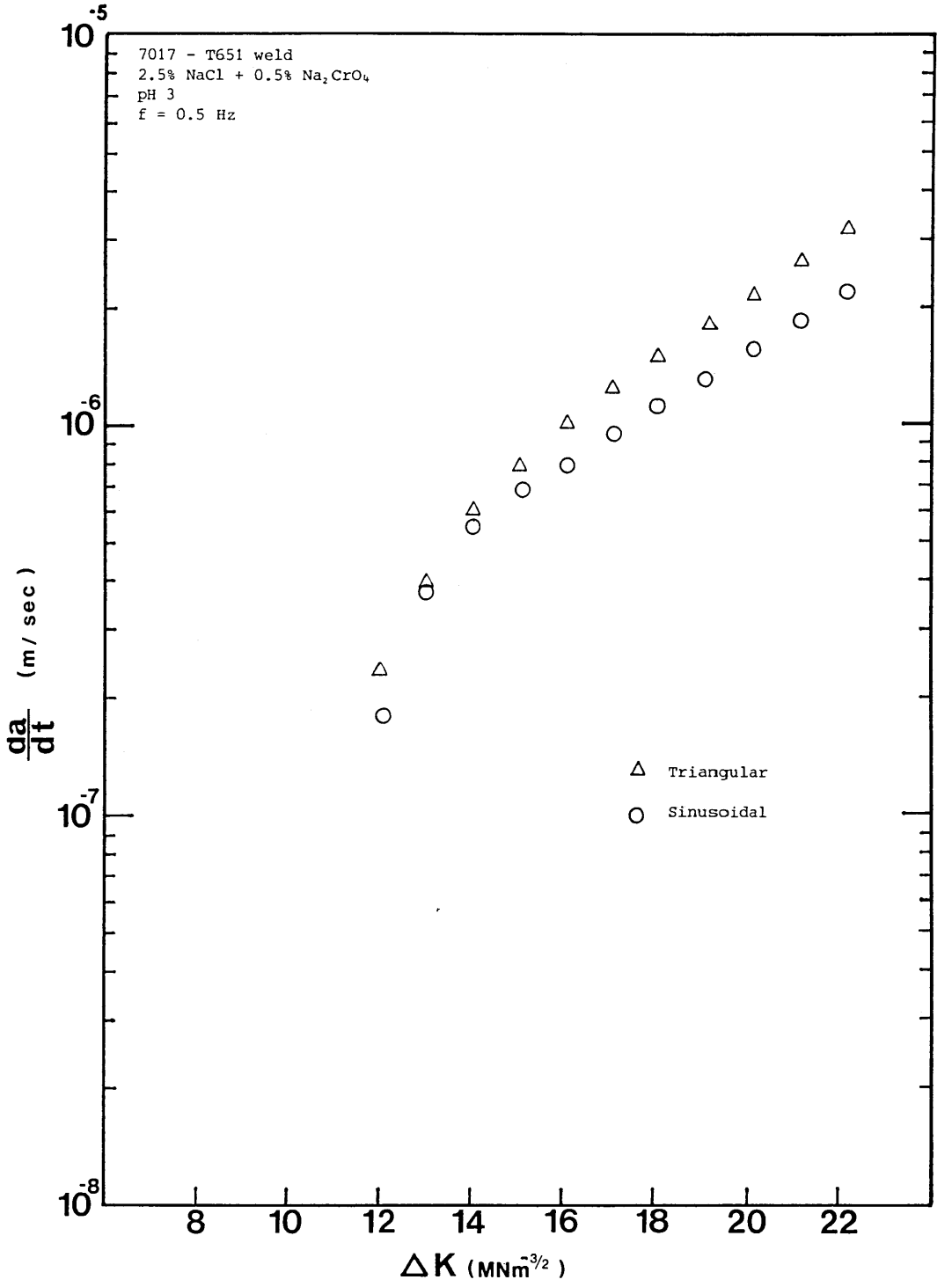

Fig 7.6.ii.b Comparison between fatigue crack growth rates obtained using triangular and sinusoidal waveforms at 0.5Hz frequency

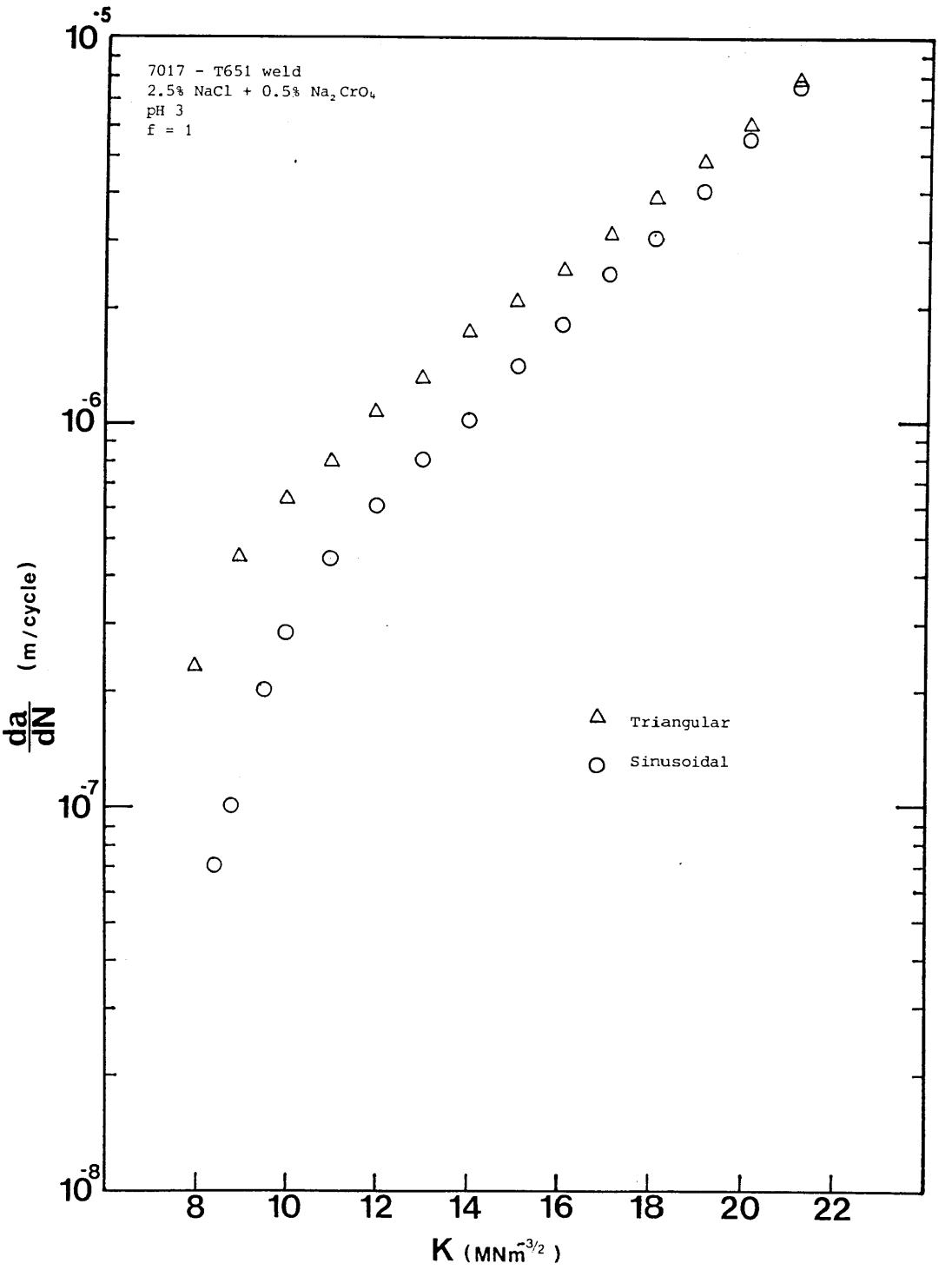

Fig 7.6.ii.c Comparison between fatigue crack growth rates obtained using triangular and sinusoidal waveforms at 1Hz frequency.

7.7 Effect of solution pH

The effect of the solution pH on the corrosion fatigue crack growth rates of the white-zone was investigated by performing tests at 0.5, 1 and 2 Hz using as prepared 2.5% NaCl + 0.5% Na_2CrO_4 solution, pH 7.8 . The results are shown in fig 7.7.i. Also a plot is given of the variation of crack growth rate with frequency at various ΔK levels, fig 7.7.ii.

7.8 High frequency tests

Tests were performed at loading frequencies up to 40 Hz but no results were obtained as fatigue cracks did not follow the white-zone but turned into the heat affected zone and propagated there to failure (crack growth direction almost parallel to the direction of action of load). Although precracking took place in the white-zone, as soon as the environment was introduced severe crack branching took place and a change in the direction of crack growth. One example is shown in fig 7.8.i.

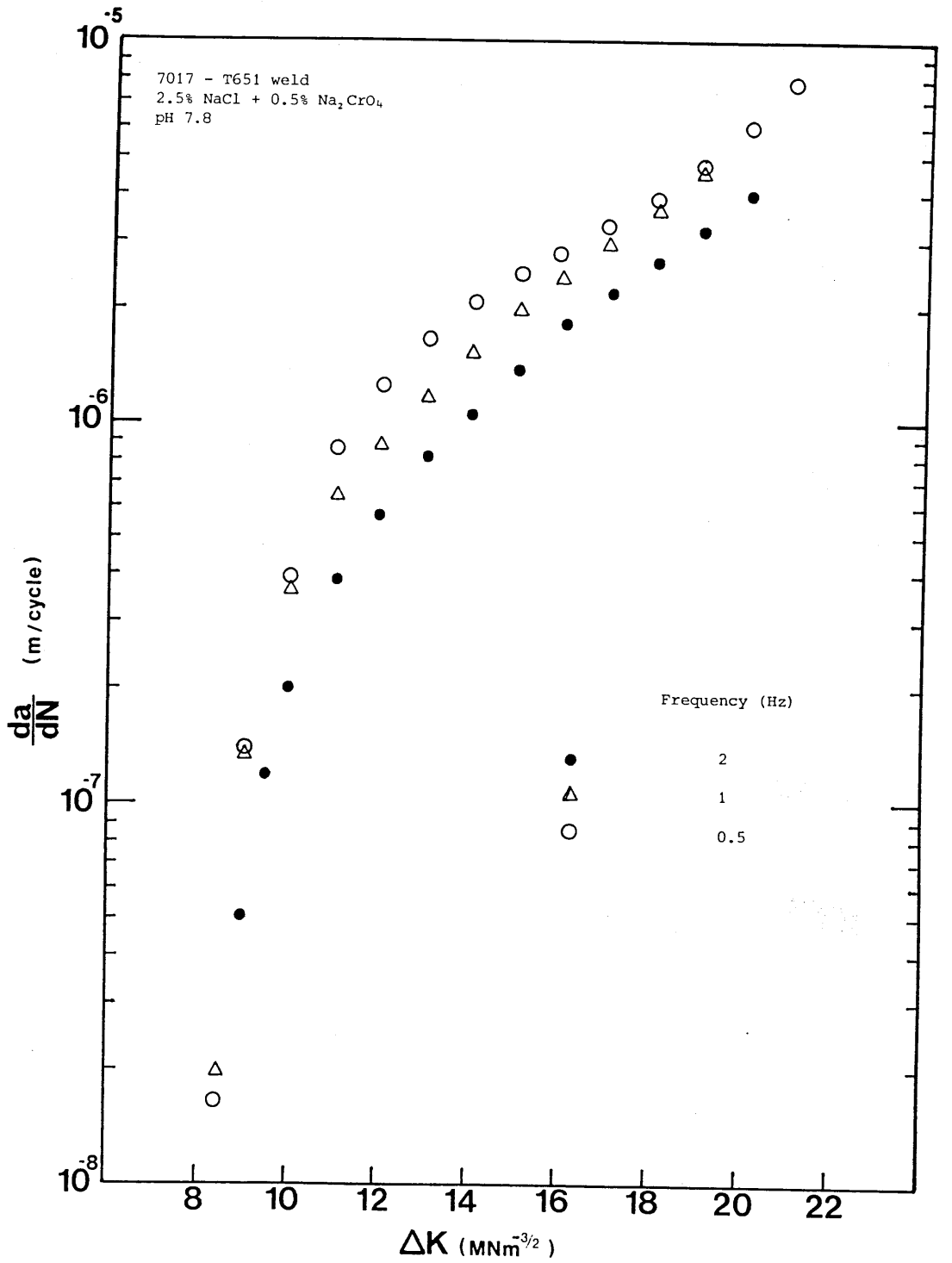

Fig 7.7.i Crack growth rates during fatigue of 7017-T651 white zone in 2.5%NaCl+0.5%Na_2CrO_4 , pH7.8 .

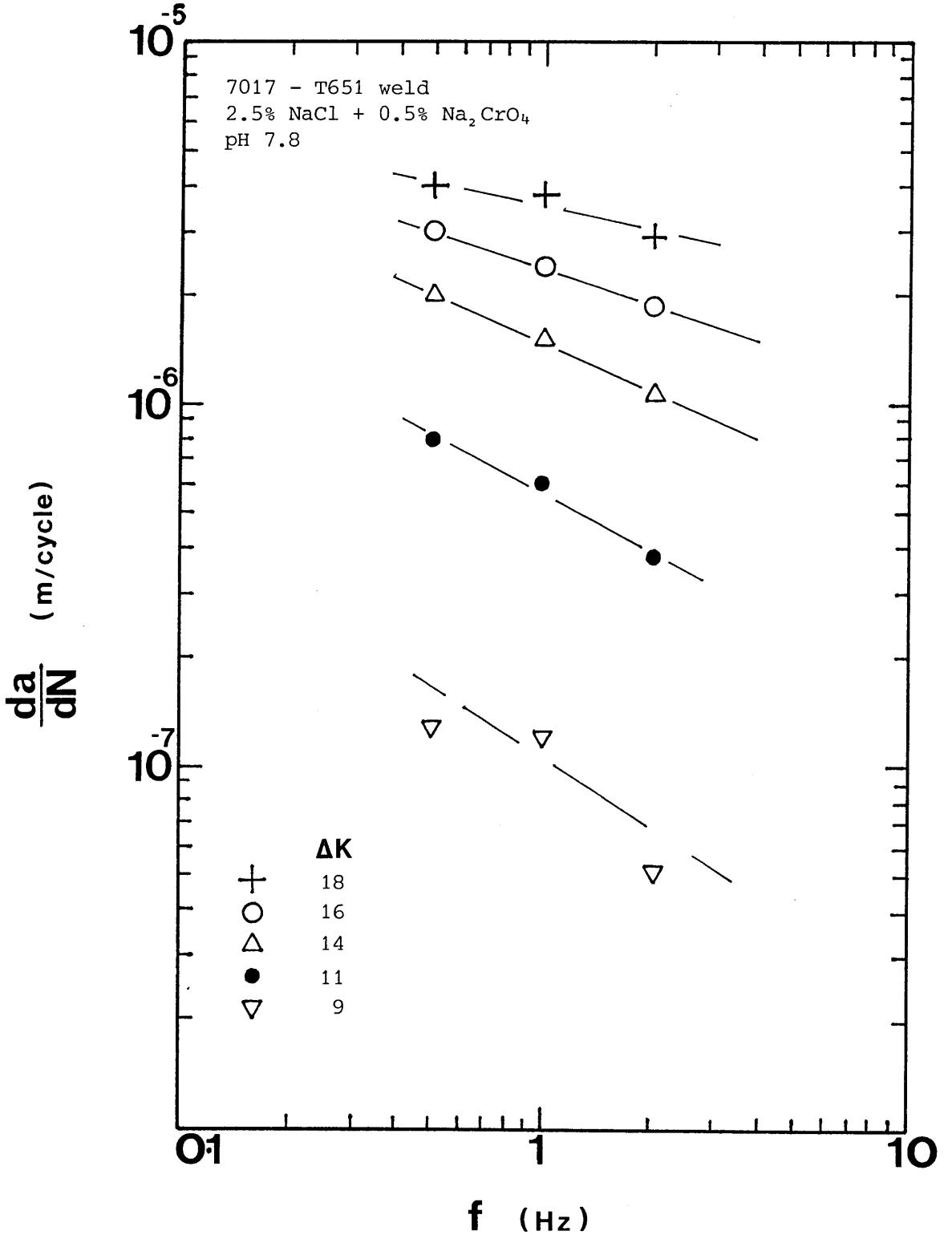

Fig 7.7.ii Variation of crack growth rate with frequency during fatigue of 7017-T651 white-zones in 2.5% NaCl + 0.5% Na_2CrO_4, pH7.8 .

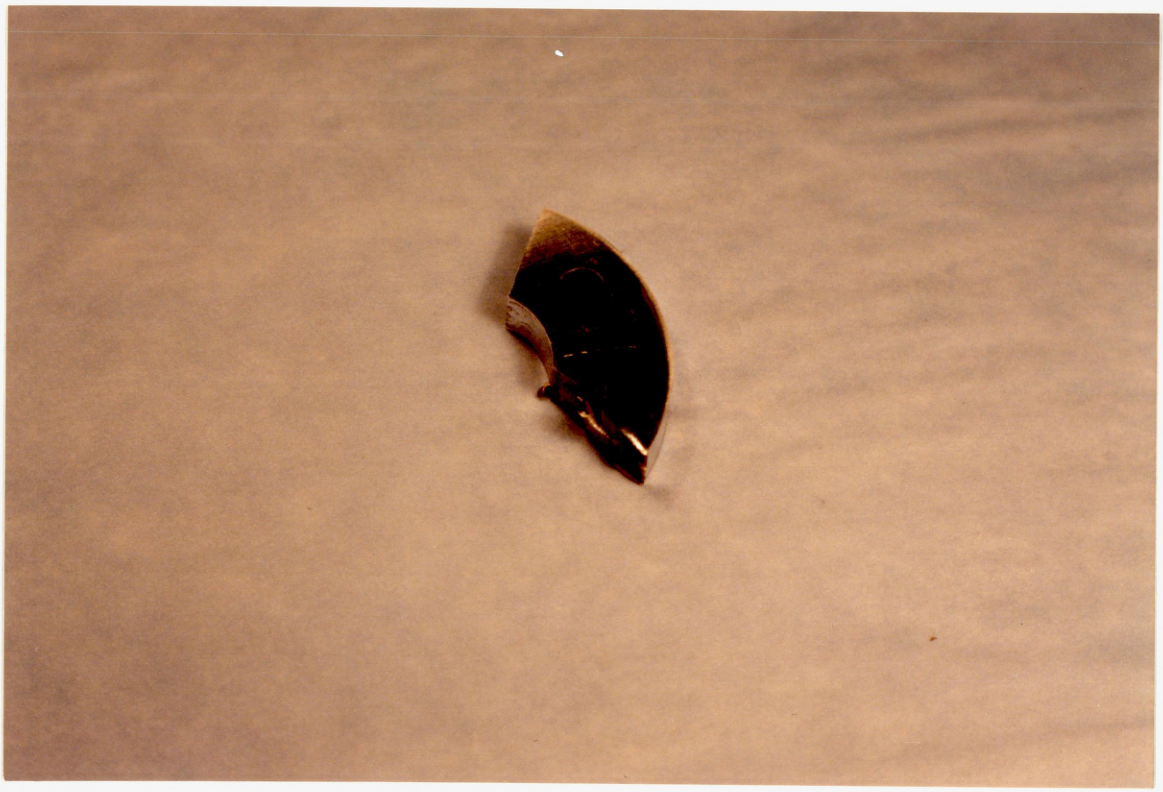

Fig 7.8.i. Typical failure of arc specimen when tested at frequencies above 10 Hz.(Specimen shown tested at 30 Hz.)

CHAPTER 8

8. DISCUSSION.

The interaction between stress corrosion cracking and corrosion fatigue has received extensive investigation over the past few years. Wei and Landes (78) have proposed that the corrosion fatigue crack growth rate in a corrosive environment can be considered as the sum of two components, one representing crack extension under cyclic loading in the abs ence of an aggressive environment and the second representing crack extension due to stress corrosion cracking. This is expressed by the equation

$$(da/dN)c = (da/dN)in + \int (da/dt)\ K(t)\ dt\ ,$$

where (da/dN)c and (da/dN)in represent the crack extension per cycle due to cyclic loading in a corrosive and in an inert environment respectively, and the integral represents the sustained load crack extension during the time for a single fatigue loading cycle. This integral is used to account for the effects of frequency, mean load, range of cyclic loads and the load-time waveform on the sustained load growth component, assuming da/dt is related to the instantaneous value of the stress intensity factor during cyclic loading, K(t).

The model has been applied successfully to materials that exhibit a high stress corrosion component, such as the 7079 aluminium alloy in the T651 condition, which exhibits a stress corrosion component 2 to 3 orders of magnitude higher than other 7xxx alloys. (80).

Holroyd and Hardie, fatigue testing 7017-T651 aluminium alloy plate in the short tranverse direction in seawater over a range of frequencies from 0.1 to 70 Hz (85), have established the weakness of the above model. They suggested that, since a superposition model cannot account for the observed crack growth rates in corrosion fatigue, then either

i) the stress corrosion and fatigue processes are synergistically additive, or

ii) as suggested by Austin & Walker (79), that stress corrosion cracking under cyclic loading conditions and fatigue are independent of one another and the cracking process is the one that produces the faster crack growth rate under the particular conditions,

are possible alternatives.

Wei and Simmons (132) have recently improved the summation model by including a component (da/dN)cf, which is a cyclic dependent contribution requiring synergistic interaction of fatigue and environment attack (108):

$$(da/dN)CF = (da/dN)f + (da/dN)cf + \int (da/dt)scc\ K(t)\ dt$$

The mathematical modelling of (da/dN)cf has been restricted to gaseous environments and has been developed for the limiting cases of transport-controlled and surface-reaction controlled embrittlement without detailed investigation of any frequency effects.

If the Wei and Landes model is applied to the results of this work for the white-zone it can be seen that the summation model is not applicable.

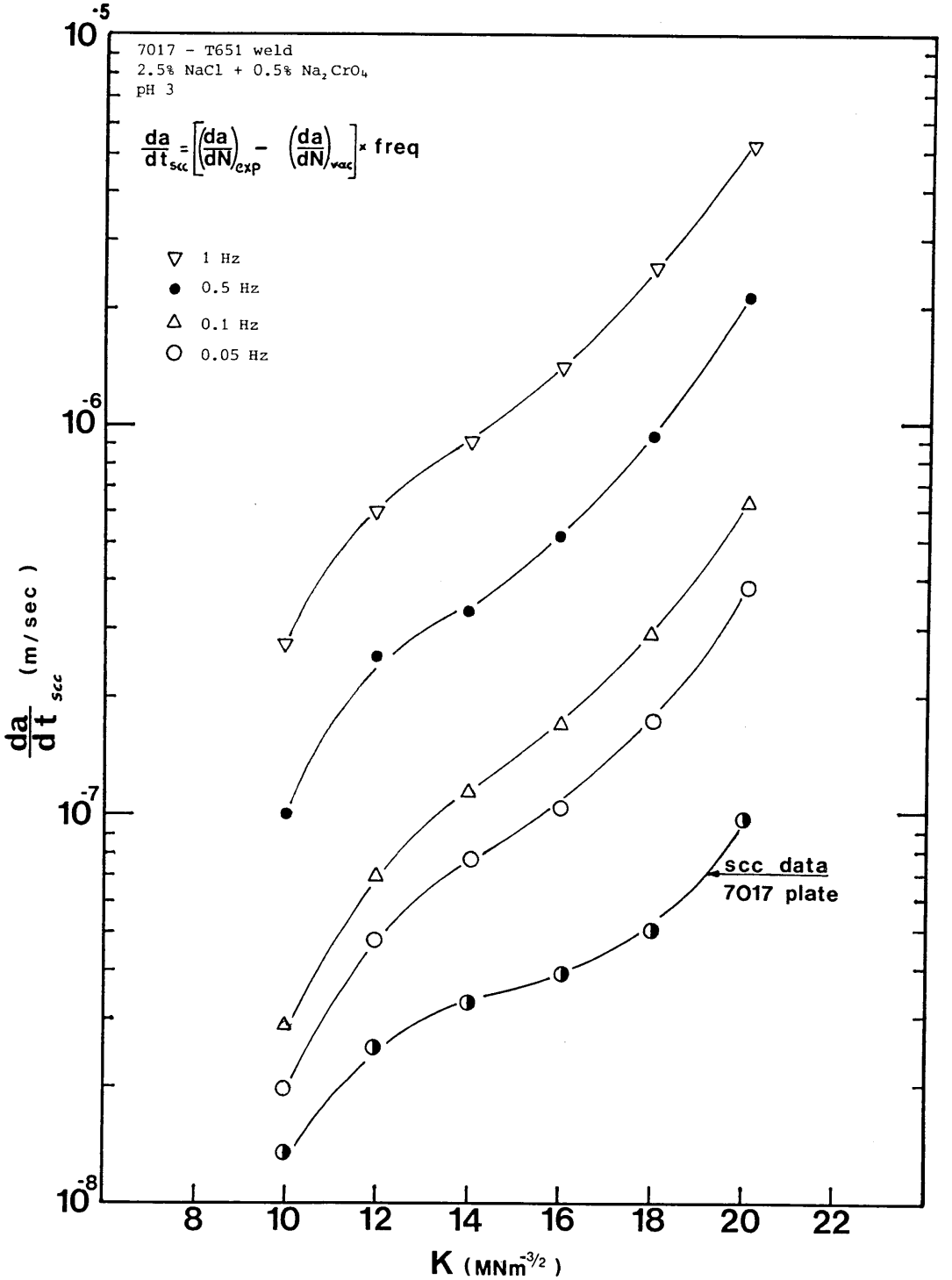

Fig 8.i SCC growth rates for 7017-T651 weld as determined by adopting the Wei & Landes (78) summation model.

For the white-zone tests there was also observed an unexpected increase in the crack growth rates at 1Hz frequency over the whole ΔK range. The result is better demonstrated in fig 7.3.iii. Such a behaviour has not been observed for 7017 parent plate but it has been observed by Speidel (14) and Austin & Walker (79) for other 7xxx series alloys.

Speidel has termed this enhancement in crack growth rates "true corrosion fatigue". In the author's opinion this term cannot explain the phenomenon for the following reasons.

i) The term "true corrosion fatigue" applies to systems that do not exhibit stress corrosion susceptibility but show enhancement of crack growth rates in an aggressive environment over those observed in vacuum. The fracture morphology in such systems is always transgranular. The white zone is known to suffer stress corrosion cracking and the fracture morphology can be either intergranular or transgranular depending on frequency or ΔK value.

ii) Speidel attributes the crack growth enhancement to a mechanical effect. He tested rolled plate in the long transverse direction, where the elongated grains facilitated growth due to a mechanically preferential path. In the white zone, however, there is a recrystallised equiaxed grain structure, so the above argument cannot hold.

iii) Austin & Walker attribute that,to an effect of frequency over the inert fatigue component, fig 8.ii (79). If that were true then the enhancement would occur at all frequencies above 1Hz. The tests for the white zone clearly indicate that crack growth rates fall back to expected values beyond 1Hz frequency (fig 7.3.iii). Speidel also claims that this enhancement takes place at 1Hz frequency and above but no data above 1Hz have been provided in his published work.

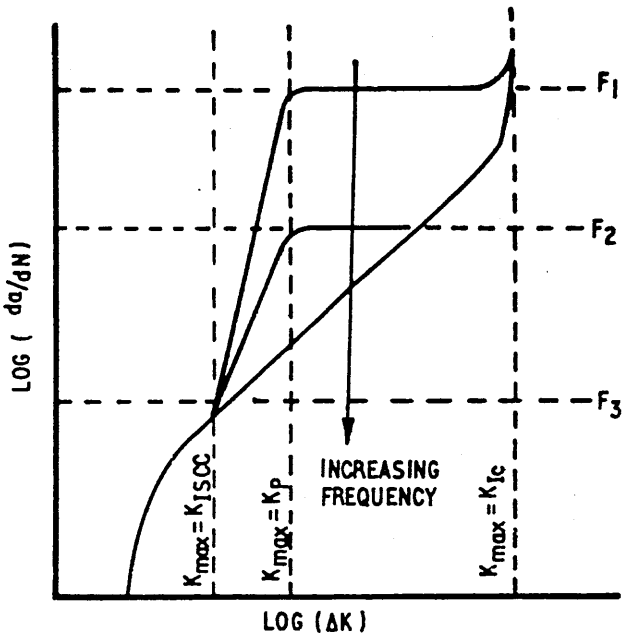

Fig 8.ii Effect of cyclic loading frequency on corrosion fatigue crack growth rates (79).

It was thought that, since there was no frequency effect observed for the 7017 parent plate, (85) at 1Hz frequency, this could have been produced in the present work by an external factor such as an idiomorphy of the fatigue testing rig at the particular frequency. This was tested by isolating the inbuilt oscillator of the Dartec fatigue testing rig and connecting an external function

generator to produce the cyclic loading waveform. Also a dial gauge was used to measure the displacement of the oscillating ram to detect any overshoot during testing. The crack growth rates produced with the use of the external function generator, were within the scatter band of the previous 1Hz tests and the dial gauge did not show any overshoot of displacement from the set values. This result suggests that the 1Hz effect is real and eliminates an apparatus involvement.

Another possible explanation could be a change in the rate of transport of the environment at the crack tip due to the opening and closing of the crack faces. It is envisaged that as the frequency increases fluid is "pumped" in and out of the crack enclave at increasing rates altering the environmental conditions at the crack tip. A maximum effect is reached at 1Hz favouring accelerated crack growth, while at higher frequencies mixing of the crack electrolyte and bulk solution is not so effective. Work done in this area by Hartt et al (109) demonstrates that, at least theoretically, mixing of crack electrolyte and bulk solution is to be expected to take place during fatigue. Their observations are summarised in table 8.a.

Fatigue variable	Influence upon electrolyte mixing
Crack angle opening range β	mixing is predicted to increase with increasing β
Mean stress	mixing is predicted to increase with decreasing mean stress
Frequency	mixing is predicted to increase linearly with increasing frequency
Crack length	mixing is predicted to increase with the cube of crack length
Temperature	mixing is predicted to increase with increasing temperature
Specimen geometry and test method	fatigue test procedures which enhance relative motion between the crack and bulk electrolyte are predicted to enhance mixing

Table 8.a. Fatigue variables and the projected influence of each upon crack electrolyte modification or mixing with the bulk solution.

It is important to note from Hartt's results that crack solution momentum becomes sensitive to mean stress when the value for α/β (the ratio of mean crack-opening angle to half angular range of crack opening, which also denotes mean stress) is approximately 1.2

which corresponds to an R ratio of 0.1, fig 8.iii.

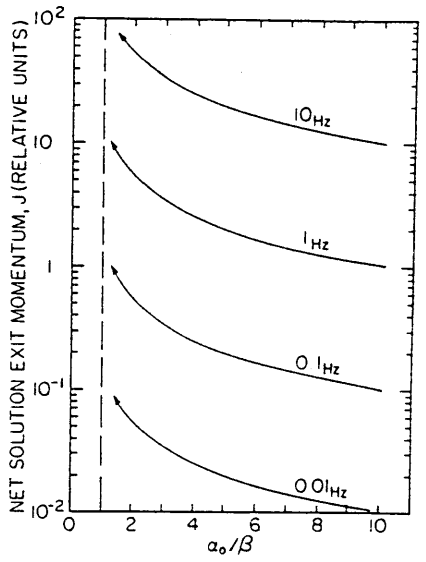

Fig 8.iii Net solution exit momentum as a function of mean stress α/β, and for a range of frequencies

Turnbull & Ferris (110) have also investigated the solution modification during corrosion fatigue of structural steels, resulting from the movement of crack walls. They suggest that mass transport of a dissolved species in a corrosion fatigue crack can occur due to advection, arising from fluid motion induced by the cyclic displacement of the crack walls, and diffusion and ion migration which are consequences of electrode reactions on the walls and tip of the crack. This has been expressed by a mass transport equation:

$$J = Cv - D_o \frac{\partial C}{\partial x} - \frac{DF}{RT} C \frac{\partial \phi}{\partial x}$$

where C = concentration of ionic species
v = fluid velocity
D_o = diffusion coeficient of ionic species
F = Faraday constant
R' = gas constant
T = temperature
ϕ = potential drop (pot at crack mouth - electrode pot)

They have found that the extent of ingress of fresh electrolyte into a crack by advection is not affected by frequency provided that the frequency is less than or equal to 1Hz. Also they observed a decrease in pH with an accompanying increase in potential drop in the crack as the frequency increased from 0.1 to 1Hz.

It can therefore be suggested that the unexpected enhancement of crack growth rates observed around 1Hz for the white zone is a result of solution modification within the crack enclave. A similar effect has not been observed for 7017-T651 (85), but this could be due to the different solution used there (natural sea-water, as opposed to salt-chromate solution acidified to pH3 in the present work). To investigate whether acidification of the electrolyte has an effect tests were carried out at 0.5, 1 and 2Hz with as-prepared, non acidified, salt-chromate solution, (pH 7.8). The results are shown in fig 7.7.i. and fig 7.7.ii.

It can be seen from these results that no enhancement of crack growth rates is exhibited at 1Hz for the the non-acidified salt chromate solution. Studies of crack tip solution chemistries have established that the pH of the electrolyte near the crack tip of a propagating crack quickly attains a value of about 3, irrespective of the bulk solution pH (29). This means that ingress

of fresh solution into the crack-enclave should not significantly affect the solution pH at the crack tip, but solution chemistry composition in the crack enclave would change. Therefore electrolyte mixing seems to be the most probable explanation for the enhancement of crack growth rates at 1Hz for the acidified solution, pH3.

Furthermore, a comparative plot of the corrosion fatigue crack growth rates as a function of ΔK for pH3 and pH7.8 (fig 8.iii) shows that the crack growth rates for the alkaline solution are higher.

The above results could be attributed to the following.

1) The solubility of the oxide at various pH values. It is known that the oxide is stable between pH4 and pH8.5 so that general dissolution is unlikely to occur. At low pH values (pH3 in the present work) oxide dissolution may lead to general corrosion resulting in blunting of the tip of the crack leading to lower crack growth rates. De Jong (27) has observed that stress corrosion crack growth rates increase logarithmically either side of pH7 for a 7075-T651 alloy in NaCl solution (fig 2.5.3.iii) associating this to solubility of corrosion products.

2) The effect that the pH of the solution has on the free corrosion potential. Measurements of the fcp during tests in the ph3 solution have established a value of -900 mV while for the pH7.8 the measured value was -850 mV.

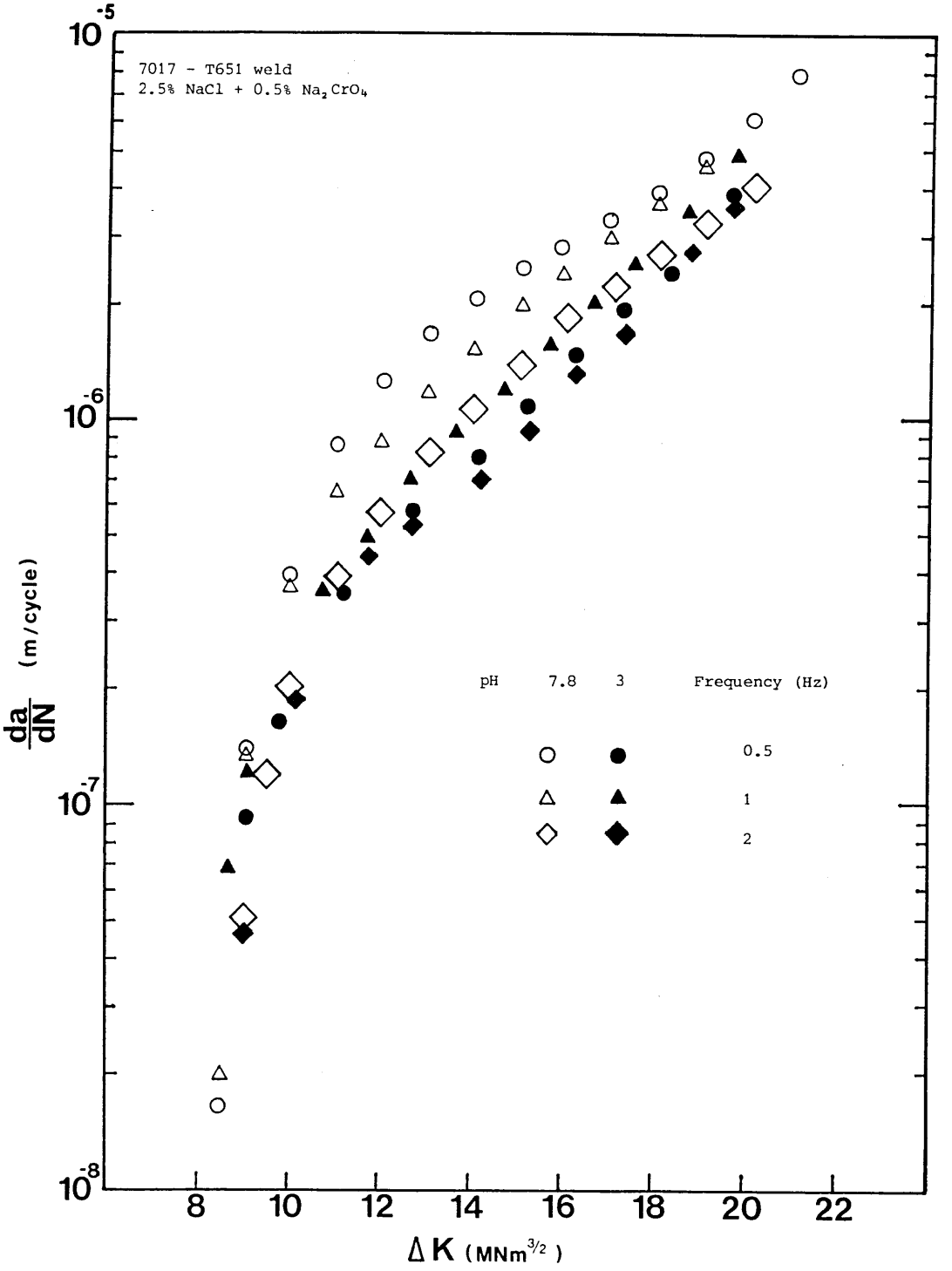

Fig 8.iii Crack growth rate against stress intensity range for 7017-T651 weld in 2.5% NaCl + 0.5% Na_2CrO_4 for frequencies of 0.5, 1, 2 Hz at pH3 (closed symbols) and pH7.8 (open symbols).

Data published by Speidel (21) and Edwards (38) have shown for a 7017-T651 alloy in a 5M KI solution that the stress corrosion stage II crack growth rate increases as the crack tip potential moves to more anodic values.

It is important to note that for the pH3 solution the free corrosion potential reached its stable value within minutes of the introduction of the solution while for the pH7.8 solution stability was established about two hours from the introduction of the solution implying oxide dissolution effects at the low pH value.

3) Any effect that the presence of chromate ions may have on the stability of the oxide (Hydrated chromium oxide, CrOOH, may form which is more stable in acidified environments (122)), or hydrogen consumption by chromate (CrO_4^{--}) which otherwise would be free to enter the material.

8.1. Role of Hydrogen

The presence of striations on the fracture surface of the white zone, together with increasing evidence in the literature that cracking in 7xxx series aluminium alloys is hydrogen controlled, led to a close examination for such a process in the white-zone. Results of pre-exposure tests performed in this work are consistent with hydrogen diffusing through the white-zone boundaries and an implied diffusion coefficient of 3×10^{-13} $m^2 s^{-1}$.

If it is assumed that the controlling process for crack propagation is hydrogen diffusion then during the cycle hydrogen will diffuse ahead of the crack tip a distance x given by

$$x = 4\sqrt{Dt}$$

where t is the period of the cycle (ie 1/f)

Expressing this in logarithmic form gives

$$\log \left[\frac{da}{dN}\right] = -\frac{1}{2} \log (f) + \log 4\sqrt{D} \qquad (1)$$

Linear regression of the results in fig 7.4.ii. for the transition from intergranular to transgranular fracture mode gives a slope of -0.56 and an intercept of -6.22.

$$\log \left[\frac{da}{dN}\right] = -0.56 \log(f) - 6.22$$

The diffusion coefficient would be involved in the intercept value, implying a hydrogen diffusion coefficient D of 2.27×10^{-14} $m^2 s^{-1}$.

This value is much lower than the one determined from the pre-exposure tests and those reported in the literature for other 7xxx series aluminium alloys. This discrepancy could be due to intergranular failure requiring a higher local concentration of hydrogen than that involved in transgranular failure, as proposed by several authors (48,111). In particular, Holroyd & Hardie (85), using the same approach, found an implied diffusion coefficient for the transition from flat transgranular to striated transgranular fracture in 7017-T651 plate of 3.2×10^{-13} $m^2 s^{-1}$, which agrees well with published data for 7xxx series alloys. When the data for the transition from intergranular to transgranular failure mode were analysed, the implied diffusion coefficient was a much lower value of 4.5×10^{-14} $m^2 s^{-1}$.

It can be argued therefore that the hydrogen level necessary for intergranular failure will be attained at a distance closer to the crack tip than $x = 4\sqrt{Dt}$. Applying the value for the hydrogen diffusion coefficient established from the pre-exposure tests to equation (1) above allows the determination of an appropriate error function :

$$\log (da/dN) = -0.5 \log(f) + \log(2z\sqrt{D})$$

This gives a value of $z = 0.55$

If the model for steady state diffusion of hydrogen in a semi-infinite solid is applicable to the hydrogen concentration profile ahead of the crack for a given concentration, Cs, at the

crack tip (corresponding to the availability of hydrogen from the aqueous environment) then the hydrogen concentration at a distance x is Cx, as given by

$$Cx = Cs[1-erfz] = Cs[1-erf(x/2\sqrt{Dt})$$

The ratio of the hydrogen concentration at this point Cx to that at the tip of the original crack Cs would then be [1-erfz] ie 0.437 . The individual ratios Cx/Cs derived from the experimental data give a mean value of 0.43 (for frequencies of 0.1 to 10 Hz) table 8.1.a.

Frequency (Hz)	Period (sec)	ΔKtrans ($MNm^{-3/2}$)	Critical C.G.R (m/cycle)	Cx/Cs
0.01	100	22	5.2×10^{-5}	0.0001
0.02	50	21.5	2.3×10^{-5}	0.0001
0.05	20	19.5	7.0×10^{-6}	0.048
0.1	10	17.4	2.4×10^{-6}	0.30
0.2	5	16	1.4×10^{-6}	0.42
0.5	2	13.5	7.8×10^{-7}	0.476
0.7	1.43	13.3	7.3×10^{-7}	0.43
1	1	12.4	6.7×10^{-7}	0.39
2	0.5	11	3.8×10^{-7}	0.49
4	0.25	10.3	2.6×10^{-7}	0.5
10	0.1	10	1.8×10^{-7}	0.462

Table 8.1.a. Critical hydrogen concentration ratios Cx/Cs for the occurrence of intergranular failure, derived from the critical crack growth rates at different frequencies.

The best evidence of a hydrogen embrittlement mechanism being involved in the stress corrosion cracking of 7xxx series alloys has been provided by Gruhl & Ratke from their cylinder experiment (49) which was discussed in section 2.4.2. Their work showed that cracking initiates remote from the environment at the region of maximum stress ahead of the crack tip. This was explained in terms of grain boundary diffusion of hydrogen and accumulation at a region of high stress triaxiality, leading to embrittlement and fracture.

If such a mechanism is adopted in the present work then the distance of maximum stress ahead of the crack tip is given by

$$X = 2CTOD = K^2/\sigma_y E$$

or, in terms of the cyclic CTOD,

$$X = 0.5\Delta K^2/\sigma_y E$$

where σ_y is the yield stress and E is the Young's modulus

If it is assumed that this distance is equal to the distance that hydrogen diffuses ahead of the crack tip during each cycle, then

$$X = 2z\sqrt{Dt} = 0.5\Delta K^2/\sigma_y E$$

or
$$\Delta K^2 = 4z\sigma_y E D^{0.5}\sqrt{t} \qquad (2)$$

Thus a plot of ΔK^2 versus $\sqrt{t}$ for the transition from intergranular to transgranular cracking (critical stress intensity) should be a straight line with a slope of $4z\sigma_y ED^{0.5}$.

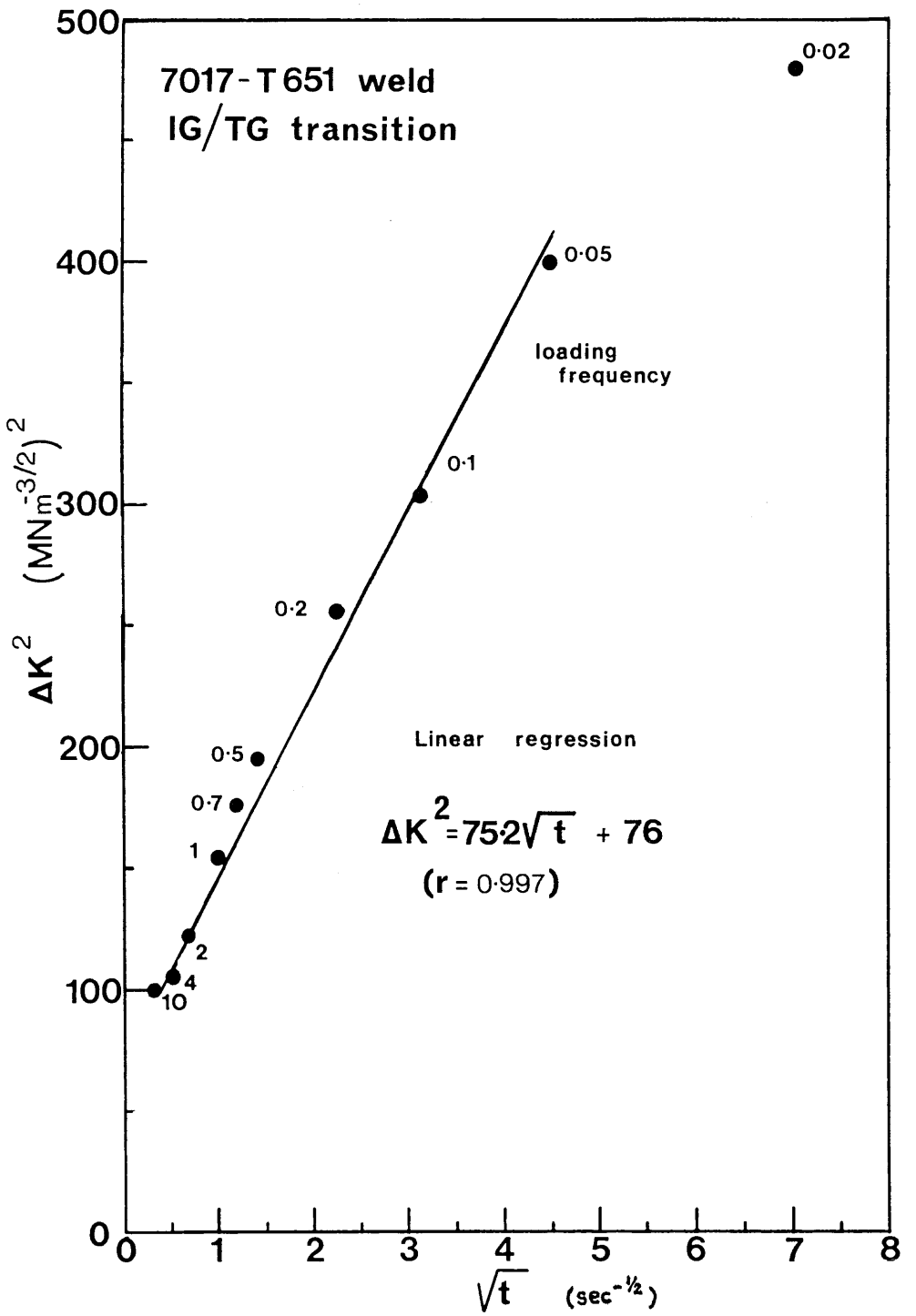

Fig 8.1.i. Dependence of critical stress intensity range for transition from IG to TG fracture mode in corrosion fatigue of 7017-T651 weld with cycle period.

Linear regression of the plot in fig 8.1.i gives a slope of 75.2 with an intercept of 73.3 ie

$$\Delta K^2 = 75.2 \sqrt{t} + 75.9$$

Substituting σ_y = 350 MN/m^2, E = 72 GN/m^2, z = 0.55, D = 3.0×10^{-13} $m^2 s^{-1}$ gives, for equation (2),

$$\Delta K^2 = 30.3 \sqrt{t} \quad (3)$$

this implies the involvement of a constant α = 2.5

ie.

$$\Delta K^2 = 30.3\alpha \sqrt{t}$$

In order to investigate whether a similar relationship applies to the parent plate, the data provided by Holroyd & Hardie for 7017-T651 plate, tested in the short transverse direction (85), were subjected to a similar analysis (their results are presented in a tabular form in appendix 3). A plot of ΔK^2 against $\sqrt{t}$ for the parent plate is shown in fig 8.1.ii. A linear relationship was also observed although of a different slope. This was expected since the values of z and σ are different for the white-zone. Linear regression of these results gives

$$\Delta K^2 = 81.35\sqrt{t} + 42.97$$

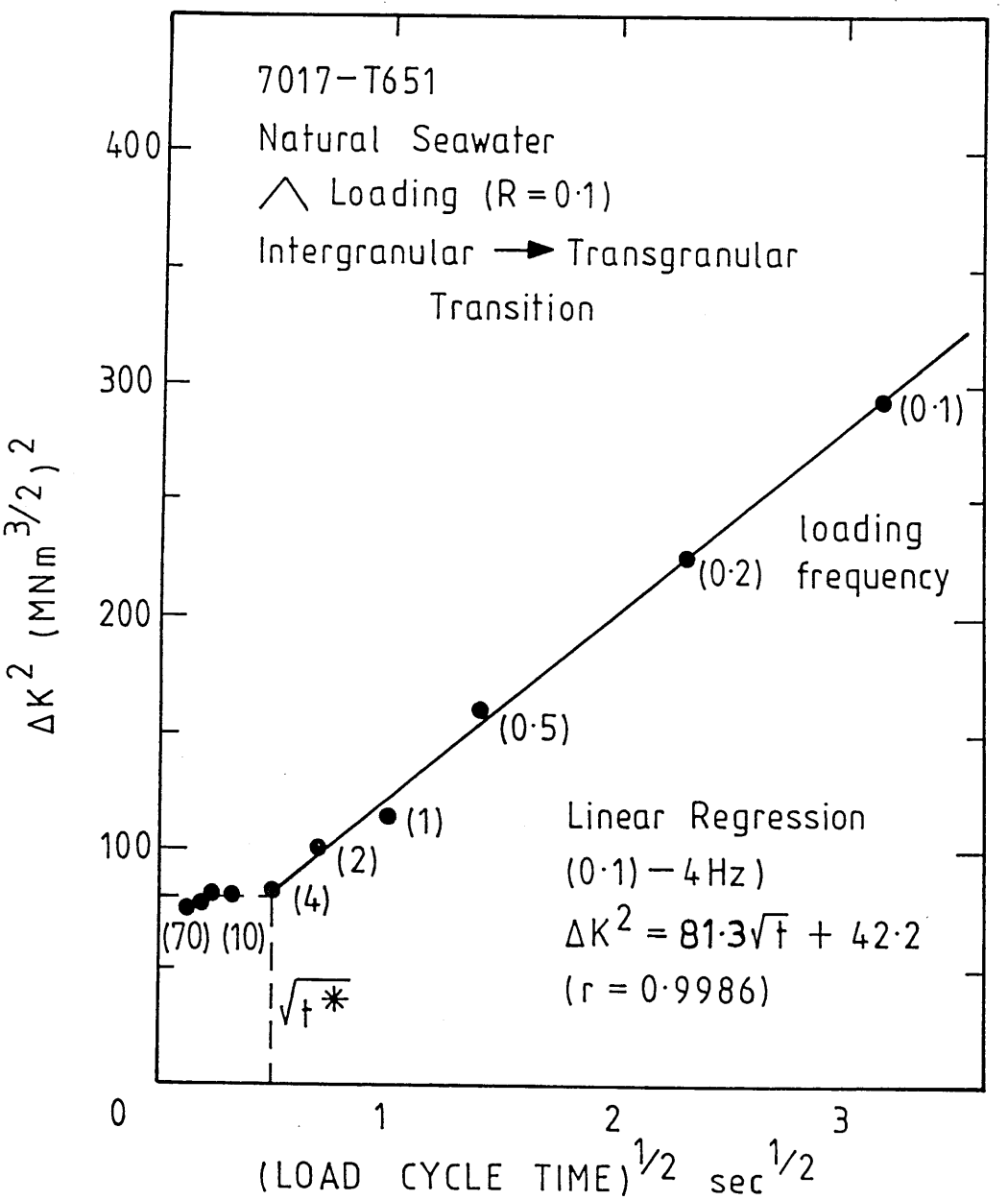

Fig 8.1.ii Dependence of critical stress intensity range for transition from IG to TG fracture mode in corrosion fatigue of 7017-T651 plate with cycle period.

Substituting for σ_y=435 MN/m^2, E=72 GN/m^2, z=0.75, D=3.2x10^{-11} m^{2}s^{-1} in equation (2) gives

$$\Delta K^2 = 53.15\sqrt{t} \qquad (4)$$

which implies a constant $\alpha = 1.5$

Their results also show a change of slope at 4Hz which also seems to appear in the plot for the white zone although it is not so evident since only tests up to 10Hz were performed. This result suggests that above 4Hz the stress intensity ranges are higher than the expected ones. Linear regression of the results gives

a) for 7017-T651 plate $\Delta K^2=18.45\sqrt{t} + 76$

b) for 7017 white zone $\Delta K^2=33.1\sqrt{t} + 89.5$

N.B. It is important to note that for the white-zone only one value at 10Hz exists above 4Hz so the result in b) should be treated with caution.

There is an inherent difficulty in interpreting these results since the amount of intergranular cracking is very small and is seen only at low stress intensity ranges. One explanation of this change in slope at 4Hz was thought to be due to crack closure effects.

8.2. Effect of crack closure

The concept of crack closure was first introduced by Elber (112), who suggested that plastic deformation left in the wake of a growing crack interferes with subsequent crack opening and closing. This means that closure of the crack faces can occur at positive loads during fatigue cycling and growth is controlled by an effective stress intensity factor range ΔKeff, defined as

$$\Delta Keff = Kmax - Kop$$

where Kop is the stress intensity level at which the crack opens, which will be less than the applied stress intensity factor ΔK. Although crack closure can undoubtedly occur during fatigue crack growth, its relative importance is debated (113) due to the complexity of the phenomenon, as it depends on several interacting variables, and also to the experimental difficulties with detection of closure and interpretation of results.

For fatigue in aggressive environments crack closure effects have been suggested to arise from oxide built up on the fracture surface (oxide induced crack closure) (114,115). The significance of the oxide layer thickness is more pronounced at low ΔK and low R ratios. The importance of the "oxide-induced crack closure" is demonstrated in fig 8.2.ii, where ΔKo is lower in dry argon or dry air than in moist air tests at low R (114)

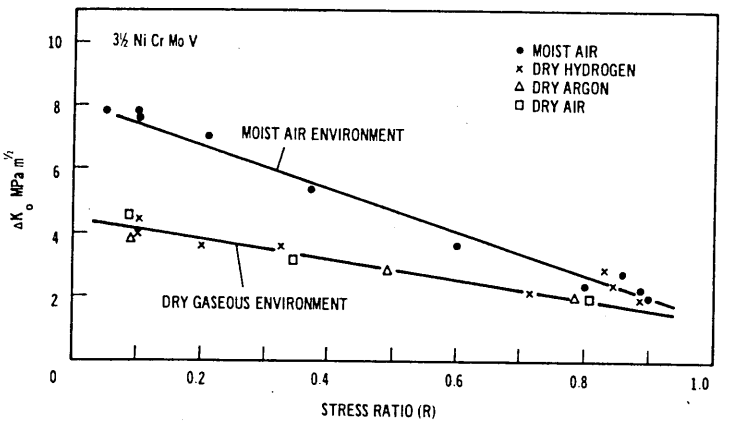

Fig 8.2.ii Influence of stress ratio R on threshold ΔKo in moist and dry environments in 3.5Ni-Cr-Mo-V steel (114)

Originally Elber (112) proposed for a 2024-T3 alloy the relationship

$$\Delta Keff = (0.5 + 0.4R)\Delta K$$

Later this was improved by Schijve (116) to a relationship of the form:

$$\Delta Keff = (0.55 + 0.33R + 0.12R^2)\Delta K$$

which takes account of both positive and negative R ratios.

For this work, however, these two formulae cannot be confidently used, since if crack closure effects occur they will be due to oxide built up on the crack walls while these formulae have been developed for the case of plastic zone deformation left in the wake of a growing crack.

Oxide induced closure effects are known to be more significant for small crack lengths, which is certainly the case for the tests in this work, where the change in slope occurs at near-threshold ΔK levels and the amount of intergranular cracking is very small.

If we now consider for the white-zone the equations:

$\Delta K^2 = 75.2\sqrt{t} + 76$ for 0.1 to 4Hz and

$\Delta K^2 = 33.1\sqrt{t} + 89.5$ for 4 to 10Hz

then for the high frequency case the slope is 2.27 times lower ie

$\Delta K^2 = (33.1)*(2.27)*\sqrt{t}$ or $\frac{\Delta K^2}{2.27} = 33.1\sqrt{t}$

It can be easily seen that the difference in slope suggests the existence of an effective stress intensity

$$\Delta K_{eff} = 0.66\ \Delta K \quad \text{for the white-zone}$$

A similar value has been reported by Suresh et al (115) for oxide induced closure effects for an overaged 7075 alloy fatigue tested in 97% humid air with a stress ratio of 0.1.

If the results for the plate are considered (85) and a similar analysis is made, then

$$\Delta K_{eff} = 0.47\ \Delta K \qquad \text{for 7017-T651 plate}$$

Suresh et al (115) report a similar value (0.45) for an underaged 7075 alloy fatigue tested in 97% humid air with a stress ratio of 0.1. The discrepancy between the underaged 7075 and 7017 in the T651 condition could be due to the nature of the oxide or its thickness. In the latter case the environment was natural sea-water

One way of determining if oxide induced closure occurs would be to calculate the CTOD for various Kmin levels and compare that to oxide thickness on the crack walls. This is very difficult, however as the oxide layer thickens continuously and accurate measurement of its thickness measurements would be extremely difficult if not impossible.

From fig 8.1.i. it can be seen that the relationship does not apply for frequencies below 0.05 Hz. For such frequencies the crack propagation rate approaches that of stress corrosion cracking under static loading conditions. This in turn could mean that crack propagation is controlled by the strain rate at the particular frequency, with cracking taking place during the whole cycle with a minimal or no effect of loading frequency. If the above argument is correct then there should be a significant difference between the crack growth rates produced by a sinusoidal loading waveform and a triangular waveform, as they produce

different strain rates. Unfortunately, tests using a triangular waveform for frequencies of 0.05Hz and below could not be carried out, since the control valve of the Dartec fatigue testing rig could not cope with triangular waveforms at such low frequencies (the control valve was sticking after a few hours of operation).

The sensitivity to strain rate of the crack growth rate of aluminium alloys has been demonstrated by Holroyd & Hardie (59) and tests done for the white zone using triangular waveforms for frequencies of 0.1, 0.5 and 1Hz have shown that crack growth rates are higher for triangular waveforms. Although the difference is not very large and it could easily be argued that the results are close to the experimental scatter-band, fig 7.6.ii.a,b,c. The fact that it has been observed at all frequencies tested allows the above statement to be treated with confidence.

8.3. Discontinuous crack propagation model.

It has been suggested by several workers that cracking in 7xxx series aluminium alloys is discontinuous (105) and time lapse video recording during stress corrosion cracking of bolt loaded DCB specimens in a saline environment, at Alcan laboratories, has demonstrated this discontinuity (117). The presence of striations on the fatigue surface of the white-zone in this work is also evidence of such a propagation mechanism. It is envisaged that the following sequence of events takes place.

Hydrogen accumulates at regions of high stress triaxiality ahead of the crack tip with a subsequent development and growth of microcracks there. The microcracks grow to a certain length until the stress at the ligament between the existing macrocrack and the growing microcrack becomes critical and fracture of the ligament and linkage take place. This is shown schematically below fig 8.3.i

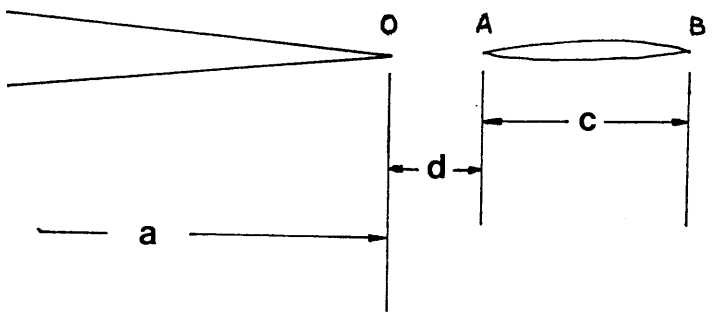

Fig 8.3.i Model of discontinuous crack propagation due to the formation of microcracks ahead of the crack tip

Such a mechanism has been investigated by Shang & Ritchie (118) for fatigue crack growth in SiC reinforced aluminium alloy composites. The striations observed on the fracture surface of the white-zone could therefore be ductile dimples rather than locally thickened oxide due to crack arrest.

Evidence in support of such a crack growth mechanism can account for the caustic swelling observed by Holroyd & Hermann (33) prior to crack initiation during stress corrosion cracking under static loading conditions, of 7075 alloy. The method of shadow caustics, as described in section 6.5., gives directly the value of

the stress intensity by measurement of the diameter of the caustic formed. Holroyd and Hermann's tests showed an increase in the stress intensity prior to crack initiation without any change in the applied load. The stress intensity reduced after the formation of a visible crack fig 8.3.ii.

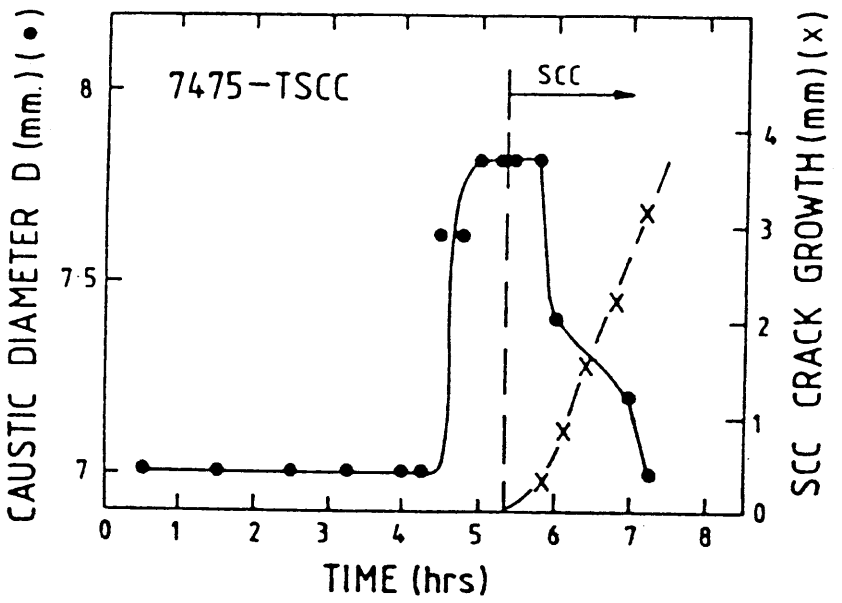

Fig 8.3.ii Swelling of the caustic diameter prior to scc crack initiation

Holroyd suggested, as an explanation to this caustic shadow swelling, that hydrogen uptake promotes a local increase in elastic modulus in the crack tip region which, would lead to increases in the stress intensity, (by analogy to the stiffening effect of lithium atoms in Al-Li alloys) Since it is not clear how hydrogen could achieve this, the suggestion of microcrack formation ahead of the crack tip seems a more plausible explanation. The caustic swelling could be caused by a local increase of the stress intensity at the crack tip as the stress at the macrocrack-

microcrack ligament increases and then the caustic diameter reduces again as fracture of the ligament takes place.

More evidence in favour of this mechanism comes in the present work from the ACPD monitoring technique. The operating principle is based on the "skin-effect" that is current flowing near the surface of the conductor (as opposed to direct current which flows through the whole cross-section of a conductor). The potenial drop is produced by the extra distance travelled by the current as it flows round the crack. The skin depth can be reduced by increasing the current frequency, this giving more accurate measurement of crack length. The potential drop is sensitive to the resistivity of a conductor and resistivity is known to change in a conductor when a stress is applied to it. In section 6.6. the problems ecountered due to this effect are mentioned. It was noted that the increase in the potential drop (or crack length) was stepped, fig 8.3.iii, or saw tooth type. Since it is physically impossible at the position of maximum stress (crack closure unlikely to be involved) for the crack length to decrease, and there was no change in the value of the maximum stress, a local change in the resistivity at the crack tip region should have taken place. That can only happen if there is a local change in the stress level. A rise in the local stress can be accounted for if it is accepted that a microcrack (or microcracks) forms ahead of the original crack thus increasing the stress level at the ligament between them and consequently the resistivity of the material there changes. When the size of the microcrack has reached a critical value fracture of the ligament takes place with a reduction in the

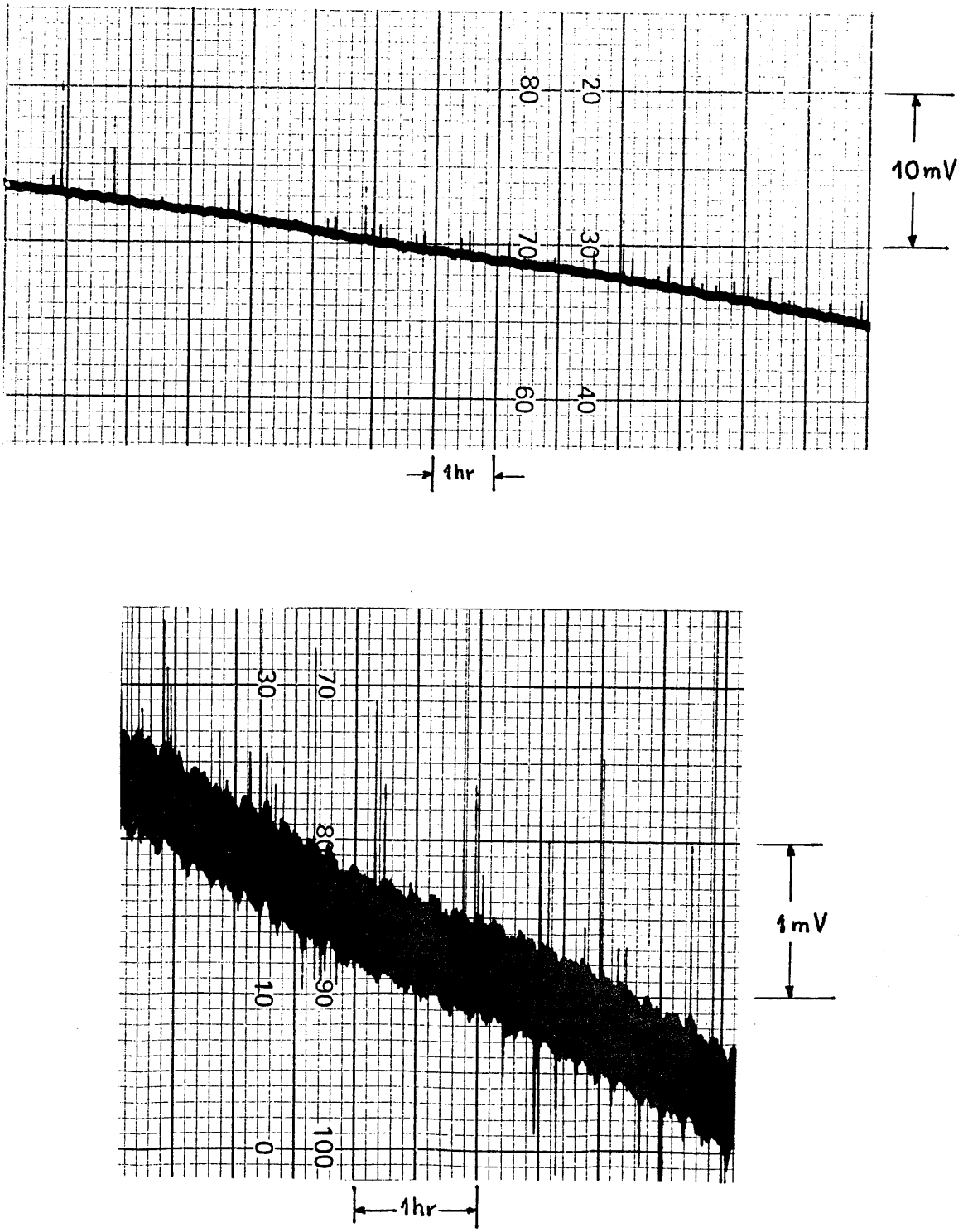

Fig 8.3.iii Section of recording of potential drop wrt time for a growing crack at 0.1Hz cyclic loading frequency showing the observed step-like pattern.

local stress level. This subsequently reduces the potential drop value. The new potential value will be higher than the initial one as linkage between original crack and microcrack have taken place and the crack is now longer.

Shang and Ritchie (118) have provided a mathematical analysis of such a crack growth mechanism and have used the equation given by Rubinstein (124) to calculate the stress intensities at the tip of the macrocrack and the front and rear of the microcrack. Referring to fig 8.3.i the local stress intensity factors at the macrocrack tip, O, and microcrack tips, A and B, are given in terms of the macrocrack stress intensity factor that applies in the absence of the microcrack K(∞) as follows:

$$\frac{K_I(O)}{K_I(\infty)} = \sqrt{\frac{D+2c}{D}} \frac{\Sigma\left[1-\left(\frac{D}{D+2c}\right)\right]}{\Gamma\left[1-\left(\frac{D}{D+2c}\right)\right]}$$

$$\frac{K_I(A)}{K_I(\infty)} = \left\{ \frac{D+2c}{D} \cdot \frac{\Sigma\left[1-\left(\frac{D}{D+2c}\right)\right]}{\Gamma\left[1-\left(\frac{D}{D+2c}\right)\right]} - 1 \right\} \div \sqrt{\frac{2c}{D}}$$

$$\frac{K_I(B)}{K_I(\infty)} = \left\{ 1 - \frac{\Sigma\left[1-\left(\frac{D}{D+2c}\right)\right]}{\Gamma\left[1-\left(\frac{D}{D+2c}\right)\right]} \right\} \div \sqrt{1-\left(\frac{D}{D+2c}\right)}$$

D= distance of microcrack from macrocrack tip

where the first and second complete elliptic integrals Γ and Σ are given by:

$$\Gamma(g) = \int_0^{\pi/2} \frac{d\theta}{\sqrt{1 - g^2 \sin^2\theta}} \qquad \theta = \text{dummy variable}$$

$$\Sigma(g) = \int_0^{\pi/2} \sqrt{1 - g^2 \sin^2\theta}\, d\theta$$

It is possible then to produce a mathematical model for crack growth using the mathematics above and the following reasoning.

If the cracking mechanism is hydrogen diffusion controlled and cracking initiates at a distance, d, ahead of the crack tip then the time taken for hydrogen to accumulate there in sufficient concentration in order to initiate intergranular cracking may be estimated from the equation $d = 2z\sqrt{Dt}$. Once a microcrack has started it will grow to a critical length, 2c, at which ductile failure of the ligament and link-up take place. The time taken for the microcrack to grow to this critical length will be given by $2c=2z\sqrt{Dt}$, since hydrogen is seen to move very quickly over free surfaces.

A computer program has been written, taking into account all the above assumptions to calculate crack velocities against the stress intensity for the 7017-T651 plate. This was done because of the abs ence of stress corrosion cracking data for the white- zone under either dynamic or static loading conditions. The plotted results are shown in fig 8.3.iv. together with results quoted in the literature for stress corrosion cracking of the parent plate for comparison. It is immediately obvious that the computer model does not show a stage II plateau. The existence of a plateau

during scc of 7017-T651 plate however can be debated as can be seen in fig 8.3.iv. Crack velocities for the computer model are very close to those quoted for the constant strain tests. Also the model breaks down as Kic is approached but this is expected since at that stage (stage III) crack growth is not controlled by hydrogen diffusion.

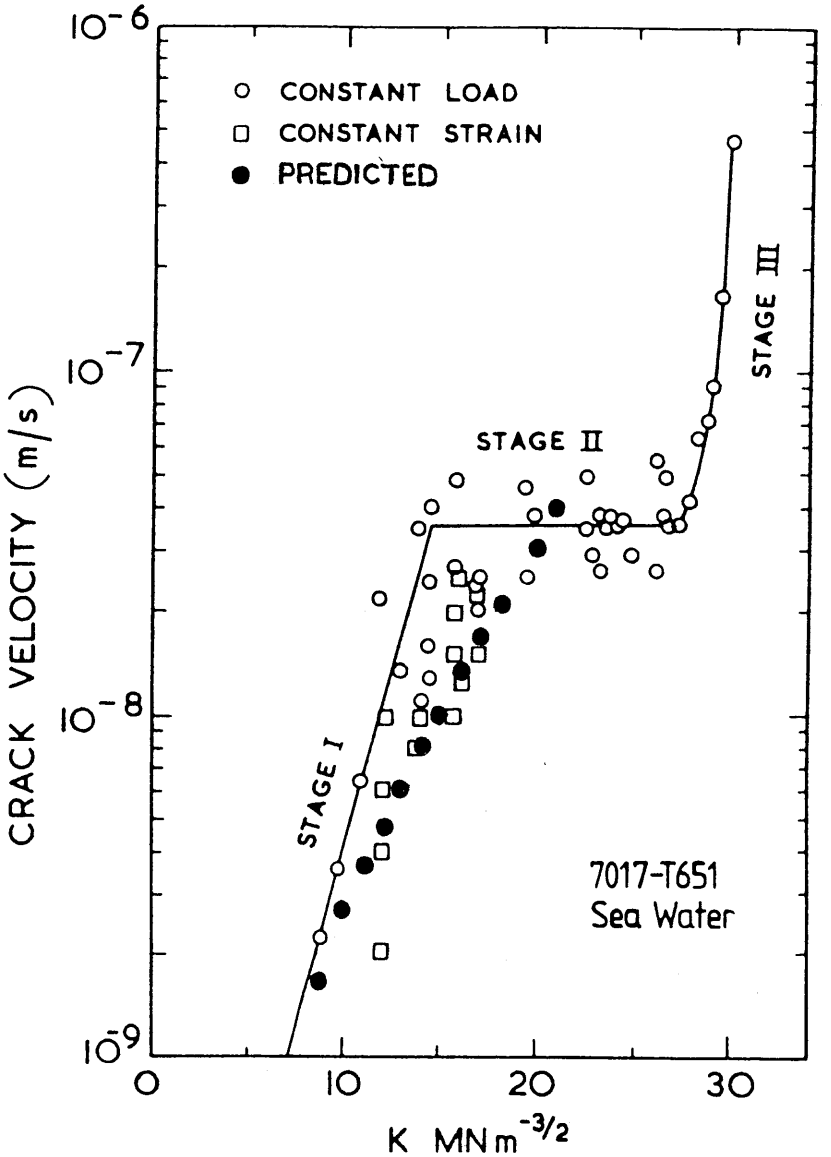

Fig 8.3.iv Comparison between experimental data for scc of 7017-T651 plate and computer model prediction.

The success of the model depends on the value of d, the distance ahead of the crack tip at which initiation of the microcrack is seen to take place. If the position of maximum stress is selected, then d is too large and the crack growth rates are much slower. If the value suggested by Scamans (129) of $3x10^{-7}$ m for the critical jump distance for incremental crack growth is used then the model successfully predicts crack velocities for the parent plate. This value for d corresponds well with the striation width observed on the white zone fracture surface of approximately 0.2μm.

8.4. Role of anodic dissolution

The work so far has concentrated on the effect that hydrogen has on the crack growth mechanism during corrosion fatigue of 7017-T651 welds. However anodic dissolution is also claimed to be responsible for the crack growth during stress corrosion of Al-Zn-Mg alloys in aqueous chloride environments (125). The debate focuses on whether the process is rate controlling or not. Anodic dissolution is accepted to be a necessary process for the generation of atomic hydrogen by a cathodic reaction, a prerequisite for diffusion of hydrogen ahead of the crack tip in sufficient quantities to promote brittle crack growth. The claim that anodic dissolution may be responsible for crack growth occurring during stress corrosion and corrosion fatigue of Al-Zn-Mg alloys is based on reports that cathodic polarization reduces crack growth rates in both stress corrosion cracking and corrosion fatigue (48, 126) and anodic polarization enhances growth rates

(48). The author accepts that some crack growth by anodic dissolution may occur at the crack tip but it is not considered to make a significant contribution to the crack growth. The argument in favour of a hydrogen embrittlement mechanism being involved in the corrosion fatigue of 7017-T651 welds in a saline environment is based on the fracture mode transition which is not associated with the attainment of a critical crack velocity as would be expected for crack growth controlled by anodic dissolution (127, 128).

8.5 High frequency tests.

It is not clear why cracking could not be produced in the white-zone if test frequencies were above 10Hz. One explanation could be the deformation mode during straining which at low strain rates is due to grain boundary sliding, while at high strain rates it is due to slip (129). At frequencies above 10Hz the strain may be high enough for transition of deformation mode leading to a more favourable path for crack growth almost parallel to the direction of action of the load. This favourable path is not thought to be mechanical since fatigue in air at 20 or 30Hz did not produce any change in the direction of crack growth. It is thought that if slip steps are generated then hydrogen from the environment may be transported by mobile dislocations rather than diffuse through grain boundaries at a direction dictated by the shear stress component.

8.6 Acoustic emission tests.

The acoustic emission tests did not produce any conclusive results on the mechanism involved during corrosion fatigue of 7017-T651 welds. One thing that is obvious is that periods of activity are accompanied by long periods of silence which suggest a discontinuous crack growth mode (appendix II) particularly evident at the fatigue stage II region with the periods of silence being more or less regular. The signal strength however was not very high in order to eliminate involvement of noise. On the other hand it has been suggested that when acoustic emission tests are performed on specimens immersed in aqueous solutions then damping effects can occur due to the presence of the solution resulting in lower strength signals (130). The small size of the specimen also caused some problems regarding the mounting of the transducer and after the termination of the tests it was seen that some bubbles had been trapped in the silicon which could have affected the results. It is clear that more tests need to be done for proper evaluation of the results.

CONCLUSIONS

C O N C L U S I O N S

1. The method developed by Stark & Ibrahim for the determination of fracture tougness of metallic materials from small circumferentially grooved cylindrical specimens has been successfully employed for the determination of fracture toughness of the white zone of 7017-T651 alloy welds.

2. Environment sensitive fracture of the white-zone under cyclic loading takes place only when the appropriate condition of stress triaxiality is established.

3. Arc-type specimens similar to the one described in ASTM E399 can be successfully employed for quantitative studies of crack growth in white zones of 7017 welds. In fact such a specimen can be used to test any area of a weldment.

4. Crack growth rates in the white zone show enhancement in the acidified salt chromate solution over those observed in dry air for all frequencies tested.

5. A simple superposition model, where the corrosion fatigue component is derived by simple addition of crack growth rates during fatigue in an inert environment and stress corrosion under static loading, cannot account for the observed crack growth rates in fatigue during corrosion fatigue in the white zone.

6. Pre-exposure embrittlement tests have shown that hydrogen diffuses through the grain boundaries and a diffusion coefficient $D=3x10^{-13}$ m^2/s has been established that is consistent with existing values in the literature.

7. The crack velocity for the transition from intergranular to transgranular fracture mode depends on frequency and (on a log log basis) is proportional to the square root of the reciprocal of the loading frequency, for frequencies from 0.1 to 10 Hz. Below 0.1Hz frequency it is almost directly proportional to the reciprocal of the frequency.

8. The rate determining process for transition from intergranular to transgranular failure appears to be grain boundary diffusion of atomic hydrogen with crack advance in intergranular fracture being associated with the attainment of a critical hydrogen concentration level higher than that required by $4\sqrt{Dt}$ which appears to take place at the region of maximum stress ahead of the crack tip, with the ratio of hydrogen concentation at this point Cx to that at the tip of the original crack Cs found to be equal to 0.43.

9. At cycling frequencies in the region of 1Hz, an enhancement of crack growth rate is observed over the whole range of stress intensities and is believed to arise, at least in part, from modification of the solution at the crack tip due to cyclic movement of the crack walls.

10. At low frequencies (below 0.1Hz) the observed crack growth rates approach stress corrosion cracking velocities under static loading conditions, with the cyclic loading frequency having no effect other than affecting the crack tip strain rate.

11. Triangular waveforms are found to increase the corrosion fatigue crack growth rates compared with tests performed with sinusoidal waveforms, for all frequencies tested, implying a strong influence of the crack tip strain rate.

12. Crack growth rates observed in the acidified salt chromate solution are lower than those observed in an alkaline one, this being attributed to either oxide dissolution and crack tip blunting or an influence of the chromate and dichromate ions on the crack tip solution chemistry.

13. The output signal from the ACPD technique for crack growth monitoring suggests that cracking initiates ahead of the crack tip, remote from the environment, with subsequent growth there and link-up with the original crack. This is consistent with a discontinous cracking mechanism controlled by diffusion of hydrogen.

14. A computer model produced to predict crack velocities during stress corrosion cracking of the white-zone assuming a discontinuous hydrogen diffusion controlled cracking mechanism has produced encouraging results.

15. The change in direction of crack growth towards the parent metal when tests were performed at frequencies above 10Hz may be attributed to an effect of strain rate which when low produces grain boundary sliding and when high produces crystallographic slip.

RECOMENDATIONS FOR FURTHER WORK

The observations and results discussed in the foregoing give rise to several points which merit further investigation.

1. The effect of triangular, as opposed to sinusoidal, waveforms on crack growth rates in corrosion fatigue needs to be investigated further, particularly at low frequencies. The uncertainty of whether the result in conclusion 11 represents a real effect or is due to scatter may be resolved by switching from sinusoidal to triangular waveform during the course of a test and observing any change in growth rate.

2. Explanation of the role of the pH of the bulk solution on crack growth rate during corrosion fatigue might be aided by conducting tests at various pH levels at particular frequencies and using microelectrodes to follow the changes in pH and potential close to the crack front.

3. The indirect evidence, seen in the present work, that crack closure effects are involved in corrosion fatigue crack growth rates in the white-zone of 7017 welds should be followed by examination for direct evidence.

4. Although the significance of the results from the acoustic emission tests (appendix II), in relation to the cracking mechanism, seems unclear, further use should be made of the technique.

5. In order to enable more accurate prediction of crack growth behaviour, the computer model presented in this work should be further refined to include all parameters involved during fatigue.

APPENDIX I

```
cls
input "Yield strength of material is ";sy
input "Hydrogen diffusion coefficient =";DH
input "Correction factor for hydrogen permeation =";z
input "Young's modulus is ";e
'input "Incremental step =";d
input "max load (kN)  P=";P

P=P/1000
Pm=P*0.1
DP=P-Pm
input "specimen width  (mm)  W=";W
W=W/1000
input "thickness  (mm)  B=";b1
b1=b1/1000
input "ins radius  (mm)  R1=";R1
R1=R1/1000
R2=R1+W
input "crack  (mm)  a=";a0
a0=a0/1000
c1=a0/W
F=18.23*(c1^0.5)-106.2*(c1^1.5)+389.7*(c1^2.5)
-582*(c1^3.5)+369.1*(c1^4.5)

DK=(DP/(b1*W^0.5))*(1+0.5*c1)*(1+0.221
*(1-c1^0.5)*(1-R1/R2))*F


lprint "This programm calculates the stress intensity"
lprint "values in the case where a microcrack develops"
lprint "ahead of the crack tip and calculates the crack "
lprint "velocity associated with such a cracking mechanism."



' "Ko is the stress intensity of the macrocrack"
' "Ka is the stress intensity at the front of the microcrack"
' "Kb is the stress intensity at the back of the microcrack"
' "c is the half length of the microcrack"
lprint
lprint
lprint "DK";tab(18);"da/dt";tab(48);"2c"
lprint "_____________________________________________________"
lprint "DK=";DK
lprint
goto start
redo:
l=2*c
tc=((1/(2*z))^2)*(1/DH)
tc2=((d/(2*z))^2)*(1/DH)
ti=tc+tc2

da=d+l
v=da/ti
a0=a0+d+l

c1=a0/W
F=18.23*(c1^0.5)-106.2*(c1^1.5)+389.7*(c1^2.5)
-582*(c1^3.5)+369.1*(c1^4.5)
DK=(DP/(b1*W^0.5))*(1+0.5*c1)*(1+0.221
*(1-c1^0.5)*(1-R1/R2))*F
```

```
lprint using "##.###";DK;
lprint tab(10);v;tab(42);l

if DK>=22 then end
start:

d=0.2178*(DK^2)/(sy*e)
c=0.00000001

again:


r=(d+2*c)/d
t=2*c/d
g=1-1/r
def fnx(x)=(1-(g*sin(x))^2)^(-0.5)
goto integral
arhi:
gamma=a2
def fny(x)=(1-(g*sin(x))^2)^(0.5)
goto integral2
archi:
sigma=a22

Ko=(r^0.5)*(sigma/gamma)*DK
Ka=((r*sigma/gamma-1)/(t^0.5))*DK
Kb=((1-sigma/gamma)/(g^0.5))*DK
if Ko >=22 then redo

jump:

c=c+0.00000001
goto again

'goto redo
end

integral:
'print "integral 1 calculating"
a=0
b=1.57
h1=b-a
a1=h1*(fnx(a)+fnx(b))/2
h2=(b-a)/2
x1=a+h2
a2=h2*(fnx(a)+fnx(b)+2*fnx(x1))/2
nstrip=2
compare:
p=a2-a1
'print "a2-a1=";p
if abs(p)<0.0001 then  telos
a1=a2
h2=h2/2
a2=h2*(fnx(a)+fnx(b))/2
x=a
nstrip=nstrip*2
for I=1 to (nstrip-1)
x=x+h2
a2=a2+fnx(x)*h2
next I
```

```
goto compare
telos:
goto arhi

integral2:
'print "integral 2 calculating"
a=0
b=1.57
h1=b-a
a11=h1*(fny(a)+fny(b))/2
h2=(b-a)/2
x1=a+h2
a22=h2*(fny(a)+fny(b)+2*fny(x1))/2
nstrip=2
dial:
q=a22-a11
'print "a22-a11=";q
if abs(a22-a11) < 0.0001 then fini
a11=a22
h2=h2/2
a22=h2*(fny(a)+fny(b))/2
x=a
nstrip=nstrip*2
for I=1 to (nstrip-1)
x=x+h2
a22=a22+fny(x)*h2
next I
goto dial
fini:
goto archi
```

```
'com1 1024
rem MATELECT.BAS -prog to read/print results from
rem Matelect Crack Growth Monitor
rem
cls

print "Program MATELECT  :  press Ctrl and BREAK to stop running."
print "-------------------------------------------------------------------------"
print
print "This program reads the (serial) computer interface"
print "of the MATELECT Crack Growth Monitor CGM5, and displays"
print "the results on the screen."
print
PRINT "                    Press any key to HALT this program..."


open "COM1: 9600,E,8,2,RS,CS,DS,CD" AS #1
print "Device file is opened.."

open "na2hz.dat" FOR OUTPUT AS #2

dim x$(20)
dim x%(5)
dim digit#(5)
locate 12,30
print "Voltage :"
locate  20,10
print"    C O M M U N I C A T I O N    S U C C E S S F U L"
i=0

WHILE NOT INSTAT
i=i+1

X$ = INPUT$(5, #1)
FOR Z = 1 TO 5
            CH1$ = MID$(X$,Z,1)
            X%(Z) = ASC(CH1$)
            locate 10, 20 + (5 * z)
            print "  "
            locate 10, 20 + (5 * z)
            print x%(z),
NEXT Z
rem
rem  x(1)..x(5) represent the ASCII codes of the 5 characters
rem  which have been detected by the MATELEC monitor.
rem
rem     Now we have to convert them into a usable number..
rem
rem               declare some constants..
rem
positive = 1
negative = 0
firstdec = 0
secondec = 1

for b = 1 to 5
rem
rem     Make a binary string out of the number..
rem
        b$ = bin$(x%(b))
```

```
rem     Pad the binary string at the left-hand end if necessary,
rem     with zeros, to make it always 8 characters long...
rem
        if len(b$) = 1 then b$ = "0000000" + b$
        if len(b$) = 2 then b$ = "000000" + b$
        if len(b$) = 3 then b$ = "00000" + b$
        if len(b$) = 4 then b$ = "0000" + b$
        if len(b$) = 5 then b$ = "000" + b$
        if len(b$) = 6 then b$ = "00" + b$
        if len(b$) = 7 then b$ = "0" + b$
rem
rem     Then take the 4 left-most characters of the binary string,
rem     representing the 4 most significant bits..
rem

        b1$ = left$(b$,4)

rem     We now have a 4-digit binary string, representing
rem     our actual decimal digit (0-9), so if we take
rem     each binary digit in turn, we can sum our decimal digit...
rem
x8 = (asc(mid$(b1$,1,1)) - 48) * 8
x4 = (asc(mid$(b1$,2,1)) - 48) * 4
x2 = (asc(mid$(b1$,3,1)) - 48) * 2
x1 = (asc(mid$(b1$,4,1)) - 48)
locate 1,1

if b = 1 then
        x8 = (asc(mid$(b1$,1,1)) - 48)
        x4 = (asc(mid$(b1$,2,1)) - 48)
        x2 = (asc(mid$(b1$,3,1)) - 48)
        x1 = (asc(mid$(b1$,4,1)) - 48)
    if x8 = 1 then
        signal = overrange
    else
        signal = withinrange
    end if
    if x2 = 1 then
         sign = positive
     else
         sign = negative
     end if
     if x4 = firstdec then
         decimal = firstdec
     else
         decimal = secondec
     end if
else
        digit#(b) = x8 + x4 + x2 + x1
end if
next b

number# = digit#(2) + (digit#(3) / 10)
          + (digit#(4) / 100) + (digit#(5) / 1000)

if decimal = firstdec then
rem     print "Decimal = firstdec"
        number# = number# /10
else
```

```
rem      print "Decimal = secondec
end if

if Sign = Negative then
      Number# = 0 - Number#
end if

locate 12,40
print "          "
locate 12,40
print using "+#.####"; number#
rem   Setting of delay time for readings to be stored ...
rem   Division by  5 units is delay of 2 sec,
rem   division by 10 units is delay of 4 sec  etc...

if i/150=int(i/150) then
print #2, using "+#.####";number# : print number#

wend

CLOSE #2
CLOSE #1

cls
locate 12,40
print "PROGRAM INTERUPTED "
END
```

```
'Program :  ARCSPEC2.BAS

cls
cf#=0.0
print
input "Enter calibration factor for CGM :"; cf#
print
input "Enter max  fatigue load in  kN:"; P2
p2 = p2 /1000    ' convert to MN
print
input "Enter min fatigue load in kN:";P1
p1 = p1 /1000    ' convert to MN
print
input "Enter specimen thickness (B) (in mm) ";b
b = b /1000      ' convert to meters
print
input "Enter specimen width (W) (in mm) ";w
w = w/1000       ' convert to meters
print
input "Enter specimen's inside radius  R1 (in mm) ";R1
R1=R1/1000       ' convert to meters
print
'input "Enter specimen's outer radius  R2 (in mm) ";R2
'R2=R2/1000       ' convert to meters
R2=R1+w
print
input "Enter depth of precrack (in mm) ";pr
pr = pr /1000    ' convert to meters
print
input "Enter No of cycles elapsed per reading :"; cpr

a# = 0.0
old# = 0.0

'Open CRACK.DAT file & read values
open "na2hz.dat" for input as #2

' Open PLOT.DAT for output
open "pna2Hz.dat" for output as #1

input #2, old#
      old#=pr+((old#*cf#)/1000)


do while not eof(2)
      cnt=0
      input #2, a#
      a# = pr + ((a# * cf#) /1000)

      if a#<old# or a#=old# then
      cnt=1

      do while a#<old# or a#=old#

input #2, a#
      a#=pr+((a#*cf#)/1000)
      cnt=cnt+1
      wend
      end if
      cnt=cnt+1
```

```
        c#=a#/w
f  = 16.23*(c#^0.5)-106.2*(c#^1.5)+389.7*(c#^2.5)
     -582*(c#^3.5)+369.1*(c#^4.5)

        diff# = a#-old#
        dp = p2-p1

        y# = (dp/(b*(w^.5)))*(1+.5*c#)*(1+.221
             *(1-c#^.5)*(1-R1/R2))*f

        x# = diff#/(cpr*cnt)

        print #1,x#,y#

        old# = a#
loop until eof(2)
print
print "**** Calculations finished... data stored on plot.dat ****"
close #2
close #1
end
```

```
10 CLS
20 PRINT " CALCULATION OF FRACTURE TOUGHNESS USING"
25 PRINT " THE STARK & IBRAHIM APPROACH"
30 PRINT
40 PRINT "INPUT YIELD STRENGTH OF MATERIAL  (MPa)"
50 INPUT S
60 PRINT "INPUT LOAD TO FRACTURE OF FINAL LIGAMENT  (N)"
70 INPUT P
80 PRINT "INPUT AVERAGE FATIGUE CRACK LENGTH  (m)"
90 INPUT B
100 PRINT "Input machined notch depth (mm)"
110 INPUT M
120 PRINT "INPUT LIGAMENT ECCENTRICITY  (m)"
130 INPUT E
140 D=8.3
150 ST=4*P/(3.14*D^2)
160 SB=16*P*E/(3.1416*D^3)
170 FO=1.25/((1-(2*B/D)^1.47)^2.4)
180 AL=22.188*EXP(-4.889*(2*B/D))
190 F=FO*EXP(AL*(E/D))
200 K1=(ST+SB)*(3.1416*B*F/1000)^.5
210 R=(((K1/S)^2)*1000)/18.8496
220 LD=D-2*B
230 B=B+R
240 CLS
250 LPRINT "yield strength of material  ";S;"  Mpa"
260 LPRINT:LPRINT
270 LPRINT "A first approximation for K1c =";K1
280 LPRINT
290 FO=1.25/((1-(2*B/D)^1.47)^2.4)
300 AL=22.188*EXP(-4.889*(2*B/D))
310 F=FO*EXP(AL*(E/D))
320 K1=(ST+SB)*(3.1416*B*F/1000)^.5
330 LPRINT "The final result is :
340 LPRINT
350 LPRINT "       K1c =  ";K1
360 LPRINT
370 LPRINT "         r =  ";R
380 DFC=E+(D-2*M-LD)/2
390 LPRINT:PRINT
400 LPRINT "Deepest fatigue crack is =";DFC;"  (mm)
410 IF DFC>2*R THEN 440
420 IF DFC<2*R THEN 430
430 LPRINT "THE RESULT IS INVALID"
440 LPRINT "this is greater than twice  r"
445 LPRINT " therefore the result is VALID"
450 END
```

APPENDIX II

0.1 Hz

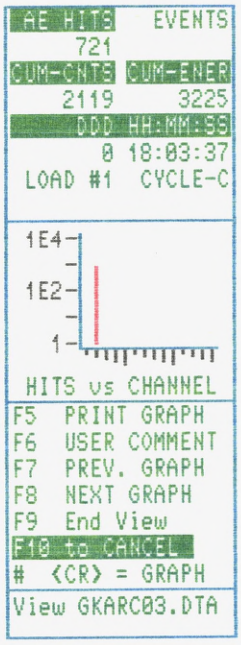
AE HITS
EVENTS
721
CUM-CNTS
CUM-ENER
2119
3225
DDD HH:MM:SS
0 18:03:37
LOAD #1 CYCLE-C
1E4
1E2
1
HITS vs CHANNEL
F5 PRINT GRAPH
F6 USER COMMENT
F7 PREV. GRAPH
F8 NEXT GRAPH
F9 End View
F10 to CANCEL
<CR> = GRAPH
View GKARC03.DTA

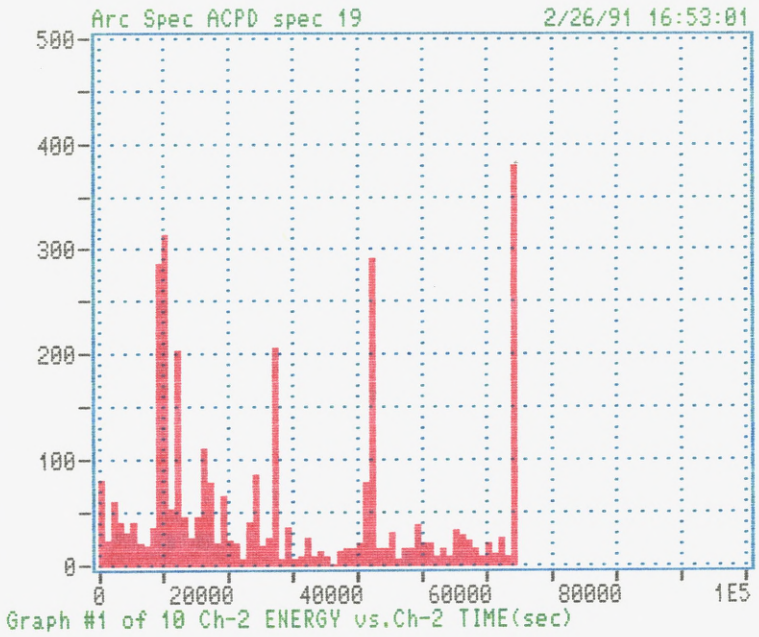
Arc Spec ACPD spec 19
2/26/91 16:53:01
500
400
300
200
100
0
0
20000
40000
60000
80000
1E5
Graph #1 of 10 Ch-2 ENERGY vs.Ch-2 TIME(sec)

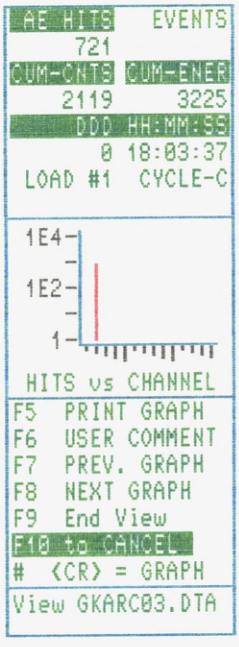
AE HITS
EVENTS
721
CUM-CNTS
CUM-ENER
2119
3225
DDD HH:MM:SS
0 18:03:37
LOAD #1 CYCLE-C
1E4
1E2
1
HITS vs CHANNEL
F5 PRINT GRAPH
F6 USER COMMENT
F7 PREV. GRAPH
F8 NEXT GRAPH
F9 End View
F10 to CANCEL
<CR> = GRAPH
View GKARC03.DTA

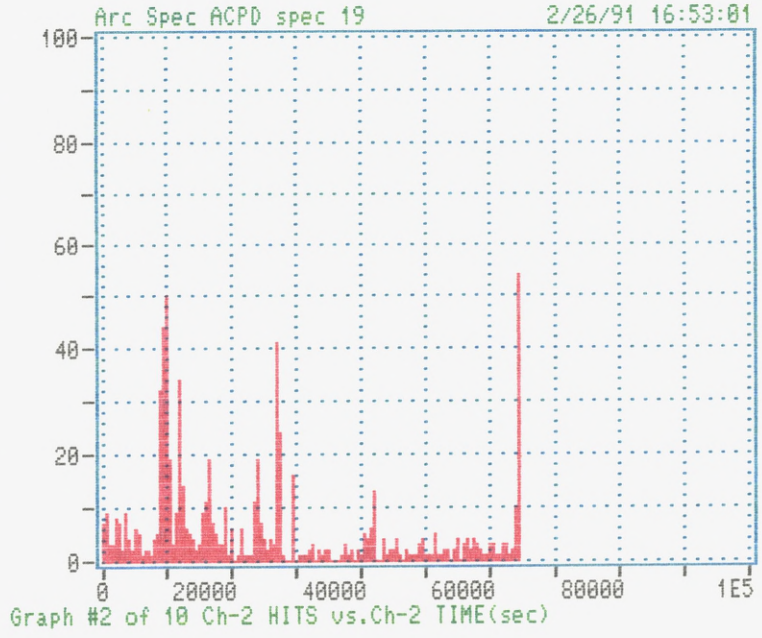
Arc Spec ACPD spec 19
2/26/91 16:53:01
100
80
60
40
20
0
0
20000
40000
60000
80000
1E5
Graph #2 of 10 Ch-2 HITS vs.Ch-2 TIME(sec)

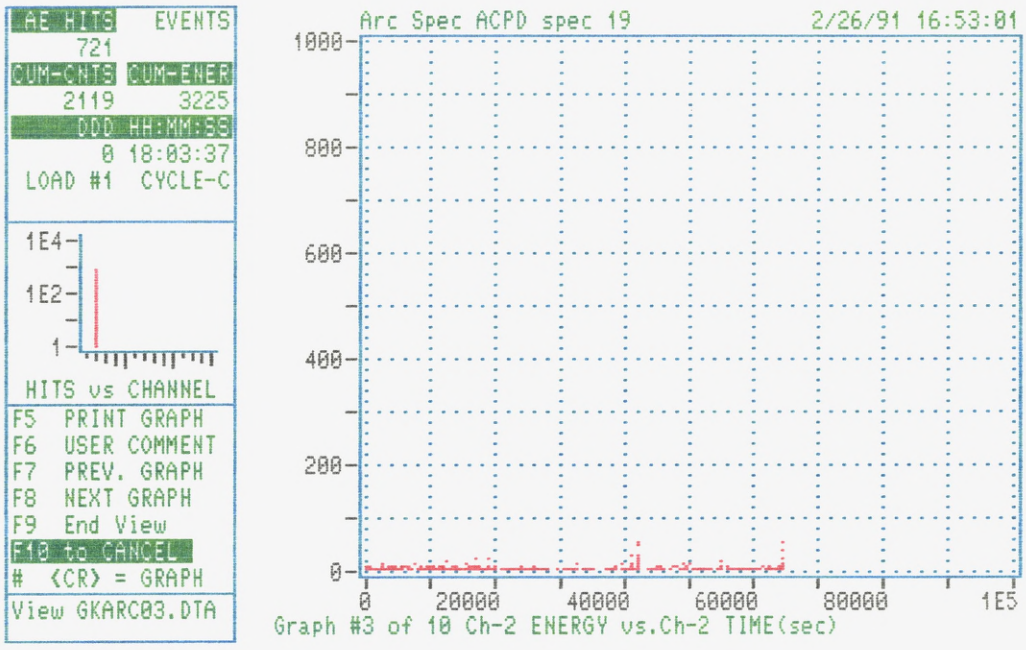
AE HITS
EVENTS
721
CUM-CNTS
CUM-ENER
2119
3225
DDD HH:MM:SS
0 18:03:37
LOAD #1 CYCLE-C
1E4
1E2
1
HITS vs CHANNEL
F5 PRINT GRAPH
F6 USER COMMENT
F7 PREV. GRAPH
F8 NEXT GRAPH
F9 End View
F10 to CANCEL
<CR> = GRAPH
View GKARC03.DTA
Arc Spec ACPD spec 19
2/26/91 16:53:01
1000
800
600
400
200
0
0
20000
40000
60000
80000
1E5
Graph #3 of 10 Ch-2 ENERGY vs.Ch-2 TIME(sec)

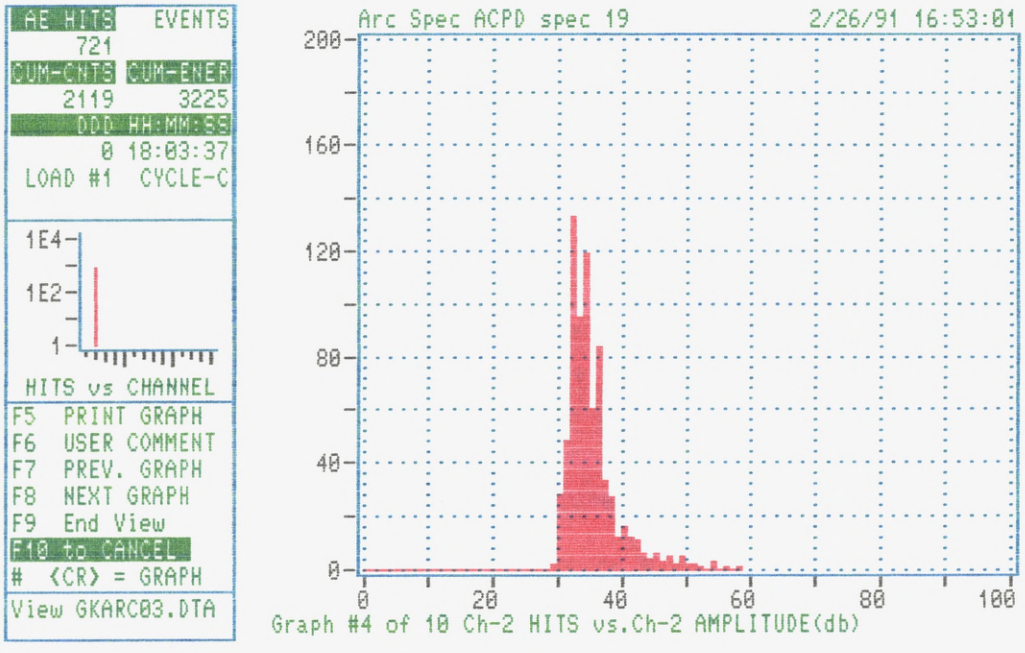
AE HITS
EVENTS
721
CUM-CNTS
CUM-ENER
2119
3225
DDD HH:MM:SS
0 18:03:37
LOAD #1 CYCLE-C
1E4
1E2
1
HITS vs CHANNEL
F5 PRINT GRAPH
F6 USER COMMENT
F7 PREV. GRAPH
F8 NEXT GRAPH
F9 End View
F10 to CANCEL
<CR> = GRAPH
View GKARC03.DTA
Arc Spec ACPD spec 19
2/26/91 16:53:01
200
160
120
80
40
0
0
20
40
60
80
100
Graph #4 of 10 Ch-2 HITS vs.Ch-2 AMPLITUDE(db)

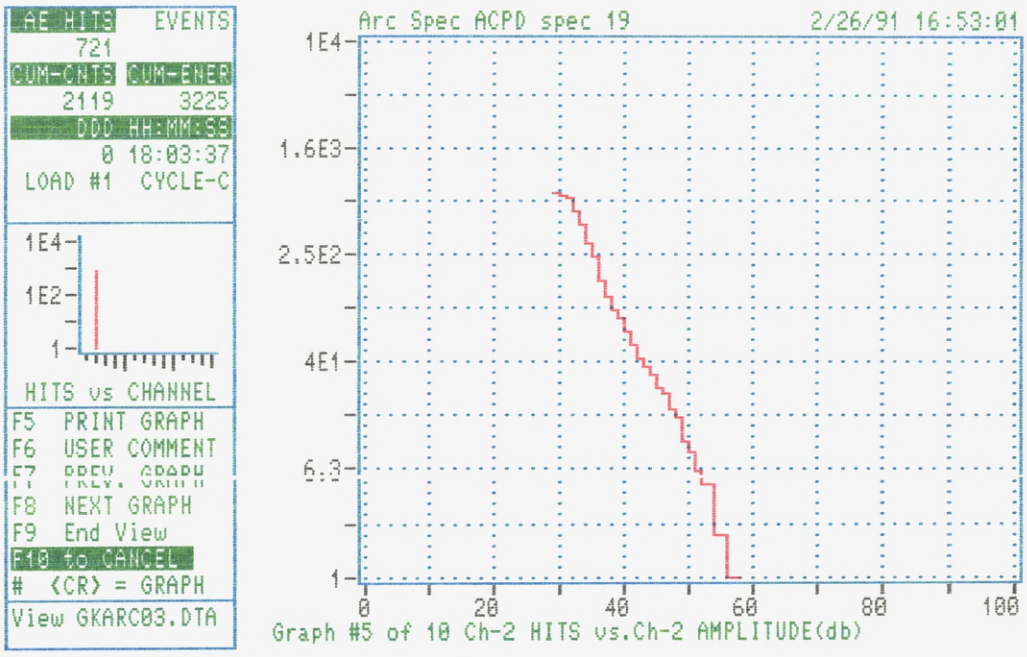
AE HITS EVENTS
721
CUM-CNTS CUM-ENER
2119 3225
DDD HH:MM:SS
0 18:03:37
LOAD #1 CYCLE-C
1E4
1E2
1
HITS vs CHANNEL
F5 PRINT GRAPH
F6 USER COMMENT
F7 PREV. GRAPH
F8 NEXT GRAPH
F9 End View
F10 to CANCEL
<CR> = GRAPH
View GKARC03.DTA
Arc Spec ACPD spec 19
2/26/91 16:53:01
1E4
1.6E3
2.5E2
4E1
6.3
1
0
20
40
60
80
100
Graph #5 of 10 Ch-2 HITS vs.Ch-2 AMPLITUDE(db)

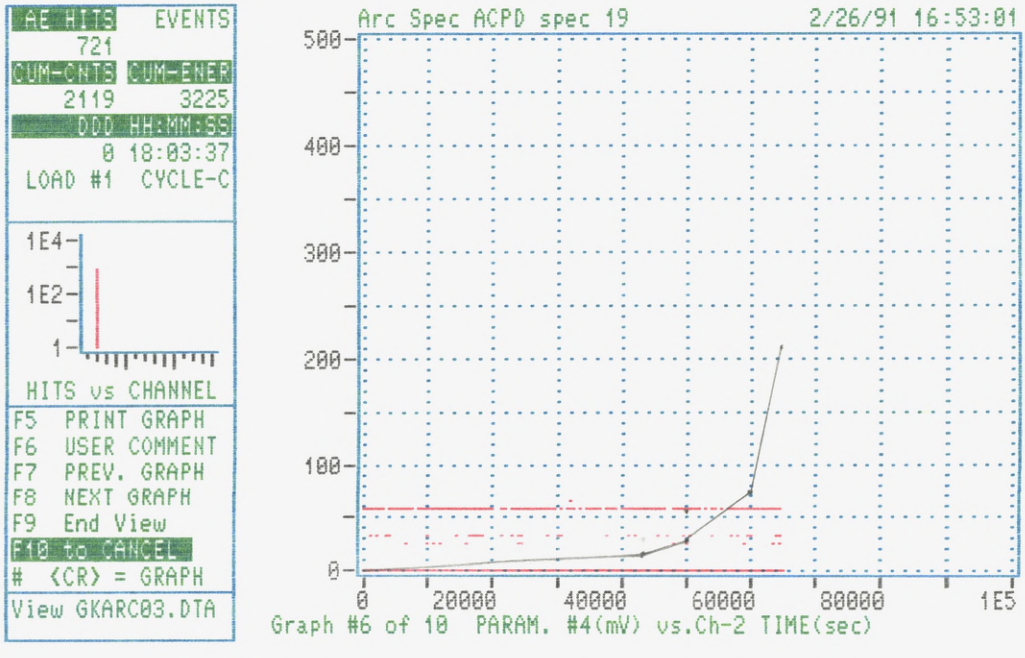
AE HITS EVENTS
721
CUM-CNTS CUM-ENER
2119 3225
DDD HH:MM:SS
0 18:03:37
LOAD #1 CYCLE-C
1E4
1E2
1
HITS vs CHANNEL
F5 PRINT GRAPH
F6 USER COMMENT
F7 PREV. GRAPH
F8 NEXT GRAPH
F9 End View
F10 to CANCEL
<CR> = GRAPH
View GKARC03.DTA
Arc Spec ACPD spec 19
2/26/91 16:53:01
500
400
300
200
100
0
0
20000
40000
60000
80000
1E5
Graph #6 of 10 PARAM. #4(mV) vs.Ch-2 TIME(sec)

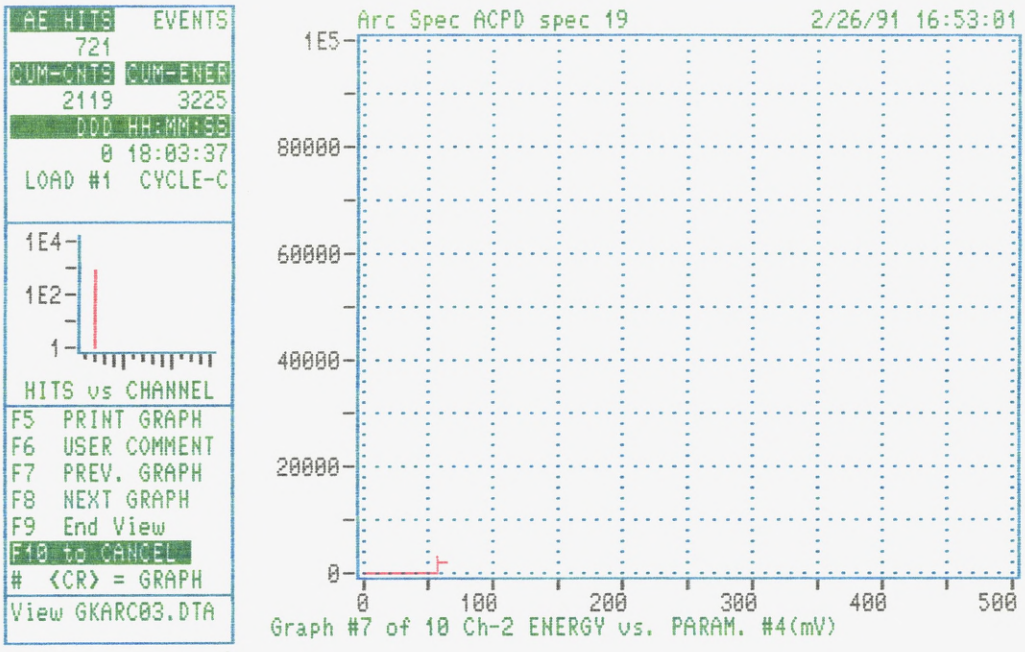
AE HITS
EVENTS
721
CUM-CNTS
CUM-ENER
2119
3225
DDD HH:MM:SS
0 18:03:37
LOAD #1 CYCLE-C
1E4
1E2
1
HITS vs CHANNEL
F5 PRINT GRAPH
F6 USER COMMENT
F7 PREV. GRAPH
F8 NEXT GRAPH
F9 End View
F10 to CANCEL
<CR> = GRAPH
View GKARC03.DTA
Arc Spec ACPD spec 19
2/26/91 16:53:01
1E5
80000
60000
40000
20000
0
0
100
200
300
400
500
Graph #7 of 10 Ch-2 ENERGY vs. PARAM. #4(mV)

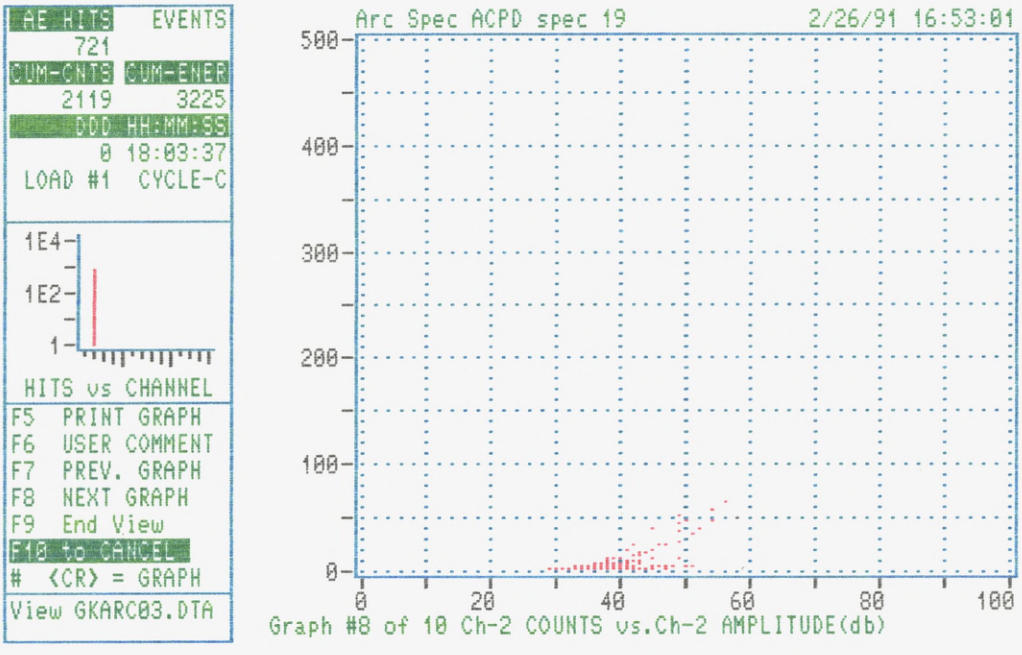
AE HITS
EVENTS
721
CUM-CNTS
CUM-ENER
2119
3225
DDD HH:MM:SS
0 18:03:37
LOAD #1 CYCLE-C
1E4
1E2
1
HITS vs CHANNEL
F5 PRINT GRAPH
F6 USER COMMENT
F7 PREV. GRAPH
F8 NEXT GRAPH
F9 End View
F10 to CANCEL
<CR> = GRAPH
View GKARC03.DTA
Arc Spec ACPD spec 19
2/26/91 16:53:01
500
400
300
200
100
0
0
20
40
60
80
100
Graph #8 of 10 Ch-2 COUNTS vs.Ch-2 AMPLITUDE(db)

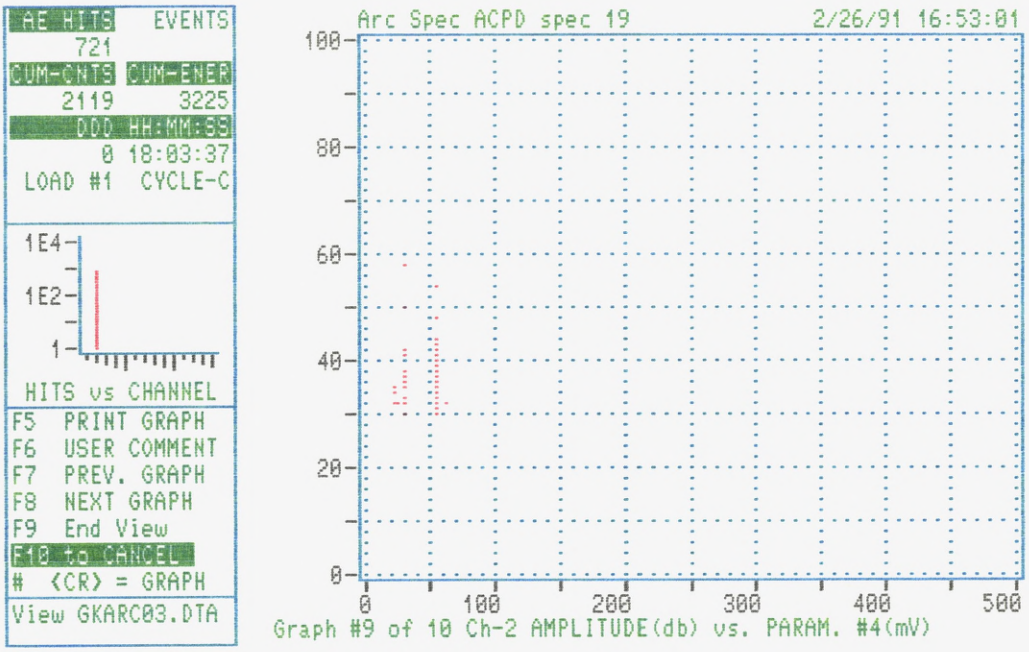
AE HITS
EVENTS
721
CUM-CNTS
CUM-ENER
2119
3225
DDD HH:MM:SS
0 18:03:37
LOAD #1 CYCLE-C
1E4
1E2
1
HITS vs CHANNEL
F5 PRINT GRAPH
F6 USER COMMENT
F7 PREV. GRAPH
F8 NEXT GRAPH
F9 End View
F10 to CANCEL
<CR> = GRAPH
View GKARC03.DTA
Arc Spec ACPD spec 19
2/26/91 16:53:01
100
80
60
40
20
0
0
100
200
300
400
500
Graph #9 of 10 Ch-2 AMPLITUDE(db) vs. PARAM. #4(mV)

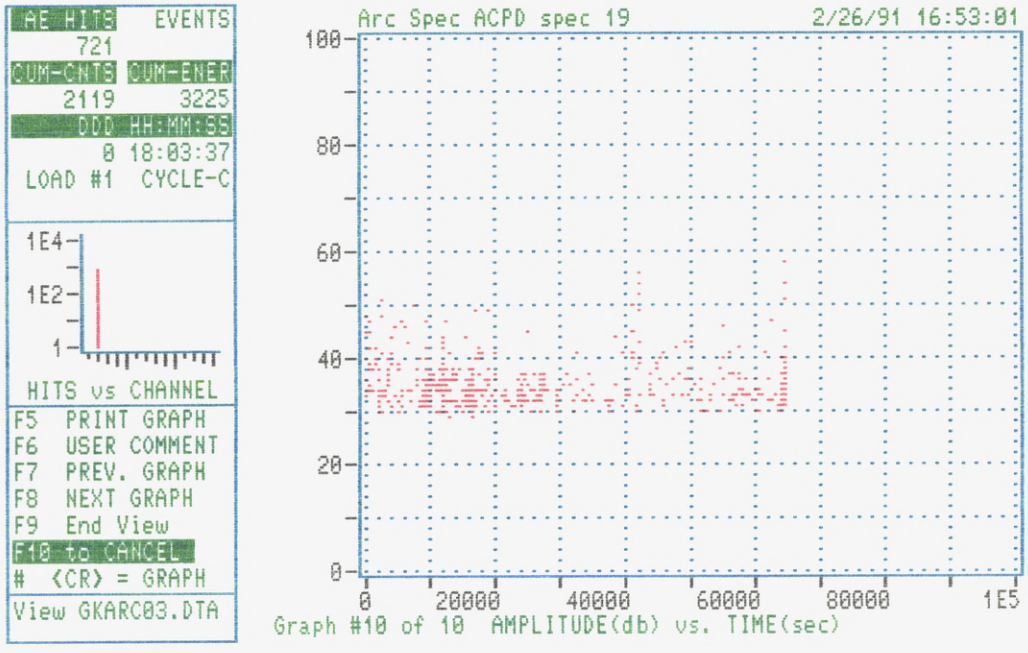
AE HITS
EVENTS
721
CUM-CNTS
CUM-ENER
2119
3225
DDD HH:MM:SS
0 18:03:37
LOAD #1 CYCLE-C
1E4
1E2
1
HITS vs CHANNEL
F5 PRINT GRAPH
F6 USER COMMENT
F7 PREV. GRAPH
F8 NEXT GRAPH
F9 End View
F10 to CANCEL
<CR> = GRAPH
View GKARC03.DTA
Arc Spec ACPD spec 19
2/26/91 16:53:01
100
80
60
40
20
0
0
20000
40000
60000
80000
1E5
Graph #10 of 10 AMPLITUDE(db) vs. TIME(sec)

0.1 Hz

Expanded time scale

AE HITS 505 EVENTS
CUM-CNTS 1065 CUM-ENER 1977
DDD HH:MM:SS
0 08:02:51
LOAD #1 CYCLE-C

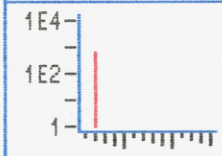

F5 PRINT GRAPH
F6 USER COMMENT
F7 PREV. GRAPH
F8 NEXT GRAPH
F9 Resume
F10 to CANCEL
<CR> = GRAPH
Replay Start

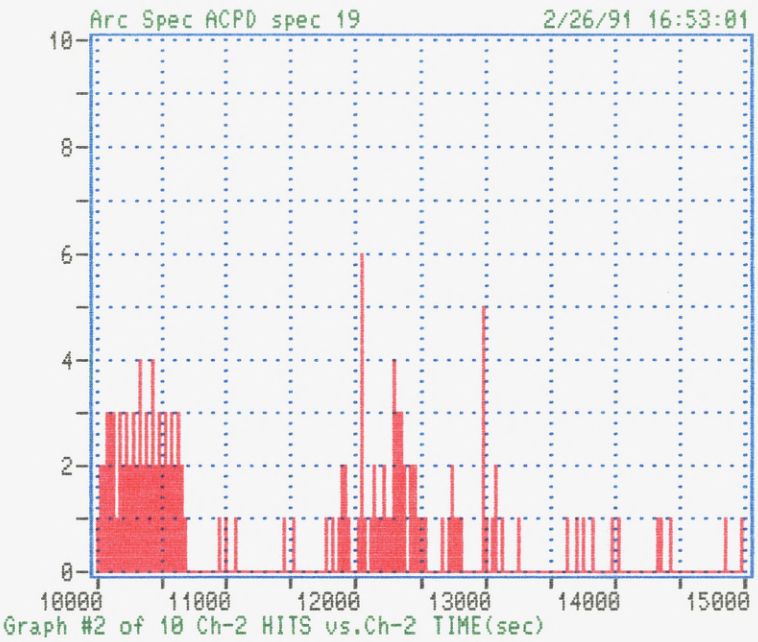

AE HITS 531 EVENTS
CUM-CNTS 1111 CUM-ENER 2056
DDD HH:MM:SS
0 09:24:20
LOAD #1 CYCLE-C

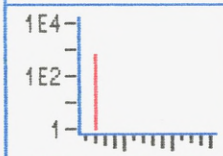

F5 PRINT GRAPH
F6 USER COMMENT
F7 PREV. GRAPH
F8 NEXT GRAPH
F9 Resume
F10 to CANCEL
<CR> = GRAPH
Replay Start

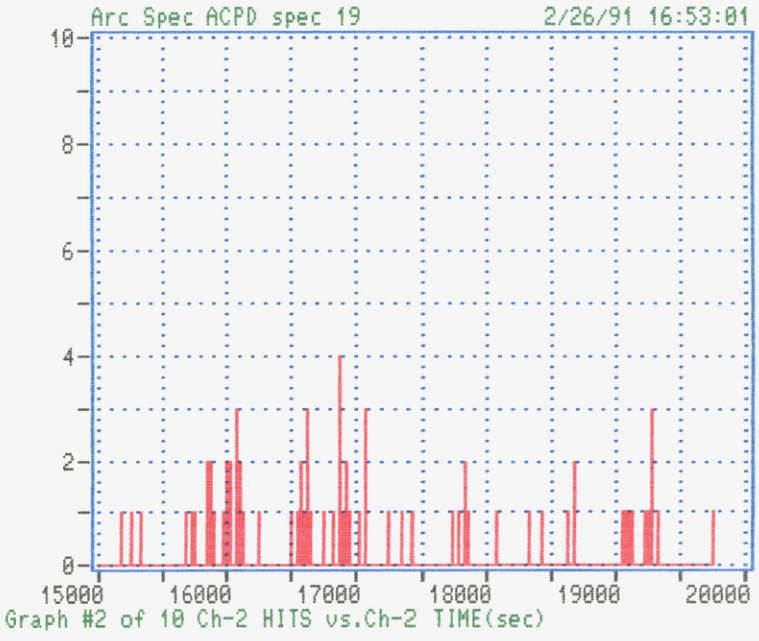

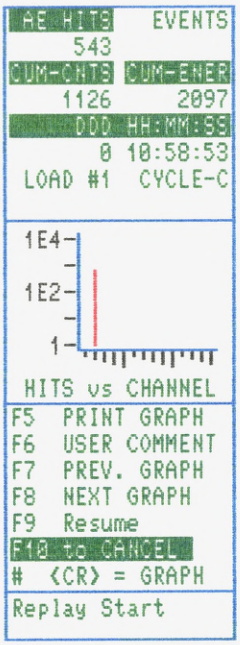
AE HITS EVENTS
543
CUM-CNTS CUM-ENER
1126 2097
DDD HH:MM:SS
0 10:58:53
LOAD #1 CYCLE-C
1E4
1E2
1
HITS vs CHANNEL
F5 PRINT GRAPH
F6 USER COMMENT
F7 PREV. GRAPH
F8 NEXT GRAPH
F9 Resume
F10 to CANCEL
<CR> = GRAPH
Replay Start

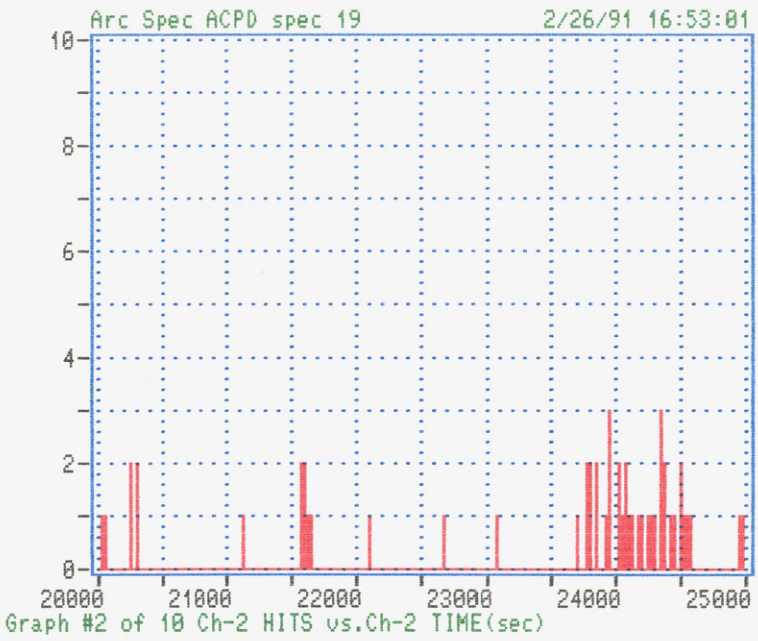
Arc Spec ACPD spec 19
2/26/91 16:53:01
10
8
6
4
2
0
20000
21000
22000
23000
24000
25000
Graph #2 of 10 Ch-2 HITS vs.Ch-2 TIME(sec)

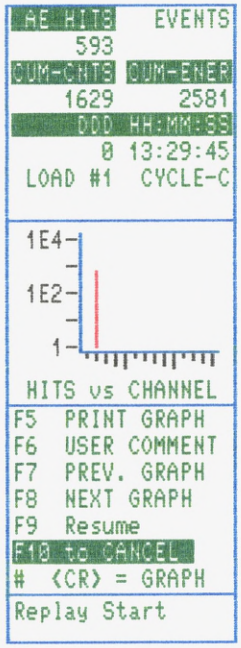
AE HITS EVENTS
593
CUM-CNTS CUM-ENER
1629 2581
DDD HH:MM:SS
0 13:29:45
LOAD #1 CYCLE-C
1E4
1E2
1
HITS vs CHANNEL
F5 PRINT GRAPH
F6 USER COMMENT
F7 PREV. GRAPH
F8 NEXT GRAPH
F9 Resume
F10 to CANCEL
<CR> = GRAPH
Replay Start

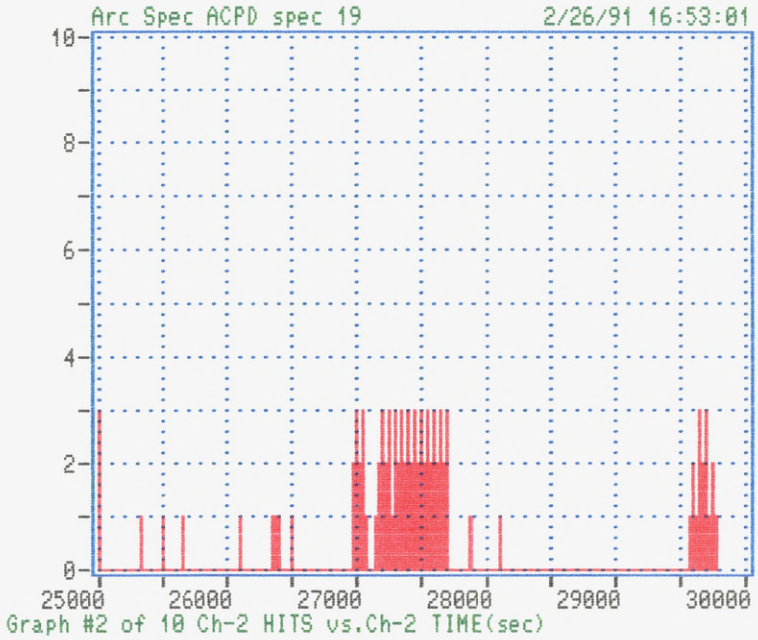
Arc Spec ACPD spec 19
2/26/91 16:53:01
10
8
6
4
2
0
25000
26000
27000
28000
29000
30000
Graph #2 of 10 Ch-2 HITS vs.Ch-2 TIME(sec)

AE HITS EVENTS
647
CUM-CNTS CUM-ENER
1746 2807
DDD HH:MM:SS
0 17:04:00
LOAD #1 CYCLE-C

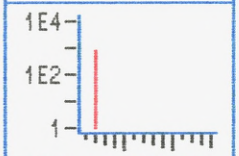

F5 PRINT GRAPH
F6 USER COMMENT
F7 PREV. GRAPH
F8 NEXT GRAPH
F9 Resume
F10 to CANCEL
<CR> = GRAPH

Replay Start

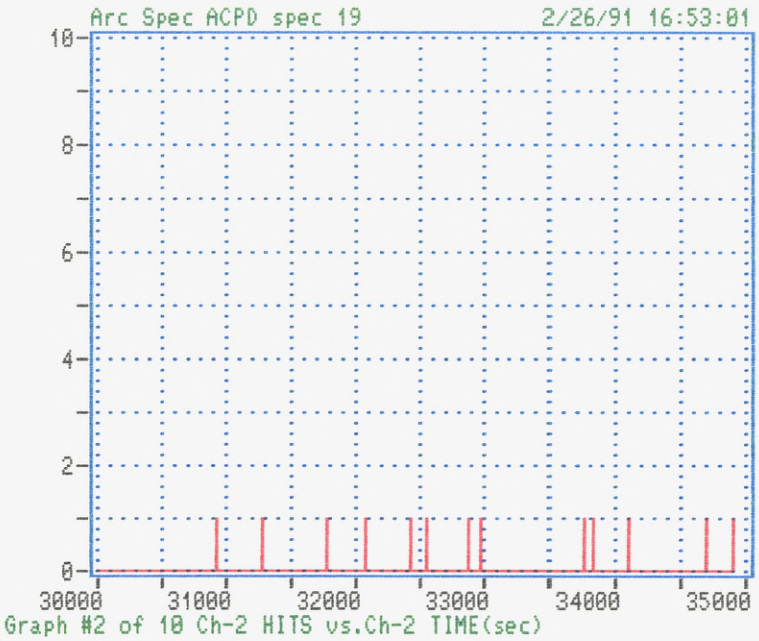

AE HITS EVENTS
721
CUM-CNTS CUM-ENER
2119 3225
DDD HH:MM:SS
0 18:03:37
LOAD #1 CYCLE-C

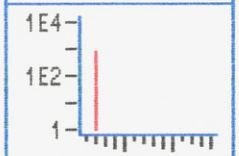

F5 PRINT GRAPH
F6 USER COMMENT
F7 PREV. GRAPH
F8 NEXT GRAPH
F10 Stop
F10 to CANCEL
<CR> = GRAPH

Replay END

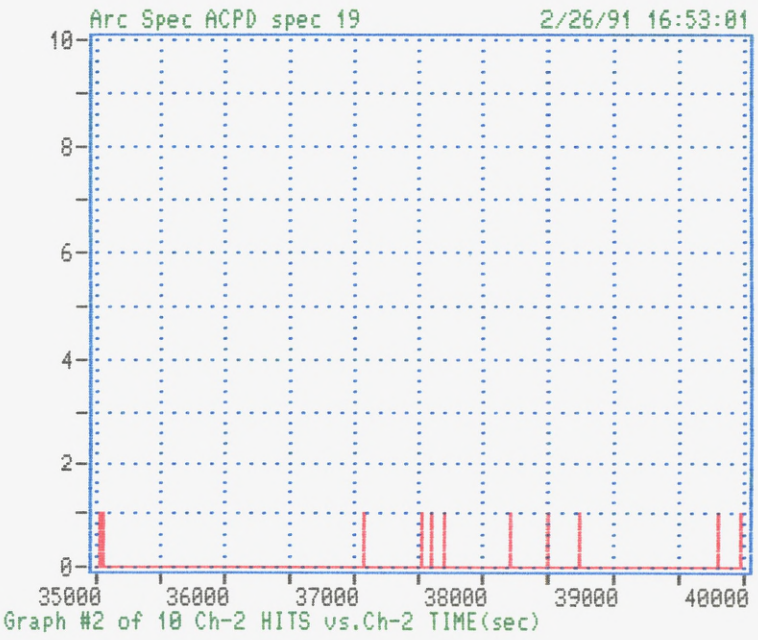

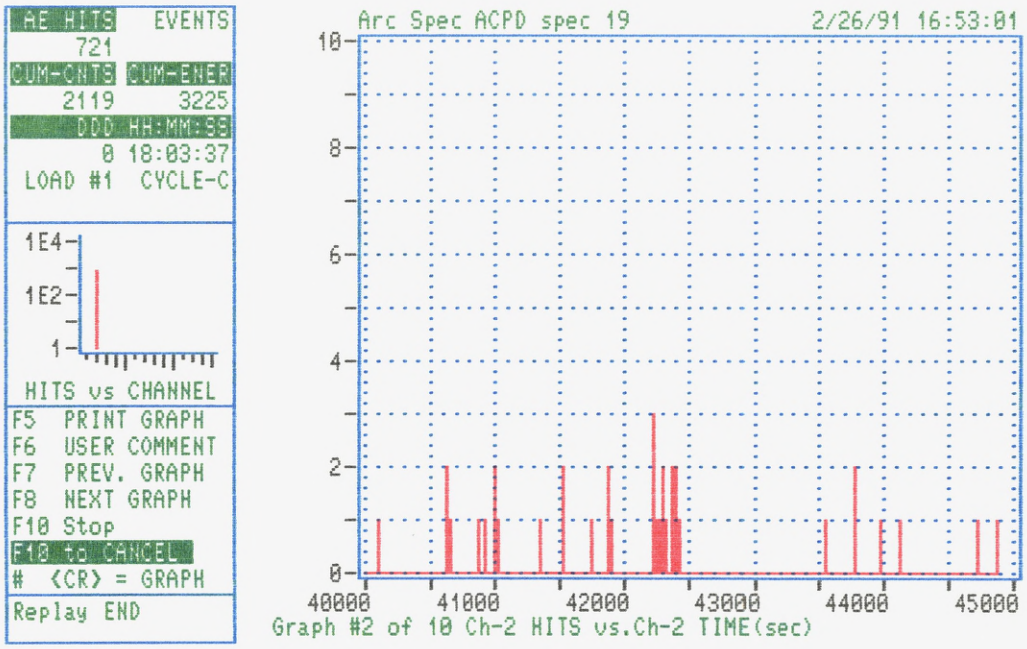
AE HITS
EVENTS
721
CUM-CNTS
CUM-ENER
2119
3225
DDD HH:MM:SS
0 18:03:37
LOAD #1 CYCLE-C
1E4
1E2
1
HITS vs CHANNEL
F5 PRINT GRAPH
F6 USER COMMENT
F7 PREV. GRAPH
F8 NEXT GRAPH
F10 Stop
F10 to CANCEL
<CR> = GRAPH
Replay END
Arc Spec ACPD spec 19
2/26/91 16:53:01
10
8
6
4
2
0
40000
41000
42000
43000
44000
45000
Graph #2 of 10 Ch-2 HITS vs.Ch-2 TIME(sec)

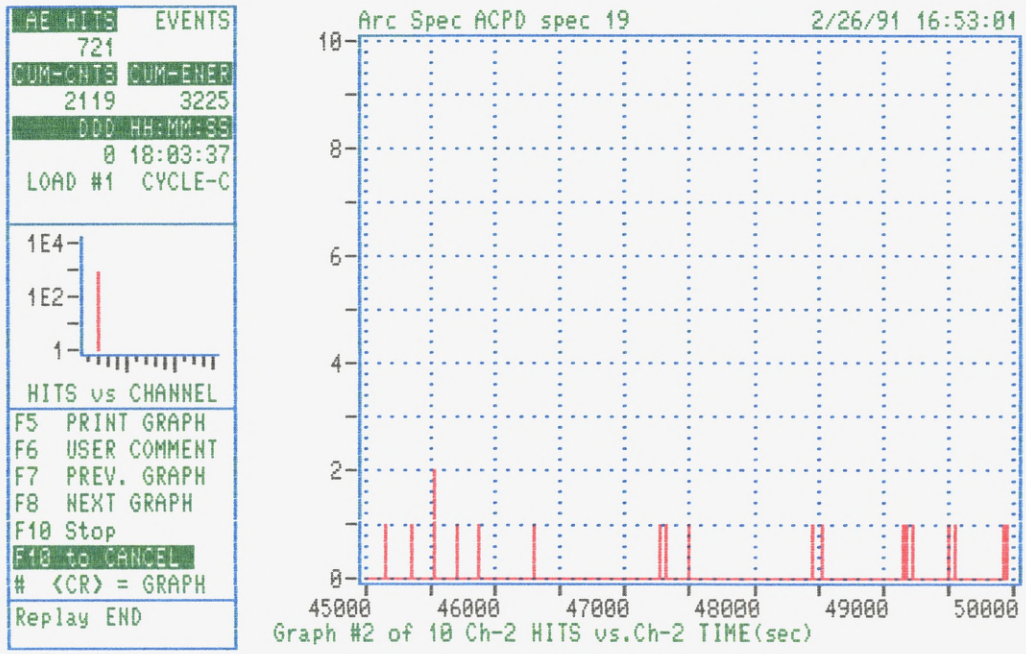
AE HITS
EVENTS
721
CUM-CNTS
CUM-ENER
2119
3225
DDD HH:MM:SS
0 18:03:37
LOAD #1 CYCLE-C
1E4
1E2
1
HITS vs CHANNEL
F5 PRINT GRAPH
F6 USER COMMENT
F7 PREV. GRAPH
F8 NEXT GRAPH
F10 Stop
F10 to CANCEL
<CR> = GRAPH
Replay END
Arc Spec ACPD spec 19
2/26/91 16:53:01
10
8
6
4
2
0
45000
46000
47000
48000
49000
50000
Graph #2 of 10 Ch-2 HITS vs.Ch-2 TIME(sec)

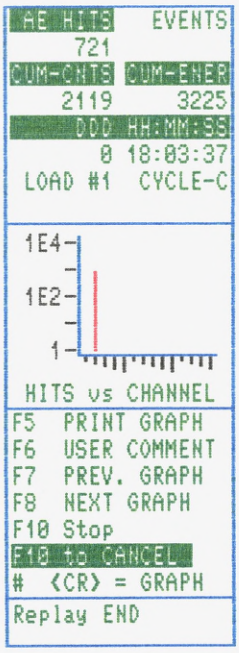
AE HITS
EVENTS
721
CUM-CNTS
CUM-ENER
2119
3225
DDD HH:MM:SS
0 18:03:37
LOAD #1 CYCLE-C
1E4
1E2
1
HITS vs CHANNEL
F5 PRINT GRAPH
F6 USER COMMENT
F7 PREV. GRAPH
F8 NEXT GRAPH
F10 Stop
F10 to CANCEL
<CR> = GRAPH
Replay END

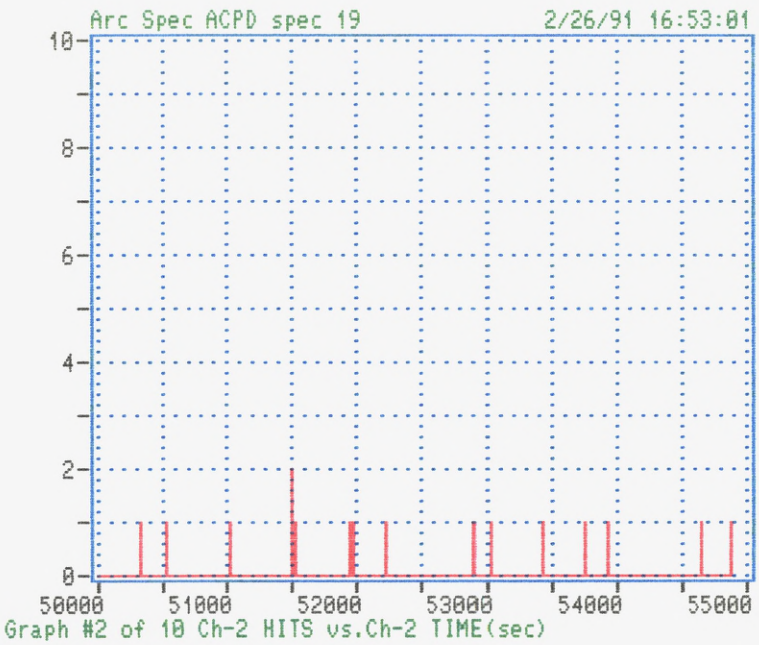
Arc Spec ACPD spec 19
2/26/91 16:53:01
10
8
6
4
2
0
50000
51000
52000
53000
54000
55000
Graph #2 of 10 Ch-2 HITS vs.Ch-2 TIME(sec)

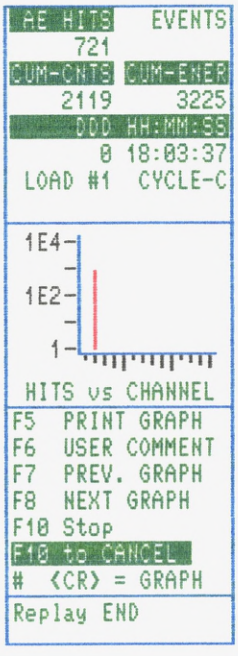
AE HITS
EVENTS
721
CUM-CNTS
CUM-ENER
2119
3225
DDD HH:MM:SS
0 18:03:37
LOAD #1 CYCLE-C
1E4
1E2
1
HITS vs CHANNEL
F5 PRINT GRAPH
F6 USER COMMENT
F7 PREV. GRAPH
F8 NEXT GRAPH
F10 Stop
F10 to CANCEL
<CR> = GRAPH
Replay END

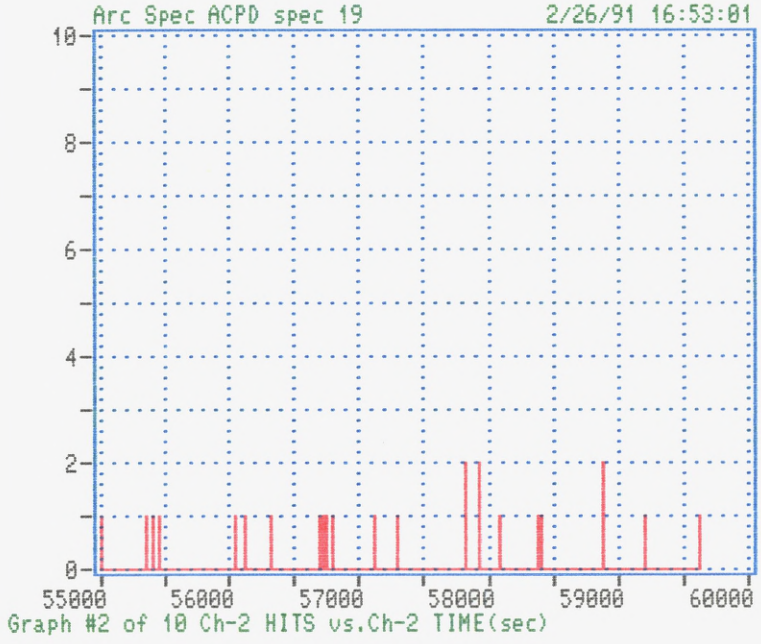
Arc Spec ACPD spec 19
2/26/91 16:53:01
10
8
6
4
2
0
55000
56000
57000
58000
59000
60000
Graph #2 of 10 Ch-2 HITS vs.Ch-2 TIME(sec)

0.1 Hz

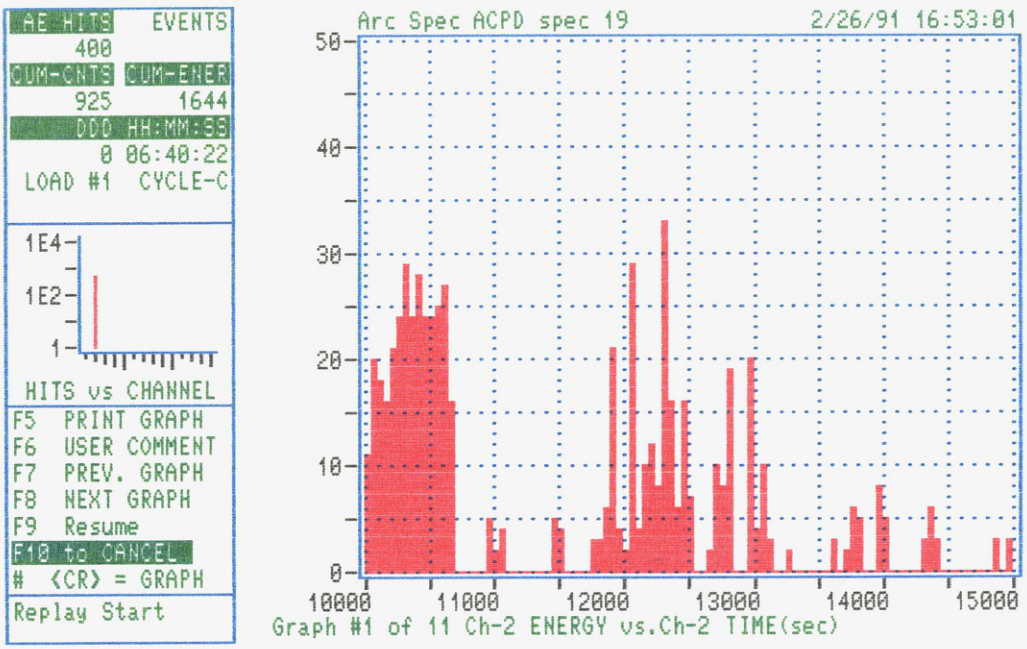
AE HITS EVENTS
400
CUM-CNTS CUM-ENER
925 1644
DDD HH:MM:SS
0 06:40:22
LOAD #1 CYCLE-C
1E4
1E2
1
HITS vs CHANNEL
F5 PRINT GRAPH
F6 USER COMMENT
F7 PREV. GRAPH
F8 NEXT GRAPH
F9 Resume
F10 to CANCEL
<CR> = GRAPH
Replay Start
Arc Spec ACPD spec 19
2/26/91 16:53:01
50
40
30
20
10
0
10000
11000
12000
13000
14000
15000
Graph #1 of 11 Ch-2 ENERGY vs.Ch-2 TIME(sec)

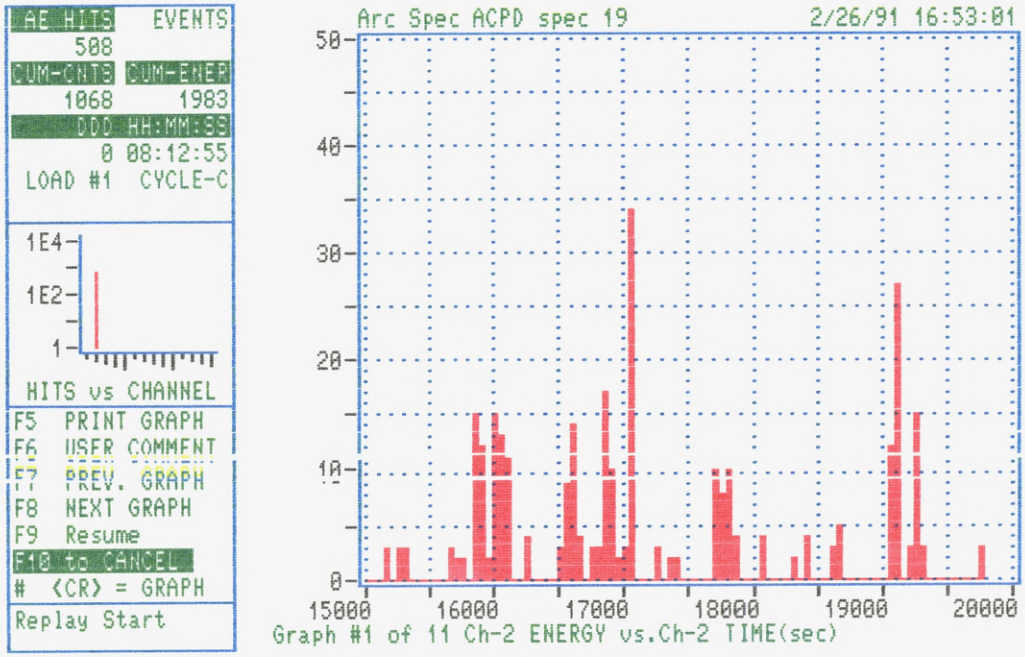
AE HITS EVENTS
508
CUM-CNTS CUM-ENER
1068 1983
DDD HH:MM:SS
0 08:12:55
LOAD #1 CYCLE-C
1E4
1E2
1
HITS vs CHANNEL
F5 PRINT GRAPH
F6 USER COMMENT
F7 PREV. GRAPH
F8 NEXT GRAPH
F9 Resume
F10 to CANCEL
<CR> = GRAPH
Replay Start
Arc Spec ACPD spec 19
2/26/91 16:53:01
50
40
30
20
10
0
15000
16000
17000
18000
19000
20000
Graph #1 of 11 Ch-2 ENERGY vs.Ch-2 TIME(sec)

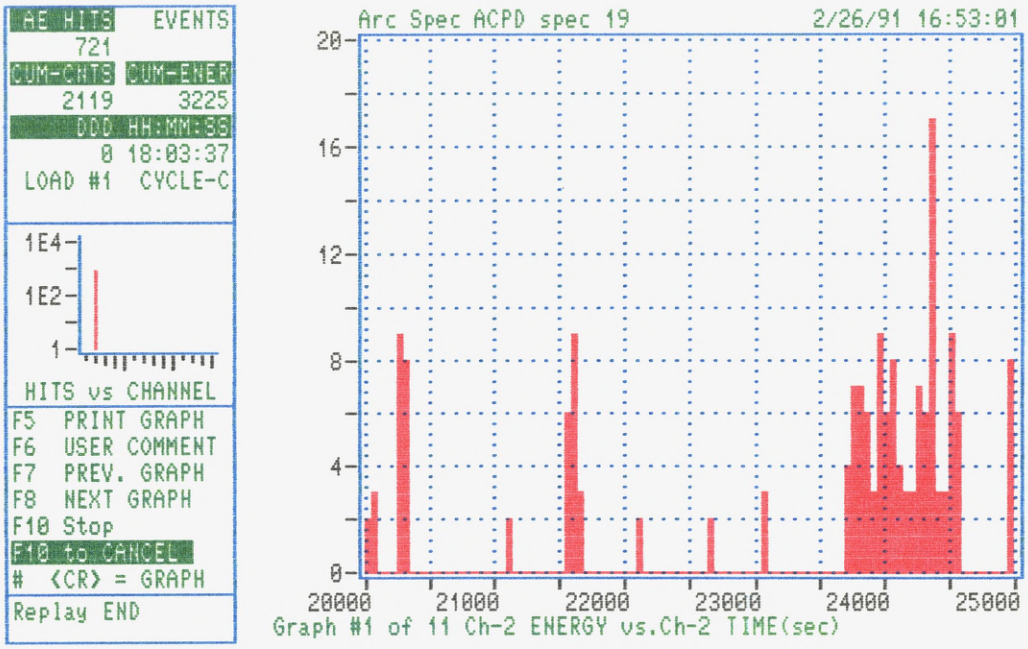
AE HITS EVENTS
721
CUM-CNTS CUM-ENER
2119 3225
DDD HH:MM:SS
0 18:03:37
LOAD #1 CYCLE-C
1E4
1E2
1
HITS vs CHANNEL
F5 PRINT GRAPH
F6 USER COMMENT
F7 PREV. GRAPH
F8 NEXT GRAPH
F10 Stop
F10 to CANCEL
<CR> = GRAPH
Replay END
Arc Spec ACPD spec 19
2/26/91 16:53:01
20
16
12
8
4
0
20000
21000
22000
23000
24000
25000
Graph #1 of 11 Ch-2 ENERGY vs.Ch-2 TIME(sec)

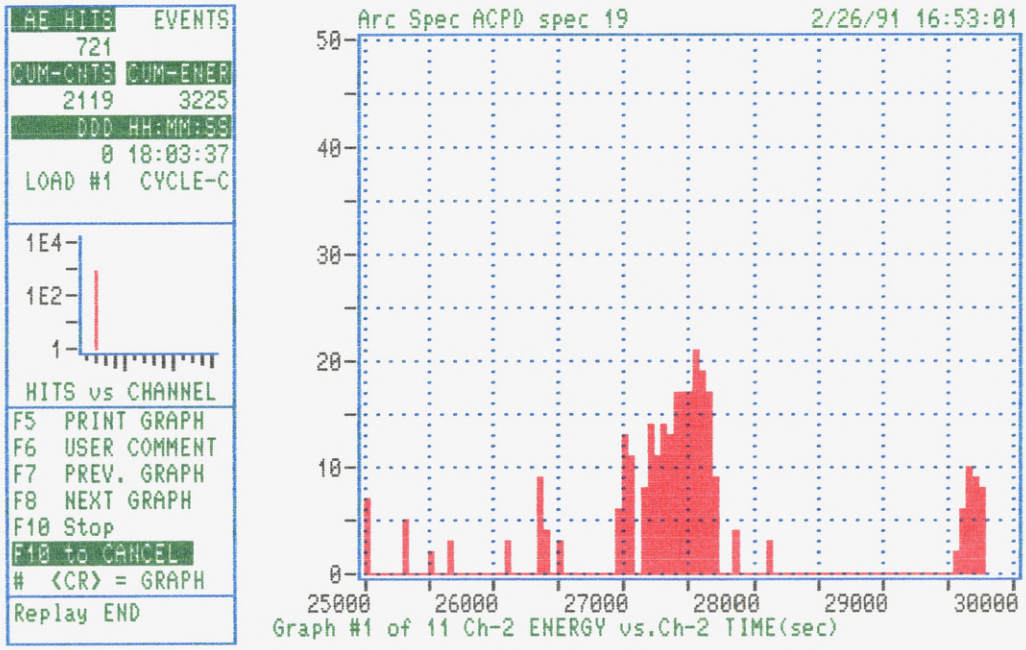
AE HITS EVENTS
721
CUM-CNTS CUM-ENER
2119 3225
DDD HH:MM:SS
0 18:03:37
LOAD #1 CYCLE-C
1E4
1E2
1
HITS vs CHANNEL
F5 PRINT GRAPH
F6 USER COMMENT
F7 PREV. GRAPH
F8 NEXT GRAPH
F10 Stop
F10 to CANCEL
<CR> = GRAPH
Replay END
Arc Spec ACPD spec 19
2/26/91 16:53:01
50
40
30
20
10
0
25000
26000
27000
28000
29000
30000
Graph #1 of 11 Ch-2 ENERGY vs.Ch-2 TIME(sec)

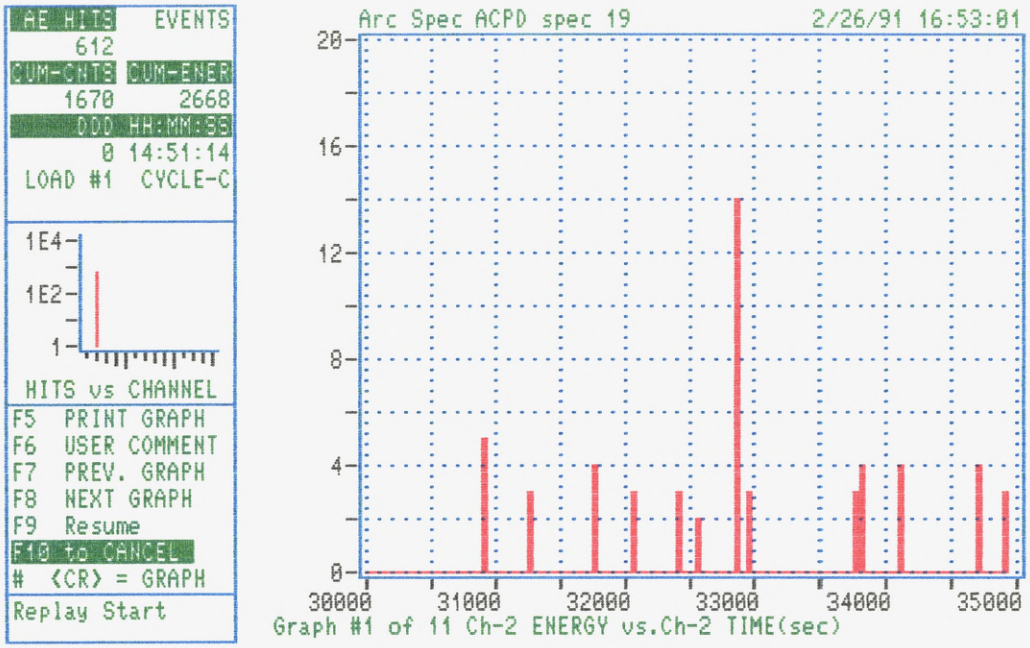
AE HITS EVENTS
612
CUM-CNTS CUM-ENER
1670 2668
DDD HH:MM:SS
0 14:51:14
LOAD #1 CYCLE-C
1E4
1E2
1
HITS vs CHANNEL
F5 PRINT GRAPH
F6 USER COMMENT
F7 PREV. GRAPH
F8 NEXT GRAPH
F9 Resume
F10 to CANCEL
<CR> = GRAPH
Replay Start
Arc Spec ACPD spec 19
2/26/91 16:53:01
20
16
12
8
4
0
30000
31000
32000
33000
34000
35000
Graph #1 of 11 Ch-2 ENERGY vs.Ch-2 TIME(sec)

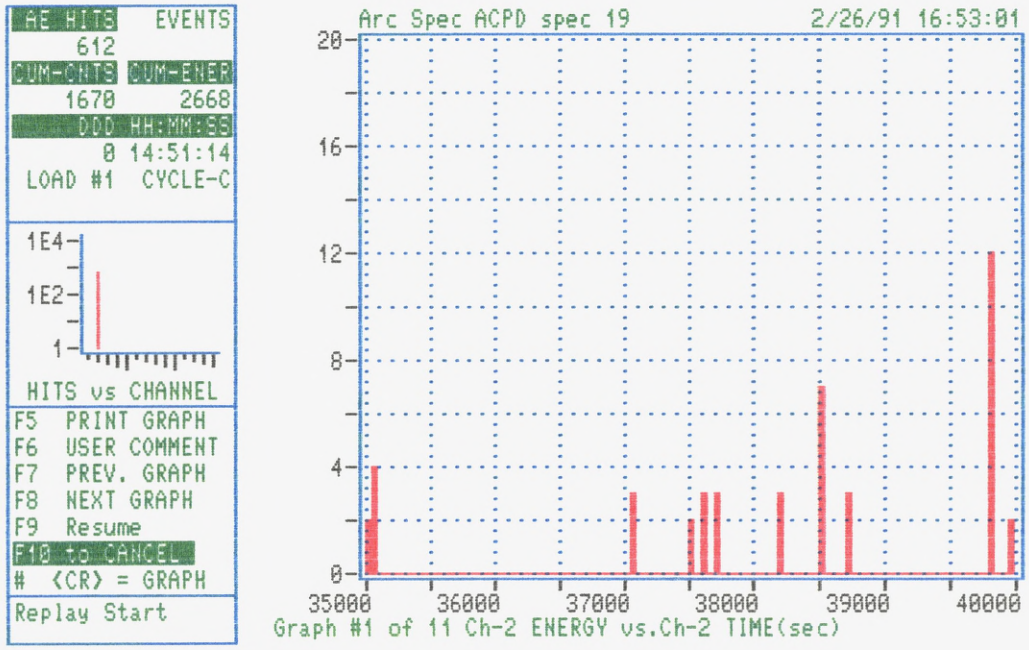
AE HITS EVENTS
612
CUM-CNTS CUM-ENER
1670 2668
DDD HH:MM:SS
0 14:51:14
LOAD #1 CYCLE-C
1E4
1E2
1
HITS vs CHANNEL
F5 PRINT GRAPH
F6 USER COMMENT
F7 PREV. GRAPH
F8 NEXT GRAPH
F9 Resume
F10 to CANCEL
<CR> = GRAPH
Replay Start
Arc Spec ACPD spec 19
2/26/91 16:53:01
20
16
12
8
4
0
35000
36000
37000
38000
39000
40000
Graph #1 of 11 Ch-2 ENERGY vs.Ch-2 TIME(sec)

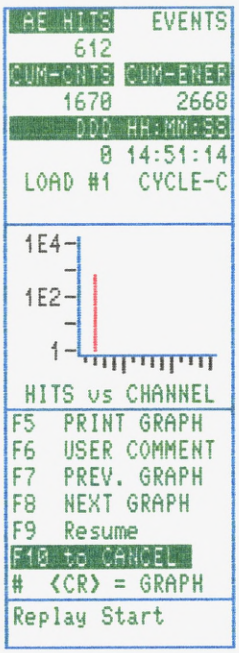
AE HITS EVENTS
612
CUM-CNTS CUM-ENER
1670 2668
DDD HH:MM:SS
0 14:51:14
LOAD #1 CYCLE-C
1E4
1E2
1
HITS vs CHANNEL
F5 PRINT GRAPH
F6 USER COMMENT
F7 PREV. GRAPH
F8 NEXT GRAPH
F9 Resume
F10 to CANCEL
<CR> = GRAPH
Replay Start

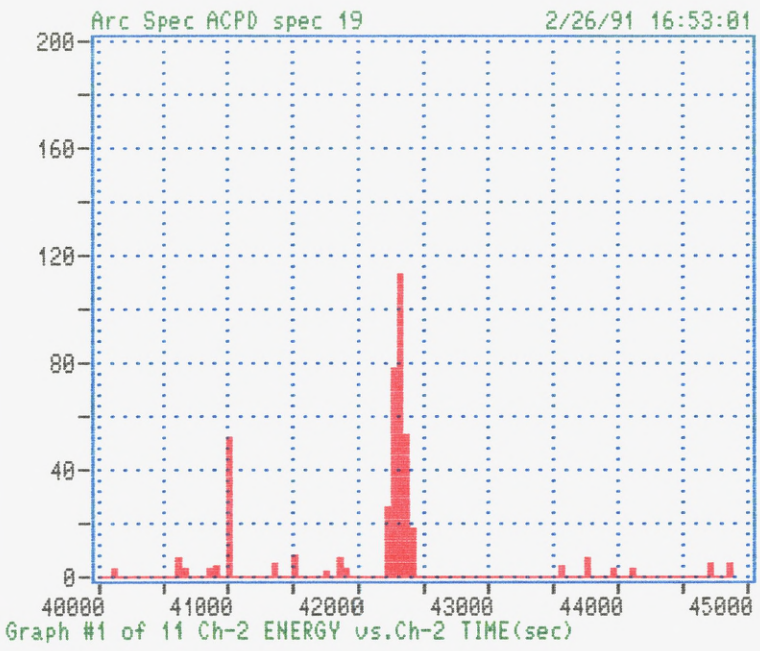
Arc Spec ACPD spec 19
2/26/91 16:53:01
200
160
120
80
40
0
40000
41000
42000
43000
44000
45000
Graph #1 of 11 Ch-2 ENERGY vs.Ch-2 TIME(sec)

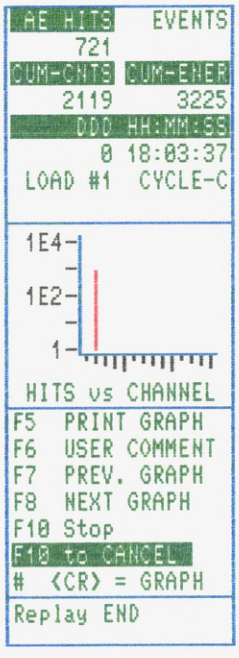
AE HITS EVENTS
721
CUM-CNTS CUM-ENER
2119 3225
DDD HH:MM:SS
0 18:03:37
LOAD #1 CYCLE-C
1E4
1E2
1
HITS vs CHANNEL
F5 PRINT GRAPH
F6 USER COMMENT
F7 PREV. GRAPH
F8 NEXT GRAPH
F10 Stop
F10 to CANCEL
<CR> = GRAPH
Replay END

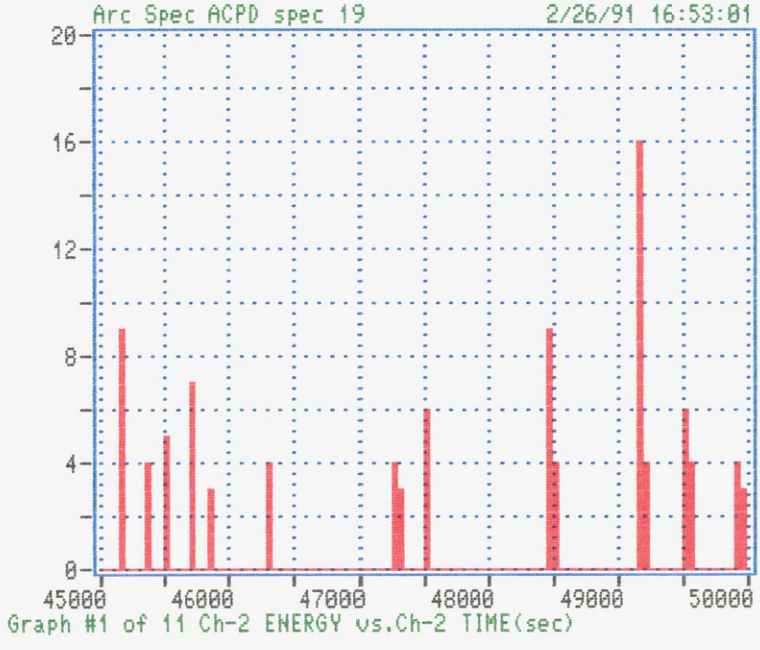
Arc Spec ACPD spec 19
2/26/91 16:53:01
20
16
12
8
4
0
45000
46000
47000
48000
49000
50000
Graph #1 of 11 Ch-2 ENERGY vs.Ch-2 TIME(sec)

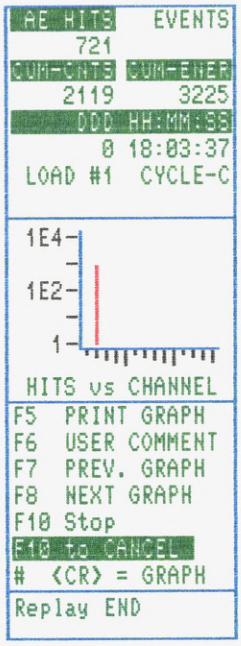
AE HITS
EVENTS
721
CUM-CNTS
CUM-ENER
2119
3225
DDD HH:MM:SS
0 18:03:37
LOAD #1 CYCLE-C
1E4
1E2
1
HITS vs CHANNEL
F5 PRINT GRAPH
F6 USER COMMENT
F7 PREV. GRAPH
F8 NEXT GRAPH
F10 Stop
F10 to CANCEL
<CR> = GRAPH
Replay END

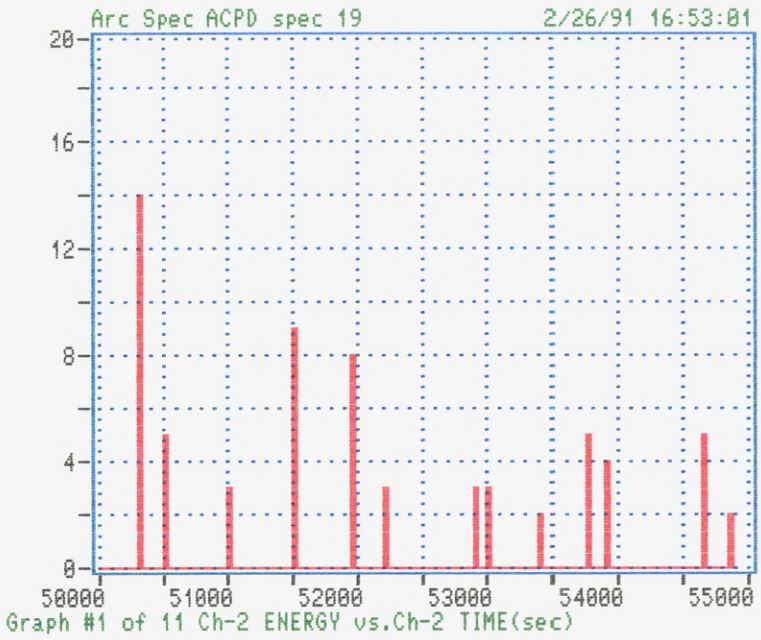
Arc Spec ACPD spec 19
2/26/91 16:53:01
20
16
12
8
4
0
50000
51000
52000
53000
54000
55000
Graph #1 of 11 Ch-2 ENERGY vs.Ch-2 TIME(sec)

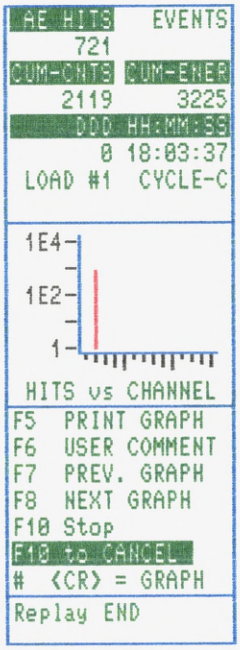
AE HITS
EVENTS
721
CUM-CNTS
CUM-ENER
2119
3225
DDD HH:MM:SS
0 18:03:37
LOAD #1 CYCLE-C
1E4
1E2
1
HITS vs CHANNEL
F5 PRINT GRAPH
F6 USER COMMENT
F7 PREV. GRAPH
F8 NEXT GRAPH
F10 Stop
F10 to CANCEL
<CR> = GRAPH
Replay END

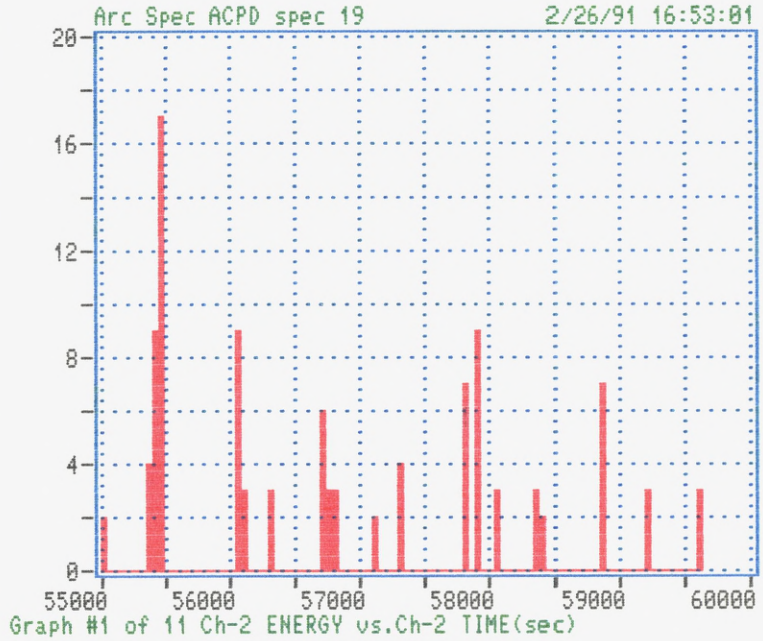
Arc Spec ACPD spec 19
2/26/91 16:53:01
20
16
12
8
4
0
55000
56000
57000
58000
59000
60000
Graph #1 of 11 Ch-2 ENERGY vs.Ch-2 TIME(sec)

0·5 Hz

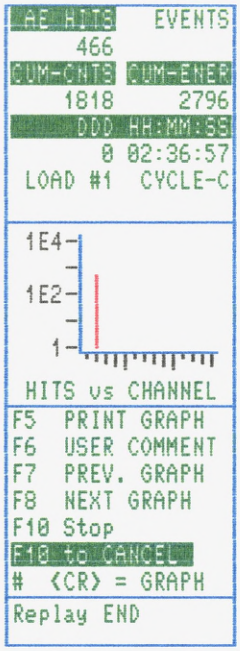
AE HITS
EVENTS
466
CUM-CNTS
CUM-ENER
1818
2796
DDD HH:MM:SS
0 02:36:57
LOAD #1 CYCLE-C
1E4
1E2
1
HITS vs CHANNEL
F5 PRINT GRAPH
F6 USER COMMENT
F7 PREV. GRAPH
F8 NEXT GRAPH
F10 Stop
F10 to CANCEL
<CR> = GRAPH
Replay END

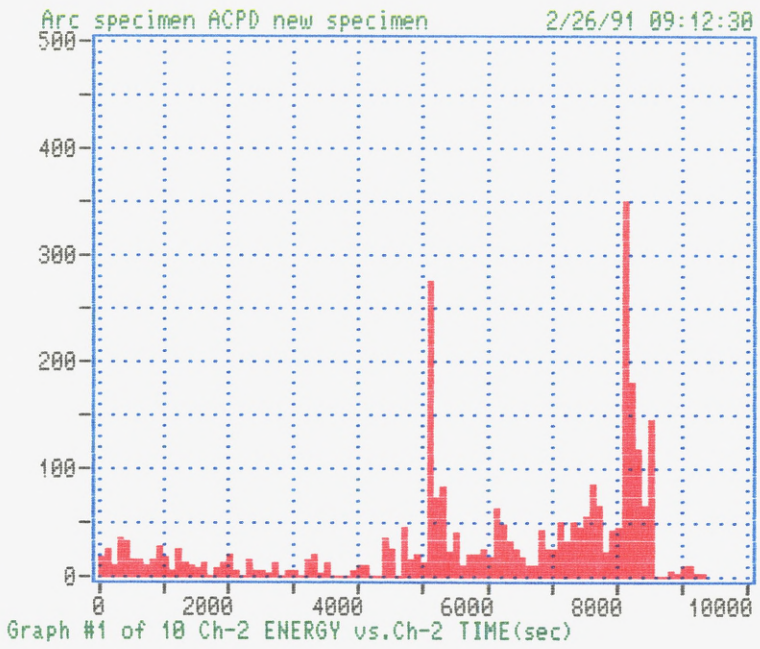
Arc specimen ACPD new specimen
2/26/91 09:12:30
500
400
300
200
100
0
0
2000
4000
6000
8000
10000
Graph #1 of 10 Ch-2 ENERGY vs.Ch-2 TIME(sec)

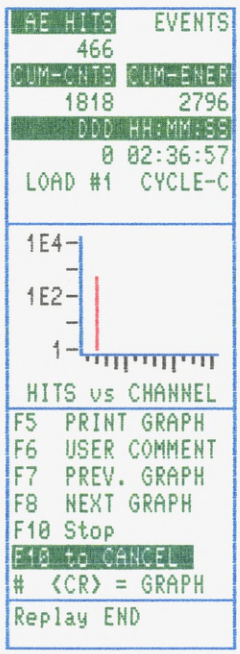
AE HITS
EVENTS
466
CUM-CNTS
CUM-ENER
1818
2796
DDD HH:MM:SS
0 02:36:57
LOAD #1 CYCLE-C
1E4
1E2
1
HITS vs CHANNEL
F5 PRINT GRAPH
F6 USER COMMENT
F7 PREV. GRAPH
F8 NEXT GRAPH
F10 Stop
F10 to CANCEL
<CR> = GRAPH
Replay END

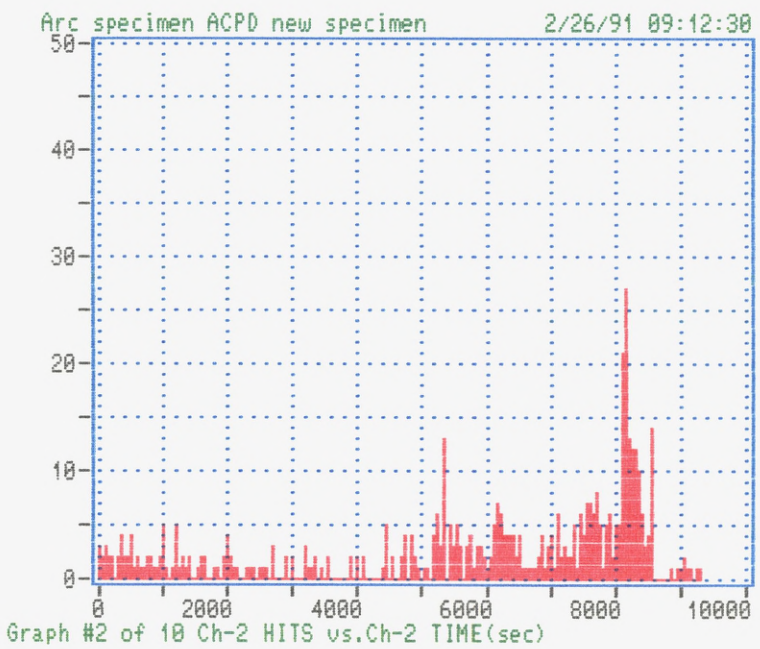
Arc specimen ACPD new specimen
2/26/91 09:12:30
50
40
30
20
10
0
0
2000
4000
6000
8000
10000
Graph #2 of 10 Ch-2 HITS vs.Ch-2 TIME(sec)

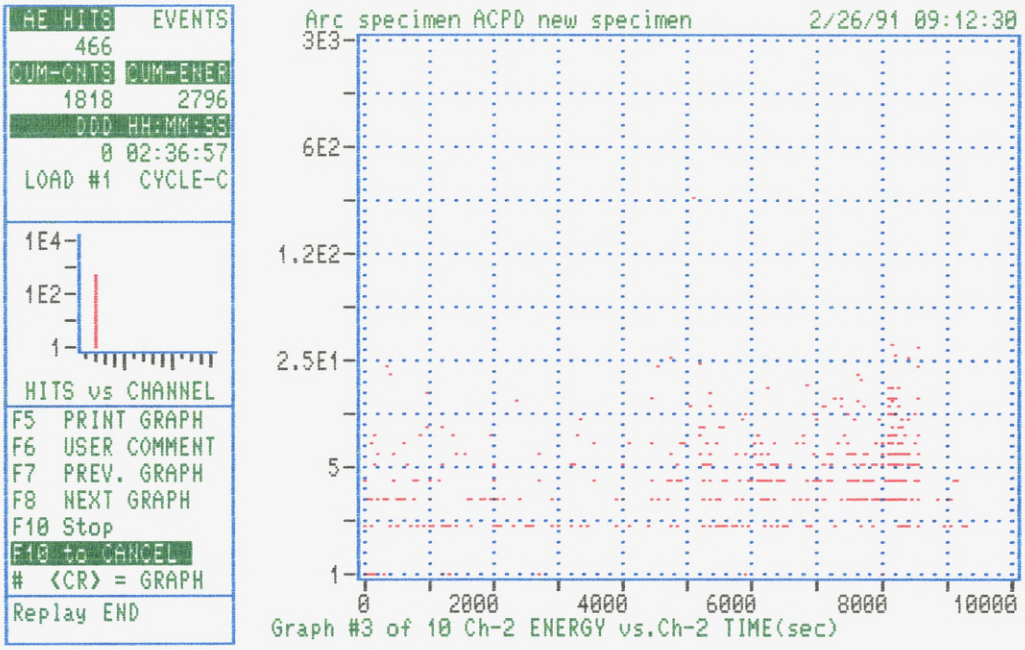
AE HITS EVENTS
466
CUM-CNTS CUM-ENER
1818 2796
DDD HH:MM:SS
0 02:36:57
LOAD #1 CYCLE-C
1E4
1E2
1
HITS vs CHANNEL
F5 PRINT GRAPH
F6 USER COMMENT
F7 PREV. GRAPH
F8 NEXT GRAPH
F10 Stop
F10 to CANCEL
<CR> = GRAPH
Replay END
Arc specimen ACPD new specimen
2/26/91 09:12:30
3E3
6E2
1.2E2
2.5E1
5
1
0
2000
4000
6000
8000
10000
Graph #3 of 10 Ch-2 ENERGY vs.Ch-2 TIME(sec)

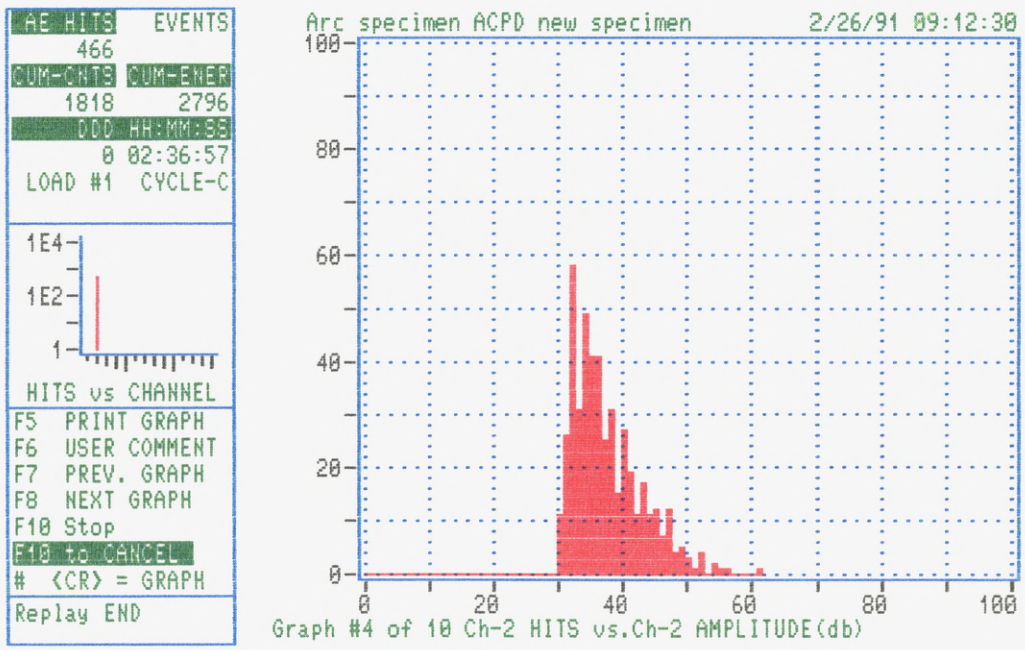
AE HITS EVENTS
466
CUM-CNTS CUM-ENER
1818 2796
DDD HH:MM:SS
0 02:36:57
LOAD #1 CYCLE-C
1E4
1E2
1
HITS vs CHANNEL
F5 PRINT GRAPH
F6 USER COMMENT
F7 PREV. GRAPH
F8 NEXT GRAPH
F10 Stop
F10 to CANCEL
<CR> = GRAPH
Replay END
Arc specimen ACPD new specimen
2/26/91 09:12:30
100
80
60
40
20
0
0
20
40
60
80
100
Graph #4 of 10 Ch-2 HITS vs.Ch-2 AMPLITUDE(db)

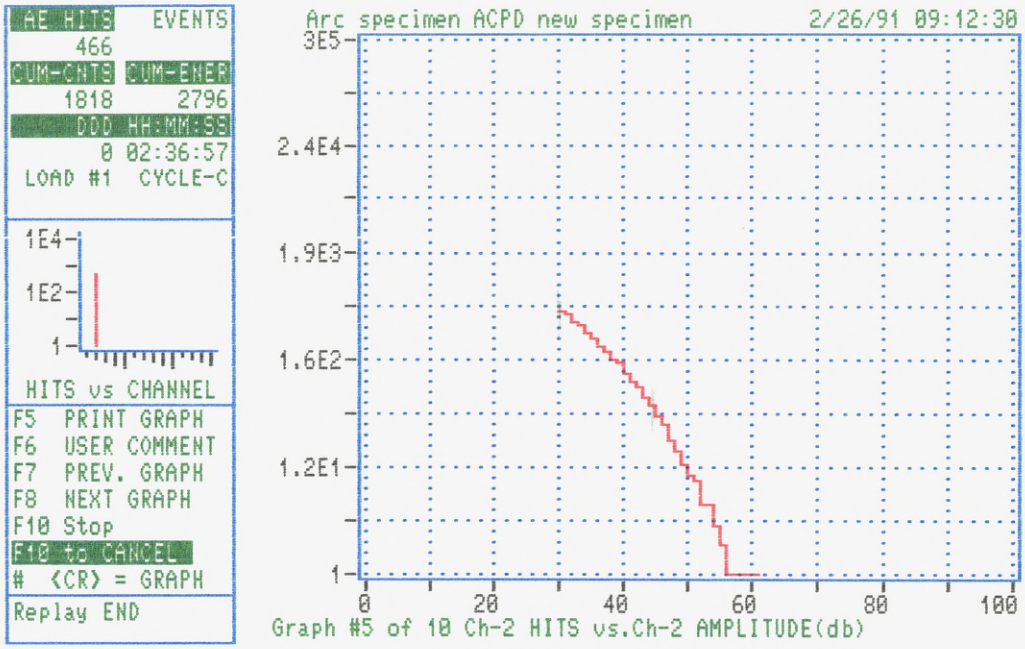
AE HITS
EVENTS
466
CUM-CNTS
CUM-ENER
1818
2796
DDD HH:MM:SS
0 02:36:57
LOAD #1 CYCLE-C
1E4
1E2
1
HITS vs CHANNEL
F5 PRINT GRAPH
F6 USER COMMENT
F7 PREV. GRAPH
F8 NEXT GRAPH
F10 Stop
F10 to CANCEL
<CR> = GRAPH
Replay END
Arc specimen ACPD new specimen
2/26/91 09:12:30
3E5
2.4E4
1.9E3
1.6E2
1.2E1
1
0
20
40
60
80
100
Graph #5 of 10 Ch-2 HITS vs.Ch-2 AMPLITUDE(db)

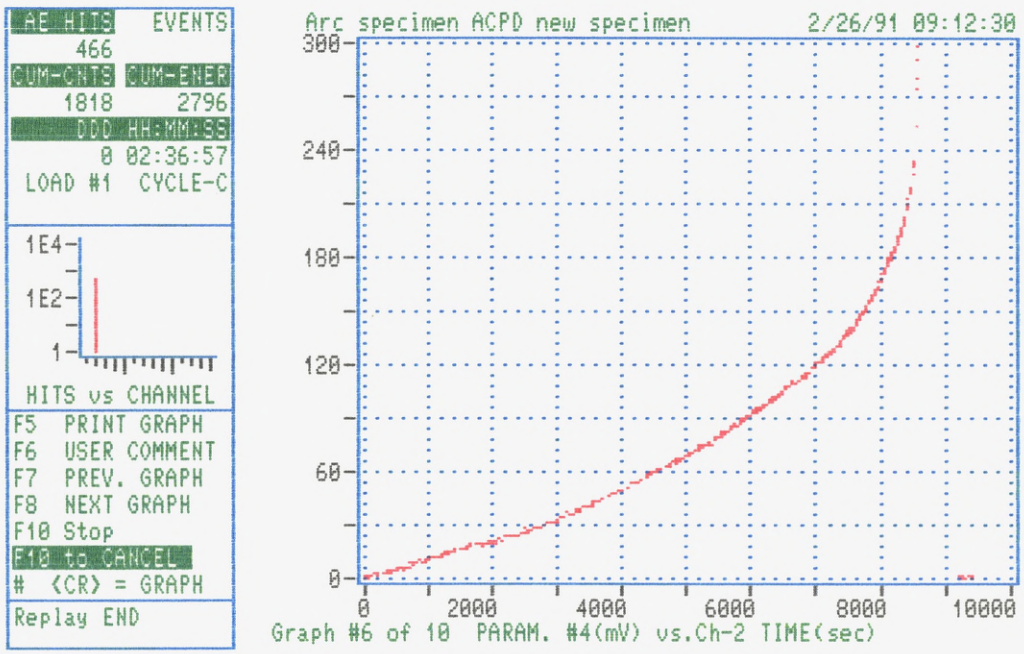
AE HITS
EVENTS
466
CUM-CNTS
CUM-ENER
1818
2796
DDD HH:MM:SS
0 02:36:57
LOAD #1 CYCLE-C
1E4
1E2
1
HITS vs CHANNEL
F5 PRINT GRAPH
F6 USER COMMENT
F7 PREV. GRAPH
F8 NEXT GRAPH
F10 Stop
F10 to CANCEL
<CR> = GRAPH
Replay END
Arc specimen ACPD new specimen
2/26/91 09:12:30
300
240
180
120
60
0
0
2000
4000
6000
8000
10000
Graph #6 of 10 PARAM. #4(mV) vs.Ch-2 TIME(sec)

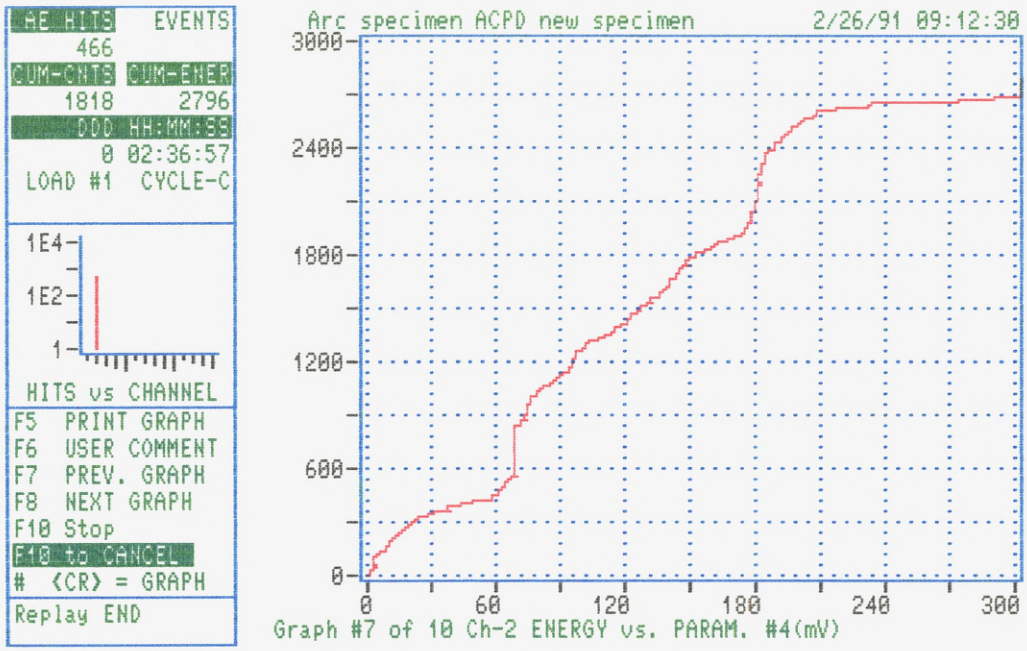
AE HITS
EVENTS
466
CUM-CNTS
CUM-ENER
1818
2796
DDD HH:MM:SS
0 02:36:57
LOAD #1 CYCLE-C
1E4
1E2
1
HITS vs CHANNEL
F5 PRINT GRAPH
F6 USER COMMENT
F7 PREV. GRAPH
F8 NEXT GRAPH
F10 Stop
F10 to CANCEL
<CR> = GRAPH
Replay END
Arc specimen ACPD new specimen
2/26/91 09:12:30
3000
2400
1800
1200
600
0
0
60
120
180
240
300
Graph #7 of 10 Ch-2 ENERGY vs. PARAM. #4(mV)

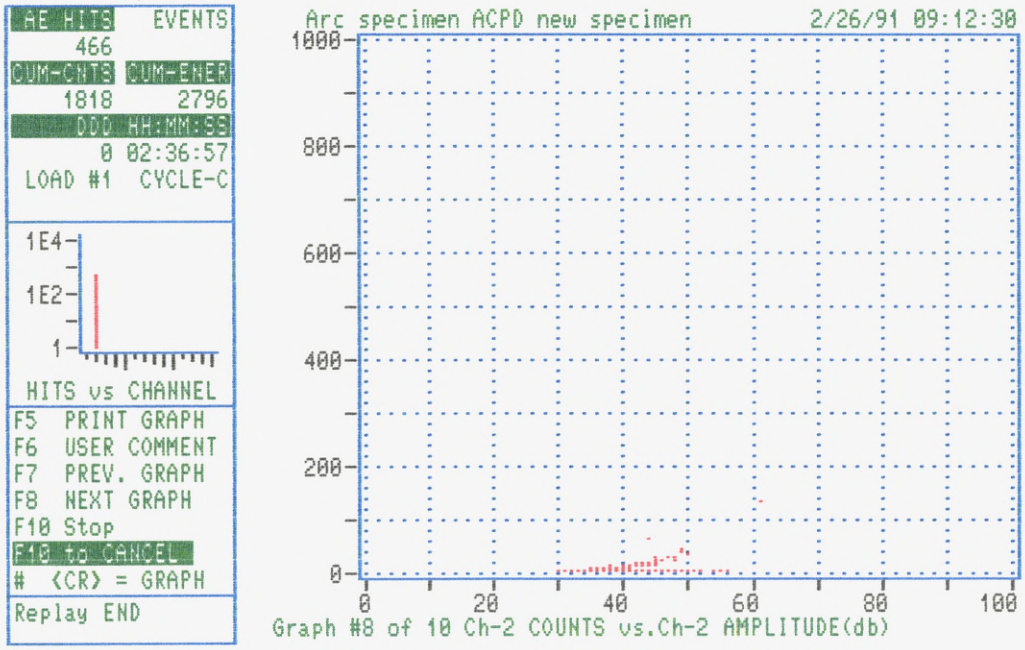
AE HITS
EVENTS
466
CUM-CNTS
CUM-ENER
1818
2796
DDD HH:MM:SS
0 02:36:57
LOAD #1 CYCLE-C
1E4
1E2
1
HITS vs CHANNEL
F5 PRINT GRAPH
F6 USER COMMENT
F7 PREV. GRAPH
F8 NEXT GRAPH
F10 Stop
F10 to CANCEL
<CR> = GRAPH
Replay END
Arc specimen ACPD new specimen
2/26/91 09:12:30
1000
800
600
400
200
0
0
20
40
60
80
100
Graph #8 of 10 Ch-2 COUNTS vs.Ch-2 AMPLITUDE(db)

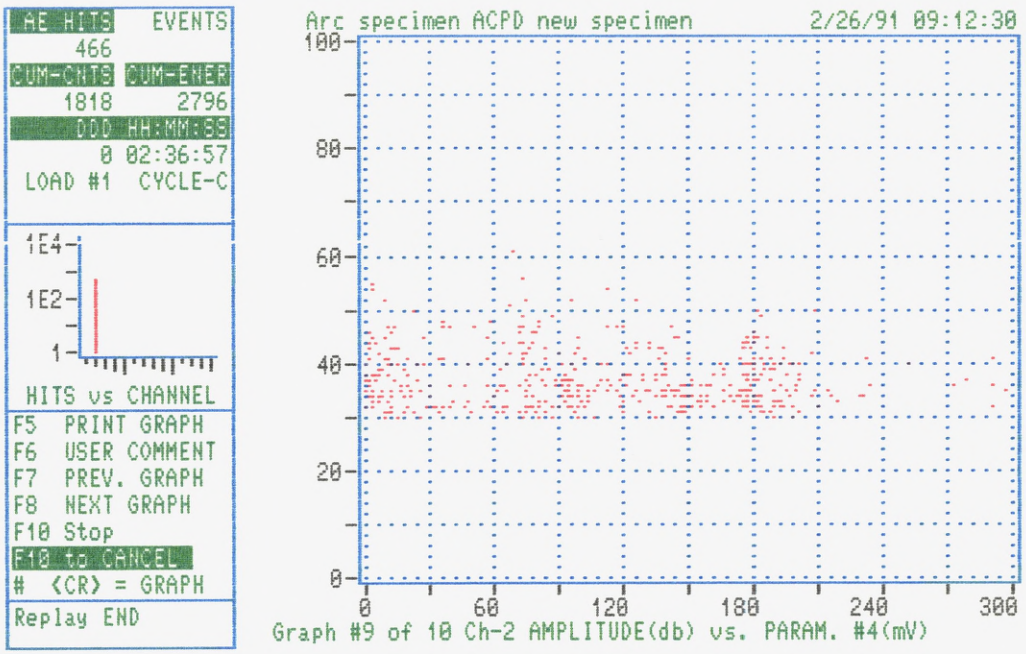
AE HITS
EVENTS
466
CUM-CNTS
CUM-ENER
1818
2796
DDD HH:MM:SS
0 02:36:57
LOAD #1 CYCLE-C
1E4
1E2
1
HITS vs CHANNEL
F5 PRINT GRAPH
F6 USER COMMENT
F7 PREV. GRAPH
F8 NEXT GRAPH
F10 Stop
F10 to CANCEL
<CR> = GRAPH
Replay END
Arc specimen ACPD new specimen
2/26/91 09:12:30
100
80
60
40
20
0
0
60
120
180
240
300
Graph #9 of 10 Ch-2 AMPLITUDE(db) vs. PARAM. #4(mV)

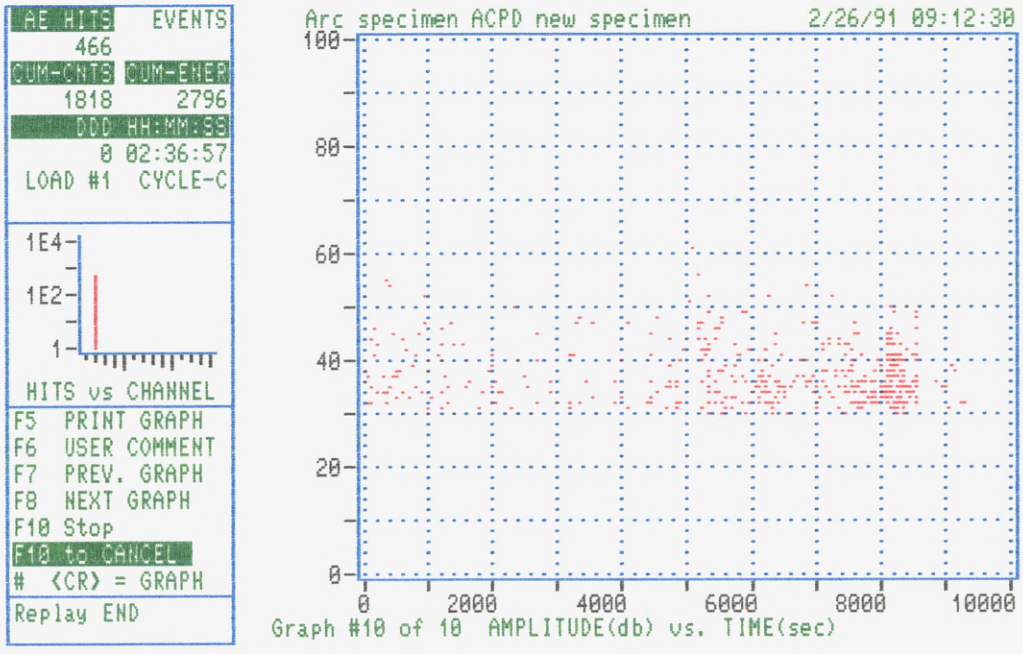
AE HITS
EVENTS
466
CUM-CNTS
CUM-ENER
1818
2796
DDD HH:MM:SS
0 02:36:57
LOAD #1 CYCLE-C
1E4
1E2
1
HITS vs CHANNEL
F5 PRINT GRAPH
F6 USER COMMENT
F7 PREV. GRAPH
F8 NEXT GRAPH
F10 Stop
F10 to CANCEL
<CR> = GRAPH
Replay END
Arc specimen ACPD new specimen
2/26/91 09:12:30
100
80
60
40
20
0
0
2000
4000
6000
8000
10000
Graph #10 of 10 AMPLITUDE(db) vs. TIME(sec)

APPENDIX III

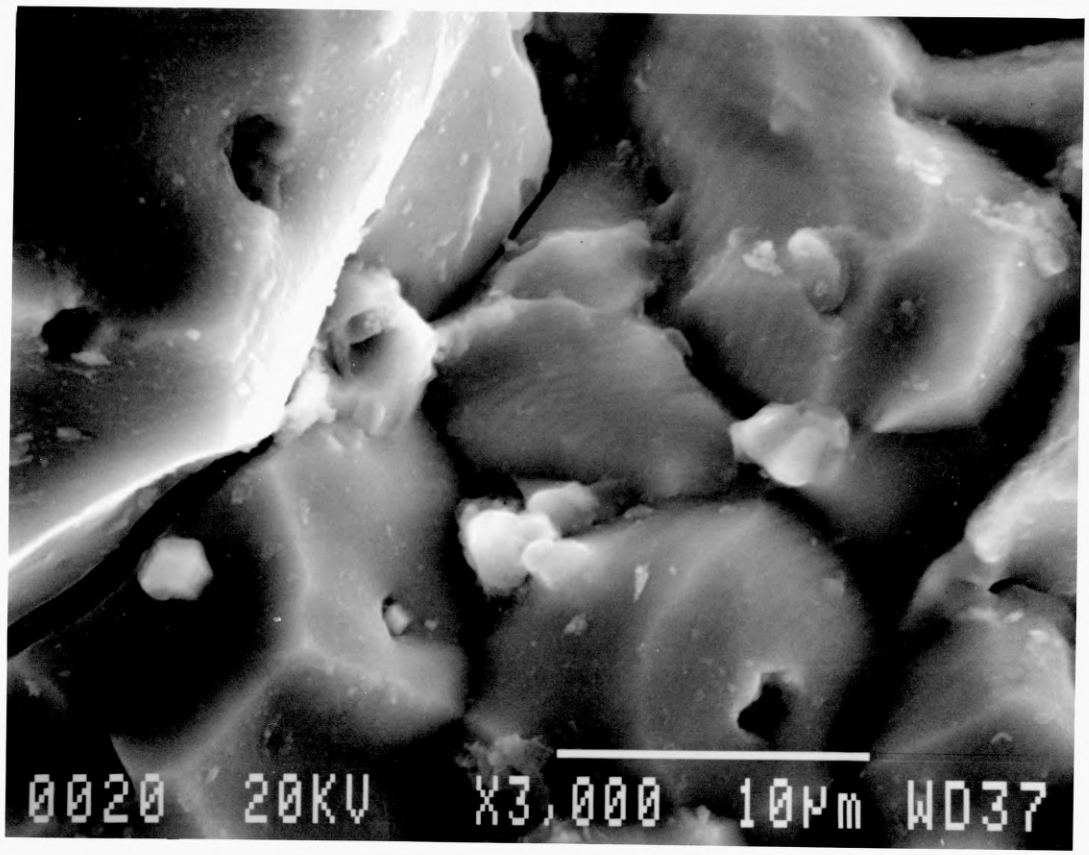

Photo 1. Striations observed on corrosion fatigue fracture surface of the white-zone, barely visible at high kV.

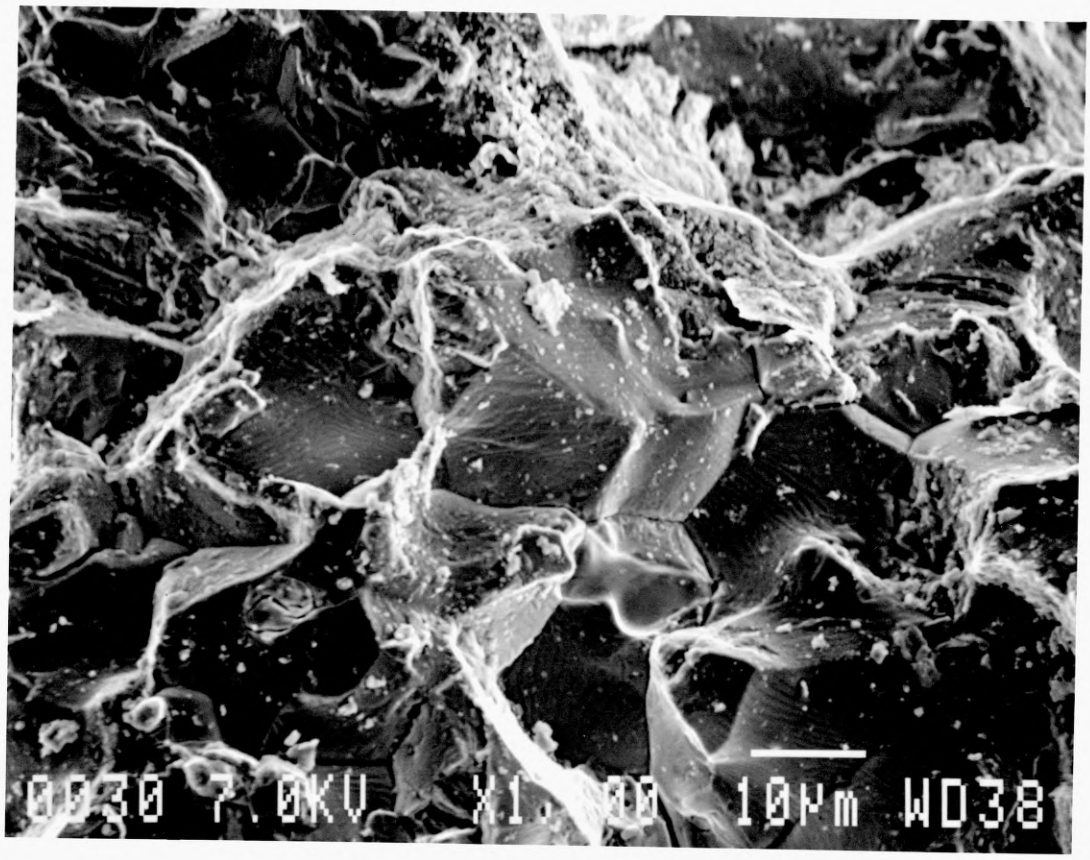

Photo 2. Striations observed on corrosion fatigue fracture surface of the white zone, clearly visible at low kV.

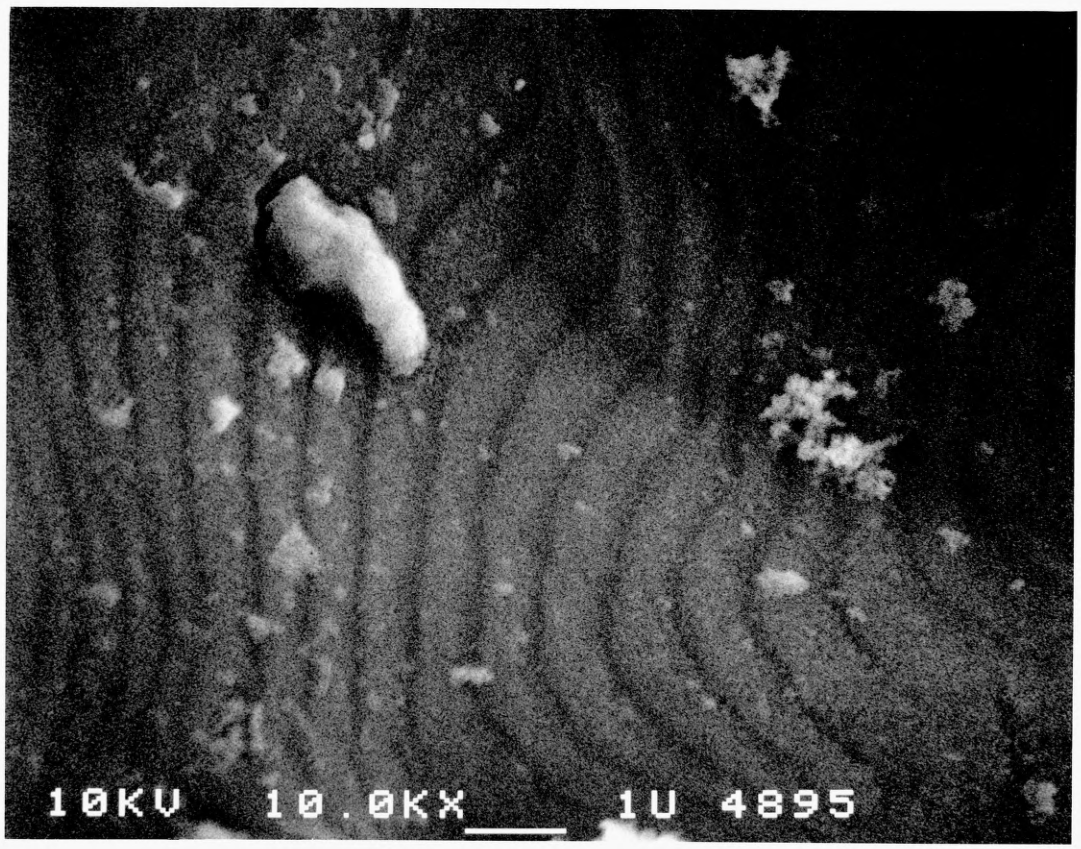

Photo 3. Detail of striations showing a spacing of approximately 1μm.

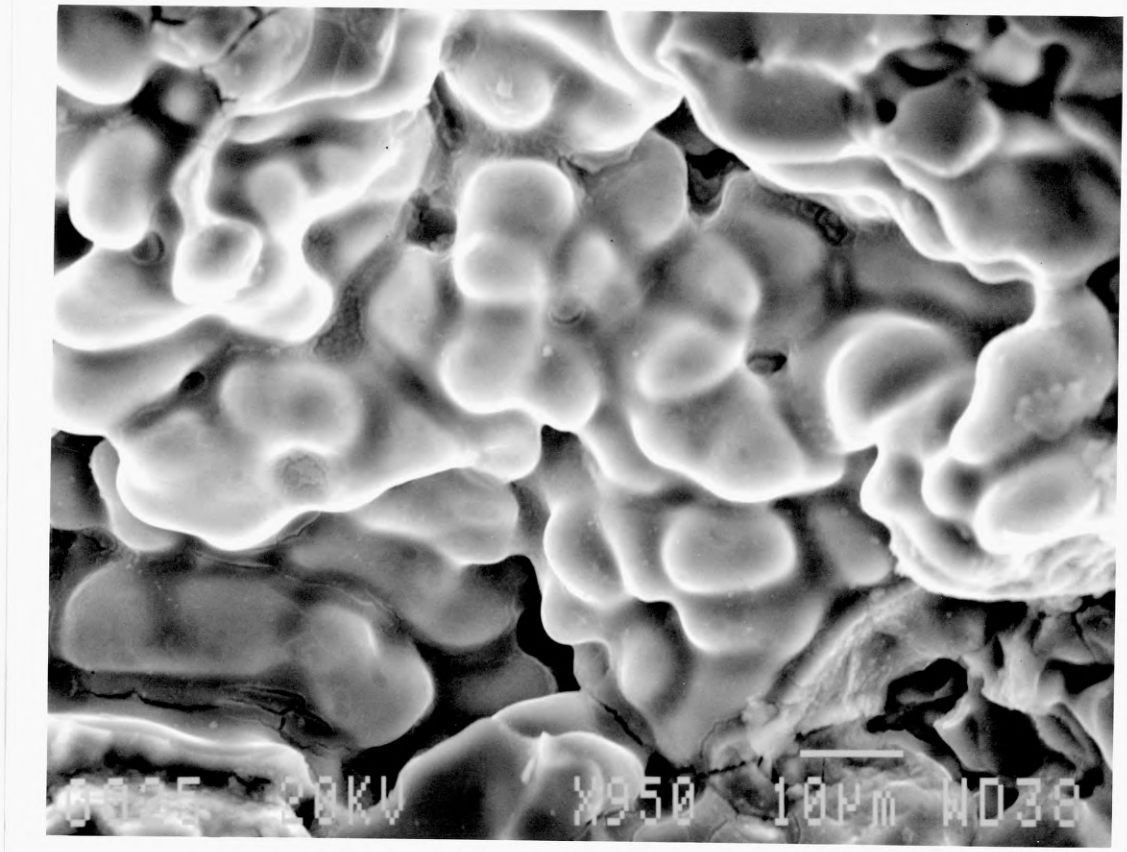

Photo 4. Liquated grains at the white-zone.

Frequency (Hz)	ΔK_{trans} IG/TG ($MNm^{-3/2}$)	da/dN (m/cycle)	ΔK_{trans}^2 IG/TG ($MNm^{-3/2})^2$
0.1	17.3	3.4×10^{-6}	299.3
0.187	15.2	2×10^{-6}	231.04
0.5	12.8	1.2×10^{-6}	163.84
1	10.8	7.8×10^{-7}	116.64
2	10.1	4.4×10^{-7}	102.01
4	9.2	3.4×10^{-7}	84.64
10	9.1	2.9×10^{-7}	82.81
20	9.0	1.8×10^{-7}	81
30	8.9	1.8×10^{-7}	79.21
70	8.8	1.7×10^{-7}	77.44

Maximum ΔK and crack growth rate da/dN for the frequency dependent intergranular-to-transgranular fracture mode transition at different loading frequencies. 7017-T651 plate, tested in the short transverse direction (85).

REFERENCES

(1) FINANCIAL TIMES, Report on aluminium Industry, 28 Oct 1987.

(2) M.C. REBOUL, B. DUBOST, M. LASHERMES, Corrosion Science, vol 25 No 11, pp 999-1018, 1985.

(3) L. CHAMBERS, P. BAXTER, Engineer, 223, p 518, 1967.

(4) S.S. BIRLEY, Weld toe cracking in Al-Zn-Mg alloys, Environmental degredation of engineering materials III, Penn. State Univ., p281, April 1987

(5) K.G. KENT, Metal. Reviews, 15, 147, p135, 1970.

(6) W. GRUHL, International congress on aluminium alloys in the aircraft industry, Turin, 1976.

(7) E.J. KUBEL Jr., Advanced materials & processes, Metals progress 11/86.

(8) R.W. STAEHLE, A.J. FORTY, D. VAN ROOYEN, Fundamantal aspects of scc, NACE, Houston (1969).

(9) J.R. PICKENS, T. LANGAN, Metall. Trans, 18A, p1735, 1987.

(10) I.T. TAYLOR, R.L. EDGAR, Metall. Trans, 2A, p833, 1971.

(11) C.R. SHASTRY, M. LEVI, A. JOSHI, Corrosion Science, 21, p673 1981

(12) K.G. KENT, Metall reviews, 15, 147, p135, 1970

(13) K.G. KENT, J. Inst. Metals, 97, p127, 1970

(14) M.O.SPEIDEL, Fundamental aspects of scc, NACE, Houston Texas p561, 1969

(15) S.P. LYNCH, Mechanisms of environment sensitive cracking of materials, The metals society, London, England, p201, 1977

(16) W.R. MIDDLETON, R.N. PARKINS, Corrosion, 28, p88, 1972.

(17) P.K. POULOSE, J.E. MORALL, A.J. McEVILY, Metall. Trans, 5A, p1393, 1974.

(18) J. K. PARK, Mater. Sc. Eng. A103, p223, 1988.

(19) B. SARKAR, M. MAREK, E.A. STARKE, Metall Trans., 12A, p1939 1981.

(20) D.O. SPROWLS, R.H. BROWN, Fundamantal aspects of scc, NACE, Houston Texas, p466, 1969.

(21) M.O. SPEIDEL, Metall trans., 6A, p631, 1975.

(22) B. SARKAR, M. MAREK, E.A. STARKE, Metall Trans., 12A. p1939 1981.

(23) M.O. SPEIDEL, Theory of scc in alloys, ed J.C. Scully, Brussels, Belgium: NATO, p289, 1971

(24) M.O. SPEIDEL, M.V. HYATT, Advances in corrosion science and Technology, vol 2, N.Y. Plenum press, p115, 1972.

(25) A.H. LE, B.F. BROWN, R.T. FOLEY, Corrosion, 36, p673, 1980.

(26) E.H. HOLLINGSWORTH, J. McHARDY, US Navy contract report, NOW 65-0327f, 1966

(27) H.F. de JONG, Brit. Corros. J., 15, p118, 1980.

(28) N.J.H. HOLROYD, G.M. SCAMANS ASTM-STP 821, p202.

(28) A.J. SEDRICKS, J.A.S. GREEN, P.L. NOVAK, Corrosion, 27, p198, 1971.

(29) N.J.H.HOLROYD, G.M. SCAMANS, R. HERMAN, Corrosion chemistry within pits crevices and cracks, ed. A. Turnbull, London, England HMSO, p495, 1987.

(30) J.A. DAVIES, Localised corrosion, p168, 1972

(31) R.T. FOLEY, T.H. NGUYEN, J. Elctrochem. Soc., p464, 1982.

(32) B.F. BROWN, C.T. FUJII, E.P. DAHLBERG, J. Electrochem Soc, 116, p218, 1969

(33) N.J.H. HOLROYD, G.M. SCAMANS, R. HERMANN, Embrittlement by the localised crack environment, ed. R.P.Gangloff, Warrendale, PA: The metallurgical society, American Institute of Mining, Metallurgical and Petroleum Engineers, p327, 1984.

(34) R.C. TURNER, G.J.ROSS, Canadian J. Chem., 48, p723, 1970.

(35) N.J.H. HOLROYD, D. HARDIE, Hydrogen effects in metals, p449.

(36) K. EBTEHAJ, D. HARDIE, Brit. Corr. J., 24, p183, 1989

(37) J.A. DAVIES, Localised corrosion, p168, 1972.

(38) R.A.H. EDWARDS, Predictive capabilities in Environmentally assisted cracking, N.Y.: American Society of Chemical Engineers, p153, 1985.

(39) Y.C.CHU, S.M. SHU, S.Y. POU, 8th International Congress on Metallic corrosion, vol 1, FRG, Dechema, p499, 1981.

(40) T. OSHINI, Y. NAKATANI, J. Japanese Inst of Light Metals, 27, p224, 1977.

(41) J.K. TIEN, A.W. THOMPSON, I.M. BERNSTEIN, R.J. RICHARDS, Metall. Trans., 7A, p821, 1976.

(42) R.A. ORIANI, P.H. JOSEPHIC, Acta Met. 22, p1065, 1974.

(43) W. GRUHL, Metall. 17, p197, 1963.

(44) F.K. HAYNIE, W.K. BOYD, Scc of aluminium alloys, Battele, DMIC report 228, July 1, 1966.

(45) R.J. GEST, A.R. TROIANO, Corrosion, 30, p247, 1974.

(46) G.M. SCAMANS, C.D.S. TUCK, International conference on mechanisms of environment sensitive cracking of materials, Univ of Surrey, p482, 1977.

(47) G.M. SCAMANS, R. ALANI, P.R. SWANN, Corros, Sc., 16, p443, 1976.

(48) N.J.H. HOLROYD, D. HARDIE, Corr. Sc., 21, p129, 1981.

(49) L. RATKE, W. GRUHL, Werkst u corros., 31, p768, 1980.

(50) P. MARTIN, J.I. DICKSON, J.P. BAILON, Mater. Sc. Eng., 69, p29, 1985.

(51) G. KOTSIKOS own results.

(52) N.J.H. HOLROYD, W. HEPPLES, G.M. SCAMANS, Protection of Al-Zn-Mg welds against exfoliation and scc using aluminium based spray coatings, ASM 8517-046, p291, 1986.

(53) M. PIRNER, Aluminium, 53, p674, 1977.

(54) N.J.H. HOLROYD, D. HARDIE, Unpublished results (private communication with N.J.H. Holroyd, 1989.

(55) H. CORDIER, M. SCHIPPERS, I.J. POLMEAR, Microstructure and intercrystalline fracture in a weldable Al-Zn-Mg alloy, Z. Metallkunde, 68, p280-284

(56) P.M. BARTLE, HAZ embrittlement in Al-Zn-Mg alloys, Proceedings of select conference on weldable Al-Zn-Mg alloys, The welding institute, England.

(57) H. SCHMIEDEL, W. GRUHL, Contribution on the scc behaviour of weld joints in Al-Zn-Mg alloys, Metall., 38, 1, Jan 1984.

(58) G.M. SCAMANS et al, Corrosion science, 1985.

(59) N.J.H. HOLROYD, D. HARDIE, Strain rate effects on environmentally assisted fracture of a commercial high strength aluminium alloy, Corrosion science, vol 21, No 2, p129, 1981.

(60) M.B. SCHUMAKER, R.A. KELSEY, D.O. SPROWLS, J.G. WILLIAMSON, ASTM-STP, 425, p317,

(61) C.D.S. TUCK, Corrosion science, 23, p379, 1983.

(62) R.M.N. PELLOUX, Corrosion fatigue crack propagation, Boeing scientific research laboratories, Seattle, USA, 1969.

(63) R.P. WEI, G. SHIM, Fracture mechanics and corrosion fatigue, ASTM-STP, 801, p5-25, 1983.

(64) A. HARTMAN, J. SCHIJVE, Nat. Bur. Std, NLR-AP-68001-u, 1968.

(65) M.J. HORDON, Acta Met., 14, p1173, 1966.

(66) K.O. SNOWDEN, Acta Met. 12, p295, 1964.

(67) N. MILLER, R.L. SMITH, The effect of various environments on the fatigue cracking of high strength aluminium alloys, ASME 80-C2/PVP-11, 1980.

(68) L.B. VOGELSANG, J. SCHIJVE, Environmental effects on fatigue fracture mode transitions observed in Al alloys, Fatigue of engineering materials and structures, vol3, p85-98, Pergamon press, 1980.

(69) C. LAIRD, G.C. SMITH, Phil. Mag. 8, p1945, 1963.

(70) R.M.N. PELLOUX, Trans ASM 62, p281, 1969.

(71) H. SHEN, S.E. PODLASECK, I.R. KRAMER, Acta Met., 14, p341, 1966

(72) M. SIMNAD, U.R.EVANS, Proc. Roy. Soc., 188, p372-392, 1974.

(73) D.J. DUQUETTE, H.H. UHLIG, Trans ASM, 62, p839-843, 1969.

(74) R.A. OLIEH, PhD thesis, 1980, University of Newcastle upon Tyne, (Private communication with N.J.H. Holroyd).

(75) M.O. SPEIDEL, SCC and HE of iron based alloys NACE, P1071-1094, 1977.

(76) S.J. HUDACK & R.P WEI, Corrosion fatigue, NACE 2, Houston, TX, O. Deveraux, A.J. McEvily, R.W. Staehle, eds, p433, 1972

(77) P.C.PARIS, F. ERDOGAN, J. Basic Eng. ASME, Trans 85, p528, 1963.

(78) R.P. WEI, J.D. LANDES, Mat. Res. Std., 9, p23-27, 1967.

(79) J.M. AUSTEN, E.F. WALKER, Quantitative understanding of the effects of mechanical and environmental variables on corrosion fatigue crack growth behaviour, Proceedings International conf. on the effect of environment on fatigue. Inst of Mech Eng., publ 4, p1-10, 1977.

(80) M.O. SPEIDEL, Corrosion fatigue crack growth rate in high strength aluminium alloy, ICAF symposium, June 1975, Lausanne, Switzerland.

(81) T.W. CROOKER, Fatigue and corrosion fatigue crack propagation in intermediate strength aluminium alloys, ASME, paper 73, Trans ASME 1974.

(82) M.O. SPEIDEL, Corrosion fatigue, NACE, Houston, p324, 1974.

(83) P. BASTIEN, P. AZOV, Academie des sciences compte Rendus, 232, p1845, 1951.

(84) A. FRANK, Internal stresses and fatigue in metals, G.M. Rassweiler & W.L. Grube eds., Elsevier press, NY, 1959.

(85) N.J.H. HOLROYD, D. HARDIE, Factors controlling crack velocity in 7xxx series aluminium alloys during fatigue in an agressive environment, Corr. Sci., vol 23, 6, p527-546, 1983.

(86) A. OHTA, T. MAWARI, Fatigue strength of butt welded Al-Mg alloy, Fatigue fract. eng. mater. struct., vol 13, No1, p53, 1990.

(87) H. SCHMIEDEL, W. GRUHL, Contribution on the scc behaviour of weld joints of Al-Zn-Mg alloy, Metall, 38, 1, p32-37, 1984.

(88) H.L. STARK, R.N. IBRAHIM, Establishing Kic from circumferentially grooved cylindrical specimens, International journal of fracture, 1988.

(89) M. KOCAK, M. Es-SOUNI, L. CHEN, K. SCHWALBE, Microstructure and weld metal matching effects on HAZ toughness, ASME, 8th Intern conf on offshore mechanics & arctic engineering, vol 3, 1989

(90) M. KOCAK, J. KNAACK, K.H. SCHWALBE, Fracture behaviour of undermatched weld joints, Proceedings of the 9th Intern. conf of offshore mechanics & arctic engineering, 1990.

(91) D.P. ROOKE , D.J. CARTWRIGHT, Compendium of stress intensity factors. HMSO, London 1976

(92) Y.S. KIM, S.I. PYUM, Contribution to the mechanism of scc in a welded Al-Zn-Mg alloy, Br. Corr, J., No2, vol18, 1983

(93) T.G.F. GRAY, J. SPENCE, Rational welding design, 2nd ed Butterworths 1982

(94) S. KRUGER, C.E. BIRD, Corrosion of metals by applied alternating currents, Br. Corr. J., No4, vol13, 1978.

(95) H.N.G. WADLEY, C.B. SCRUBY, J.H. SPEAKE, Intern. Metals reviews, review 249, p41, 1980.

(96) E.N. PUGH, Proceedings of atomistics of fracture, ed P.M. Latanison & J.R. Pickens, NY Plenum press, p997, 1983.

(97) R.C. NEWMAN, K. SIERADZKI, Film induced cleavage during scc of ductile metals and alloys, Chemistry and physics of fracture, ed R.M. Latanison, R.H. Jones, The Netherlands, Martinus Nijhoff publishers, p597, 1987.

(98) H.L. STARK, R.N. IBRAHIM, Establishing Kıc from eccentrically fatigue cracked small circumferentially grooved cylindrical specimens. To be published.

(99) I.J. POLMEAR, Microstructural changes associated with recrystallization in the HAZ of welded aluminium alloys. 1st Intern. Symposium on Metallurgy and Materials science, p135, 1980.

(100) K. SAKANO, Precompression cracking method for fracture toughness test, IHI Eng Review, 13, 3, July 1980.

(101) C.T. FUJII, E.A. METZBAUER, Scc of steel weldments, Metals Eng. Quarterly, p15-20, Nov 1976.

(102) O.L. TOWERS, The influence of fatigue load and R ratio on fracture toughness, Welding Institute members report 146, 1981.

(103) M. BRAMAT, J.P. DOUCET, Present aspects of the application of fracture mechanics to welded joints. Soudage et techniques connexes 1977 (Welding Institute translation 484, Oct 1979).

(104) M. KOCAK, GKSS Research center, Geesthacht, private communication.

(105) G.M. SCAMANS, Evidence of crack-arrest markings on intergranular sc fracture surfaces in Al-Zn-Mg alloys, Met. Trans. vol11A, p846-850, May 1980.

(106) P.M. SCOTT, A.E. TRUSWELL, The influence of water chemistry on fatigue crack propagation in LWR pressure vessel steels, UKAEA report AERE-R 10201, June 1981.

(107) R.N. PARKINS, B.S. GREENWELL, The interface between cf and scc, Metal. Sci., 11, p405, 1977.

(108) F.J. BRADSHAW, C. WHEELER, Applied materials research, p112, April 1967.

(109) W.H. HARTT, J.S. TENNANT, W.C. HOOPER, Solution chemistry modification within CF cracks. Corr. Fatigue Technology, ASTM-STP 642, p5-18, 1978.

(110) A. TURNBULL, D.H. FERRIS, Mathematical modelling of the electrochemistry in corrosion fatigue cracks in structural steel cathodically protected in sea water, Corr. Sc., vol26, No8, p601, 1986.

(111) L. CHRISTODOULOU, H.M. FLOWER, Acta Met., 28, 481, 1980.

(112) W. ELBER, Engineering fracture mechanics, vol2, p37, 1970.

(113) T.C. LINDLEY, C.E. RICHARDS, Mat, Sci. Eng., 14, 281, 1974.

(114) A.T. STEWART, Engineering fracture mechanics, vol13, p463, 1980.

(115) S. SURESH, A.K. VASUDEVAN, P.F. BRETZ, Mechanisms of slow crack growth in high strength aluminium alloys: Role of microstructure and environment, Met. Trans. vol15A, pt2, p369, 1984.

(116) J. SCHIJVE, Some formulas for the crack opening stress level, Eng. Fract. Mechanics, vol14, p461, 1981.

(117) C. NEWMAN, Alcan International, private showing of video. (Work to be published)

(118) J.K. SHANG, R. O. RITCHIE, Crack bridging by uncracked ligaments during fatigue crack growth in SiC-reinforced aluminium alloy composites, Met Trans, 20A, p897-908, May 1989.

(119) H.F. de JONG, Aluminium, 58, p526, 1982.

(120) P. MANOGG, Int. Conf. on the Physics of non crystalline solids, Delft, North-Holland, Amsterdam, pp481-490, 1964.

(121) J. F. CALTHOFF, J. BEINERT, S. WINKLER, Fast fracture and crack arrest, G.T. KAHN & M.F. KANNINNEN (eds), ASTM, Spec. Tech Publ. 627, p161, 1977.

(122) V.S. AGARWALA & J.B. BOODEY, Control of scc in high strength aluminium alloys, Chemistry & Physics of fracture, p341-349, The Netherlands, 1977.

(123) G.M. SCAMANS, N.J.H. HOLROYD, C.D.S TUCK, Corr. Sc., vol 27, No 4, p329-347, 1987.

(124) A.A. RUBINSTEIN, Int. J. Fract., vol27, pp113-119, 1985.

(125) C.Y. CHANG, G.S. MING, P.S. YUN, Mechanism of stress corrosion cracking of high strength aluminiumalloy LC4, Proc. 8th Int Congress on metallic corrosion, Mainz, Germany, p499, 1981.

(126) R.E. STOLTZ, R.M. PELLOUX, Met Trans. 3, p2433, 1972.

(127) R.N. PARKINS, B.S. GREENWELL, Metal. Sci. 11, p405, 1977.

(128) R.N. PARKINS, Metals Techn., 9, p122, 1982.

(129) N.J.H. HOLROYD, W. HEPPLES, Private communication.

(130) H.H. CHASKELIS, W.H. CULLEN, J.M. KRAFFT, Acoustic emission from 4340 steel during stress corrosion cracking, Fracture Toughness & Slow-Stable Cracking, ASTM STP 559, p31-44, 1974

(131) P.T. GILBERT, Metallurgical Reviews, 1, pp379-417, (1956).

(132) R.P. WEI, G.W. SIMMONS, International Journal of fracture, vol 17, p235, 1981.

(133) R.G. FORMAN, V.E. KEARNEY, R.M. ENGLE, Journal of Basic Engineering, Transactions of ASME, vol89, p459, 1967.

(134) M. HASHIMOTO, R.M. LATANISION, The role of hydrogen transport in hydrogen embrittlement, Hydrogen in Metals, ASM, Metals Park, OH, p505, 1987.